Deployable Piezoelectric Thin Shell Structures: Concepts, Characterization and Vibration Control

Thesis by
Yuchen Wei

In Partial Fulfillment of the Requirements for the
Degree of
Doctor of Philosophy

CALIFORNIA INSTITUTE OF TECHNOLOGY
Pasadena, California

2019
Defended May 29, 2019

Yuchen Wei
ORCID: 0000-0002-7669-020X

In memory of my late grandparents

ACKNOWLEDGEMENTS

Prior to coming to Caltech, the biographies of three men had great influences on me: Richard Feynman, Von Karman and H. S. Tsien, who were all affiliated with this institute. It is a honor for me to conduct research in the Guggenheim building where Von Karman, his disciples and their successors opened the gate to the supersonic era.

First and foremost, I would like to express my deepest gratitude towards my advisor Professor Sergio Pellegrino. It has been a long way since our first correspondence while I was still working as a researcher in my previous institution. His insights and approaches to hard problems, and his solid support during my entire Ph.D. have been the sources of my intellectual growth. Our weekly one-to-one meetings over the past six years are invaluable. I always felt like wanting to achieve more every time I walked out of his office. He has provided such a well-equipped laboratory that I bragged about it every time I gave a lab tour. His high standards on both himself and us, and his principles of conducting new, innovative, trustworthy research have been the driving force behind this thesis. I still remember when I first started, after several fruitless weeks in the lab and refused to ask for suggestion and help from anyone else, he pointed it out to me in a memorable meeting: "You want to prove to the others, no, to yourself, that you can do anything by yourself." I won't reveal more sage advices about research and life from him, which might fill a considerable number of pages.

I have learned at least an equal amount, or even more from my truly superb past and current colleagues in the Space Structures Lab. To me, they justify the essence of Caltech: working with the best. Special thanks to Prof. Xin Ning and Dr. John Steeves who have been my mentors ever since I first joined the group. Their brilliance and sharpness inspire me to produce work of equal quality as theirs. I've been benefiting from discussions with them till today. I want to thank Serena Ferraro (who can be more rigorous than you?), Christopher Leclerc (who can be more piercing than you?), Dr. Yang Li (the true thinker), Dr. Lee Wilson (there's nothing you can't model), Dr. Maria Sakovsky (the elegant), Antonio Pedivellano, Alex Wen, Michael Marshall, Alan Truong, Harsha Reddy, Charles Dorn and Kanthasamy Ubamanyu for their discussions and unconditional support. I want to also thank Dr. Manan Arya, Dr. Keith Patterson, Dr. Ignacio Maqueda and Dr. Kristina Hogstrom for their conversations and guidance which helped to

shape my understanding of the different research styles and the vast topics covered in the group.

I will never forget the experience of working with all the French members of our group: Dr. Melanie Deplapierre, Dr. Marie Laslandes, Thibaud Talon, Charles Sommer, Fabien Royer, and the irreplaceable Dr. Wilfried Jahn. They naturally bring a sense of aesthetics into their work. My conclusion is that their aesthetics origin half from the influence of their culture and half from mathematics which flows with their blood. Through collaborations with them, I have made up my mind to actively search for French colleagues in my future career.

The current and past post-doc members of the group have always amazed me with their professionalism. Working aside them, I realized they are all top in their fields. I thank Dr. Kathryn Jackson, Dr. Stephen Bongiorno, Dr. Ashish Goel, Dr. Nicholas Lee, Dr. Armanj Hasanyan, Dr. Luke Chen, Dr. Daniel Turk, Prof. Federico Bosi, Prof. Miguel Bessa for all the fresh ideas they brought and shared. I want to thank our staff engineer Petros Arakelian for his help with experiment setups, and his kind conversations.

I would like to pay my deep respect towards Dr. James Breckinridge. He is a tireless educator on optical systems, an enthusiastic consultant for the AAReST project, and a magician who can always link us to the top researchers in the field. He has the heart, mind and curiosity of a vibrant young scholar. I wish to be like you when I am in my 80's, Jim.

I would like to thank my candidacy committee: Prof. Michael Ortiz, Prof. Dennis Kochmann, Prof. Mathiew Desbrun for providing feedback and incentives for my work. I thank Prof. Chiara Daraio, Prof. Guruswami Ravichandran and Prof. Soon-Jo Chung for serving on my thesis defense committee. Prof. Christopher Lynch from UCLA was kind to open his door to me and answer my questions about the details in piezoelectric material experiments. Phone calls with Prof. Robert McMeeking helped to assure myself that I was on the right path. Discussions with Prof. Soon-Jo Chung towards the end of my Ph.D. have helped me staying on track regarding the last part of this work, and I also thank him for letting me audit his state of the art control system classes. Faculties in the AE, MCE and CMS departments have provided a curriculum of the highest quality one can expect, from which I have benefited greatly.

The 2003 Mars landing of the Exploration rover has had a huge impact on me.

It is the view in the JPL control room on that day which navigated me into the fascinating world of aerospace. Gaining the opportunity to interact with the JPL associates are just incredible experiences. I appreciate the mentorship of the amazing Dr. Greg Davis and Dr. Anthony Freeman during the project formation years for the AAReST telescope. It was one of the peak moments in my life when Mr. John Baker introduced me to Mr. Wayne Lee, who led the system design of the historical Exploration landing. Dr. Dan Scharf has shown me the importance of being a good communicator and trying your best to enjoy life. I thank him for introducing me to the world of control system with great patience, and his efforts in helping me improve the clarity of the work. I thank the erudite Dr. Andrew Shapiro for all the expertise and resources he brought into the group.

My friendships have been the force and strength that accompanied me through the happy and bitter times of the past six years. I thank my genius roommate Nicholas White, the second-to-none aerospace engineer Finn Carlsvi, the pro-gamer Dr. Nathan Martin, Cong Wang, Xiaoxing Xia, Dr. Yujie Tang, Chenxi Zhang, Dr. Xiaoyue Ni, and many more. Special thanks to Mr. Zheng Tao who has shown me the spirit, grit and skills of a true aviator and a Beihang graduate.

I want to thank the administrators of GALCIT: Jackson Kathleen, Christine Ramirez, Peggy Blue and Dimity Nelson who have been the fabrics of this department. They've made my experience at Caltech organized and left nothing to worry about. Laura Kim and Daniel Yoder from the International Students Program office are always there with their warm help at every point of my immigration process.

In the end, besides my own work, I attribute all my achievements to my parents. They have endured my long absence from home, which is hard to imagine from a child's point of view. I look forward to sharing my next journey with them.

ABSTRACT

The thesis presents three interconnected technology paths to the design and realization of novel deployable active thin shell structures. The baseline concept envisioned is built upon a deployable ultra-thin piezoelectric active thin shell architecture, with segmented tessellations. This vision is motivated by the need to deploy and control large, curved and precise surfaces for a variety of applications including future space telescopes, and is made possible by recent progress in ultra-thin high-performance composites and active material technologies. The thesis uses a combination of heuristic design, theoretical analysis, numerical modeling and novel experimental techniques to construct and validate proposed concepts for deployable piezoelectric thin shells.

Specifically, the thesis answers the following questions: i) How to design and manufacture precise, foldable and curved piezoelectric shells. ii) How to deploy these shells reliably and maintain shape correctability in the deployed state. iii) How to synthesize large, curved deployable surfaces with the aforementioned advantages. iv) How to characterize and predict the nonlinear behavior of piezoelectric materials and thin structures under high electric field actuation and large bending deformations. v) How to improve the shape stability of piezoelectric active thin shells under dynamic disturbances without introducing external sensors.

First, the thesis proposes new methodologies and design criteria to synthesize deployable, modular edge-supported thin shells based on a combination of origami-inspired folding patterns and spatial mechanisms. In contrast to traditional deployable surface designs, which attach rigid shells to deployable trusses, the proposed methodology enables concurrent folding of flat or curved shells along with the support structures. Starting from a basic module, a variety of deployable surface concepts are proposed through tessellations of the module.

A piezoelectric material unimorph architecture is further introduced, providing global curvature and shape correction capabilities. All components of the basic concept are validated through model prototyping and material folding tests, and it is discovered that both the ultra thin carbon fiber composites and piezoelectric ceramic materials can achieve a small folding radius without failure. A composite, doubly-curved foldable shell is also designed and manufactured while still maintaining low shape error. These efforts have led to a new family of deployable piezoelectric thin

shell structures that integrate low areal density, high shape accuracy, and structural foldability to an unprecedented degree.

The thesis then tackles the challenge of estimating the actuation response and residual structural deformation of unimorph active thin shells under high electric field and large bending motion. A rate-independent, full field phenomenological constitutive model for a polycrystalline piezoelectric material is characterized experimentally. It successfully captures both the observed ferroelectric and ferroelastic domain switching effects. To overcome the difficulty of testing ultra thin piezoelectric plates, a set of novel characterization techniques is developed and implemented to measure the dielectric and mechanical responses of this material. The characterized material constitutive relation is implemented in an efficient model for estimating the structural response of unimorph thin shells under general electric and mechanical loading. The complete set of governing equations is integrated with a Backward-Euler algorithm, reproducing the measured responses of both the material and the structure under complex loading sequences.

Active vibration damping based on self-sensing piezoelectric thin shells is then analyzed and demonstrated on testbed. The self-sensing architecture removes redundant external sensors by making dual use of the piezoelectric layer of the active shell. An adaptive identification method with the associated hardware to track the evolution of field dependent piezoelectric capacitance is implemented, and a new identification strategy is proposed. Closed loop damping with in-situ capacitance adaptation is conducted in bench tests on self-sensing cantilever beams and achieves -12 dB attenuation at the resonance frequency. A highly efficient modeling technique for general self-sensing piezoelectric thin shell structures is proposed which is able to construct closed loop dynamic models based on the vibration eigenmodes and actuation responses obtained from commercial finite element software. These validated modeling techniques are extended to a multi-electrode doubly curved thin shell, where the improvements of shape stability under closed loop damping are evaluated through simulations. It is discovered that the electrode pattern of the self-sensing piezoelectric layer determines the damping performance under the specific boundary conditions of the shell.

PUBLISHED CONTENT AND CONTRIBUTIONS

[1] **Y. Wei** and S. Pellegrino, "Phenomenological model for coupled multi-axial piezoelectricity," *Behavior and Mechanics of Multifunctional Materials and Composites XII*, vol. 10596, 105960R, 2018. DOI: 10.1117/12.2296346,
Y, Wei. performed experimental characterization of the piezoelectric materials, implemented the phenomenological model, performed model calibrations and wrote the manuscript.

[2] ——, "Modular foldable surfaces: A novel approach based on spatial mechanisms and thin shells," *4th AIAA Spacecraft Structures Conference*, p. 1345, 2017. DOI: 10.2514/6.2017-1345,
Y, Wei. proposed the concept of edge supported modular thin shell surfaces, performed FEM analysis of the foldable assembly, constructed the prototype and wrote the manuscript.

TABLE OF CONTENTS

LIST OF ILLUSTRATIONS

LIST OF TABLES

Chapter 1

INTRODUCTION

1.1 Motivation

Deployable thin shells are a class of shell structure able to endure large local or global deflections, and then restore the original shape. Deployable thin shells are attractive for both aesthetic and functional reasons. Up until the last decade, deployable thin shells were mostly limited to boom-like geometries, which functioned as actuators to deploy antennas, solar sails, and solar panels. The pull from the applications side have called for deployable thin shell structures with more complicated geometries, which have posed new challenges in terms of packaging, deployment, and shape stability.

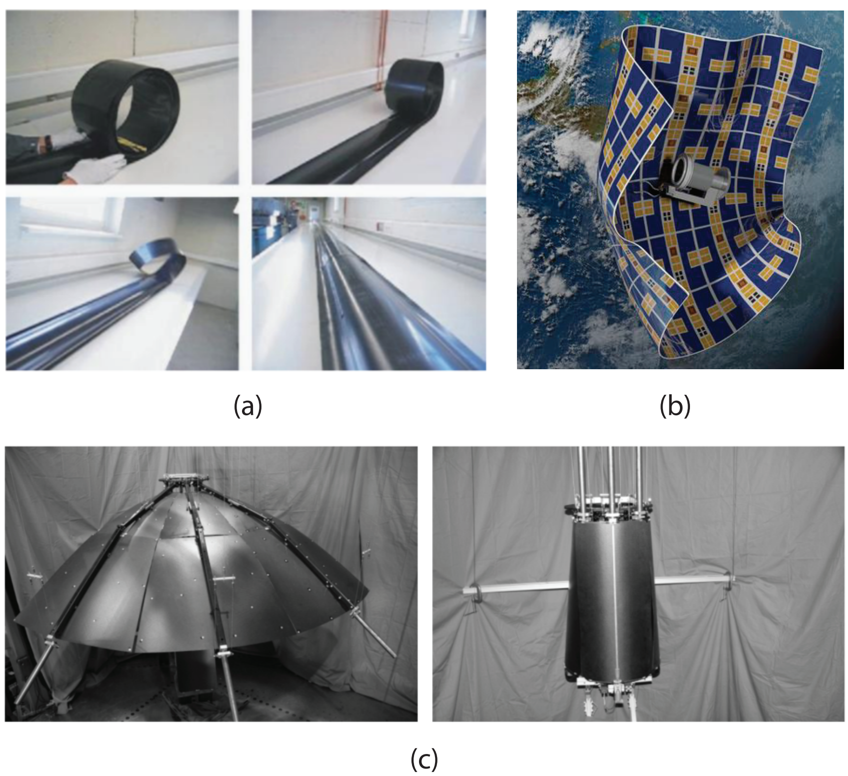

Figure 1.1: Examples of deployable thin shells in space applications: (a) Self deployment of a 14 m deployable boom developed at the German Aerospace Center (DLR) [1]. (b) The Brane Craft space debris removal spacecraft from Aerospace Corporation [2], and (c) Deployed and stowed configurations of the Multi-Arm Radial Composite (MARCO) reflector with segmented high strain composite shells [3].

Many application areas could benefit greatly from the shape morphing capability of deployable thin shells, which offers attractive attributes in terms of launch cost and structural mass [4]. Specific examples are space based observation platforms, such as space telescopes. For these optical systems, the size of the main aperture determines the capability to observe with a high resolution and level of signal to noise ratio. Concepts have also been proposed for space debris removal [2] and large scale space solar power generation [5] which involve deploying large shell structures in orbit. Deployable thin shell structures are key function enablers for these missions.

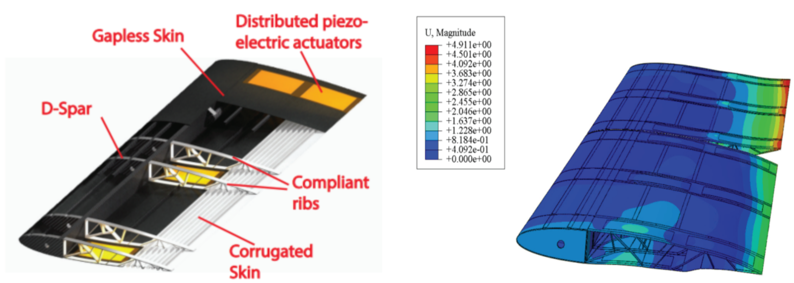

(a)

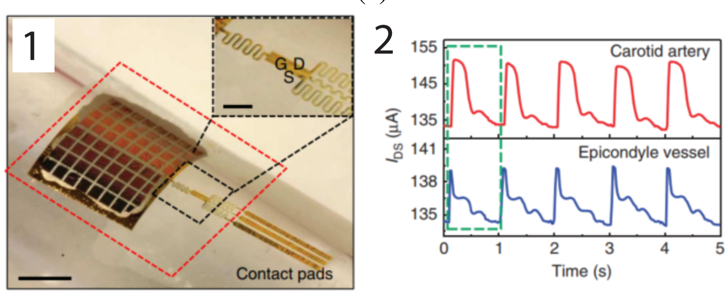

(b)

Figure 1.2: Macroscopic and microscopic piezoelectric thin shell structures: (a) The piezoelectric morphing wing and the displacement contour to command a roll maneuver of the aircraft [6], (b) (1) A Lead Zirconate Titanate (PZT) pressure sensor wrapped around a cylindrical glass substrate. (2) Current responses measured on a human body [7].

The introduction of piezoelectric components to thin shells enables the structures to be active and adaptive, and have been widely studied over the past two decades. Piezoelectric based active thin shells have enabled shape correction [8], buckling control [9], vibration damping [10] and in-situ sensing [11] applications with great precision and a broad bandwidth. Recently there has been an increase of piezoelectric active thin shells in shape morphing applications, with a trend moving towards light-weight, high-strain, and high structural efficiency designs. At the macroscopic scale, piezoelectric Macro Fiber Composite (MFC) based morphing skins have been used to introduce chord-wise deformation of aircraft wings to supplant conventional ailerons [6]. At the microscopic scale, devices based on piezoelectric shells have been used for mechanical energy harvesting, sensing and actuation which can be stretchable and conformable to different curvatures [7].

Recent advances in material science and deployable structures have created new design opportunities for piezoelectric-based deployable thin shell structures. Advances include: i) ultra-thin, high modulus, and high strength carbon fiber composites, ii) ultra-thin piezoelectric materials with high electro-mechanical coupling coefficients, and iii) origami inspired packaging schemes. Despite the large body of studies in individual fields, novel deployable thin shell structure concepts built upon these advancements remain scarce. In addition, the interactions between the piezoelectric components and the thin shell substrates must be understood in order to facilitate precise actuation and sensing functionalities. These challenges form the main focuses of this thesis.

1.2 Background

1.2.1 Existing Deployable Shell Structure Concepts

Packaging and deploying thin shell structures remains difficult, with challenges from both the material and the kinematics. Conventional designs focus on packaging rigid shells with deployable space frames. A representative conventional packaging design is used by the James Webb Space Telescope (JWST) [12]. Its primary segmented mirror is composed of a tessellation of 16×1.2 m beryllium rigid shells, attached to a foldable, articulated back truss. Although these packaging schemes are capable of achieving a determinant and precise post deployment configuration, weight penalty and structural complexity are typical disadvantages. Moreover, these designs cannot fully exploit the folding potential of thin shell structures. Two paths were identified as candidates to further develop deployable thin shell structures: thin shells with elastically foldable surfaces and origami inspired folding pattern designs. Both paths will be briefly reviewed in the following sections.

1.2.1.1 Deployable Thin Shells Based on Ultra Thin Substrates

Advanced laminates made from carbon fiber reinforced composite (CFRP) materials are quickly replacing isotropic materials in thin shell applications [15]. As higher

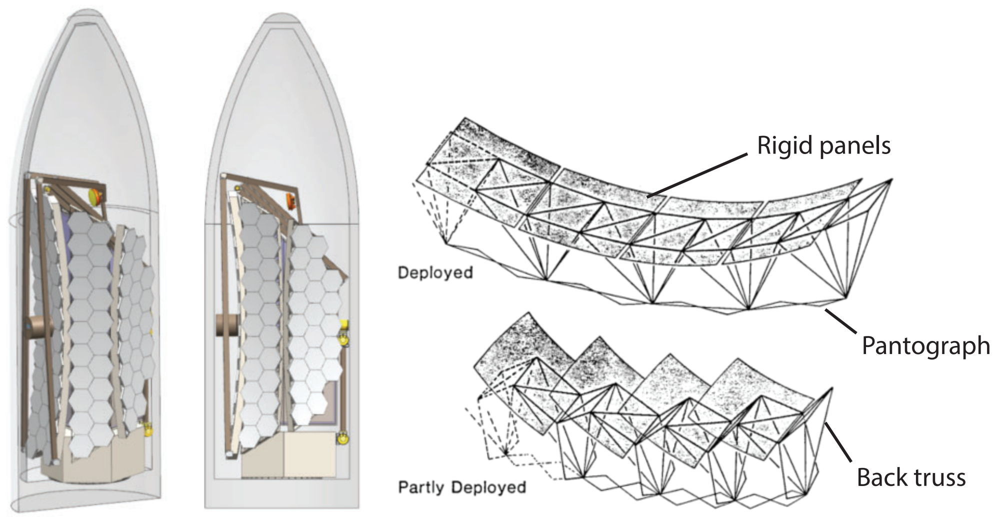

(a) (b)

Figure 1.3: Two deployment schemes for rigid shells with foldable trusses: (a) Folding scheme of Luvoir-A aperture in stowed configuration inside launch fairing [13], (b) Synchronously deployable concept for stiff-panel reflectors proposed by Hedgepeth to deploy large solar concetrators [14].

modulus, higher tensile strain limit carbon fibers have emerged, bending/rolling of ultra-thin CFRP substrates has become possible, which has resulted in a series of self-deployable shell designs. The Boeing Tracking and Data Relay Satellites (TDRS) springback reflector is a representative design (figure 1.4a) [16]. Two reflectors are attached to the side of the satellite platform with arms and spring mechanisms; each shell can be rolled to half its original size over the other shell. Each reflector shell is made completely from triaxially-woven CFRP materials and is manufactured as a single part. DLR and the Technische Universitaet Muenchen have developed similar folding concepts with a new radio frequency (RF) reflecting material, based on carbon fiber reinforced soft silicone (CFRS) [17]. The material provides good in-plane stiffness and can be folded and deployed easily. Based on the mixture usage of CFRP and CFRS materials, a foldable shell-membrane reflector was manufactured and tested, as shown in figure 1.4b. The shell's stiff back ribs and soft surface can be folded and deployed simultaneously.

Two outstanding issues of woven composite-based thin shells are the attainable shape accuracy and surface roughness. It is a challenging task to achieve a surface accuracy lower than 500 μm, which limits its applications to L and S band telecommunications with a surface requirement of $\lambda/50$ (λ is the operating wave length). The semi-transparent mesh-like reflector surface also precludes usage in the visible light

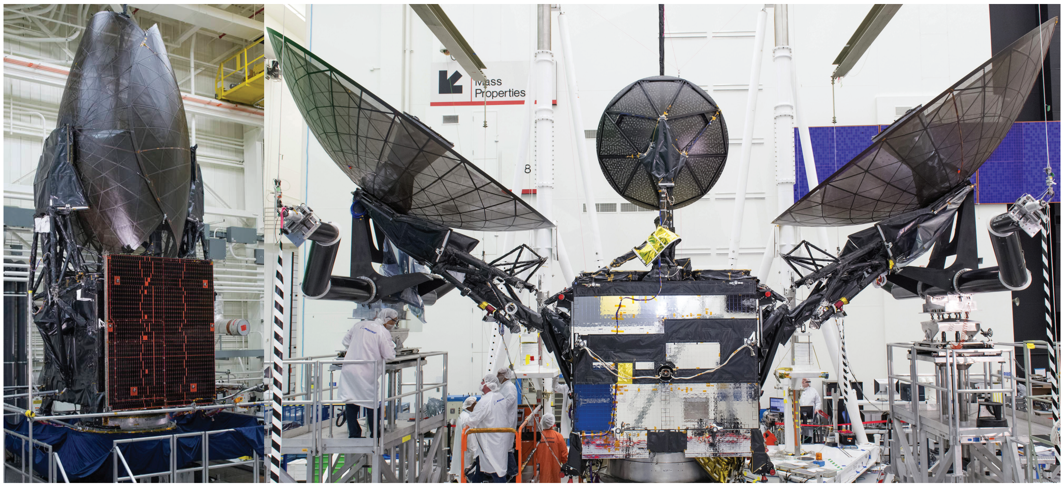

(a)

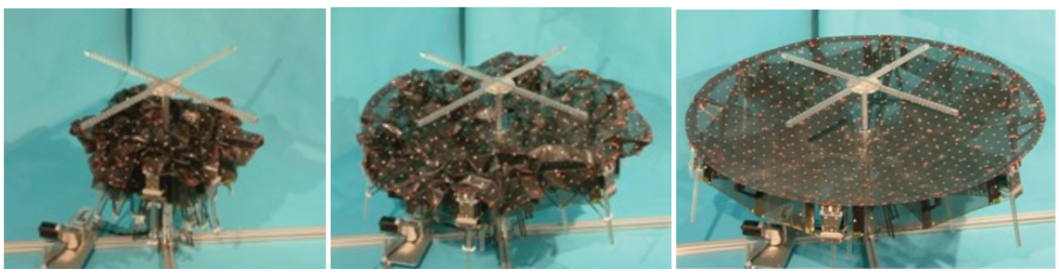

(b)

Figure 1.4: Examples of foldable flexible shells: (a) Spring back reflector based on woven CFRP material of Boeing TDRS satellite, in folded and deployed configurations [16]. (b) Deployment of the structurally adaptive fiber reinforced surface made from carbon fiber reinforced elastomer [17].

spectrum. Researchers in the CFRP mirror manufacturing field have further pushed the limits of thin, rollable shell technology. CFRP mirrors are usually made from multi-layer prepreg-based laminates through an optical replication process and are cured in autoclave. Commercial products with a global wavefront error of less than $\lambda/10$ @ 638 nm have been demonstrated [20]. To overcome the difficulty in achieving high post cure shape precision, existing carbon fiber mirrors usually have high thickness and ply number to increase the bending stiffness, typically on the order of 1 mm or higher.

It was discovered that thin and flexible high-strain composites under flexural loading can endure higher strain than under compression and tension. Taking advantage of this phenomenon, when the ply count and thickness of a CFRP laminate shell was significantly reduced, precise rolling or folding of a shell became possible [21]. A 90 *cm* diameter, 1 mm thick doubly-curved rollable CFRP mirror was manufactured

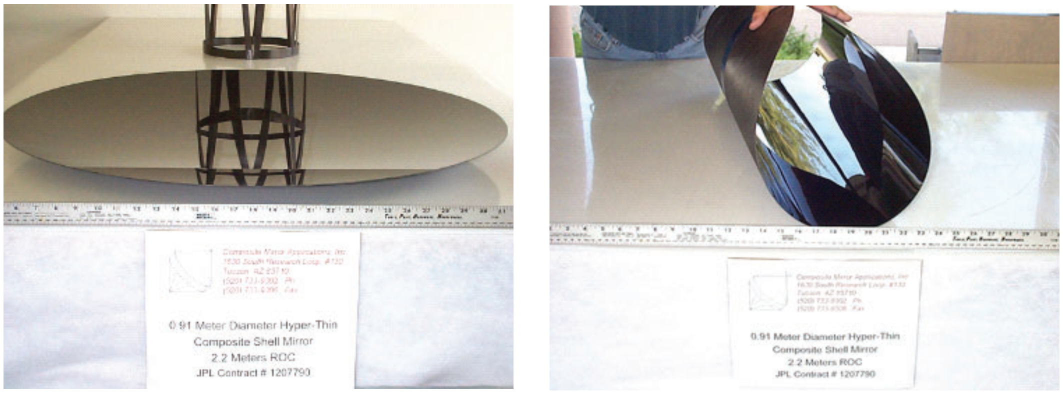

(a)

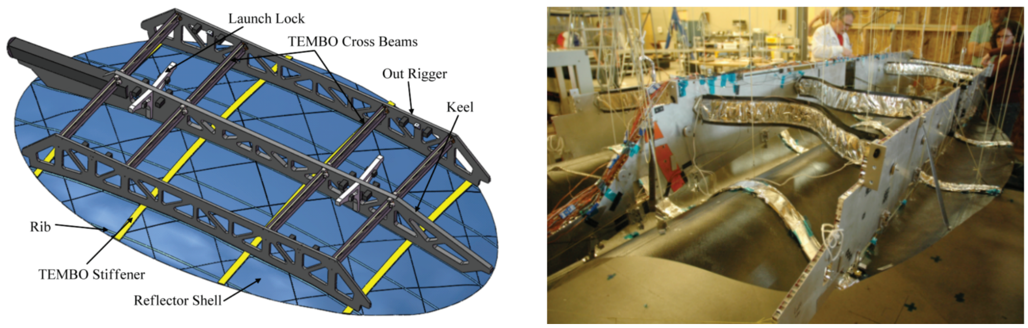

(b)

Figure 1.5: Examples of continuously rollable CFRP shells: (a) A 90 cm CFRP mirror in deployed and rolled up state [18], by courtesy of the authors. (b) Deployable solid surface reflector developed by Composite Technology Development (CTD) Inc. [19]

and successfully rolled into a taco-shape. The front surface was coated with a thin layer of reflective material. No hysteresis deformation was reported after unrolling the shell, given a short stowage time. A systematic study was conducted by Banik in AFRL to evaluate the stowage and deployment strength of thin, composite shells of large dimensions [22].

Compared to the successful applications of woven composites based deployable shells, to the author's best knowledge none of the rollable CFRP thin shell prototypes have reached a Technology Readiness Level (TRL) sufficient for a flight mission, mainly due to the substrate's high level of residual deformation after long-term storage. Reducing the shell's thickness may alleviate the bending strain and viscoplastic deformation during folding and storage; however, it gives rise to more pronounced manufacture induced errors, typically in the form of astigmatism on the global shape. The challenges remain to improve the folding design, processing, and to develop shape correction technique of ultra-thin CFRP substrates for deployable thin shells.

1.2.1.2 Origami-inspired Deployable Thin Shell Structures

Recent years have seen rapid growth of applications inspired by origami engineering [23]. Origami is the art of paper folding without cutting or stretching the paper. It has brought the morphology capability of thin shells to a new level. For space applications, it has long been adopted to transform structures from compact configurations to highly-expanded configurations. Such structures span from sun shields to solar arrays and solar sails. Rigid origami eliminates elastic deformation during folding, and is favored in engineering applications due to its scalability, small degree of freedom, and flat-foldability [24]. The most famous and wide-spread rigid origami pattern is the Miura-Ori, adopted for the deployment of rigid solar panels. It has only one degree of freedom, and is flat foldable. The Japan Aerospace eXploration Agency (JAXA) successfully deployed a solar array folding experiment flown by NASA's Space Shuttle mission STS-72 [25].

Another representative origami pattern is the flasher model, shown in figure 1.6. Zirbel et al. proposed a flasher-based solar array, which is rigid foldable and can be deployed by a peripheral deployable truss [26]. The array was stowed around the circumference of a hexagonal spacecraft and was capable of accommodating the thickness of panels by adjusting the foldline width. This technique has been used to construct segmented diffractive lenses [27].

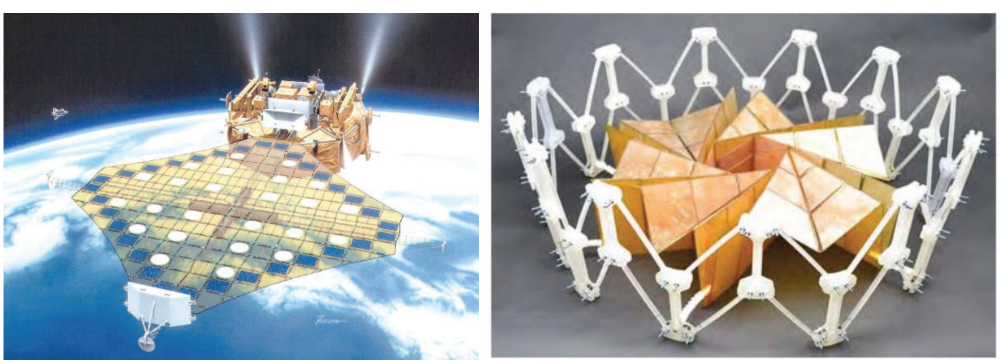

(a) (b)

Figure 1.6: Origami inspired solar arrays a) the 2D array experiment onboard the Space Flyer Unit [28] b) Partially opened rigid foldable deployable solar array [26].

However, origami based folding designs are not suitable for deploying curved thin shells, and usually suffer from excessive degree of freedom. Among the many concepts proposed, flexible material based origami by and large is still a territory seldom explored. The problem of how to deploy curved surfaces precisely and reliably remains unsolved. Traditionally, curved origami can be produced by introducing curved crease lines [29]. For substrates with finite thicknesses, this technique can easily induce micro-buckling or failure in the material, thus, having limited application in engineering.

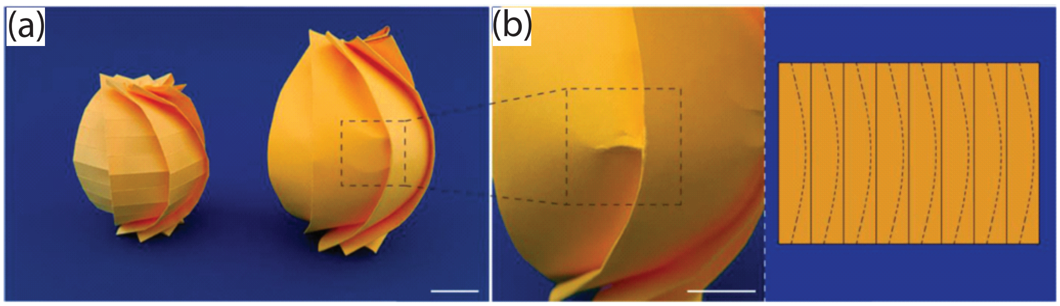

Figure 1.7: Curved-crease origami examples: (a) Standard origami sphere obtained from Mitani's method [30] (left) and smooth variant (right) [31]. (b) Closer view of local buckling between curved and straight creases [31].

1.2.2 Overview of Piezoelectric Active Thin Shells

Piezoelectric materials have long been used for sensing and actuation within thin shell structures. Piezoelectricity is a material property that commonly appears in ferroelectric materials [32]. The direct piezoelectric effect represents the material's ability to generate electric charge when subjected to mechanical stress. The inverse piezoelectric effect represents the relation between the mechanical displacement (strain) and the applied electric field or charge. In the following, the direct and inverse piezoelectric effects are collectively referred to as 'piezoelectric effect.' The term 'piezoelectric material' denotes ferroelectric materials that exhibit piezoelectric effect.

Typical selections of piezoelectric materials include polyvinylidene fluoride (PVDF) polymers and lead zirconate titanate (PZT) ceramics, which both have unet spontaneous polarizations even when no electric field is applied [33]. Due to their broad bandwidth, fast response, high stiffness, and high blocking force, piezoelectric ceramics are especially suitable for driving thin shell structures with stiff substrates.

1.2.2.1 Thin Shell Actuation Schemes

Active mirror technology for adaptive optic applications continues to evolve. Representative actuation schemes include: i) surface normal actuation, ii) boundary actuation, iii) surface parallel actuation (known as the unimorph configuration), and iv) a combination of individual methods. An illustration of the first three actuation schemes is shown in figure 1.8.

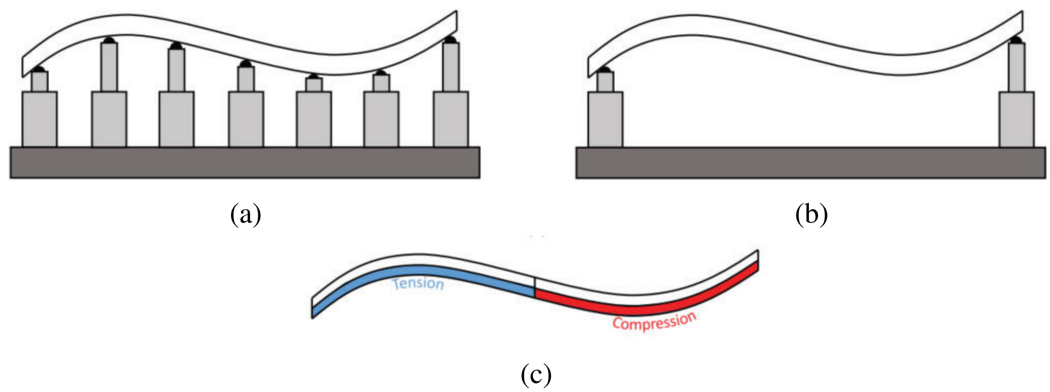

Figure 1.8: Actuation schemes for deformable mirrors: (a) surface normal; (b) boundary actuation; (c) surface parallel (unimorph configuration).

For small scale applications, Micro-Electro-Mechanical Systems (MEMS) based commercial active thin shell structures have been used extensively in adaptive optics [34]. Typical substrate materials include silicon membrane [35], [36] and glass [37], [38], as shown in figure 1.9. These mirrors can have thousands of actuation channels with ultra-fine adjustment capability. Boston Micromachines Corp developed a 4096 element membrane deformable mirror for a planet imaging instrument, with a 4 μm stroke and < 10 nm root mean square (RMS) error [39].

For medium to large dimension applications, a light-weight, deformable and actively controlled primary mirror plays a crucial role in future space missions [40]. The deformation capability eases the requirement of initial shape precision of the substrate, and is key to attaining a diffraction limited imaging in visible and infrared spectrum. Both surface normal and surface parallel actuation scheme have been applied to existing and future space telescope systems, but with a much more limited actuator count.

Active CFRP thin shells have also seen significant developments over the years [43]. Lan et al. [44] developed an adaptive control scheme for a 1 m diameter graphite composite reflector with triangular patterned back ribs and PZT actuators fitted

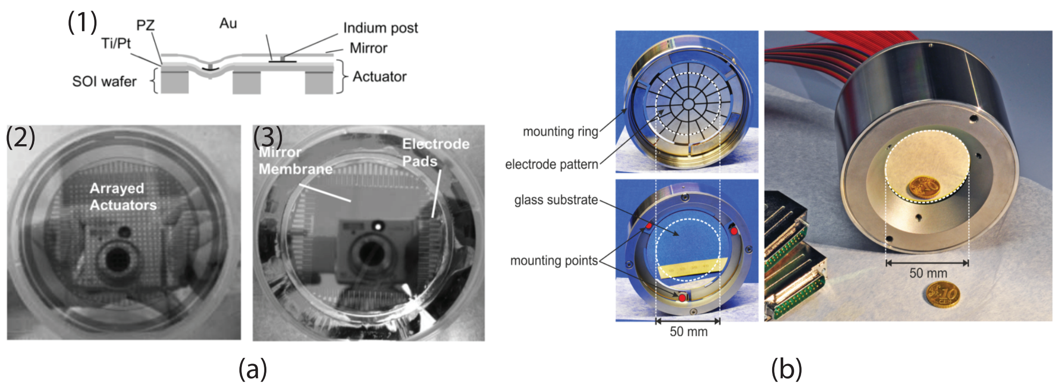

Figure 1.9: (a) A deformable mirror with 20 × 20 piezoelectric unimorph actuator array. (1) Cross-sectional schematic. (2), (3) Actuator arrays (back side) and the reflective surface (front side) [36]. (b) A 44 actuator unimorph deformable mirror for space telescopes [38]. Left: back and front side of the mirror structure with the mounting ring. Right: fully assembled deformable mirror.

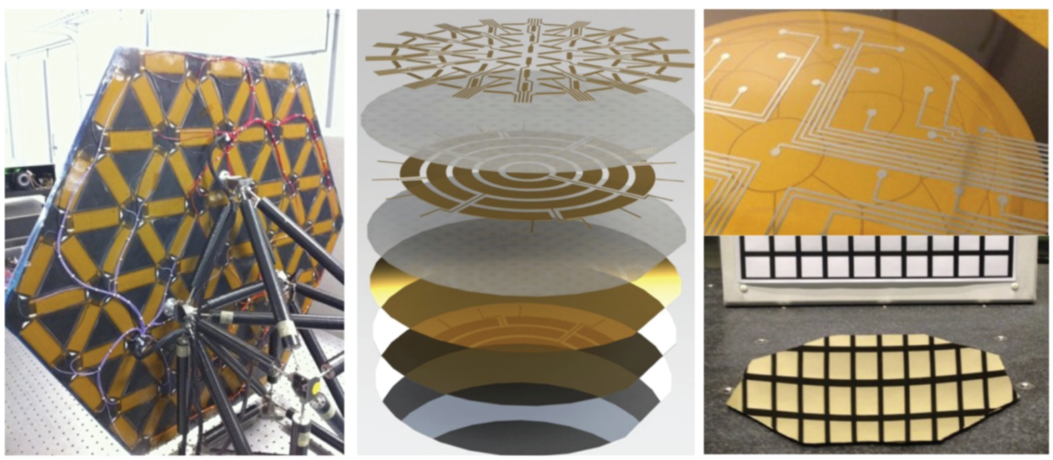

Figure 1.10: Several active CFRP shell concepts and prototypes. Left to right: Active Composite Reflector (JPL), sectioned view of a PVDF membrane mirror (Caltech), back and front side view of a Carbon Shell Mirror (Caltech/JPL) [41], [42].

within the U-shape cut-outs of the ribs. Steeves [41] developed the design and manufacturing technique for laminated carbon fiber composite mirrors of 41 surface parallel actuators with an optimized electrode pattern.

1.2.2.2 Piezoelectric Material Nonlinearity under High Fields

Advances in the understanding of the underlying mechanisms and processing techniques have led to a surge of new ferroelectric materials with giant piezoelectric effects. The mechanical response of piezoelectric ceramics originates from two sources: the intrinsic effect due to a change of polarization at the atomic scale and the extrinsic effect due to domain switching [45]. The two effects are illustrated in figure 1.11. By doping the raw material with different chemical compositions, the sintered piezoelectric ceramic's energy barrier of switching can be reduced, and large piezoelectric strain can be achieved. This is achieved in PZT with 52% Ti, and the resulting crystal possessed small intergranular constraints during domain switching. Crystals are referred to as being at the morphotropic phase boundary in this condition [46]. An alternative method to lower the switching energy barrier is working with single crystal materials.

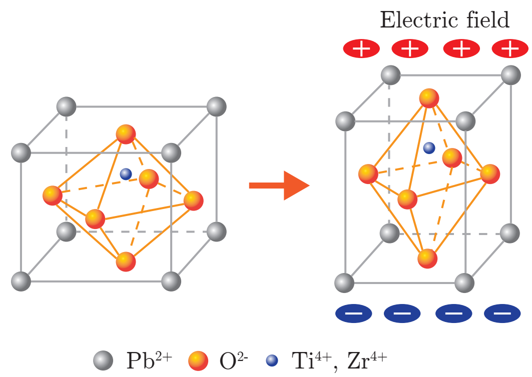

(a)

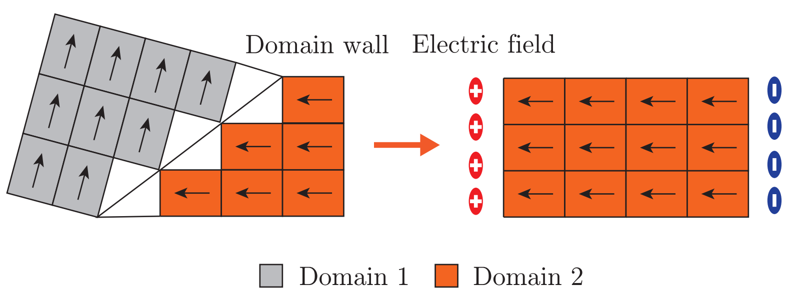

(b)

Figure 1.11: (a) The intrinsic piezoelectric response under applied electric field. (b) The extrinsic piezoelectric response due to field-induced domain movement and realignment.

For thin shell actuation applications, in order to harvest the inherent large actuation capability that comes from the extrinsic response of piezoelectric materials, strong electric fields must be applied to the piezoelectric components embedded in the structure. Within this range, the linear piezoelectric constitutive equation will fail to correctly predict the material behavior.

For piezoelectric unimorph structures which consist of one active layer (actuator)

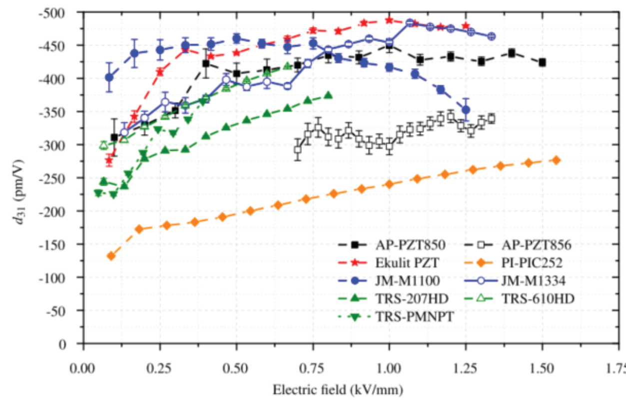

Figure 1.12: The electromechanical coupling coefficient d_{31} of different piezoelectric materials as a function of the driving electric field [47].

and one inactive layer (substrate), as the thicknesses of the substrate and actuators decrease, stress levels due to actuation in the piezoelectric layer rise significantly, as shown in figure 1.13. Experiments have also demonstrated that stress fields can seriously alter the values of permittivity and piezoelectric constants d_{31}, d_{32} and d_{33} when the material is subjected to stress parallel or perpendicular to the polarization direction [48] [49]. For piezoelectric thin shell structures operating under prestress or high loading conditions, such effects must be taken into account during the design stage.

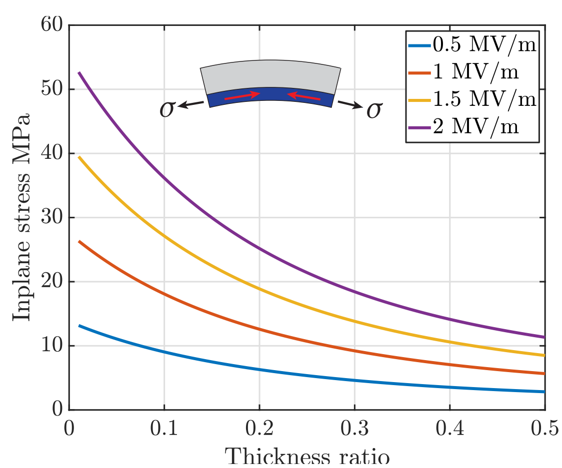

Figure 1.13: The average stress inside the piezoelectric layer as a function of the ratio between substrate and the active layer R and electric field.

Recently, a limited number of efforts has been devoted to the quantification and modeling of piezoelectric nonlinearity within high electric fields or high stress fields [47], [50], [51]. However, the literature providing the experimental quantifi-

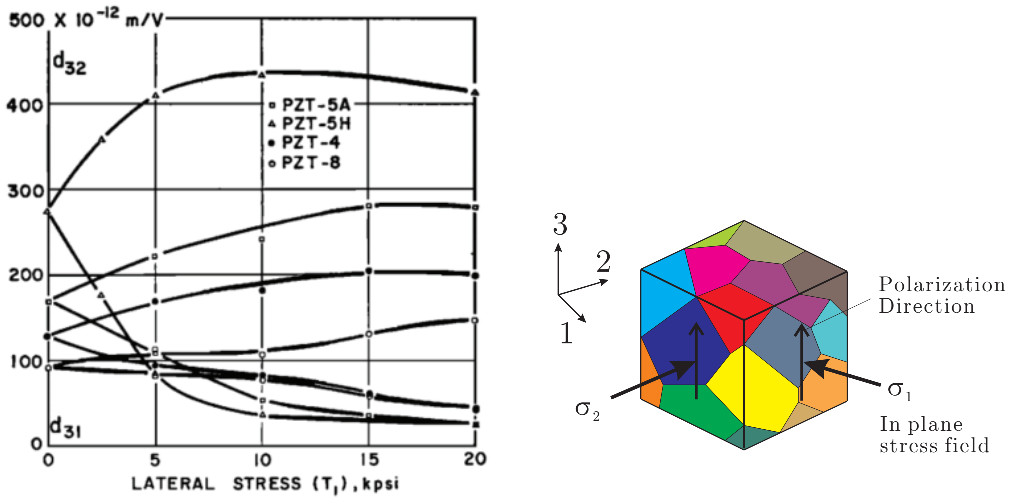

(a) (b)

Figure 1.14: (a) d_{31} and d_{32} values vs lateral stress field T_1 amplitudes. Electromechanical coupling coefficient values taken at the end of the 10th stress cycle [49]. (b) Illustration of stress field and polarization direction during the tests.

cation of fully-coupled (mechanical and electric field) constitutive models are still extremely rare [52]. A systematic method to describe and quantify the nonlinearity of piezoelectric materials that unifies the observation at different length scales and of different physical quantities has yet to be proposed. This can only be achieved with advances in both the modeling framework and novel experimental methods.

1.2.3 Vibration Control of Active Shells

Due to the lightweight, flexible and low damping characteristics, thin shell structures are prone to disturbances from vibrations during operation. In contrast to damping these vibrations passively through stiffening, the response of the structure can be adjusted adaptively through the introduction of sensors, actuators, and controllers. An example of the active shell structure in a civil engineering application is shown in figure 1.15.

Piezoelectric sensors and actuators distributed on the surface of the shell are able to estimate the structural deformation and provide active damping in a precise, compact and energy efficient manner. Intensive studies have been performed on the vibration control of piezoelectric thin shell structures, dating back to the 1970s when Hughes et al. [54] modeled piezoelectric structural dynamics using the finite element method. Many aspects of the subject have been studied thoroughly, including control law design, controllability, and observability with respect to sensor/actuator topology,

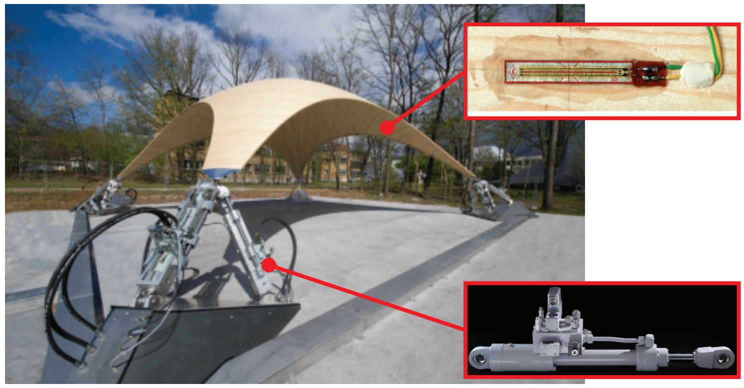

Figure 1.15: The Stuttgart Smart Shell: a double-curved thin shell structure with hydraulic edge support [53]. Red boxes outline the strain sensor and the hydraulic actuator for vibration sensing and control.

optimal placement of the sensors/actuators, and geometrical linear and nonlinear finite element modeling. An overview of the subject and detailed introductions to the technologies can be found in the seminal books by Preumont [55] and Tzou [56].

Today, two gaps exist in the study of vibration control for piezoelectric thin shell structures. First, piezoelectric material nonlinearities are seldom taken into account both theoretically and experimentally. Most research treated the piezoelectric system as a linear, time invariant system and have implemented linear piezoelectric constitutive relations in the control law design process. Second, control design and vibration damping experiments on doubly-curved shells remain rare due to the modeling complexity. The existing literature mostly studied thin shells with regular geometries; for instance, flat plates or semi-sphere shells with regular sensor/actuator shapes. Such simplified models cannot reflect the complicated structures and boundary conditions that are ubiquitous in civil engineering and aerospace applications. This status quo greatly limited the applications of techniques developed from simplified lab prototypes to solve complicated engineering problems.

1.3 Objective and Scope

The overall objective of this thesis is to identify the potential paths to address the challenges and constraints faced by piezoelectric deployable thin shell structures. This thesis envisages that the combination of ultra-thin foldable substrates, piezoelectric actuators, and origami-inspired deployable structures will offer unparalleled advantages in terms of packaging efficiency, areal density, shape accuracy, and adaptability over conventional approaches.

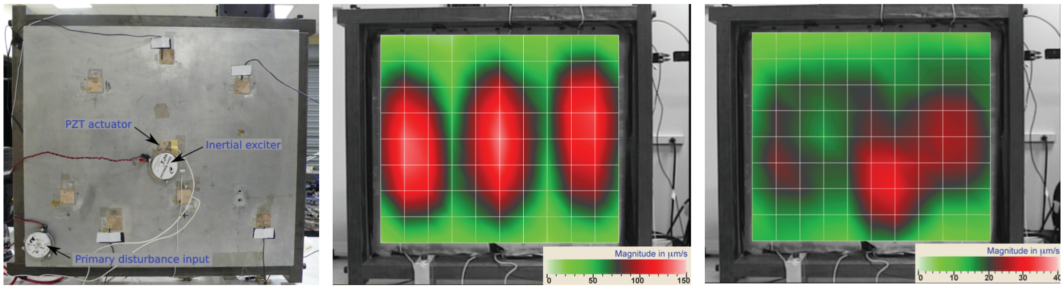

(a)

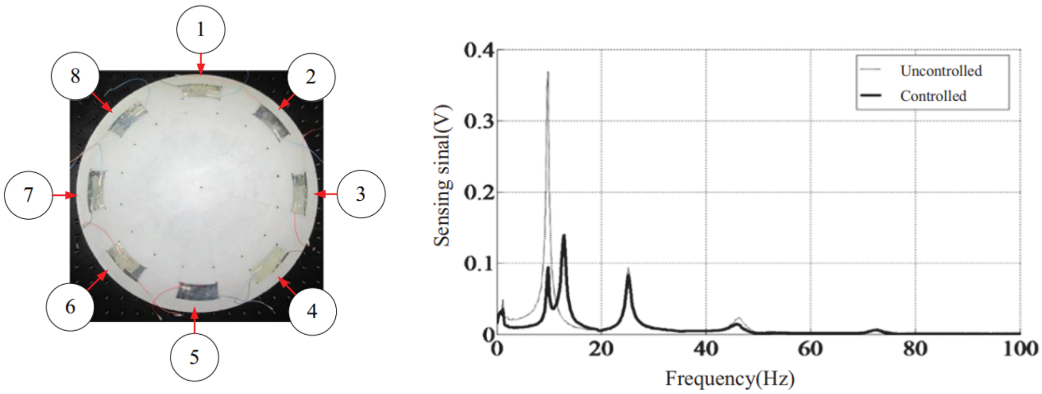

(b)

Figure 1.16: (a) Active vibration control of a simply supported plate using self-sensing piezoelectric actuators [57]. Middle to right pictures: open and closed-loop velocity responses from laser vibrometer measurements. (b) A paraboloidal shell with bonded PVDF sensor/actuator pairs. Right picture: open and closed-loop frequency response from sensor output [58].

To develop a new class of deployable active thin shell structures, the thesis focuses on three underlying topics. First, the integration of foldable thin shells with deployable structures is investigated. Second, material nonlinearity for piezoelectric active structures under combined high electric and stress fields are studied experimentally. Third, the challenge of rejecting dynamic disturbances on multi-electrode thin piezoelectric shells under material property uncertainty is addressed through self-sensing collocated control with in-situ adaptation of piezoelectric properties.

Through the investigation of the above three topics, a set of numerical design tools and criteria, novel experimental techniques, and comprehensive experimental data are presented that will serve as building blocks and data-bases for the design of future active deployable thin shell structures.

1.4 Layout of the Thesis

The thesis is structured as follows: Chapter 2 first describes the methodology used to integrate an origami-inspired creased shell with deployable spatial mechanisms. The chapter then describes the origin of the mechanism design, and presents the development of a compactly foldable spatial mechanism based on rolling hinges. A parametric analysis of the mechanism was conducted and its kinematics were analyzed numerically. The proposed methodology was then implemented into the design of a compatible foldable thin shell, and the shell-mechanisms folding characteristic was evaluated by finite element analysis. A prototype of the basic foldable module was then constructed and folding tests were performed to validate the numerical design. A family of new deployable structural concepts based on tessellations of the single module is the presented after the validation. Candidate materials that are capable of realizing the proposed concepts were then tested under a large bending condition. The folding limits of both thin CFRP shells and of thin piezoelectric plates were experimentally measured. The end of the chapter analyzes the scaling relation between the surface error of a single module and the structural dimension.

Chapter 3 describes the characterizations of a rate-free, full field, multi-axial coupled phenomenological model of polycrystalline piezoelectric materials. First, the adopted constitutive law is briefly reviewed, followed by an introduction of a backward-Euler integration algorithm for the model. The model is then incorporated into a simplified, homogenized actuation estimation algorithm for thin piezoelectric unimorph structures. Integration algorithms for both plane strain and plane stress conditions are presented. To obtain the parameters of the phenomenological model, systematic experimental investigations were carried out on pre-poled thin PZT plates and structures manufactured from the same. Both ferroelastic and ferroelectric tests were performed with novel experimental techniques. At the end of the chapter, model predictions are validated through comparisons with test results of unimorph structures under complex loading and actuation conditions. Certain deficiencies of the macroscopic constitutive law exposed during calibration are discussed.

Chapter 4 presents the self-sensing active vibration damping scheme which is implemented on piezoelectric thin shells with multiple electrodes. Signal conditioning circuits for feedback control using the scheme are first reviewed. Feedback signal from the self-sensing piezoelectric layer under mechanical disturbance and electric field excitation is analyzed, and decomposed into linear and nonlinear components. An efficient model discretization method was then proposed to establish the open and closed-loop governing equations for self-sensing piezoelectric thin shell structures with arbitrary geometry and actuator distribution. As an example, the closed-loop response of a piezoelectric cantilever beam was simulated with the proposed algorithm. Dielectric responses of the PZT plates used in chapter 3 were characterized under a wide range of frequencies and amplitudes of the input electric fields. Closed-loop self-sensing active damping experiments were performed on unimorph cantilever beams with single electrode. An adaptive self-balanced circuit was constructed to minimize the feedthrough component of the feedback signal and to compensate for the change of the actuator's dielectric properties due to environmental changes and material aging. With the experimentally-validated closed-loop model, the proposed architecture's effectiveness in improving the dimensional stability of multi-electrode self-sensing piezoelectric thin shell structures was demonstrated through closed-loop simulations of a hypothetical large shell under dynamic disturbance.

Chapter 5 concludes the thesis and lists potential directions that may broaden the results presented.

Chapter 2

DEPLOYABLE ACTIVE THIN SHELLS WITH EDGE SUPPORT

2.1 Introduction

This chapter investigates a set of novel techniques that lead to modular, deployable thin shell structures which could be either flat or curved in the deployed shape. The two components of the proposed concepts are thin shells with smooth folds and spatial mechanisms with rolling hinges. Kinematics of the mechanism and motion of the shell is shown to be fully compatible with each other during folding and unfolding. This basic module is then articulated to create multiple modular tessellations, which form a series of foldable surfaces. Curvature was introduced to the initially flat shells using surface-bonded piezoelectric actuators. The strain limits of candidate carbon fiber composite and piezoelectric ceramic plates were tested under large curvature conditions. The scalability of the proposed deployable module was investigated through numerical simulations.

2.2 Background and Motivation

Large, precision reflectors composed of rigid plates and shells have many applications, including telescope mirrors, solar concentrators, and antennas, but thus far very few studies have addressed the challenges of packaging and deployment of such structures. Studies of rigid-surface antennas and reflectors consisting of rigid petals that wrap around a central hub were conducted in the 1980's and 1990's; examples include the TRW Sunflower [59], the Dornier/ESA FIRST antenna [60], the Cambridge Solid Surface Deployable Antenna (SSDA) [61], and the deployable telescope mirror concept by Lake [62]. However, structural complexity and high areal density have been obstacles to further development. There are also fundamental difficulties in scaling up or tessellating these concepts. Similar concepts have recently been adopted for small satellite applications [63], [64]. A growing need from the application side has resulted in recent studies on alternative approaches. One example is the robotic assembly of a 100 m diameter telescope proposed by Lee [65] based on identical deployable truss modules. Other examples include several proposals of deployable annular space telescope concepts based on tensegrity and pantograph structures, including a 30-m space based observatory by Rey [66] and a 20 m diameter annular mirror by Durand [67].

Parallel advances in manufacturing and shape control of thin shell mirrors have provided another avenue to support new solutions. Rollable thin shells made from carbon-fiber composite have been proposed [22], [68], [69] to store the reflector compactly. Patterson [70] and Steeves [71] have developed deformable thin mirror technologies based on active laminates consisting of thin shell substrates and active layers.

Packaging schemes emerging from recent research on rigid-foldable origami have also stimulated the appearance of a new series of deployable structures. Tachi [24] presented solutions for designing rigid-foldable structures based on triangular and quadrilateral mesh. Chen [72] has proposed a systematic solution based on spatial mechanisms for thick rigid panels connected by hinges of zero width. Because the solution is based on rigid origami, foldability into a tight package was achieved without incurring any deformation of the panels.

2.3 Attaching Flat Thin Shells to Articulated Rigid Links

Consider the problem of attaching a rectangular thin shell with an elastic fold of width w, to a simple mechanism, consisting of a pair of rigid links connected by revolute joints that are rotated through an angle γ. The fold region of the shell has lower bending stiffness, whereas the rest of the shell is thicker. The shell is fixed along the edge to the mechanism, except for the fold region, as shown in figure 2.1a.

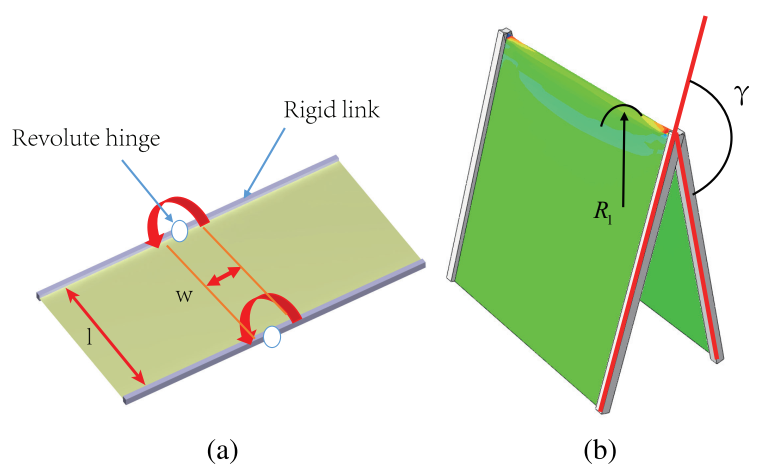

Figure 2.1: Thin shell attached to an articulated mechanism: (a) Flat and unstressed configuration. (b) Folded configuration from finite element simulation.

2.3.1 Avoiding Ridge Singularity in the Folded Shell

A “ridge singularity" will appear along the fold line when the hinges of the mechanism are rotated, as shown in figure 2.1b. This problem is well studied and understood [73], thus, it can be shown that:

$$R_1 \sim t^{1/3} l^{2/3} \gamma^{-4/3} \tag{2.1}$$

where R_1 is the fold radius, t, l are the thickness and width of the crease region of the shell, respectively, and γ is the dihedral angle. Note that R_1 tends to be singular as $t \to 0$ and $\gamma \to \pi$, which are common assumptions in conventional origami studies. The induced strain in the fold region causes local buckling, plastic deformation, or even material failure.

A way to eliminate the ridge singularity is by separating the hinge lines in the mechanism, to better match the kinematics to the deformation of the elastic shell. The width of the fold region is also increased, as shown in figure 2.2a and discussed in detail in the next section. In effect, this doubles the number of hinges, as a pair of hinges can better accommodate a smooth transition in the shell during folding. Moreover, it decreases the strain energy stored in the shell, as shown in figure 2.2b, by nearly eliminating the bending deformation in the fold region. This property is key to the integration of foldable thin shells in spatial mechanisms.

2.3.2 Influence of Fold Width and Bending Stiffness on Folded Shape

A parametric study of the influence of the crease region width and bending stiffness on the folded shape was conducted, as shown in Figure 2.3. The goal was to minimize the separation distance between the panels on either side of the folded shell. In all these studies: 1) the shell was only partially supported along the edges (indicated by the black lines in the figure); 2) the width of the fold region was set to $w = \pi/2 \times d$. The bending stiffness ratio β was defined as the ratio between the stiffness of the panel and the crease region of the shell:

$$\beta = \frac{D_{panel}}{D_{crease}} \tag{2.2}$$

and D is the bending stiffness of a flat isotropic plate:

$$D = \frac{Et^3}{12(1-\nu^2)} \tag{2.3}$$

The results are presented in Figure 2.4, which shows that when the stiffness ratio β drops below 0.1, the maximum separation distance of the shell d' in the folded

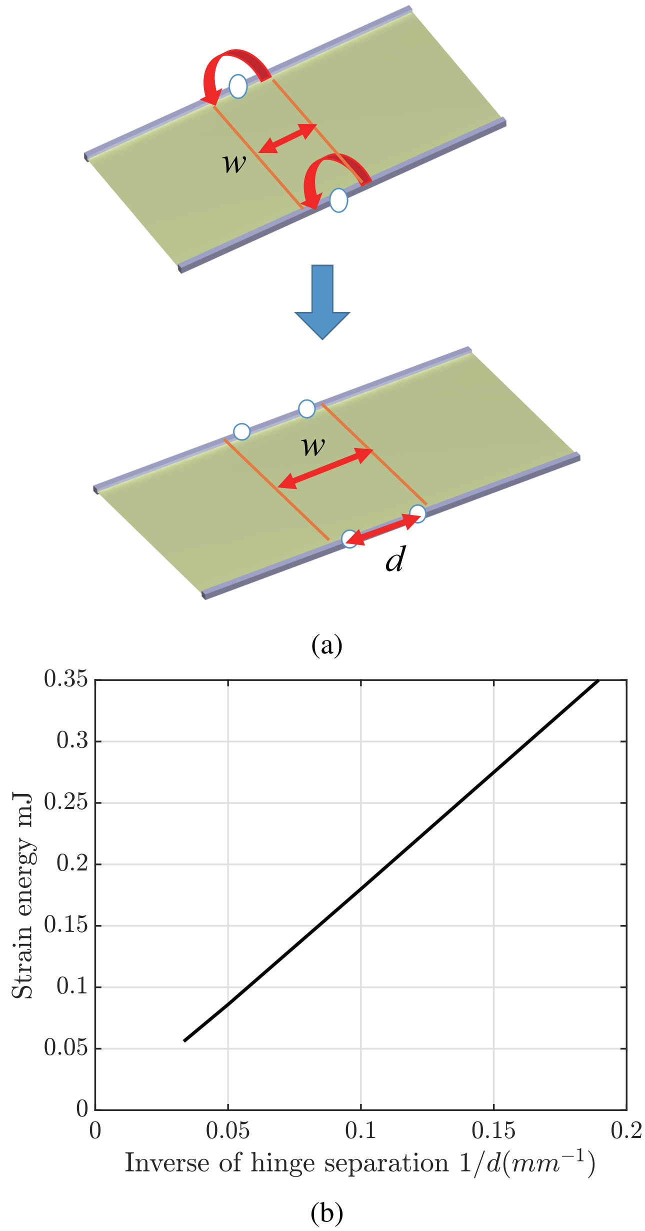

Figure 2.2: (a) Introduction of hinge separation in folded thin shell attached to rigid link assembly. (b) Bending energy of shell scales inversely with crease width.

configuration is close to the value of the hinge line separation d. From numerical simulations, $\dfrac{d'}{d} \propto (\beta)^3$. This conclusion will be used for the design of foldable shells in section 2.5.

2.4 Modular Spatial Mechanism with Rolling Hinges

The mechanism concept proposed in this section was inspired by the Miura-Ori folding pattern [74]. The basic repeating unit of Miura-Ori is the symmetric degree-

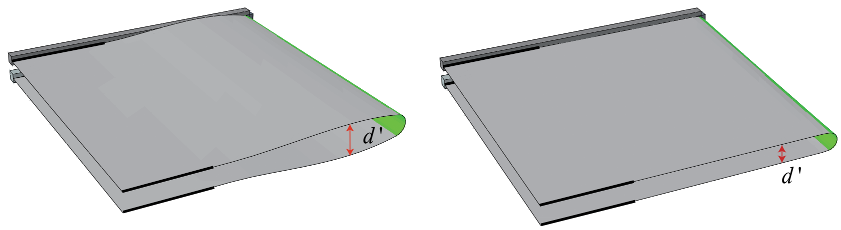

Figure 2.3: Effect of hinge separation distance on the shell's folded shape. The mechanism on the front side is hidden. The black line denotes the fixed position.

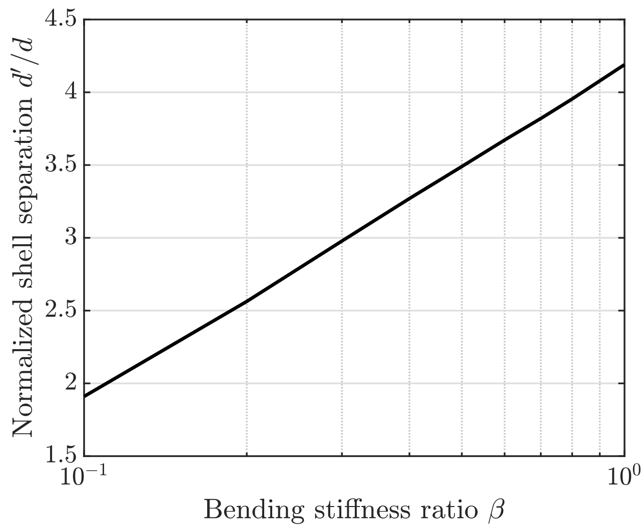

Figure 2.4: Crease region bending ratio effect on shell separation distance in folded configuration. Results based on finite element simulations.

four vertices pattern shown in Figure 2.5b. It is kinematically equivalent to a four-bar spherical mechanism and, hence, possesses one degree of freedom. This can be shown by replacing the zero-width crease lines with revolute joints, and noting that the four hinge lines intersect at a point throughout folding and deployment. Variations of this unit led to both the spatial mechanism and the foldable thin shell concept presented in the following section.

2.4.1 Four-bar Spatial Mechanism

The main challenges in transforming the chosen origami pattern into a compactly foldable spatial mechanism are the need to accommodate the thickness of the structure and to preserve the single degree of freedom. Conventional revolute hinges will prevent the mechanism from being folded beyond the point of first self-contact between the linkages of the mechanism. To remove these constraints, the original single hinge was split into a pair of coupled revolute joints whose axes intersect at

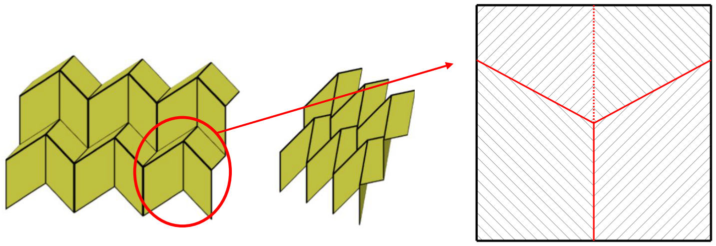

(a)

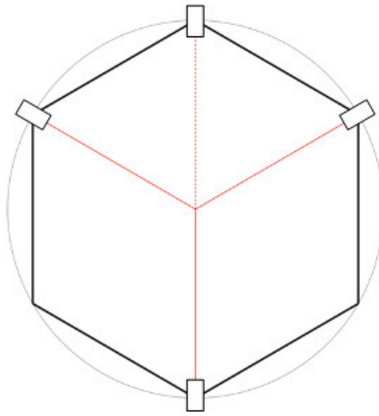

(b)

Figure 2.5: (a) Miura-Ori pattern [75]. Red lines denote fold lines, shaded regions denote panels. (b) Spherical mechanism equivalent to repeating unit. Rectangles denote revolute joints.

a common point, as shown in Figure 2.6. By introducing rolling hinge pairs, both challenges were addressed.

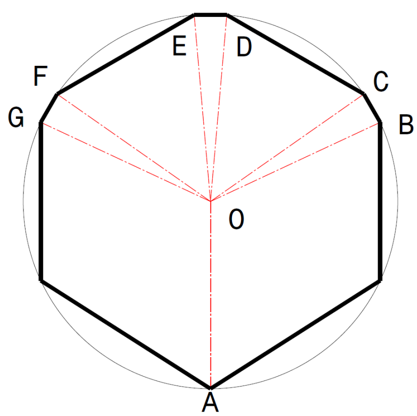

(a)

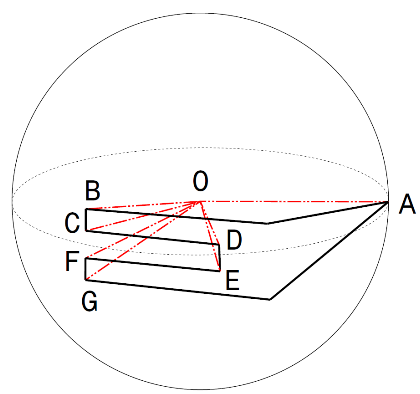

(b)

Figure 2.6: (a) Introduction of coupled revolute joints into the mechanism. b) Folded configuration of modified mechanism. All vertices rest on the same spherical surface.

A conventional rolling hinge is composed of two elements: a pair of curved contact surfaces and tensioned cables/bands [76]. The surface pairs are held in contact by the tensioned cables to prevent sliding, and thus provide a single degree of freedom (DOF). This hinge is attractive for space applications due to its high stiffness, low friction and structural simplicity [76]. The profile of the contact surface was designed to achieve different relative motions, e.g. multi-stability [77]. In this application, the contact surfaces were conical, such that the hinge axes intersected at a common point O, as is required in a spherical mechanism. Kinematically, the relative motion of this modified rolling hinge pair was equivalent to a three-bar mechanism with mirror symmetry and common hinge axes intersection, as shown in Figure 2.7. In Figure 2.6 conical rolling hinge pairs were introduced to replace the revolute hinge pairs GF, ED, and CB. Joint A did not need to be replaced with a hinge pair, because it does not close fully.

More importantly, these hinge pairs preserved the single DOF of the original degree-four vertices pattern. This can be shown by considering the modified Grubler-Kutzbach equation for the mobility of the proposed spherical mechanism:

$$M = 3(n - 1) - 2j - r \tag{2.4}$$

where $n = 7$ is the number of links, $j = 7$ is the number of hinge lines, and $r = 3$ is the number of contact surface pairs. Here the mobility M is defined without considering the entire mechanism's rigid body motion in space, and can be examined in a coordinate system fixed to one element; e.g. bar AG. The position of each element can be determined by three independent parameters, normally the Euler angles. Both the revolute and rolling joints allow one DOF rotation between adjacent members of the mechanism, thus remove 2 DOF from M. Thus the mobility of the mechanism in Figure 2.6 was reduced from:

$$M = 3(7 - 1) - 2 \times 7 - 0 = 4 \tag{2.5}$$

to the single DOF mechanism in Figure 2.6:

$$M = 3(7 - 1) - 2 \times 7 - 3 = 1 \tag{2.6}$$

The following sections are based on use of this modified mechanism.

2.4.2 Kinematic Analysis of Spatial Mechanism

The kinematics of the proposed four-bar mechanism were studied by constructing the loop closure equation, using the Denavit-Hartenberg notation [78], as shown in

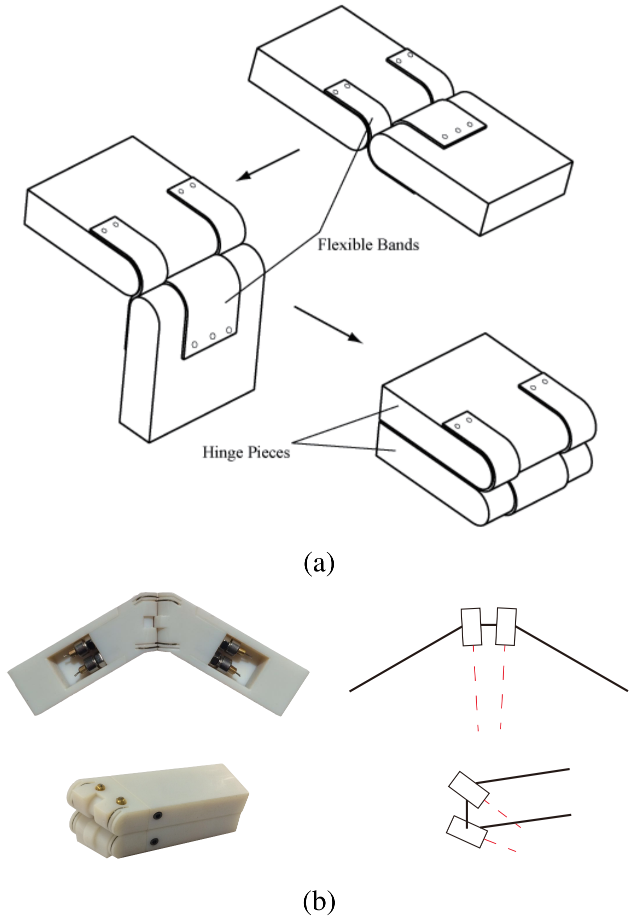

Figure 2.7: (a) Conventional rolling hinge with cylindrical contact surface pair. (b) Rolling hinge with conical contact surface pair equivalent to a three-bar mechanism with angular symmetry constraint.

Figure 2.10. A 4 by 4 transformation matrix A_N converted the coordinates on hinge N to $N-1$ through the matrix multiplication:

$$p'_{N-1} = A_N p'_N \tag{2.7}$$

where the matrix A_N has the following structure:

$$A_N = \begin{bmatrix} \cos\theta_N & -\sin\theta_N\cos\alpha_N & \sin\theta_N\sin\alpha_N & a_N\cos\theta_N \\ \sin\theta_N & \cos\theta_N\cos\alpha_N & -\cos\theta_N\sin\alpha_N & a_N\sin\theta_N \\ 0 & \sin\alpha_N & \cos\alpha_N & r_N \\ 0 & 0 & 0 & 1 \end{bmatrix} \tag{2.8}$$

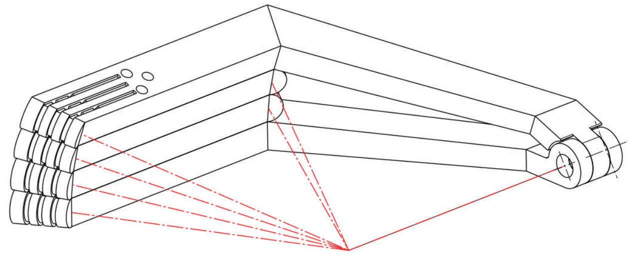

(a)

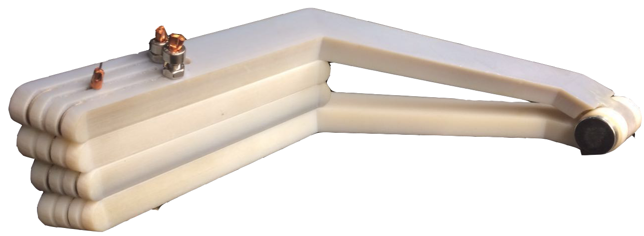

(b)

Figure 2.8: (a) Spatial mechanism with conical rolling hinges. Grooves on the surface hold the tension wires. (b) Folded configuration of 3D-printed mechanism prototype shows compact folding. Screws on the model are used to tension the cable.

and its inverse is:

$$A_N^{-1} = \begin{bmatrix} \cos\theta_N & -\sin\theta_N & 0 & -a_N \\ -\sin\theta_N\cos\alpha_N & \cos\theta_N\cos\alpha_N & \sin\alpha_N & -r_N\sin\alpha_N \\ \sin\theta_N\sin\alpha_N & -\cos\theta_N\sin\alpha_N & \cos\alpha_N & -r_N\cos\alpha_N \\ 0 & 0 & 0 & 1 \end{bmatrix} \tag{2.9}$$

where, r_N is the adjacent joint displacement, a_N is the hinge axes normal distance, θ_N represents the displacement of each joint, and α_N is the twist angle between adjacent joints. For the mechanism studied here, $\alpha_N = 0$ (no twisting) and $a_N = 0$ since all hinge axes intersected at a common center.

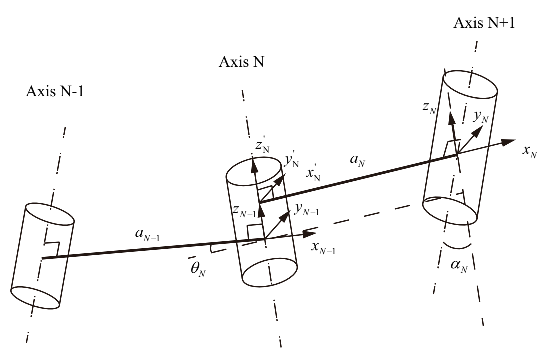

Figure 2.9: Denavit - Hartenberg notation of coordinate transformation

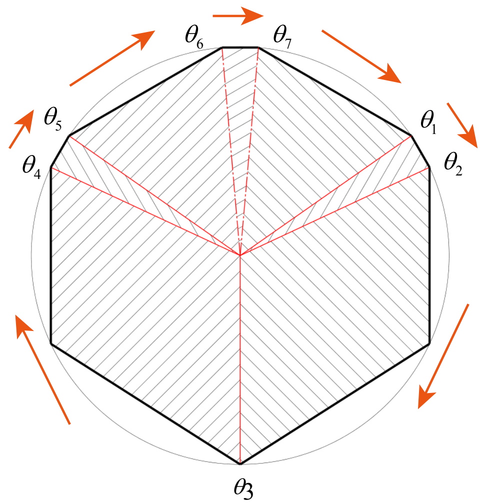

Figure 2.10: Arrows denote the sequence of coordinate transformations

The loop-closure condition can then be obtained by applying coordinate transformations sequentially around the links of the mechanism [79]:

$$A_1A_2A_3A_4A_5A_6A_7 = I \tag{2.10}$$

Note that the angles θ_N are the only variables that control the motion of the mechanism. Due to the symmetry of the rolling hinges and the mechanism, $\theta_4 = \theta_5 = \theta_1 = \theta_2$, and $\theta_6 = \theta_7$. Hence, the final expressions only contain θ_1, θ_3 and θ_6. The simplest form of the closure equation can be achieved by the transformation:

$$\begin{aligned} & A_3A_4A_5 - A_2^{-1}A_1^{-1}A_7^{-1}A_6^{-1} = 0 \\ \Rightarrow & \begin{bmatrix} f_1(\theta_1,\theta_3,\theta_6) & f_2(\theta_1,\theta_3,\theta_6) & f_3(\theta_1,\theta_3,\theta_6) & 0 \\ f_4(\theta_1,\theta_3,\theta_6) & f_5(\theta_1,\theta_3,\theta_6) & f_6(\theta_1,\theta_3,\theta_6) & 0 \\ f_7(\theta_1,\theta_6) & f_8(\theta_1,\theta_6) & f_9(\theta_1,\theta_6) & 0 \\ 0 & 0 & 0 & 0 \end{bmatrix} = 0 \end{aligned} \tag{2.11}$$

Here each entry is a 6th-order transcendental equation and solving this system of equations numerically yields the angular input-output relation of the mechanism. Equation 2.11 also reveals the mechanism's single DOF nature. Once the relation between θ_1 and θ_6 has been obtained by solving the third row, the value of θ_3 at each solution step can be calculated from any entry of the first or second row.

These kinematic relations were solved using the Newton-Ralphson method. Taking θ_1 as the input angle, $\theta_1 \in [0, \pi/2]$, θ_3 and θ_6 can be calculated. The analysis procedure is illustrated in Figure 2.11.

The numerical solution was highly-sensitive to the step size when the mechanism was in the flat configuration; i.e. when $\theta_1 = \theta_3 = \theta_6 = 0$. In this configuration, by decreasing the step size of the solver, the solution jumped to a different branch, as shown in Figure 2.12. This result indicates that the flat configuration is a bifurcation point for the kinematic path of the mechanism. Note that the numerical solution captured this behavior without any apriori data. The second solution branch corresponds to the alternative (and less interesting) folded configuration shown in Figure 2.12.

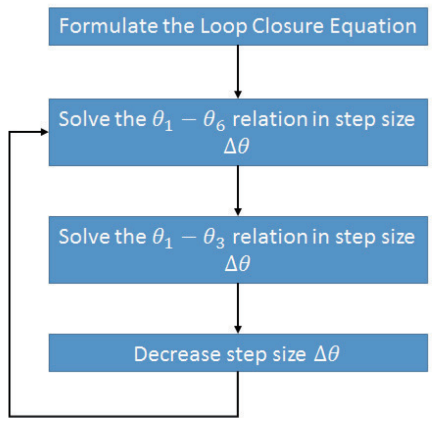

Figure 2.11: Solution procedure for loop closure equation.

2.5 Integration of Thin Shell with Spatial Mechanism

This section presents the design, simulation, and prototyping steps that led to a mechanism-supported foldable thin shell with finite width crease pattern. The folding motion can be guided by the mechanism synthesized in Section 2.4.1. The approach that led to a smooth integration of the two structures is presented.

The starting point is the Miura-Ori-derived folding pattern, trimmed along the edges to obtain a hexagonal shape. The mountain and valley folds were replaced with finite-width elastic folds. To guarantee a smooth integration with the mechanism (i.e. no significant changes in deformation are induced due to the integration of the two structures), a series of finite element analyses were performed.

2.5.1 Finite Element Model Description

The shell was modeled using S3R triangular shell elements in Abaqus/Explicit 6.14-5. The radius of the circumscribed circle of the shell was 125 mm, and the thickness of the panels was 150 µm. To capture the deformation of the fold region, the largest element size was decreased to 1.3 mm, compared to the 5.7 mm

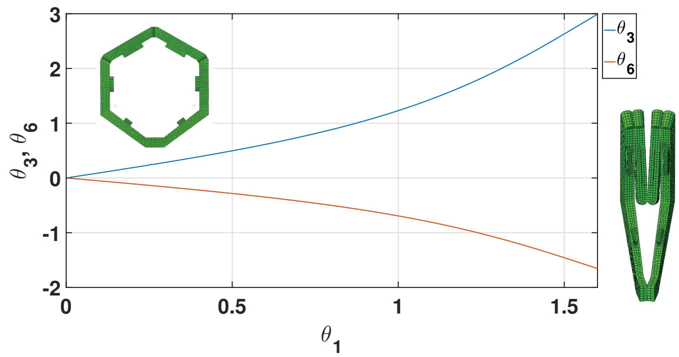

(a)

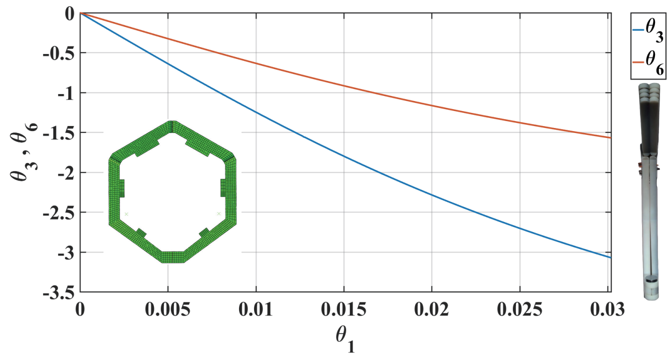

(b)

Figure 2.12: (a) Branch 1 of bifurcated solution to loop closure equation, corresponds to normal folded configuration. (b) Branch 2 corresponds to structure folding in half.

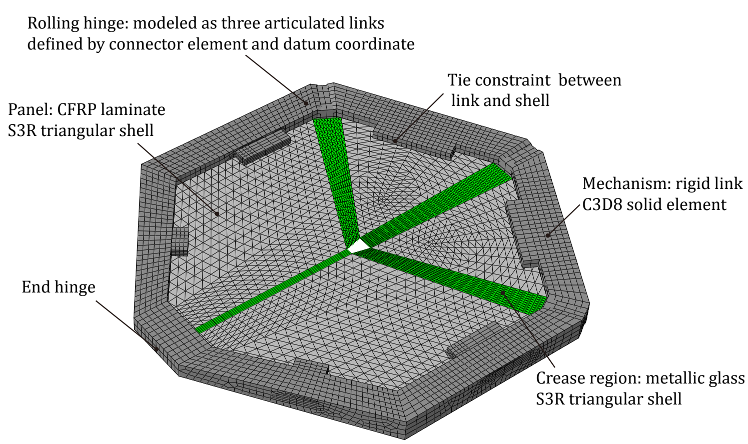

Figure 2.13: Finite element model of foldable thin shell with edge supported mechanism. Shell is perforated at the center to avoid singularity. Rolling hinge is modeled as three articulated hinges with equal angle constraint during folding.

elements in the panels of the shell. The mechanism was modeled using C3D8

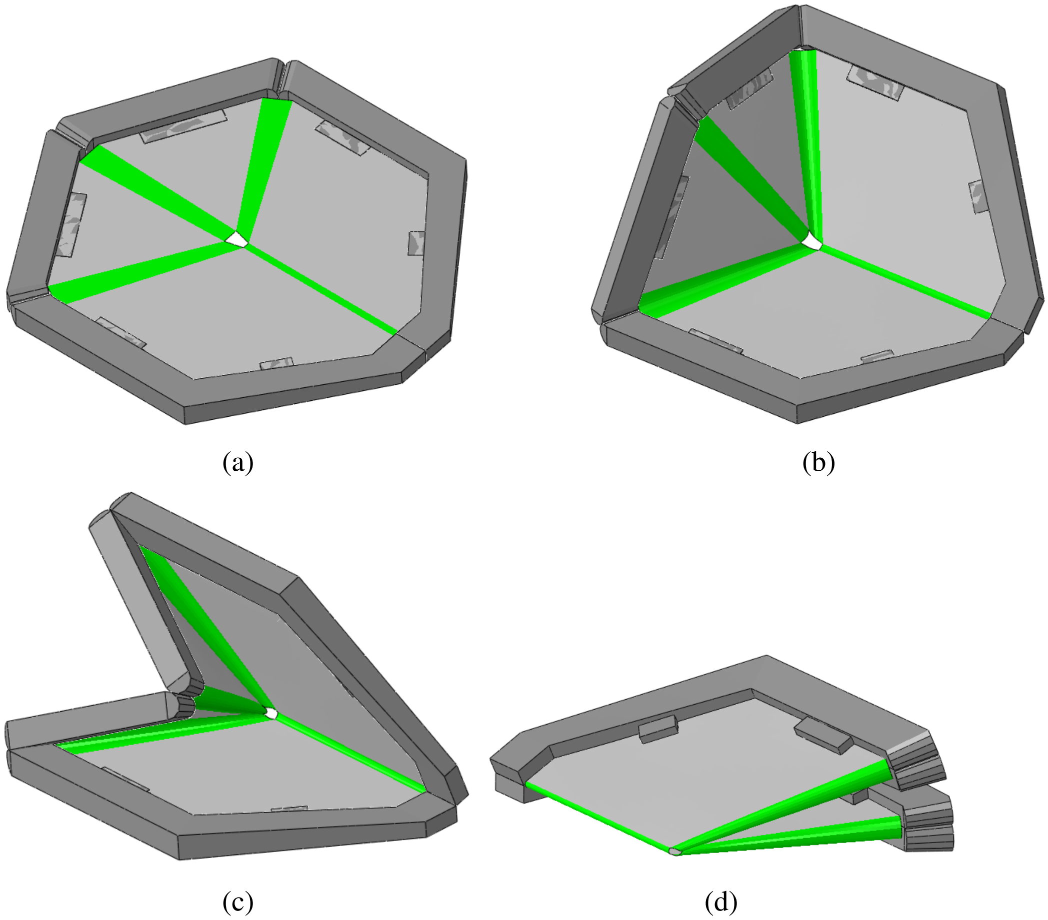

(a) (b) (c) (d)

Figure 2.14: Folding sequence simulated in Abaqus/Explicit. Folding was driven by applying rotations to the connector elements that simulated the rolling hinges.

linear hexahedron elements, and each link was defined as a rigid body. Each rolling hinge was modeled as two revolute joints with intersecting hinge lines using the connector element CONN3D2, and the rotation angles were defined as identical throughout the folding process. Folding was imposed by prescribed rotations of the rolling hinges. To implement a quasi-static folding procedure in the explicit solver, the techniques described by Mallikarachchi [80] were implemented. The complete simulated folding sequence is shown in Figure 2.14.

2.5.2 Sensitivity of Shell Deformation to Fold Width Ratio

In the simulation, the bending stiffness ratio between panels and fold regions, β, was chosen as 90, based on the available material for the crease and the layup of the composite shell (more details are provided in Section 2.6). A series of simulations was performed with different width ratios for the fold region. For

$\alpha < \pi/2$, significant out-of-plane panel deformation appeared in the final folded configuration even for small values of β, as shown in Figure 2.15. This result guided the design of the physical prototype in the next section.

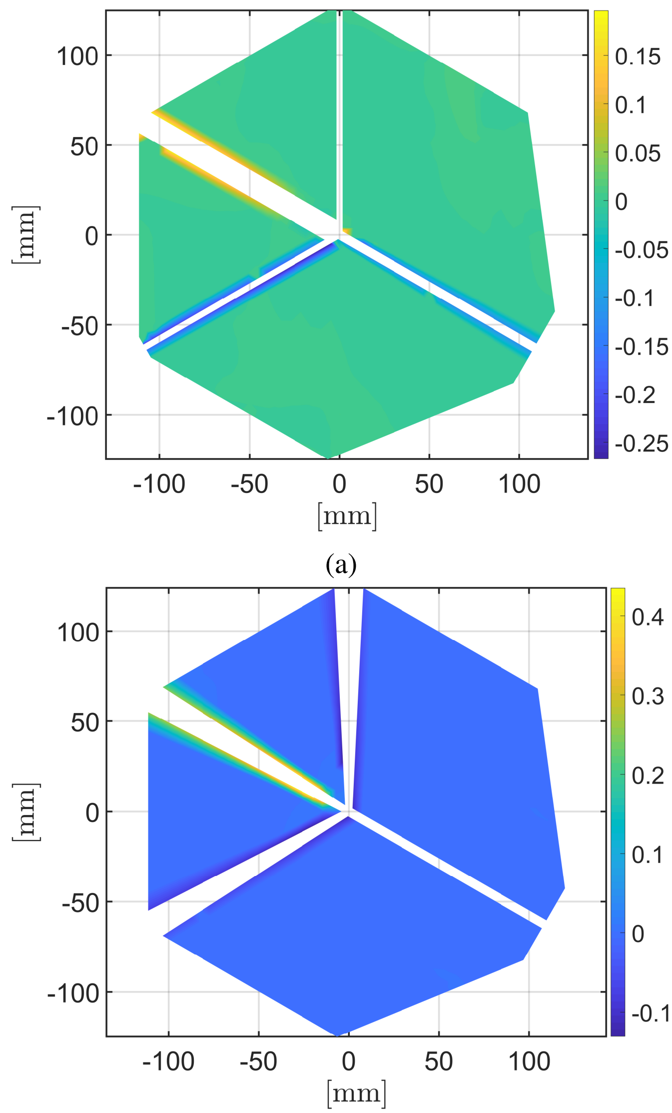

(b)

Figure 2.15: Curvature of the panels in folded configurations, units in mm^{-1}: a) Local α smaller than $\pi/2$, b) Crease pattern of the final design, with $\alpha = \pi/2$ satisfied globally and panel curvature orders of magnitude lower than in a).

2.6 Shell-Mechanism Prototype

A prototype of the mechanism-supported thin shell was built based on a design verified by the folding simulations. There were a number of challenges in the realization of such a concept, the most crucial being finding the appropriate material for the crease region of the foldable shell. The thin shell consisted of carbon fiber reinforced plastic (CFRP) unidirectional tape with a layup orientation of $[60°/120°/0°]_s$ and a thickness of 150 μm. The tape contained M55J fibers impregnated with ThinPreg^{TM} 120EPHTg-1 epoxy. Thin amorphous metal sheet was used for the fold regions due to its high yield stress. The particular sheet used in the prototype was an iron-nickel based product from Metglas [81] with a thickness of 24 μm. The laminate and metal sheets were cured together in an autoclave.

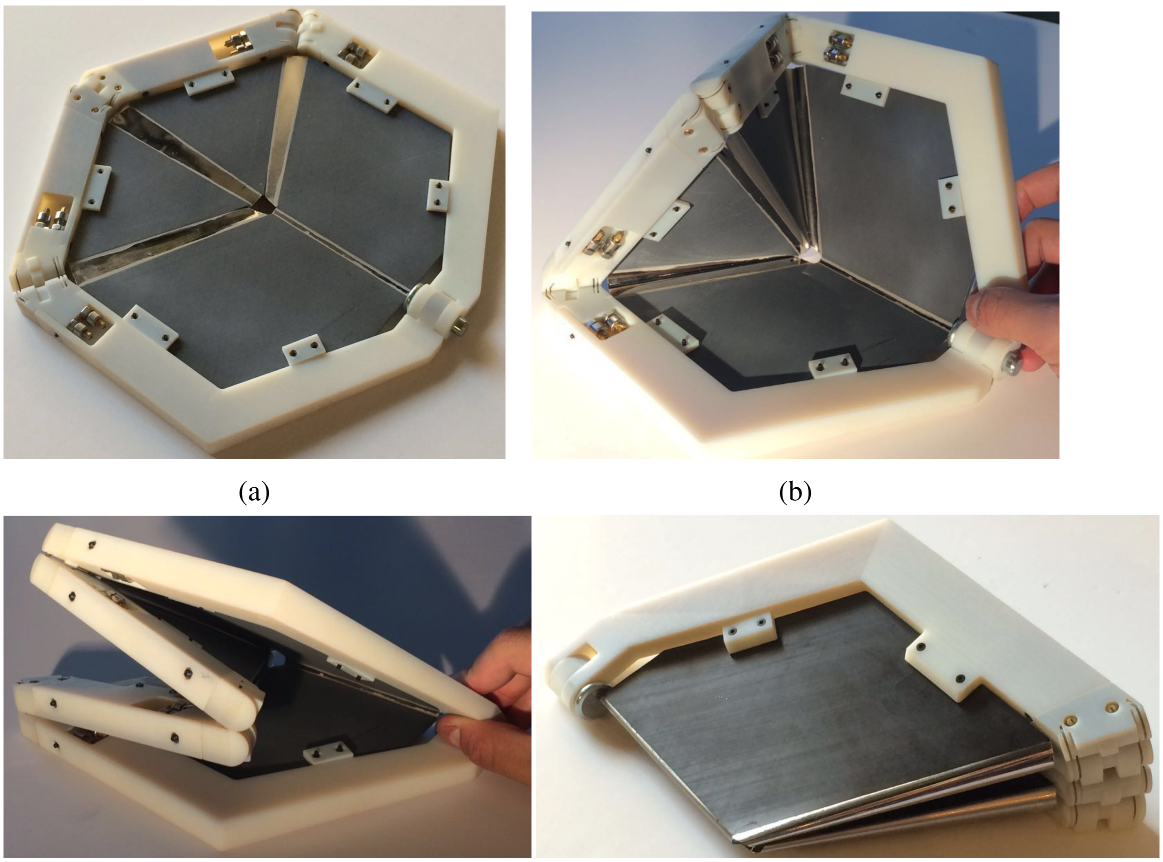

(a) (b) (c) (d)

Figure 2.16: Folding sequence of the prototype is driven solely by rotating the end hinge.

The prototype was folded by rotating the end joint, as shown in Figure 2.16. As predicted by the simulation, the shell panels stayed flat during folding, and the entire shell remained intact after ten times of folding and deployment cycles.

2.7 Flat and Curved Deployable Mechanism Based on Modular Tessellations

Larger structures can be obtained from a tessellation of the basic module described in the previous section. The efficiency of a certain deployable mechanism was measured by the deployment ratio, defined as the ratio between the radii of the spheres circumscribed to the vertices of the mechanism in the deployed and folded configurations.

The basic module was first tessellated into several symmetric assemblies, both flat and curved. All adjacent modules were connected through revolute joints. Folding of each concept was simulated with Abaqus/Explicit 6.14-5, using the same methods developed in section 2.5. For simplicity and reduced simulation time, the embedded shells were not included in the simulations. The rolling hinge pairs were modeled as three-bar mechanisms with equal angle constraints using connector elements.

2.7.1 Tessellation of Hexagonal Modules Based on Three-Fold Symmetry

As a first example, the regular hexagonal modules were connected by revolute hinges along the bars connected to the root hinge in order to create a flat tessellation. The axes of the hinges joining adjacent modules intersected at a common point O, which was separate from the common mid-surface of the bars. This configuration formed a six-bar Bricard mechanism around the connected bars. The Bricard mechanism was thoroughly studied by You [82], and has been shown to possess only one DOF. Thus, the entire tessellation also possesses a single DOF, since the folding and unfolding of each module was determined by the rotation of the end hinge. This result was confirmed by the simulations shown in Figure 2.17 and Figure 2.18. The complete folding of the entire tessellation was driven by folding only one module.

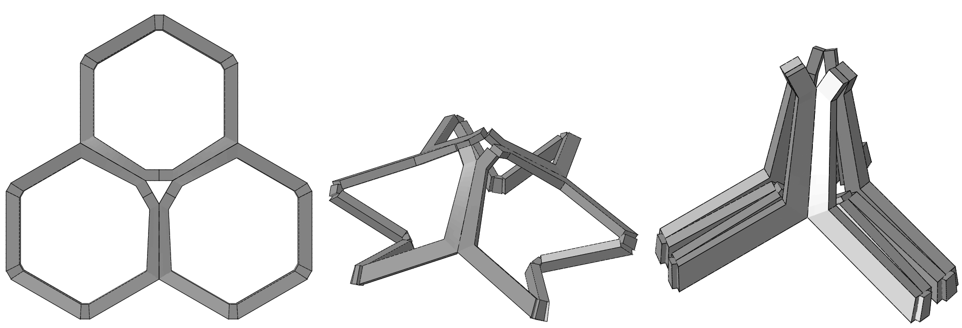

(a) (b) (c)

Figure 2.17: Tessellation of basic module on flat surface: (a) One degree of freedom, three-fold symmetry tessellation concept with flat deployed configuration. (b) and (c) show the half and fully-folded state, respectively. This concept has a deployment ratio of 2.1. The subplots do not share the same scale.

To form a non-flat tessellation configuration with all the vertices resting on a spherical surface, small modifications were made to the original deployable module. The

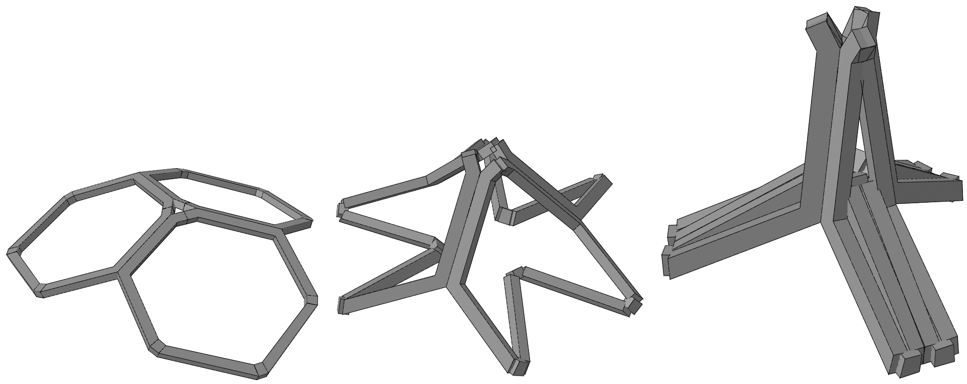

(a) (b) (c)

Figure 2.18: Tessellation of basic module on spherical surface: (a) One degree of freedom, three-fold symmetry tessellation concept with vertices located on the same sphere. (b) and (c) shows the half and fully-folded state, respectively. This concept has a deployment ratio of 2.

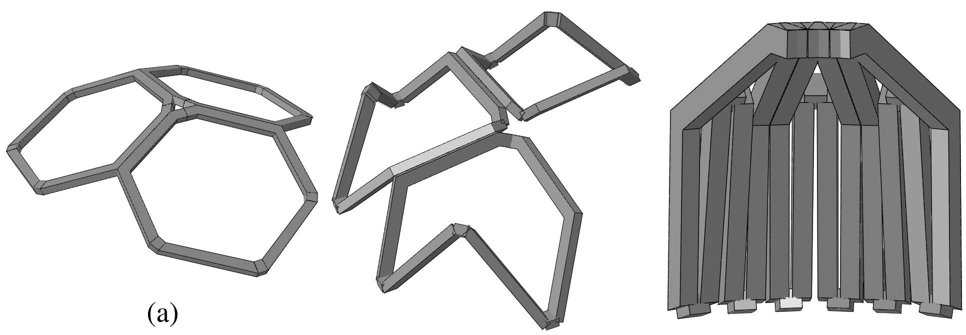

(a) (b) (c)

Figure 2.19: Curved tessellation concept with detached inter-module connection: (a) Three-fold symmetry tessellation concept with vertices located on the same spherical surface, with one detached inter-module connection. Additional rotation displacement control needs to be applied to the inter-module hinges to fold it compactly. (b) and (c) show the half and fully-folded state, respectively. This concept has a higher volumetric efficiency, i.e., the volume of enclosing box of the folded mechanism is smaller than the concept shown in figure 2.18.

basic modules were no longer regular hexagons, due to the angular defect at the vertex of the tessellation. However, since each module still lays on a plane and remained symmetric, the two sides only needed to be slightly shortened. The module also remained foldable, since the center part of the tessellation remained a six-bar Bricard mechanism with angular defect. The deployment process is shown in Figure 2.18. The dihedral angle between adjacent hexagons was 38.975°. The deployment ratio could be further increased by detaching one of the inter-module hinges as illustrated in figure 2.19; however, the mechanism would no longer preserve a single DOF.

2.7.2 Other Tessellation Concepts

The two tessellations shown here are extensions of the basic module and its adaptations, exploiting higher order of symmetry. These tessellations were synthesized following the same logic: articulating adjacent modules into multi-link spatial mechanisms. The mechanisms have higher degrees of freedom, thus require higher control authorities to ensure smooth folding and deployments.

The mechanism in Figure 2.20 was adapted from the truncated icosahedron. The basic module was a four-link spherical mechanism forming a modified version of the module in figure 2.16, but the hinges were placed on the edges instead of at the vertices.

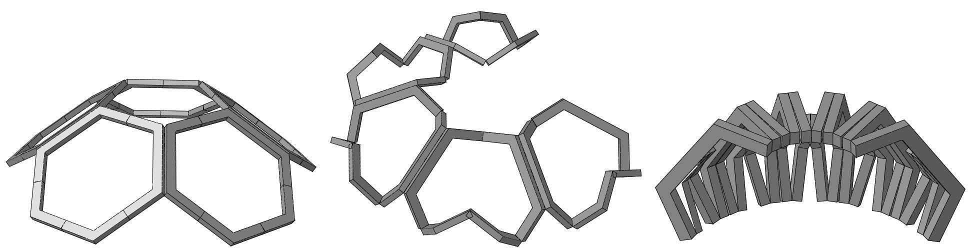

(a) (b) (c)

Figure 2.20: Tessellation concept based on part of a truncated icosahedron, with one detached inter-module connection. The folding pattern was rotated 30° in this case, compared to figure 2.14. This concept has a deployment ratio of 1.6.

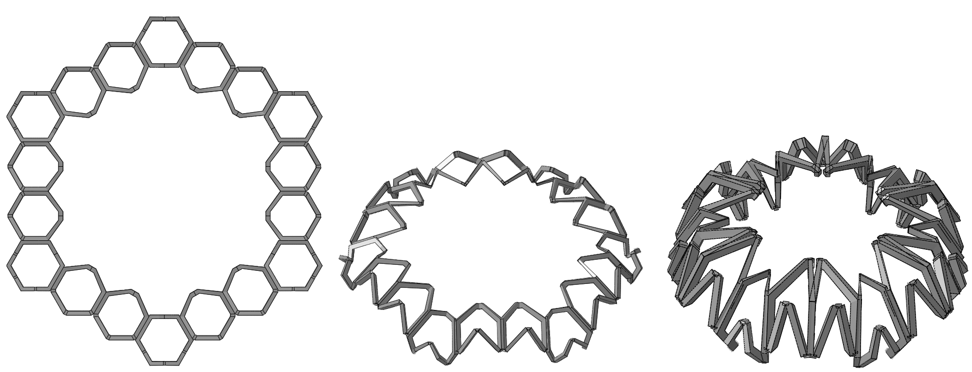

(a) (b) (c)

Figure 2.21: Tessellation ring concept based on two types of basic modules. This concept has a deployment ratio of 4.1.

Employing higher orders of symmetry increased the tessellated mechanism's degrees of freedom, as shown in figure 2.21. This concept deploys into a flat configuration, which employs the two basic modules shown in Figure 2.14 and Figure 2.20. It possesses six-fold symmetry, and the inner ring is a 36-link spatial mechanism. Further analysis must be conducted to fully characterize the kinematics of these multi-link spatial mechanisms.

2.8 Modular Doubly-Curved Surface Array with Edge Support

This section proposes an innovative method to stow, deploy and adjust curved shells based on active structures and the modular deployable surface arrays from section 2.7. The unimorph architecture is introduced as the curvature actuation scheme, and the material selection is briefly discussed in this section. The achievable curvature for a CFRP substrate bonded to the piezoelectric plates was estimated under a high electric field. An example concept of a curved active surface array with small package volume and post deployment shape correctability is given at the end of the section.

2.8.1 Introducing Non-Zero Gaussian Curvature to Flat Shell

2.8.1.1 Unimorph Architecture and Material Selection

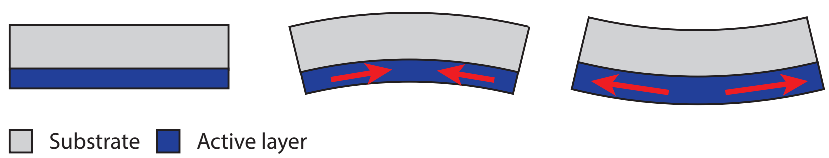

Figure 2.22: The unimorph actuation architecture for thin shell structure. Middle plot: Active layer shrinks in-plane. Right plot: Active layer expands in-plane.

Unimorph structures, composed of substrates bonded to thin shells of in-plane active materials, typically piezoelectric as shown in figure 2.22, are an effective architecture for shape actuation. The architecture converts the non-uniform in plane strain distribution over the thickness to a local or global curvature change of the shell. This architecture has been widely used to construct deformable mirrors which compensate for the incoming light's wavefront error [70]. Hence, the peak-to-valley deformation of such active shells is generally at sub-micron level. However, under the following conditions, a significant change of the global curvature can be introduced to an initially flat shell 1) the thickness ratio between the substrate and the active layer is optimal; 2) the active layer's electro-mechanical coupling coefficient is adequate; 3) the active layer covers sufficient area of the shell. The level of actuation response greatly depends on the material choice of the active shell. Table 2.1 displays the parameters of various candidate materials, which are necessary for designing active shells:

Table 2.1: Material Selections for Active Shell

		Density (Kg/m^3)	Modulus (GPa)	CTE* (ppm/K)	EM coupling (pm/V)
Substrate material	Glass[1]	2.4×10^3	68	1.964	-
	Beryllium[2]	1.84×10^3	303	15	-
	CFRP[3]	1.6×10^3	395.3/6.26	-2 ~2	-
Active material	PVDF[4]	1.78×10^3	1.5	50 ~300	16
	PZT[5]	7.6×10^3	62	4	- 190

[1] Schott D263 borosilicate glass [83].
[2] Type O-30 [84].
[3] Properties measured in lab, modulus measured along and perpendicular to fiber directions. CTE data quoted for general CFRP materials.
[4] From Patterson [85]. CTE and coupling coefficient are temperature dependent.
[5] PSI-5A4E from Piezo Systems, Inc [86].
* Coefficient of Thermal Expansion.

2.8.1.2 Curvature Response Estimation

The curvature response of an actuated unimorph structure depends on the ratio of the thickness between the substrate and the active layer and the electro-mechanical coupling coefficient of the active layer. It can be approximated by the general form of the classical laminate theory (CLT) which takes into account the hygrothermal effect [87]. The mid-plane strain $\boldsymbol{\varepsilon}_0$ and the global curvature $\boldsymbol{\kappa}$ vectors are given by:

$$\begin{bmatrix} \boldsymbol{N} \\ \boldsymbol{M} \end{bmatrix} + \begin{bmatrix} \boldsymbol{N}^{HT} \\ \boldsymbol{M}^{HT} \end{bmatrix} = \begin{bmatrix} \boldsymbol{A} & \boldsymbol{B} \\ \boldsymbol{B} & \boldsymbol{D} \end{bmatrix} \begin{bmatrix} \boldsymbol{\varepsilon}_0 \\ \boldsymbol{\kappa} \end{bmatrix} \tag{2.12}$$

Here $\boldsymbol{N}$ and $\boldsymbol{M}$ are the external force and moments per unit length applied on the laminate. $\boldsymbol{N}^{HT}$ and $\boldsymbol{M}^{HT}$ are the force and moments generated by the hygrothermal strain due to the temperature change ΔT and the moisture concentration ΔC. In the case of a unimorph shell under actuation:

- There are no external loads, hence $\boldsymbol{N} = \boldsymbol{0}$ and $\boldsymbol{M} = \boldsymbol{0}$.
- Estimation of actuation force and moments $\boldsymbol{N}^A$ and $\boldsymbol{M}^A$ follow the same derivations of $\boldsymbol{N}^{HT}$ and $\boldsymbol{M}^{HT}$ [87].

$\boldsymbol{N}^A$ and $\boldsymbol{M}^A$ can be calculated as follows:

$$\begin{aligned} \boldsymbol{N}^A &= \boldsymbol{Q}_a \boldsymbol{\varepsilon}_a t_a \\ \boldsymbol{M}^A &= \boldsymbol{Q}_a \boldsymbol{\varepsilon}_a z_a t_a \end{aligned} \tag{2.13}$$

where $\boldsymbol{Q}_a$ is the in-plane stiffness matrix of the active layer, $\boldsymbol{\varepsilon}_a$ is the piezoelectric strain due to the electric field actuation, t_a is the thickness of the active layer, and z_a is the distance between the reference plane of the laminate and the mid surface of the active layer. The piezoelectric actuators were assumed to be pre-poled along the thickness direction, thus the applied electric field activates the d_{31} mode of the material [71]. Using the formulation, the curvature response of a 16 layer laminate with layup sequence [0 / 90 / ± 45]s made from 30 gsm prepreg bonded with different thicknesses of thin piezoelectric sheets is shown in figure 2.23. Material properties for the parametric study are shown in table 2.2. An electric field of 0.8 MV/m was assumed to be applied across the thickness of the active layer, and the material was assumed to respond linearly to the excitation.

Table 2.2: Material Properties for Active Laminate Actuation Response Estimation

Material	E_1 (GPa)	E_2 (Gpa)	G (GPa)	ν_{12}	ρ (kg/m^3)	t (μm)	d_{31} (PC/N)
Prepreg	395.3	6.3	4.24	0.33	1.6×10^3	28	-
PZT-5A	62	-	23.8	0.31	7.6×10^3	-	-190

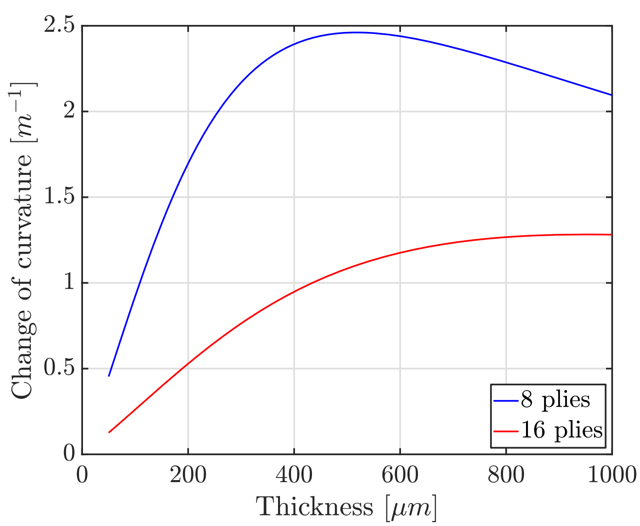

Figure 2.23: Unimorph available curvature under electric field actuation.

From the estimation results, a radius of curvature of less than 2 m can be achieved on an active laminate shell with a total thickness less than 1 mm. The optimal active layer ratio depends on the laminate layup and the in-plane elastic properties of both materials. The architecture offers flexible design of the actuation response.

2.8.2 Curved Reflector Array Deployment and Actuation Concept

The deployable reflector concept shown in figure 2.24 is based on the curved three-fold symmetry tessellation and also adopts the unimorph-based curvature actuation scheme discussed above. This concept involves two steps: deploying the support mechanism made of circular beams, and then actuating the active shell. The deployment scheme for the mechanism can be based either on figure 2.18 or on the detached version in figure 2.19. After reaching the fully deployed configuration, the rolling hinges are locked and an electric field is applied to the unimorph reflector segments to achieve the final predefined global curvature. Both the panel and crease regions were assumed to include active layer. The selection of materials and laminate designs for the crease region are discussed in section 2.9.

In this particular concept, the reflecting surface (panel region) fills 70% of the total aperture. It has an aperture size of 200 with a focal length of 70 (unitless), which resulted in an F number of 0.35, where $F = \frac{R_1}{4R_2}$. This ratio could be continuously adjusted over a wide range of values, by altering the dihedral angle between adjacent modules. The concept can be generalized in order to deploy other curved surfaces.

2.9 Folding Limits for Candidate Thin Materials

2.9.1 Material Selections for Crease Regions

To provide post-deployment shape correctability for the foldable shell shown in figure 2.24, the entire surface must to be covered with an active material. Thus, the functionality of the deployed active shell depends on whether the crease region can endure the folding and deployment motion. Under the pure bending assumption, the maximum strain of of thin, initially flat or singly-curved shell appears at the top and bottom layer and can be estimated as:

$$\varepsilon_{max} = t_t \cdot \Delta\kappa, \quad \varepsilon_{min} = t_c \cdot \Delta\kappa \tag{2.14}$$

where κ is the curvature of the folded crease region, t_t is the distance of the tensile surface side to the neutral axis of the shell, and t_c is the distance on the compression side. $\Delta\kappa$ is the change in curvature between initial and fully folded configurations.

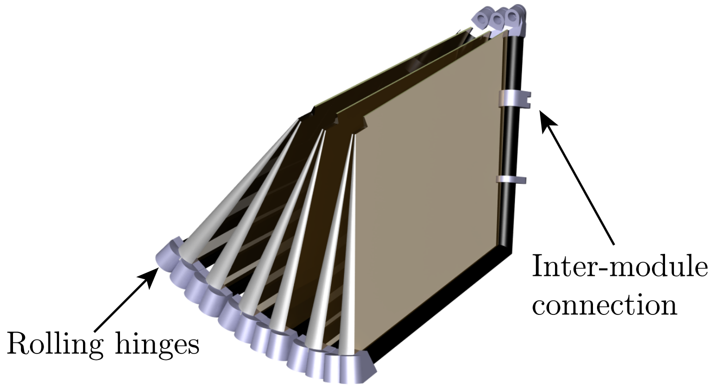

(a)

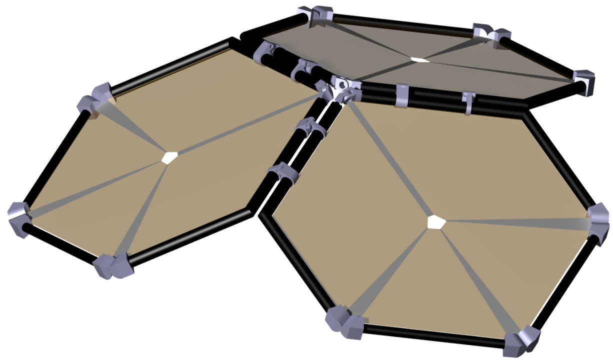

(b)

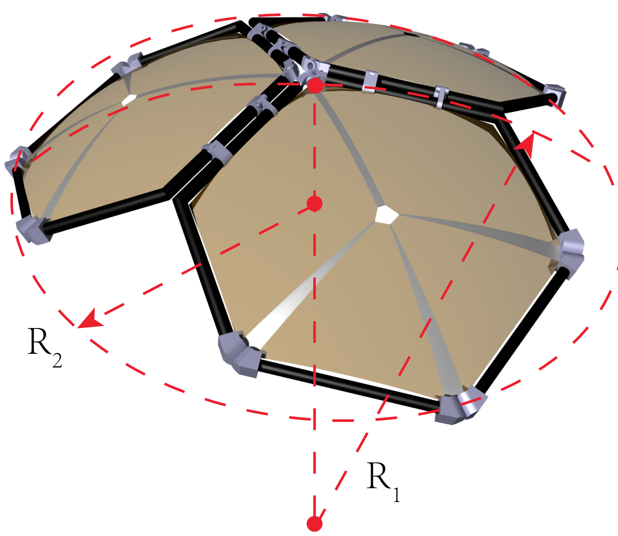

(c)

Figure 2.24: Concept of a modular deployable spherical reflector array deployment sequence, in pre- and post- actuation configuration. R_1 is the radius of the aperture, R_2 is the radius of the actuated active shell.

Piezoelectric ceramics are known to be brittle and have small tensile failure strain limit; however, it is possible to achieve a moderate or large folding curvature ($\Delta\kappa > 50\ m^{-1}$) for piezoelectric plates when the thickness is sufficiently small and the material is under compression. Recent studies have revealed that under large bending deformations, ultra thin composite laminates can attain significantly higher failure strains compared to flat coupon test values. These properties were exploited on the foldable unimorph laminated structure at the crease regions of the shell.

Accurate measurements of the candidate material's flexural strain limits are key to the development of foldable unimorph shells. Two types of ultra-thin materials were chosen: 127 μm thick thin piezoelectric plates from Piezo Systems Inc. [86] and laminates made from M55J(fiber) - Thinpreg120(epoxy) prepregs obtained from North Thin Ply Technology (NTPT) [88]. Both the tensile and compressive flexural strain limits were measured using the platen method.

2.9.2 Platen Test Set Up

The platen test (figure 2.25) is a flexural test method designed to investigate the failure strain of thin, stiff materials under large bending deformations [89]. During the test, the coupon is taped to the edges of both the top and bottom platens in an initially vertical state. The platens are then monotonically driven towards each other to trigger the post buckling deformation of the coupon, and both the moment-curvature relationship and the failure strain limit can be obtained for the material.

The surface strain history of the coupon during the large bending process was recorded through 3D Digital Image Correlation (DIC) measurements. In order to obtain the absolute failure strain, the unloaded configuration of the tested sample (figure 2.25a) was chosen as the reference state for strain calculations. Maintaining the speckle pattern in focus during the large in-depth deformation is crucial for the DIC measurements, thus a deep field of view was used for the stereo cameras' lenses by choosing an aperture with an F number of 12. All tests were conducted on an Instron material test machine with quasi-static loading rate.

2.9.3 Platen Tests of Ultra-thin Piezoelectric Laminates

Due to its high brittleness, testing a pure plate of piezoelectric ceramic was impossible with the available lab set up. The following flexural strain measurements were made on piezoelectric ceramic-CFRP laminate coupons. 127 μm thick PZT-5A plates were bonded to 4-ply, pre-cured CFRP laminate with [90/0]s layup. Here the 0 direction of the laminates was defined to be parallel to the longer side of the sam-

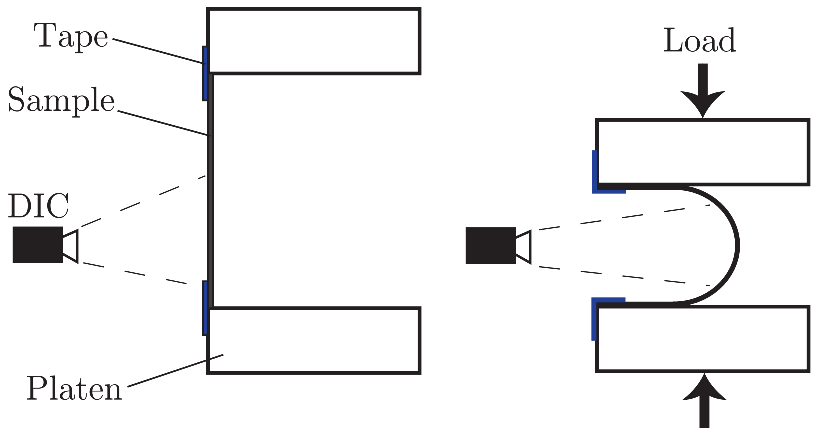

(a)

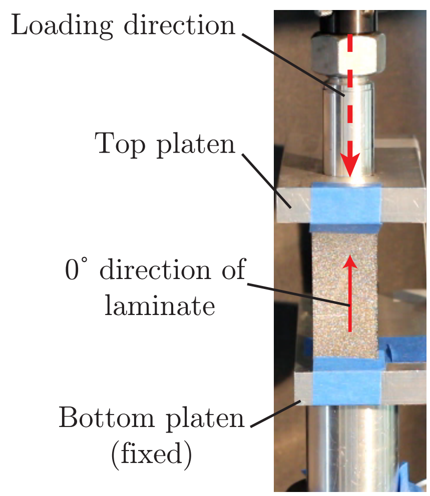

(b)

Figure 2.25: (a) The platen test procedure. The test assembly is placed between the loading heads of the material test machine. (b) Experiment set up and definition of the 0°direction of laminate samples.

ples, as shown in figure 2.25. The bonding agent was a low viscosity, liquid epoxy system. To ensure a thin bonding line, the piezoelectric plates and the laminates were bonded using a vacuum bag that applied 1 atm of pressure on the coupon. Thicknesses of each layer of the coupons were measured through micrographs of polished cross-sections of the tested samples, as shown in figure 2.26. The average thickness of a four-ply, 30 gsm thin laminate was 120 μm.

To control the direction of the post buckling deformations, at the beginning of each test the coupon was slightly perturbed towards the desired deformation direction to trigger tensile or compressive failure of the PZT. For tension and compression platen tests, five PZT-laminate coupons were manufactured for each case. The

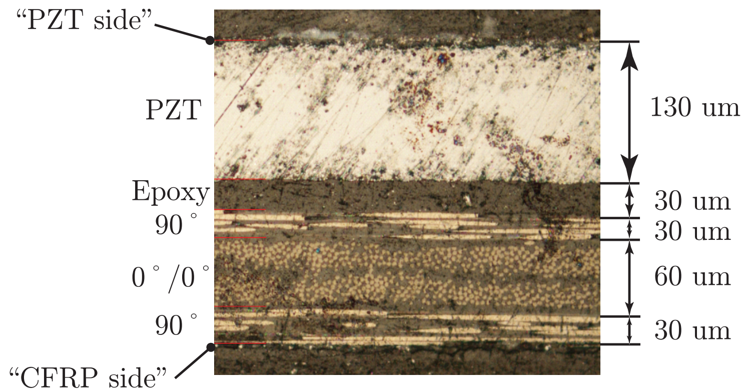

Figure 2.26: Micrograph of the PZT laminate coupon cross section.

critical DIC frame before failure for both compressive and tensile failures are shown in figure2.27. In all tests, the PZT-laminate coupons showed a catastrophic failure mode.

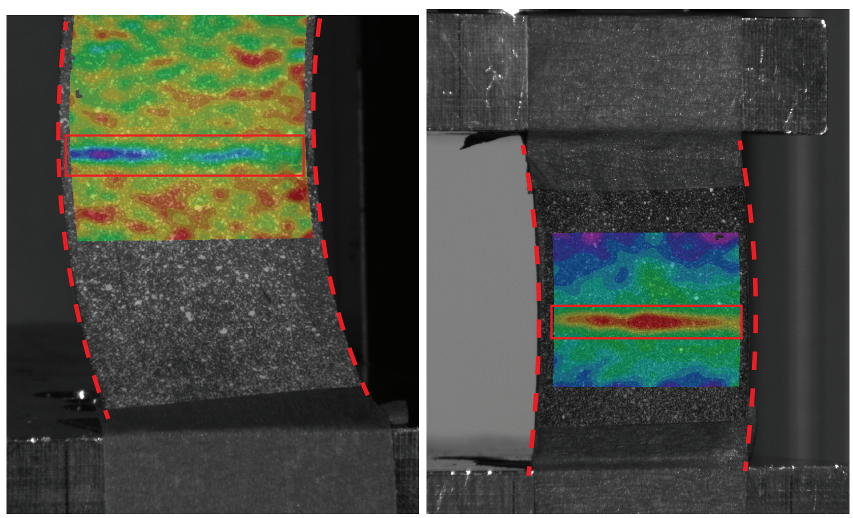

(a) (b)

Figure 2.27: Surface strain distribution from DIC measurements of PZT-CFRP coupon before failure: (a) PZT under compression, (b) PZT under tension. Red box represents the area from which the curvature-strain relation was extracted.

2.9.4 Platen Tests of Carbon Fiber Laminates

The strain limits of CFRP prepreg are discussed in this section. Because it is a highly-orthotropic material, the failure mechanism of a single ply of prepreg parallel and perpendicular to the fiber direction dominates. Thus, ε_{tmax} and ε_{cmax} were measured along both directions. For the 0°direction, the failure strains are

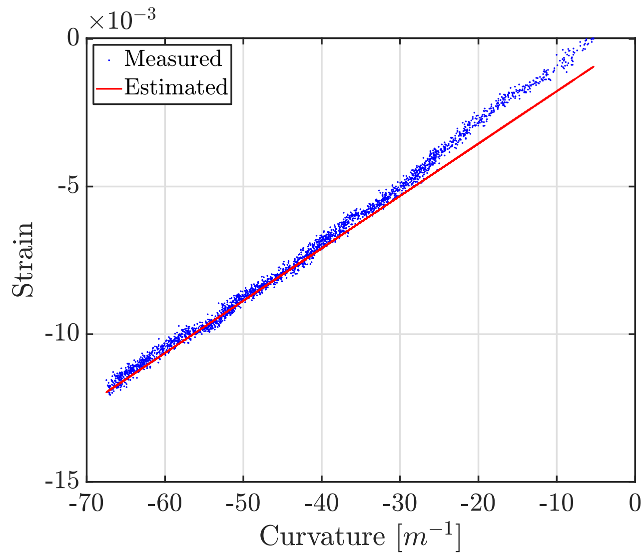

Figure 2.28: Compressive strain history of the "PZT side" of the PZT-CFRP coupon. The curvature-strain relation was linear up until failure.

measured with [0/90]s coupons and the 90°direction was measured with [90/0]s coupons. The critical DIC frame before failure is shown in figure 2.29.

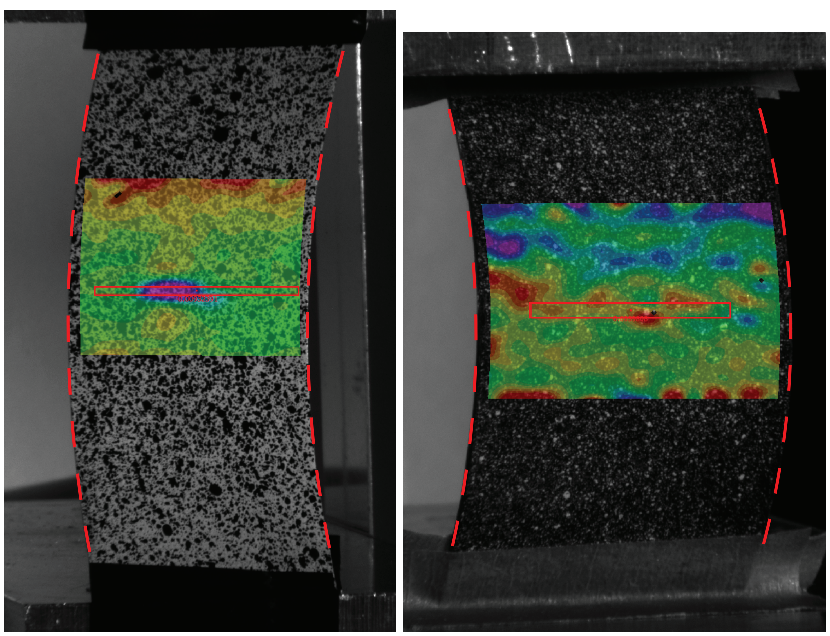

(a) (b)

Figure 2.29: Surface strain distribution from DIC measurement of CFRP only coupons before failure: (a) compressive side, (b) tensile side. Red boxes represent the areas from which the curvature-strain relations were extracted.

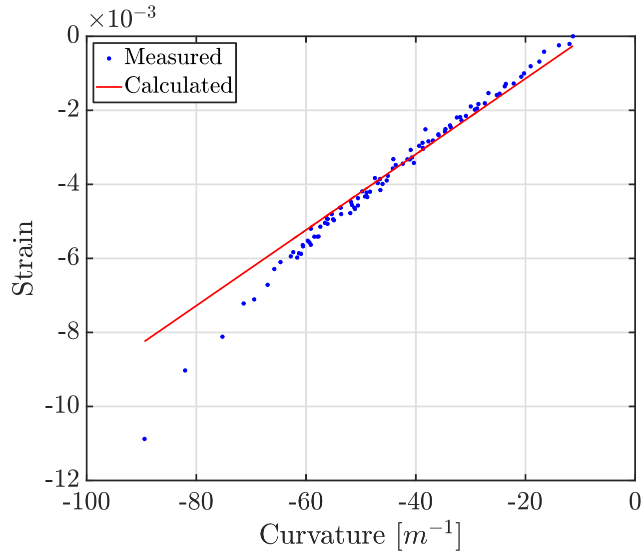

(a)

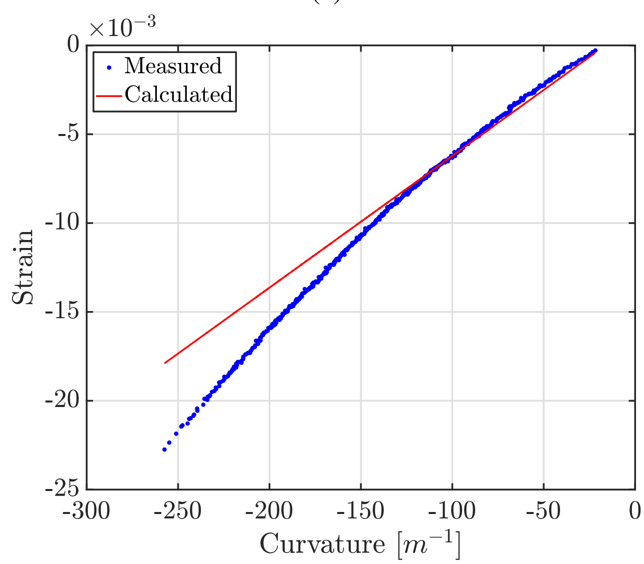

(b)

Figure 2.30: Compressive strain history of CFRP only coupons up until failure: (a) Eight-ply coupons, (b) Four-ply coupons. For thinner coupons, the strain started to deviate significantly from linear relation with measured curvature.

2.9.5 Laminate Folding Limit Estimations Based On Failure Strain Measurements

The failure strain measurements of the prepreg and the piezoelectric ceramic plates are summarized in table 2.3:

Table 2.3: Flexural Failure Strain Measurements of Candidate Materials

Material	Compressive failure strain ε_{max}	Tensile failure strain ε_{min}
0 prepreg	< -0.8 %	0.8 %
90 prepreg	-1 %	0.65 %
PZT-5A	-1.3 %	0.3 %

Using the measured strain limits, the feasible folding radius of curvature was estimated with CLT based on the first ply failure principle. Assuming the unimorph structure was under a pure external bending moment, the compliance relation of the laminate is given by:

$$\begin{bmatrix} \boldsymbol{\varepsilon_0} \\ \boldsymbol{\kappa} \end{bmatrix} = \begin{bmatrix} \boldsymbol{a} & \boldsymbol{b} \\ \boldsymbol{b} & \boldsymbol{d} \end{bmatrix} \begin{bmatrix} \boldsymbol{N} \\ \boldsymbol{M} \end{bmatrix} \tag{2.15}$$

The critical layer's strain was estimated with

$$\begin{aligned} \boldsymbol{\varepsilon} &= \boldsymbol{\varepsilon}^0 + t \cdot \boldsymbol{\kappa} \\ &= \left(\frac{b}{d} + t \right) \boldsymbol{\kappa} \end{aligned} \tag{2.16}$$

The curvature limit could then be expressed as

$$\kappa_l = \frac{\varepsilon_l}{\frac{b}{d} + t} \tag{2.17}$$

where $\varepsilon_l = \varepsilon_{max}$ or ε_{min}. Four different failure scenarios were evaluated: compressive or tensile failure of the PZT layer bonded to an eight-ply laminate or 16-ply laminate. This result is summarized in figure 2.31. Compact folding radius is possible when the active layer is under compression and bonded to a thin substrate; this is reduced to 2 cm when the eight-ply substrate is evaluated. The results prove that converting the crease region into active unimorph structures for post-deployment shape actuation is feasible.

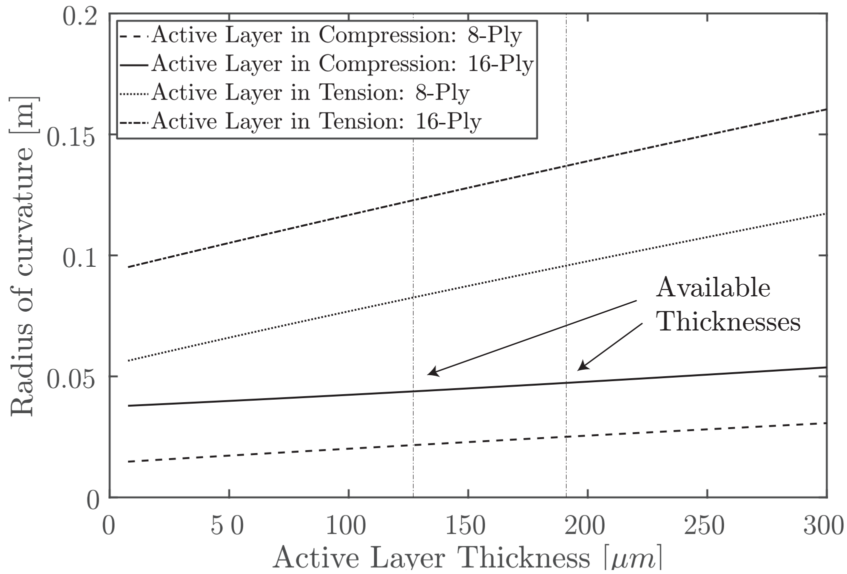

Figure 2.31: Folding limits estimations for ultra thin PZT-CFRP unimorph structures. The dashed vertical line represents the representative thicknesses of commercially-available thin PZT plates.

2.10 Foldable Curved CFRP Shell Design and Manufacturing

A major feature of the folding pattern of thin shells proposed in section 2.5 is that large deformation concentrates in the regions of the shell with reduced bending stiffness. These regions will form localized elastic folds with a smooth transition of curvature, and will be referred to as smooth folds. Because of this unique property, the panel areas of the shell can adopt a thicker layup, due to being free of folding and deployment influences. Thus, manufacturing a high precision, CFRP composite shell that is free of high strain during folding is possible. A curved CFRP shell made from materials characterized in section 2.9 was designed and manufactured.

2.10.1 Layup Blending Scheme

To implement the folding pattern with reduced bending stiffness regions along the smooth folds using carbon fiber materials, the laminate design is subject to certain constraints:

- One side of the shell should remain continuous and smooth.
- Local layup at the smooth folds is determined by the folding radius limit.
- Global layup should be symmetric everywhere on the shell.

These requirements can be achieved through laminate blending. Blending is a method of tailoring the design variables of laminates by adopting suitable ‘ply drop and add’ techniques opportunely in the composite materials. As shown in figure 2.32, two adjacent panels are outwardly (inwardly) blended if one panel is obtained by deleting a contiguous series of outermost (innermost) plies from the other. The first constraint ensured that the outwardly blending scheme was adopted.

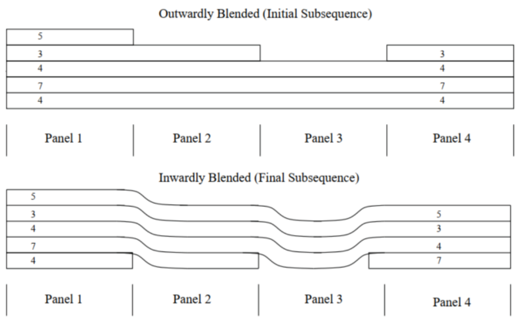

Figure 2.32: Outwardly/inwardly blended laminate examples, reprinted from [90].

The targeted folding curvature κ for the prototype conceived in this section was 0.5 cm^{-1}. Based on the strain limit listed in table 2.3 and the first ply failure analysis, a symmetric four ply layup [0/90]s was chosen for the smooth folds, with the reference direction defined parallel to each folding line. The basic layup for the panels was chosen as [[0/90] + [0/90]s + [0/90/+-45]s]s. To conform to the third constraint, additional plies were added to the outermost layer after the ply drop from the adjacent panel, which is dark grey in figure 2.33. The region is referred to as the transition region. After this modification, all the panels were symmetric with respect to the mid-plane.

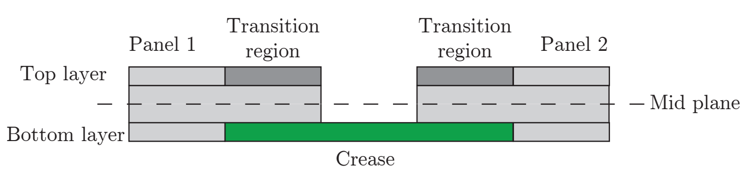

Figure 2.33: Cross-sectional view of the proposed blending scheme for merging the layup at different regions of the shell.

The partitions of regions and the local 0°directions of the laminate shell are illustrated in figure 2.34. Layups for different regions of the shell are listed in table 2.4. As illustrated in the normalized bending stiffness D_{11} map in figure 2.34 (b), the blending scheme ensures ultra low bending stiffness at the smooth folds, but also introduces fiber discontinuities at the transition lines between adjacent regions. The influence of the discontinuous D_{11} on the shape error of the shell will be shown in section 2.10.3.

Table 2.4: Layup Design for the Composite Foldable Shell

Region	Layup
Panel	[[0/90] + [0/90]s + [0/90/+-45]s]s
Transition region	[[30/120] + [0/90]s + [0/90/+-45]s]s
Smooth fold	[0/90]s

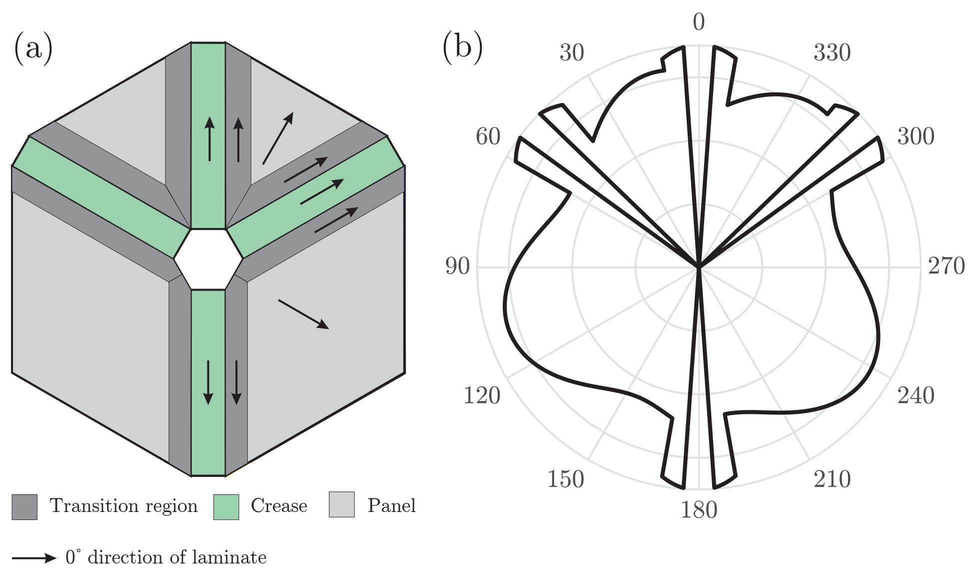

Figure 2.34: Layup design of a composite foldable shell: (a) Division of the shell regions. Layup is symmetric with respect to the vertical line, (b) Normalized D_{11} map of the shell in polar coordinates.

2.10.2 Manufacturing Technique

Optical replication is a technique commonly used for manufacturing composite shells with smooth surface and high shape precision. The procedure usually includes hand or robot assisted material lay-down processes, during which layers of thin CFRP prepregs are laid on a mandrel with optical surface quality and a precise shape. The laid down material is then cured with the mandrel in an autoclave. This process is illustrated in step 1 of figure 2.35, and can be easily scaled to larger dimensions.

To create an active thin shell structure based on a replicated foldable composite shell envisioned in section 2.8 an additional step was required, as shown in figure 2.35, step 2. During this step, ultra-thin piezoelectric plates of the same shapes as the panels are press-bonded to the substrate before debonding the shell from the mandrel. The plates can be flat or polished to the same radius of curvature as the shell. Epoxy with low viscosity and shrinkage should be used as the bonding agent to avoid inducing extra distortion after curing. The structure can then be debonded from the mandrel and the next step of processing can begin. For instance, a reflective layer coating of the front surface can be applied by vacuum sputtering.

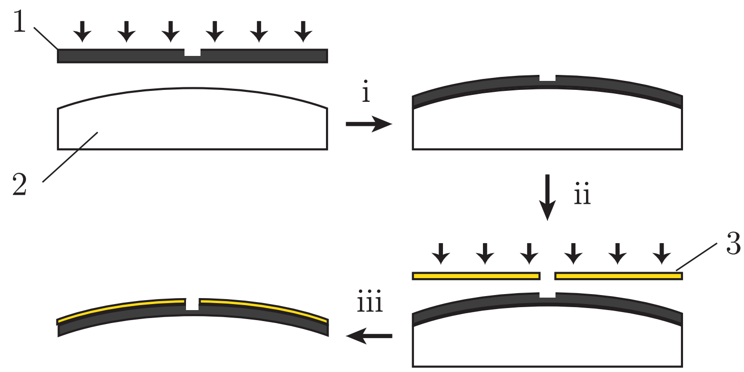

Figure 2.35: Manufacturing steps of the foldable piezoelectric shells. Step i: Laying down and curing the blended laminate with ply drop at the smooth folds. Step ii: Bonding of thin piezoelectric plates. Step iii: Demolding the bonded active shell. Small arrows denote the external pressure applied through autoclave or vacuum bag. Labeled parts: 1. Foldable composite substrate. 2. Curved mandrel. 3. Thin piezoelectric ceramic plates.

2.10.3 Manufactured Shell and Surface Measurements

To demonstrate and validate the blending scheme and the manufacturing technique, a prototype composite shell was manufactured and measured following the design in section 2.10.1. The prepreg used were M55J - Thinpreg-120, and were hand laid on an mandrel with a radius of 2 m. The size of the shell is 125 mm edge to edge. The laminate was cured inside a vacuum bag using autoclave processing at 120°C and 2 atm. The center of the shell was cut out to remove the singular point in the folded configuration.

The manufactured shell after debonding is shown in figure 2.36 (a). The average thickness of the panel was 400 µm and the smooth folds were 100 µm thick. DIC measurement of the front surface are illustrated in figure 2.36 with gravity acting perpendicular to the shell. The measured point cloud data were post-processed to remove the rigid body motion. A relatively high surface precision was achieved (22.5 µm RMS error over a diameter of 10 cm) with the proposed layup and manufacturing technique. The major error source was concentrated in the smooth folds. This was due to (1) the sharp drop of ply count at the interface between the transition and the smooth folds and (2) the local un-balanced laminate layup.

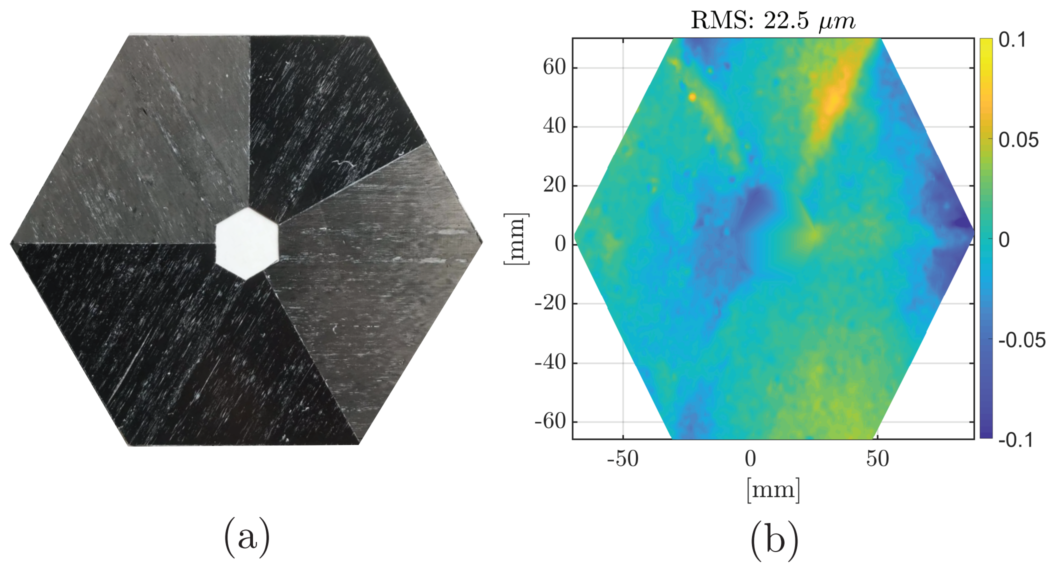

Figure 2.36: (a) Front view of the curved composite foldable shell. Seams can be seen between layups with different fiber directions. (b) Surface error map of the shell compared to a spherical surface with the same radius (2 m). RMS error of the entire surface is 22.5 µm. Color bar unit: mm.

The manufactured shell can be smoothly folded following similar kinematics to the Miura fold, as demonstrated in figure 2.37. No visible damage developed after the shell was restored to the initial unstressed state.

2.11 Scaling Analysis of a Single Module

This section provides a numerical scaling law of an initially flat, mechanism-guided, deployable active thin shell module based on the concept proposed in the previous section. The module was assumed to be simply supported around the edge and operates under gravity loading. These boundary conditions are considered as the module will be used as ground-based deployable reflectors. Using numerical simulations, the study showed the trend in maximum deformations of the shell and supporting beam, RMS values of the deformed shell surface d_{RMS}, and the fundamental frequency of vibration f of the module under the boundary conditions.

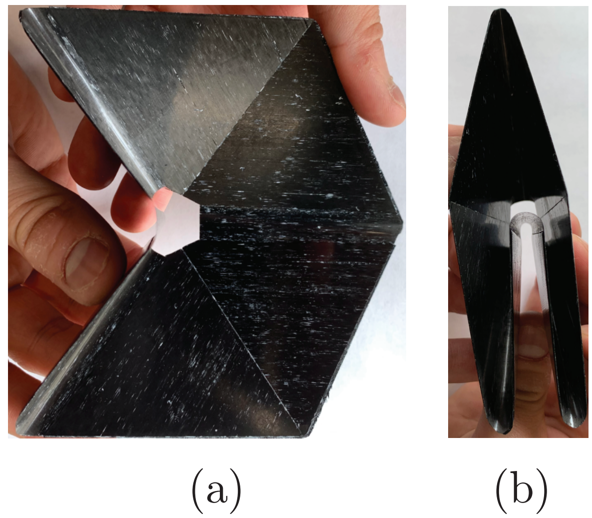

Figure 2.37: Folding of the curved composite shell with layup blending. (a) Initiation of folding by pushing around the smooth folds. (b) Fully folded configuration.

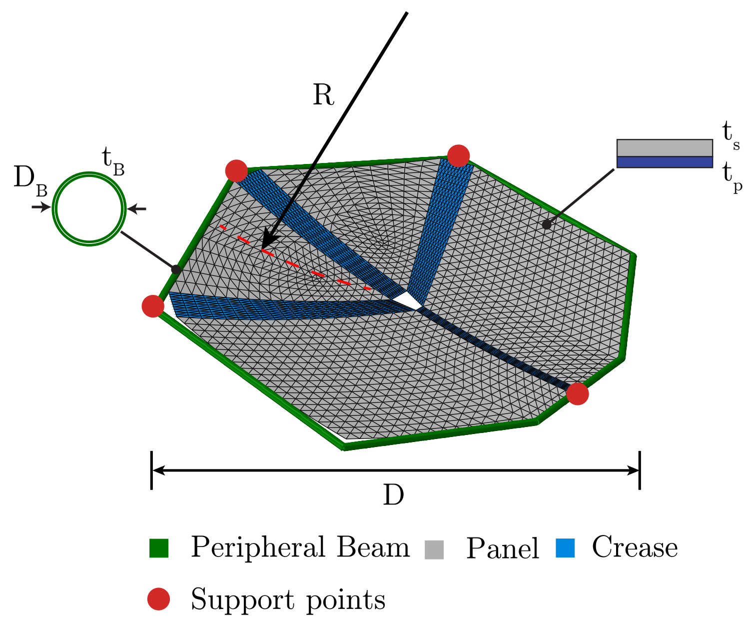

Figure 2.38: Scaling parameters for the deployable module. The shell is deployed, actuated to the desired radius, and supported at the four hinge locations of the perimeter beam. The perimeter beams are assumed to have a circular cross section.

2.11.1 Problem Description

As shown in figure 2.38, the simplified model for the scalable module was composed of: 1) four peripheral beams connected at both ends and 2) a foldable shell divided into panel and crease regions. The module was simply supported at the four connection points of the peripheral beams. Each beam was assumed to have a hollow, circular, thin wall cross section. In the analysis, the geometry and mass of the rolling hinges at the connections points of the beams were neglected since the deformation history and dynamics during the module deployment is not the focus of this scaling study. The creased shell adopted the unimorph architecture studied in section 2.8 which provides the curvature actuation capability. The shell was assumed to be actuated to the desired shape before the loading step, and the resulting internal stress was neglected. The free variables for the scaling study are shown in table 2.5.

Table 2.5: Geometric Parameters for Single Module Scaling Analysis

Radius of shell	Diameter of module	Panel thickness	Crease thickness
R	D	t_s	t_c
Perimeter beam diameter D_B	Beam wall thickness t_B	Piezoelectric layer thickness t_p	

A series of static loading and linear perturbation analyses were conducted in Abaqus/Standard. Deformation of two module types were simulated: 1) embedded shells with panels of 16-ply layup: $[0/45/-45/90]_s + [0/45/-45/90]_s$ and creases of two-ply layup: $[45/-45]$, and 2) panels of 32-ply layup: $[[0/45/-45/90]_s + [0/45/-45/90]_s]_s$ and creases of four-ply layup: $[45/-45]_s$. For the 16-ply shells, a piezoelectric layer of t_p = 127 μm was assumed to be bonded to the back side, including the creases; for the 32-ply shells, a t_p = 200 μm piezoelectric layer is bonded. Material properties used in the simulations are listed in table 2.2. The estimated areal densities of the 16-ply and 32-ply active shells were 2.1 gsm, and 2.5 gsm, respectively.

2.11.2 Scaling Simulation Results and Discussions

The main categories of performance measurements were: maximum perimeter beam deflection d_b, maximum shell deflection d_s, and fundamental frequency of vibration of the module f. Results for both the 16-ply and 32-ply modules are summarized in table 2.6 and table 2.7, respectively.

The following was concluded from the simulation results:

- The module diameter D determines the order of maximum deflection of both

Table 2.6: Scaling Results for Curved Thin Shell Modules

D (m)	Total mass (Kg)	D_B (mm)	D_B/t	Max beam deflection (mm)	Max shell deflection (mm)	Fundamental frequency (Hz)
2.44	4.3	20	20/1	0.13	0.127	42
2.44	14.7	40	40/2	0.003	0.0017	82
4.88	15.9	20	20/1	1.90	3.40	8.4
4.88	19.1	40	40/2	0.16	0.48	16
4.88	36	100	100/4	0.03	0.06	26.5
9.76	103	100	100/4	0.44	0.99	7.8

[1] $R/D = 1.5/2.4$.
[2] Total mass includes the perimeter beam.

Table 2.7: Scaling Results for Curved Thick Shell Modules

D (m)	Total mass (Kg)	D_B (mm)	D_B/t	Max beam deflection (mm)	Max shell deflection (mm)	Fundamental frequency (Hz)
2.44	22.3	100	100/4	0.008	0.01	41
4.88	62	100	100/4	0.1	0.20	13
4.88	74	120	120/4.8	0.07	0.13	13
9.76	217	100	120/4.8	1.2	2.10	4.5
9.76	356	200	200/8	0.5	0.60	5.3

$R/D = 5/2.4$.

the shell and the perimeter beam under gravity.

- Both d_b and d_s scale down exponentially as the beam diameter D_B increases. This scaling effect attenuates when D increases.

- For the same diameter D, modules with 16-ply thin active shells can achieve similar performances as the 32-ply active shells with half the total mass.

This study suggests that the design could be used as segmented deployable reflectors for ground-based infrared (IR) observations. Although modules with thinner shells were superior in terms of mass efficiency, manufacture-induced errors were more pronounced. Compromises must be made in real world applications in order to choose the right layup for the active shell.

2.12 Summary and Discussions

This chapter has proposed a series of novel design, analysis, and manufacturing techniques that led to a class of deployable piezoelectric thin shells. The proposed deployable structure concept allowed for packaging of a thin shell with edges attached to a spatial mechanism. Steps for constructing a compactly foldable spatial mechanism from a rigid origami pattern were first presented. From the same origami pattern, a flat thin shell with smooth creases was integrated with the mechanism. A simple geometrical criterion between the crease of the shell and the modified hinge of the mechanism was established, such that the folding motion affected a limited area of the shell. Design and folding analysis of the module were verified through a physical prototype. Multiple tessellation concepts are proposed by linking the basic modules with revolute hinges into spatial mechanisms. Tessellations, which could be both flat and curved in the deployed configuration, were presented.

The innovative features of the design were two fold. First, instead of rolling/folding the entire surface, only a limited part of the shell underwent large deformation. Second, the mechanism around the shell acted as both the actuator for deployment and the support structure. This feature guaranteed a quasi-static deployment of the shell and high stiffness in the post-deployment configuration. Both of these features are especially attractive when high post-deployment surface accuracy is required by the application.

One major concern for the realization of the design was the strain limit of the materials used in the crease region. The flexural strain limits for ultra thin CFRP laminates and piezoelectric plates are measured using the platen test method. A 200 µm CFRP flat shell bonded with a 120 µm piezoelectric plate could be folded to a radius of 20 cm by keeping the piezoelectric side under compression.

Several discussion points should be noted for the proposed foldable thin shell module. First, although the proposed module and tessellation concepts were all based on the Miura-Ori pattern, the design was not unique. Following the same design methodologies, a larger category of origami patterns could be converted to a light weight, deployable thin shell structure with edge supports. Second, as new types of active polymer actuators start to emerge, which can endure large stretching and bending, the folding limit of the crease can be further decreased. Third, this chapter was mainly based on the folding design of initially flat shells. Section 2.10 demonstrates that a shallow shell is also foldable with the proposed crease-panel blending scheme. A study of the relation between global deformation and the geometry and stiffness of the crease pattern of a doubly-curved shell is suggested as an extension of this work.

Chapter 3

PHENOMENOLOGICAL MODEL CHARACTERIZATION FOR PIEZOELECTRIC MATERIALS

3.1 Introduction

In the concepts proposed in chapter 2, curvature changes were introduced in the deployable thin shell structures through the unimorph architecture, by applying high electric field actuation. In general, piezoelectric materials exhibit nonlinear behavior under strong electric and/or stress fields. The effect is more evident in polycrystalline materials, such as PZT-5A tested in the previous chapter, due to the evolution of complex domain structures (the extrinsic contribution). The evolution of domain structures is also the source of large electro-mechanical coupling coefficient. Such unique properties combined with a large blocking force capability make piezoelectric material-based devices favorable in active structure applications that require both high precision and large stroke. Piezoelectric material-based unimorph and bimorph structures are typical examples that have been widely used in MEMS applications [91], [92] for displacement control and large scale adaptive optics [70]. More comprehensive introductions can be found in APC [93] and Vijaya [94]. Design and operation of piezoelectric thin shell structures pose two main challenges: tracking the evolution of the material state under complicated loading conditions (both electrical and mechanical) to guarantee precise operation, and optimal design of the structures to obtain the desired response under a certain level of actuation. This chapter aims to provide tools to tackle both challenges by calibrating a macroscopic nonlinear material model and incorporating it into an efficient estimation algorithm for piezoelectric thin shell structures. This model will then be validated against experimental measurements.

3.2 Background and Motivation

Challenges in modeling structural behavior originate from the complicated, non-linear response of piezoelectric materials under mixed fields. These phenomena usually manifest themselves in the form of ferroelectric/ferroelastic hysteresis and remnant strain under electric and mechanical loading. To predict such behaviors, realistic models of the active layer material are critical. There has been a continuous pursuit of piezoelectric material models that can capture domain switching

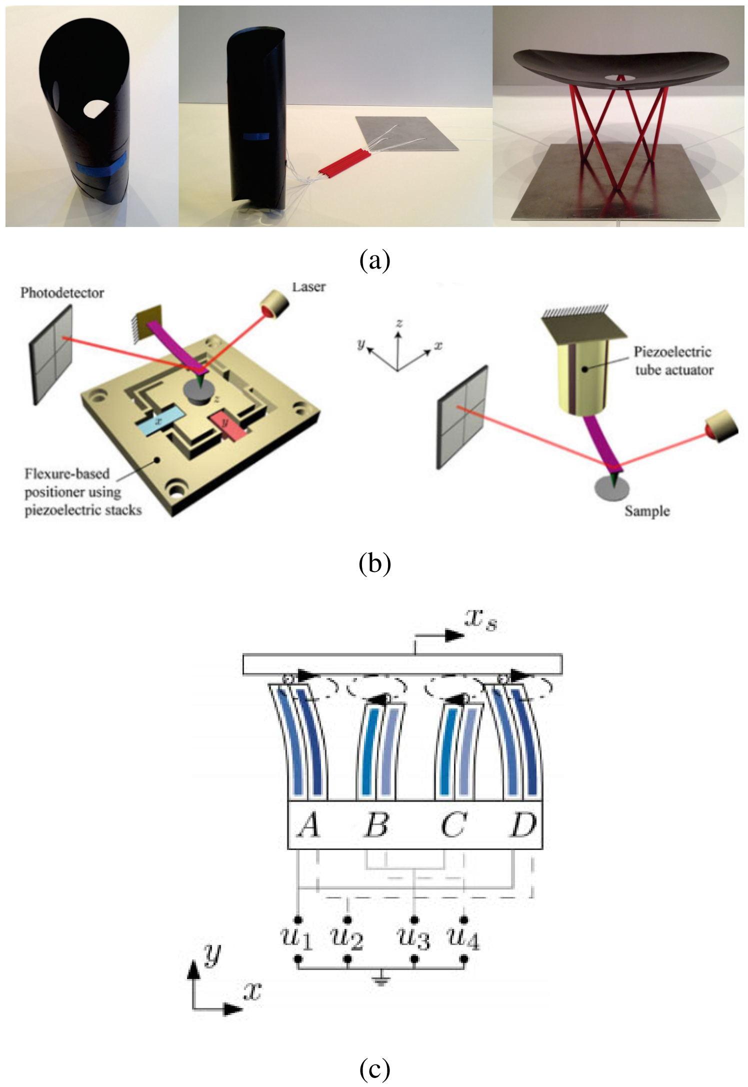

Figure 3.1: Piezoelectric unimorph structure application examples: (a) Rollable active mirror concept [41], (b) Positioning of scanning probe microscope head [91], (c) Schematic working principle of walking piezo motor [92].

induced material nonlinearity precisely. These models can be broadly categorized into microscopic and macroscopic approaches, depending on how the model relates the macroscopic level properties and responses to the microscopic domain structure evolution. An overview of the different modeling approaches to date can be found in the works by Landis [95], Potnis, Tsou, and Huber [96], Shieh, Huber, and Fleck [97] and Huber [98]. A representative microscopic approach is the phase field method, which implements a diffuse-interface modeling framework to track the evolution of ferroelectric domains. Representative works were presented by Su and Landis [99], Schrade [100], and Vidyasagar, Tan, and Kochmann [101]. The phase field model was able to capture the complicated interactions among domain walls between different variants and crystal dislocations [102]–[104]. In these models, the parameters involved were usually chosen on the basis of first-principle simulations, see Völker [105]. Compatibility conditions at the domain boundary among different variants, numerical stability, and convergence issues also pose challenges. Research in this area is increasing rapidly.

The macroscopic line of approach was initiated from the works of Hwang and McMeeking [106] and Lynch [107]. The modeling approach is mathematically sound, and generally established within the formalism of a thermodynamic framework, using the overall electro-mechanical properties of piezoelectric materials. Computational efficiency is one of the major advantages of these models, due to the reduced number of unknowns; however, it comes at the cost of calculations revealing no information on the micro-structure evolution [108]–[117]. Comprehensive reviews can be found in Shieh, Huber, and Fleck [97] and Landis [95]. Recently, a new type of model emerged that aims to combine the advantages of macroscopic phenomenological models and the microscopic approach, which was dubbed the hybrid phenomenological model. Such models account for the two different length scales by taking volume averages of micro-electromechanical phenomenological models of different domain variants [118]–[121].

Due to its superior simplicity and robustness, the macroscopic phenomenological model was chosen as the material modeling framework for polycrystalline piezoelectric materials. Comprehensive measurements on pre-poled polycrystalline PZT-5A thin plates and unimorph structures manufactured from the same were performed. Calibration of the macroscopic phenomenological model was achieved by measuring the evolution of the internal variables directly or indirectly on bulk piezoelectric samples. A set of optimal variables for the function form of the model was obtained by minimizing the discrepancy between theoretical estimations. Section 3.3 briefly reviews the full field, multi-axial constitutive law proposed by Landis [111], which was then incorporated in a classical lamination theory-based estimation model of the actuation response. An implicit, backward Euler-based integration algorithm for the constitutive law was described in detail. Section 3.4 was devoted to descriptions of experimental procedures used to calibrate the model parameters, where PZT-5A thin sheets were subjected to electrical and mechanical stress loading separately, as well as combinations of the two. Detailed results and discussions of the model parameter identification process are presented in section 3.5. Among the different model parameters fitted from various loading conditions, an optimal set of parameters was chosen, which yielded the least relative error with respect to the entire experimental measurement set. Finally, section 3.6 utilizes the framework established in the previous sections and the optimal model parameters to estimate structural responses under two complicated high field loading conditions.

3.3 Description of Constitutive Model and Implementation in Active Structures

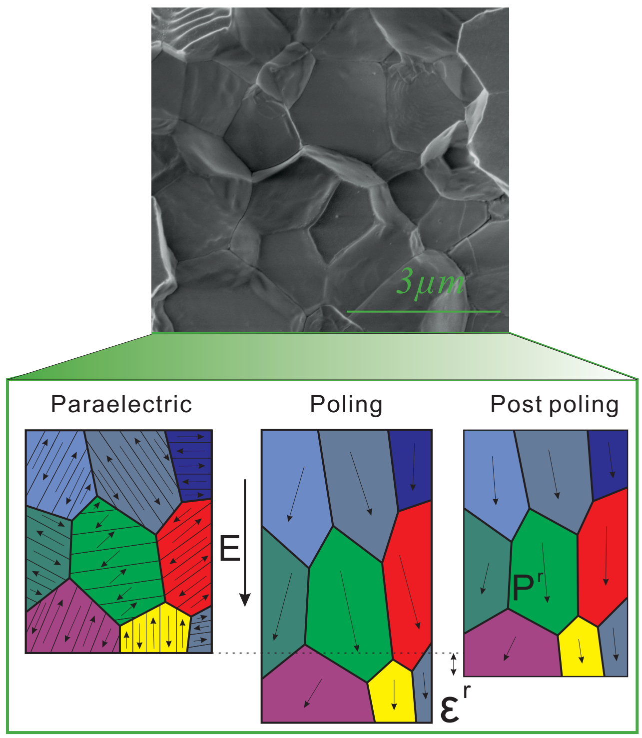

Figure 3.2: Illustration of internal variables in the phenomenological model for polycrystalline piezoelectric ceramics. Top figure is a Scanning Electron Microscope (SEM) image of the surface of a PZT-5A plate with average grain size $\sim 5\mu m$. After subjecting the material to a strong electric field, the material developed a macroscopic initial polarization and strain. Internal variables ε^r and P^r were viewed as volumetric averages of the polarization and strain over the entire domain.

The nonlinear constitutive law of piezoelectric material is described by:

$$\begin{aligned} D_m &= d_{mkl}\sigma_{kl} + \kappa_{mn}\mathcal{E}_n + P^r_m \\ \varepsilon_{ij} &= s_{ijkl}\sigma_{kl} + d_{nij}\mathcal{E}_n + \varepsilon^r_{ij} \end{aligned} \tag{3.1}$$

Here D_m is the electric displacement vector, ε_{ij} is the total strain tensor, d_{mkl} is the electro-mechanical coupling coefficient, σ_{kl} is the mechanical stress tensor, κ_{mn} is the dielectric coefficient tensor, P_m is the remnant polarization vector, s_{ijkl} is the compliance tensor, and ε^r_{ij} is the remnant strain tensor. In this section, $\alpha, \beta \in \{1, 2\}$ and $i, j, k, l \in \{1, 2, 3\}$. The constitutive law described below utilizes ε^r_{ij} and P^r_m as independent state variables and figure 3.2 shows the physical representation. The evolution of ε^r_{ij} and P^r_m can be described by a macroscopic phenomenological constitutive law.

3.3.1 Overview of Fully-Coupled Multi-Axial Constitutive Law

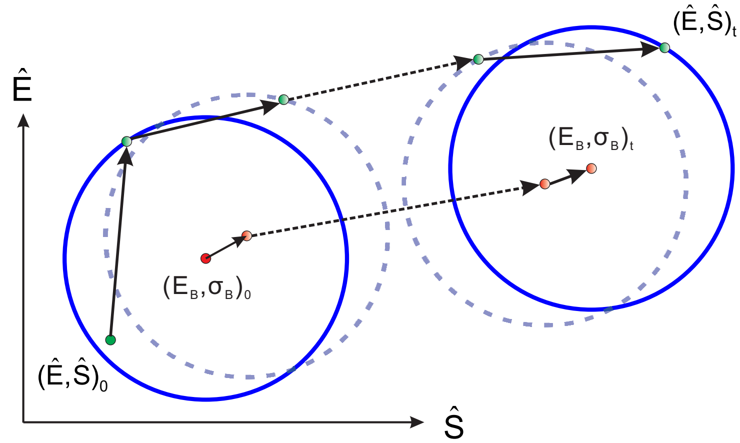

Figure 3.3: Movements of the switching surface during the domain evolution in generalized stress-electric field space. Red dots represent the center of the switching surface, determined by current values of material internal variables. Traces of green dots represent the external fields' loading history. Dotted circles represent intermediate steps during switching.

The macroscopic phenomenological model proposed by Landis [111] is briefly reviewed here. At the core of the model are functional forms of the Helmholtz free energy for electro-mechanical coupling Ψ^r, also noted as the potential function, and the switching function Φ. The switching surface adopted in this study takes the following form:

$$\Phi = \frac{3\hat{S}_{ij}\hat{S}_{ij}}{2\sigma_0^2} + \frac{\hat{\mathcal{E}}_i\hat{\mathcal{E}}_i}{\mathcal{E}_0^2} + \frac{\beta\hat{\mathcal{E}}_i P^r_j \hat{S}_{ij}}{\mathcal{E}_0 P_0 \sigma_0} - 1 = 0 \tag{3.2}$$

$\mathcal{E}_0$ is the electric coercive field, and σ_0 is the stress field when ferroelastic switching is initiated for uniaxial tension or compression. Variables with hats are effective electric fields $\mathcal{E}$ and effective deviatoric stress fields $\hat{S}$ defined as follows:

$$\begin{aligned} \hat{\mathcal{E}}_i &= \mathcal{E}_i - \mathcal{E}^B_i \\ \hat{S_{ij}} &= S_{ij} - S^B_{ij} \end{aligned} \tag{3.3}$$

$\mathcal{E}$ and S are external electric and deviatoric stress fields, respectively. Back stress field S^B_{ij} and back electric field E^B_i represent constraints during domain evolution, due to the surrounding lattice structures, and are obtained by differentiation of the potential function Ψ^r, as follows:

$$\sigma^B_{ij} = \frac{\partial \Psi^r}{\partial \epsilon^r_{ij}},\ E^B_i = \frac{\partial \Psi^r}{\partial P^r_i} \tag{3.4}$$

During switching, $\Phi = 0$ is required. This condition is equivalent to the so-called normality condition, which states that increments of internal variables are normal to the local switching surface. This can be expressed as follows:

$$\dot{\varepsilon}^r_{ij} = \lambda \frac{\partial \Psi^r}{\partial \hat{S}_{ij}} = \lambda \tilde{\varepsilon}_{ij},\ \dot{P}^r_i = \lambda \frac{\partial \Psi^r}{\partial \hat{E}_{ij}} = \lambda \tilde{P}_i \tag{3.5}$$

This incremental plasticity-like formulation of the switching process has been visualized in figure 3.3. The evolution of the material's micro structure due to domain movements is modeled as shifts of the switching surface center (red dots), once the material state is driven to the switching surface (green dots).

Implementation of the framework requires functional forms of the potential Ψ^r. Landis, Wang, and Sheng [113] proposed formulations of Ψ^r based on a semi-heuristic approximation, which assumes Ψ^r to be decomposed into Ψ^σ and Ψ^E . Hence, the free energies have the expressions:

$$\begin{aligned} \Psi^r &= \Psi^\sigma + \Psi^E \\ \Psi^\sigma &= \frac{1}{2} H^\sigma_0 \varepsilon_c \left[\frac{J^e_2}{\varepsilon_c} exp\left(\frac{m}{1 - \bar{\varepsilon}/\varepsilon} \right) \right]^2 \\ \Psi^E &= H^E_0 P_0 \left[ln\left(\frac{1}{1 - P^r/P_{sat}} - \frac{P^r}{P_{sat}} \right) \right] \end{aligned} \tag{3.6}$$

Variables and constants employed in the above functions are defined as follows: the strain-like variable $\bar{\varepsilon}$ describes the saturation condition during loading, and is defined as:

$$\bar{\varepsilon} = J^e_2 f(J^e_3/J^e_2) \tag{3.7}$$

Here J^e_2 and J^e_3 are deviatoric remnant strain invariants:

$$J^e_2 = \left(\frac{2}{3} e^r_{ij} e^r_{ij} \right)^{1/2},\ J^e_3 = \left(\frac{4}{3} e^r_{ij} e^r_{jk} e^r_{ki} \right)^{1/3} \tag{3.8}$$

The functional form of $f(J_3^e/J_2^e)$ in equation 3.7 is from the micromechanical computations performed by Huber [97], and has the following expression:

$$f(J_3^e/J_2^e) = \begin{cases} \left(\frac{J_3^e}{J_2^e}\right) < 0: \ -0.0965\left(\frac{J_3^e}{J_2^e}\right)^3 + 0.01\left(\frac{J_3^e}{J_2^e}\right)^6 + 0.8935 \\ \left(\frac{J_3^e}{J_2^e}\right) \geq 0: \ -0.1075\left(\frac{J_3^e}{J_2^e}\right)^3 - 0.027\left(\frac{J_3^e}{J_2^e}\right)^6 - 0.028\left(\frac{J_3^e}{J_2^e}\right)^{21} + 0.8935 \end{cases} \tag{3.9}$$

Thus Ψ^σ can be further divided into Ψ_1 and Ψ_2 depending on the value of $\frac{J_3^e}{J_2^e}$. P_{sat} is the saturated remnant polarization under a certain strain level:

$$P_{sat} = \frac{3P_0}{4(\varepsilon_t + \varepsilon_c)}(\varepsilon_{ij}^r n_i n_j + \varepsilon_c) + \frac{P_0}{4} \tag{3.10}$$

P_0 is the maximum attainable remnant polarization, ε_t and ε_c are the saturation strain under tension and compression. Plots of Ψ^σ and Ψ^E as functions of the deviatoric remnant strain J_2^e and J_3^e are shown in figure 3.4.

For unimorph-based applications, the piezoelectric coefficient d_{31} is the major parameter that determines the structural response, and is modeled as follows:

$$d_{31} = d_{31}^0 \frac{P_3^r}{P^r}, \ P^r = \sqrt{P_i^r P_i^r} \tag{3.11}$$

In total, 11 model parameters have to be calibrated to describe all the functional forms implemented: saturation strains ε_c and ε_t, stress potential function related constants m, H_0^σ, piezoelectric coupling coefficient d_{31}^0, electric potential function related constants H_0^e and P_0, initial switching fields σ_0 and E_0, dielectric constant γ, and the correlation constant in the switching function β. The calibration process involves estimations of D and ε under external fields E and σ. Details will be presented in section 3.5 which presents a set of parameter calibration experiments. The constitutive relations described by equation 3.1 to equation 3.11 are first integrated into the nonlinear actuation models for beam and plate types of unimorph structures in the next section.

3.3.2 Actuation Models and Integration Algorithm

The literature concerned with modeling unimorph/bimorph structures is abundant. The general approach treats the structural actuation response as a thermal expansion problem, as first presented by Crawley [123]. Similar models have been established to study the optimal design of these structures and were widely validated by experiments [124]–[126]. However, the conventional modeling techniques usually neglect

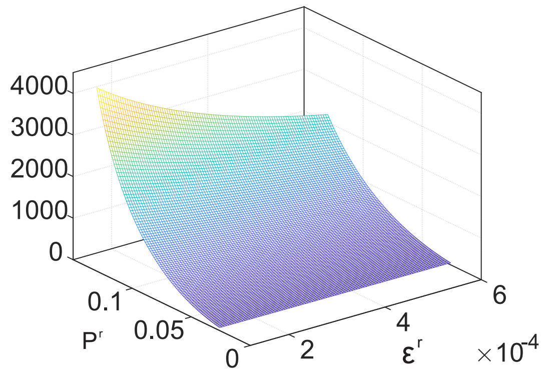

(a) Electric potential Ψ^E

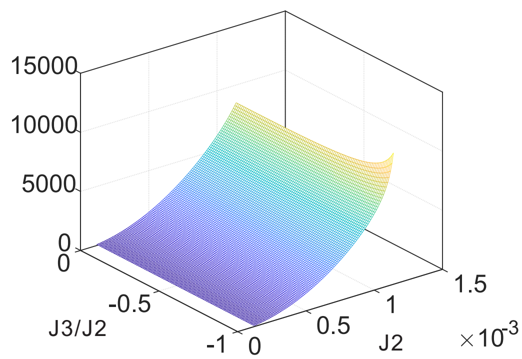

(b) Stress potential Ψ_1^σ

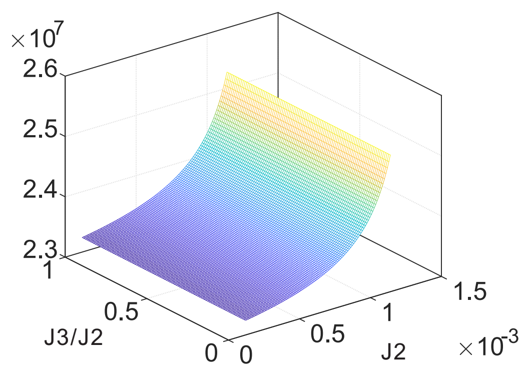

(c) Stress potential Ψ_2^σ

Figure 3.4: Potential functions implemented in equation 3.2. Stress potential Ψ^σ is divided for $J_3^e/J_2^e > 0$ and $J_3^e/J_2^e < 0$. Material constants used in plots are chosen based on suggested values in [122].

structure-material interactions, and are commonly validate against measurements under low electric field excitations, which limit their applicability.

This section presents a set of new modeling techniques for unimorph structures that take these interactions into account. The derivations of active structure responses are divided in two general categories: plane stress and plane strain conditions. The governing equations are followed by an integration algorithm that is valid for the full field, multi-axial constitutive law reviewed in the previous section. For the purpose of this thesis, the actuation models are specialized for layered structures composed of laminated active/nonactive thin plies. In the following derivations, each ply is assumed to be mechanically isotropic in-plane, including the piezoelectric active layer. The techniques can be applied to structures with in-plane orthotropic substrates. Further assumptions for modeling include:

- The response due to the of ε_z in is neglected.
- The response due to in-plane shear strain ε_{xy}, ε_{xz}, and ε_{yz} are neglected.
- Elastic moduli remain constant for the piezoelectric layer during switching.
- The thickness of the structure is uniform.
- No significant extension of the mid-surface develops.
- Planes perpendicular to the mid-surface will remain plane and perpendicular to the deformed mid-surface.

3.3.2.1 Plane Stress Condition

The representative unimorph structure, where the piezoelectric layer is under plane stress conditions, is referred to as a plate unimorph, and is shown in figure 3.5. In this paper, the global reference coordinate system of the structures coincides with the local crystallographic directions of the poled piezoelectric plates. The poling direction 3 is aligned with z axis and in-plane directions 1 and 2 are aligned with global coordinates x and y.

The constitutive equation of each layer under a plane stress condition:

$$\begin{bmatrix} \sigma_x \\ \sigma_y \\ \sigma_{xy} \end{bmatrix}_i = \begin{bmatrix} \frac{E_i}{1-\nu^2} & \frac{\nu E_i}{1-\nu^2} & 0 \\ \frac{\nu E_i}{1-\nu^2} & \frac{E_i}{1-\nu^2} & 0 \\ 0 & 0 & G_i \end{bmatrix} \begin{bmatrix} \varepsilon_x^{active} \\ \varepsilon_y^{active} \\ 0 \end{bmatrix} \tag{3.12}$$

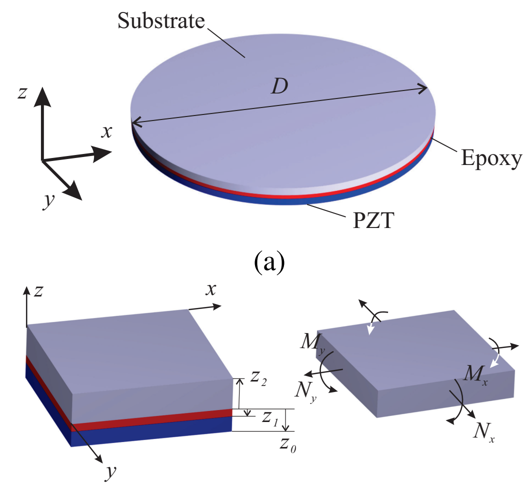

(b)

Figure 3.5: Plate unimorph and cross-sectional view.

where i denotes the number of layers. Define the matrix $\bar{Q}$ as:

$$\bar{Q} = \begin{bmatrix} \dfrac{E_i}{1-\nu^2} & \dfrac{\nu_i E_i}{1-\nu_i^2} & 0 \\ \dfrac{\nu_i E_i}{1-\nu_i^2} & \dfrac{E_i}{1-\nu_i^2} & 0 \\ 0 & 0 & G_i \end{bmatrix} \tag{3.13}$$

E_i, ν_i, and G_i are Young's modulus, Poisson's ratio, and the shear modulus of the layer. Here, the effective active strain for a single ply is:

$$\varepsilon_\alpha^{active} = \varepsilon_\alpha^0 + z \cdot \kappa_\alpha - \Lambda_\alpha - \varepsilon_\alpha^r \tag{3.14}$$

The induced strain Λ_α, which represents the linear response of material is defined as:

$$\Lambda_\alpha = \mathcal{E}_n d_{\alpha n} \tag{3.15}$$

By integrating through the thickness of the unimorph, the moments, force, and stiffness coefficients per unit length of the plate can be derived as follows:

$$\begin{aligned} \boldsymbol{F} &= \int_t \bar{\mathbf{Q}}(\boldsymbol{\varepsilon} - \boldsymbol{\Lambda} - \boldsymbol{\varepsilon}^r)dz = \int_t \bar{\mathbf{Q}}\varepsilon^0 dz + \int_t \bar{\mathbf{Q}}\boldsymbol{\kappa} z dz - \int_t \bar{\mathbf{Q}}(\boldsymbol{\Lambda} + \boldsymbol{\varepsilon}^r) z dz \\ &= \boldsymbol{A}\boldsymbol{\varepsilon}^{\mathbf{0}} + \boldsymbol{B}\boldsymbol{\kappa} - \boldsymbol{F}_\Lambda \\ \boldsymbol{M} &= \int_t \bar{\mathbf{Q}}(\boldsymbol{\varepsilon} - \boldsymbol{\Lambda} - \boldsymbol{\varepsilon}^r) z dz = \int_t \bar{\mathbf{Q}}\varepsilon^0 z dz + \int_t \bar{\mathbf{Q}}\boldsymbol{\kappa} z^2 dz - \int_t \bar{\mathbf{Q}}(\boldsymbol{\Lambda} + \boldsymbol{\varepsilon}^r) z^2 dz \\ &= \boldsymbol{B}\boldsymbol{\varepsilon}^{\mathbf{0}} + \boldsymbol{D}\boldsymbol{\kappa} - \boldsymbol{M}_\Lambda \end{aligned} \tag{3.16}$$

The induced force vector is defined as:

$$\begin{aligned} \boldsymbol{F}_\Lambda &= \int_t \bar{\boldsymbol{Q}}(\boldsymbol{\Lambda} + \boldsymbol{\varepsilon}^r)dz \\ &= \sum_{k=1}^{N} \bar{\boldsymbol{Q}}_k(\boldsymbol{\Lambda} + \boldsymbol{\varepsilon}^r)_k(h_{k+1} - h_k) \end{aligned} \tag{3.17}$$

and the induced moment vector is defined as:

$$\begin{aligned} \boldsymbol{M}_\Lambda &= \int_t \bar{\boldsymbol{Q}}(\boldsymbol{\Lambda} + \boldsymbol{\varepsilon}^r)zdz \\ &= \frac{1}{2}\sum_{k=1}^{N} \bar{\boldsymbol{Q}}_k(\boldsymbol{\Lambda} + \boldsymbol{\varepsilon}^r)_k(h_{k+1}^2 - h_k^2) \end{aligned} \tag{3.18}$$

The $\boldsymbol{A}, \boldsymbol{B}, \boldsymbol{D}$ matrices are defined as:

$$\boldsymbol{A} = \int_t \bar{\boldsymbol{Q}}dz,\ \boldsymbol{B} = \int_t \bar{\boldsymbol{Q}}zdz,\ \boldsymbol{D} = \int_t \bar{\boldsymbol{Q}}z^2dz \tag{3.19}$$

Only the piezo layer contributes to the forcing terms. The complete governing equation is:

$$\begin{bmatrix} \boldsymbol{F} \\ \boldsymbol{M} \end{bmatrix} = \begin{bmatrix} \boldsymbol{A} & \boldsymbol{B} \\ \boldsymbol{B} & \boldsymbol{D} \end{bmatrix} \begin{bmatrix} \boldsymbol{\varepsilon} \\ \boldsymbol{K} \end{bmatrix} - \begin{bmatrix} \boldsymbol{F}_\Lambda \\ \boldsymbol{M}_\Lambda \end{bmatrix} \tag{3.20}$$

For free standing samples, as studied in this work, the external loading terms $\boldsymbol{F}$ and $\boldsymbol{M}$ are zero. If the remnant strain term ε_r is neglected, equation recovers the solution presented in [127] and [124].

3.3.2.2 Plane Strain Condition

For unimorph samples, if the dimension along one direction is much larger than the other, or if it is under a lateral constraint, the structure can be considered under a plane strain condition. In this case, the curvature response along one direction is dominant. A typical situation is the case of a piezoelectric bonded narrow strip, shown in figure 3.6. A structural actuation response model can be established by modifying derivations from the previous sections.

By inversion of (3.12), the constitutive equation for the active layer can be rewritten as:

$$\begin{aligned} \varepsilon_x &= \frac{1}{E_a}(\sigma_x - \nu\sigma_y) + \Lambda_x + \varepsilon_x^r \\ \varepsilon_y &= \frac{1}{E_a}(\sigma_y - \nu\sigma_x) + \Lambda_y + \varepsilon_y^r \end{aligned} \tag{3.21}$$

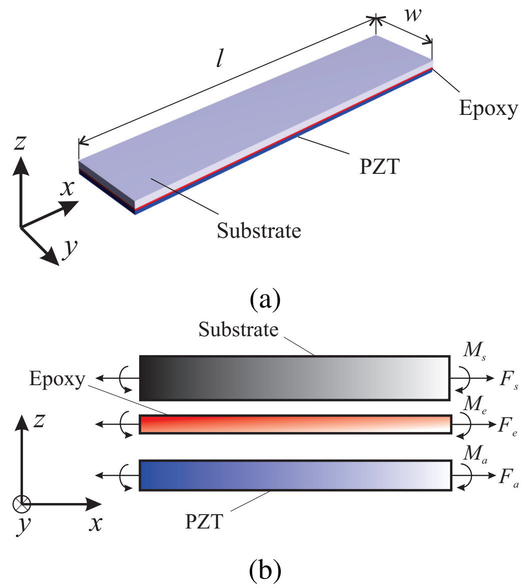

Figure 3.6: Strip unimorph and cross-sectional view.

Under the plane strain condition along the y-direction:

$$\varepsilon_y = 0 \tag{3.22}$$

Substitute the condition 3.22 into equation 3.21, further obtain:

$$\sigma_y = -(\Lambda_y + \varepsilon_y^r) \cdot E_a + \nu\sigma_x \tag{3.23}$$

Thus:

$$\varepsilon_x = \frac{1-\nu^2}{E_a}\sigma_x + (\Lambda_y + \varepsilon_y^r) \cdot (1+\nu) \tag{3.24}$$

For the substrate layer, the derivations are similar:

$$\varepsilon_x = \frac{1}{E_s}(\sigma_x - \nu^2\sigma_x) \tag{3.25}$$

In this case, the $\bar{Q}$ matrix reduces to $\bar{Q}_{strain}$:

$$\begin{aligned} \sigma_x &= \bar{Q}_{strain}\varepsilon_x^{active} \\ &= [\frac{E_a}{1-\nu^2}][\varepsilon_x - (1+\nu)(\Lambda_x + \varepsilon^r)] \end{aligned} \tag{3.26}$$

By integrating over the thickness and obtaining similar governing equation as in the case of the plane stress condition:

$$\begin{bmatrix} F_x \\ M_x \end{bmatrix} = \begin{bmatrix} \boldsymbol{A} & \boldsymbol{B} \\ \boldsymbol{B} & \boldsymbol{D} \end{bmatrix} \begin{bmatrix} \varepsilon_x^0 \\ K_x^0 \end{bmatrix} - \begin{bmatrix} F_{x\Lambda} \\ M_{x\Lambda} \end{bmatrix} \tag{3.27}$$

Here:

$$\boldsymbol{A} = \int_t \frac{E_i}{1-\nu_i^2} dz,\ \boldsymbol{B} = \int_t \frac{E_i}{1-\nu_i^2} z dz,\ \boldsymbol{D} = \int_t \frac{E_i}{1-\nu_i^2} z^2 dz \tag{3.28}$$

The actuation terms are defined as follows:

$$F_{x\Lambda} = \int_t (1+\nu_i)(\Lambda+\varepsilon^r)\frac{E_i}{1-\nu_i^2} dz,\ M_{x\Lambda} = \int_t (1+\nu_i)(\Lambda+\varepsilon^r)\frac{E_i}{1-\nu_i^2} z dz \tag{3.29}$$

3.3.3 Integration Algorithm

In general, the evolution of the material state under external fields is an irreversible boundary value problem, and the local constitutive law must be integrated along the loading path or time. Numerical issues to do with implementing macroscopic phenomenological models were discussed in detail by Stark [128]. The constitutive law is integrated using a backward Euler, fully implicit scheme, inspired by Belytschko [129]. The electric loading is divided into N steps, i.e. $\mathcal{E} = \{\mathcal{E}_1, ..., \mathcal{E}_n, \mathcal{E}_{n+1}, ..., \mathcal{E}_n\}$. The increments of remnant strain ε^r and remnant polarization P^r are found at the end of each step, by enforcing the yield condition $\Phi < Tol$. The following three residuals are introduced at the integration step $n+1$:

$$\begin{aligned} a &= -\epsilon^r_{n+1} + \epsilon^r_n + \Delta\lambda\tilde{\epsilon} = 0 \\ b &= -P^r_{n+1} + P^r_n + \Delta\lambda\tilde{P} = 0 \\ \Phi &= \Phi(\mathcal{E}_{n+1}, \epsilon^r_{n+1}, P^r_{n+1}) = 0 \end{aligned} \tag{3.30}$$

The algorithm is assumed to have obtained converged material state at the end of step n, and the linearized residua at the current step are as follows:

$$\begin{aligned} a^{(k)} - \Delta\epsilon^{r(k)} + \Delta\lambda^{(k)}\left((\frac{\partial\tilde{\epsilon}}{\partial\epsilon^r})^{(k)}\Delta\epsilon^{r(k)} + (\frac{\partial\tilde{\epsilon}}{\partial P^r})^{(k)}\Delta P^{r(k)} \right) + \delta\lambda^{(k)}\tilde{\epsilon}^{(k)} = 0 \\ b^{(k)} - \Delta P^{r(k)} + \Delta\lambda^{(k)}\left((\frac{\partial\tilde{P}}{\partial\epsilon^r})^{(k)}\Delta\epsilon^{r(k)} + (\frac{\partial\tilde{P}}{\partial P^r})^{(k)}\Delta P^{r(k)} \right) + \delta\lambda^{(k)}\tilde{P}^{(k)} = 0 \\ \Phi^{(k)} + (\frac{\partial\Phi}{\partial\epsilon^r_n})^{(k)}\Delta\epsilon^{r(k)} + (\frac{\partial\Phi}{\partial P^r_n})^{(k)}\Delta P^{r(k)} = 0 \end{aligned} \tag{3.31}$$

The solution to the nonlinear algebraic equations (3.31) is obtained by a Newton procedure:

Start Step $n+1$, given the electric field loading E_{n+1} or stress field loading σ_{n+1}, at iteration step $k=0$ assume the following material state:

$$\epsilon^{r(0)}_{n+1} = \epsilon^r_n,\ P^{r(0)}_{n+1} = P^r_n,\ \Delta\lambda^{(0)} = 0 \tag{3.32}$$

Calculate the in-plane stress field in the active layer:

$$\sigma^0_{n+1} = \bar{Q} \cdot [\varepsilon^0(\varepsilon^r, P^r, \mathcal{E}) + z \cdot \kappa(\varepsilon^r, P^r, \mathcal{E}) - \varepsilon^r - \Lambda(P^r, \mathcal{E})] \tag{3.33}$$

Prediction step Check the yield condition and convergence at the k^{th} iteration:

$$\Phi^{(k)} = \Phi(\mathcal{E}_{n+1}, \sigma^k_{n+1}, \epsilon^{r(k)}_{n+1}, P^{r(k)}_{n+1}),\ \begin{bmatrix} \tilde{a}^{(k)} \end{bmatrix} = \begin{bmatrix} a^{(k)} \\ b^{(k)} \end{bmatrix}$$

If $\Phi^{(k)} < Tol$ and $\tilde{a}^{(k)} < Tol$, then the Newton-Raphson solver has converged. Update the internal variables:

$$\begin{aligned} \epsilon^r_{n+1} &= \epsilon^{r(k)}_{n+1} \\ P^r_{n+1} &= P^{r(k)}_{n+1} \end{aligned}$$

Exit the current iteration. Otherwise go to **next step**.

Corrector step Calculate $\delta\lambda^{(k)}$ at k^{th} step by solving:

$$\begin{gathered} \begin{bmatrix} (\frac{\partial \tilde{\epsilon}}{\partial \epsilon^r})^{(k)}\Delta\lambda^{(k)} - \mathbf{I} & (\frac{\partial \tilde{\epsilon}}{\partial P^r})^{(k)}\Delta\lambda^{(k)} \\ (\frac{\partial \tilde{P}}{\partial \epsilon^r})^{(k)}\Delta\lambda^{(k)} & (\frac{\partial \tilde{P}}{\partial P^r})^{(k)}\Delta\lambda^{(k)} - 1 \end{bmatrix} \begin{bmatrix} \Delta\epsilon^{r(k)} \\ \Delta P^{r(k)} \end{bmatrix} = -\begin{bmatrix} a^{(k)} \\ b^{(k)} \end{bmatrix} - \delta\lambda^{(k)} \begin{bmatrix} \tilde{\epsilon}^{(k)} \\ \tilde{P}^{(k)} \end{bmatrix} \\ \Phi^{(k)} + (\frac{\partial \Phi}{\partial \epsilon^r_n})^{(k)}\Delta\epsilon^{r(k)} + (\frac{\partial \Phi}{\partial P^r_n})^{(k)}\Delta P^{r(k)} = 0 \end{gathered} \tag{3.34}$$

Obtain expression of $\delta\lambda^{(k)}$ in the following form:

$$\begin{aligned} \delta\lambda^{(k)} &= \frac{Num}{Den} \\ Num &= \Phi^k - \begin{bmatrix} \frac{\partial \Phi}{\partial \epsilon^r_n} & \frac{\partial \Phi}{\partial P^r_n} \end{bmatrix} M^{-1} \begin{bmatrix} a^{(k)} \\ b^{(k)} \end{bmatrix} \\ Den &= A^{-1} \begin{bmatrix} \tilde{\epsilon}^{(k)} \\ \tilde{P}^{(k)} \end{bmatrix} \end{aligned} \tag{3.35}$$

where the matrix M is defined as:

$$M = \begin{bmatrix} (\frac{\partial \tilde{\epsilon}}{\partial \epsilon^r})^{(k)}\Delta\lambda^{(k)} - \mathbf{I} & (\frac{\partial \tilde{\epsilon}}{\partial P^r})^{(k)}\Delta\lambda^{(k)} \\ (\frac{\partial \tilde{P}}{\partial \epsilon^r})^{(k)}\Delta\lambda^{(k)} & (\frac{\partial \tilde{P}}{\partial P^r})^{(k)}\Delta\lambda^{(k)} - 1 \end{bmatrix} \tag{3.36}$$

Update step Calculate increments for remnant strain and polarization:

$$\begin{bmatrix} \Delta\epsilon^{r(k)} \\ \Delta P^{r(k)} \end{bmatrix} = A^{-1}\left(-\begin{bmatrix} a^{(k)} \\ b^{(k)} \end{bmatrix} - \delta\lambda^{(k)}\begin{bmatrix} \tilde{\epsilon}^{(k)} \\ \tilde{P}^{(k)} \end{bmatrix}\right) \tag{3.37}$$

Obtain remnant strain, polarization and plastic multiplier for step $k+1$:

$$\begin{aligned} \epsilon^{r(k+1)} &= \epsilon^{r(k)} + \Delta\epsilon^{r(k)} \\ P^{r(k+1)} &= P^{r(k)} + \Delta P^{r(k)} \\ \Delta\lambda^{(k+1)} &= \Delta\lambda^{(k)} + \delta\lambda^{(k)} \end{aligned} \tag{3.38}$$

Update the inplane stress in active layer:

$$\begin{aligned} \sigma_{n+1}^{k+1} =& \bar{Q}\cdot[\varepsilon^0(\varepsilon^{r(k+1)}, P^{r(k+1)}, E_{n+1}) + z\cdot\kappa(\varepsilon^{r(k+1)}, P^r, E) \\ & - \varepsilon^{r(k+1)} - \Lambda(P^{r(k+1)}, E_{n+1})] \end{aligned} \tag{3.39}$$

Let $k = k+1$, go to **prediction step**.

The above derivations were conducted in the symbolic computation software Mathematica© and the algorithm was implemented in MATLAB.

3.4 Experimental Characterization

This section proposes a set of novel experimental methodologies that focuses on characterizing the nonlinear properties of ultra-thin piezoelectric plates, with thicknesses less than 200 μm. Piezoelectric materials of this form were not well studied in literature, mainly due to the challenges of testing ultra-thin and brittle materials. These challenges were overcome by bonding piezoelectric thin plates to thin, stiff substrates and applying electric or mechanical loadings to these unimorph samples, as shown in this section.

From the review of the full field, multi-axial phenomenological constitutive law for piezoelectric materials in section 3.3.1, the model is fully described by 11 material constants which are employed by the switching function Φ, the stress potential function Ψ^σ and the electric potential function Ψ^E. A complete experimental characterization requires the material to undergo both ferroelectric switching and ferroelastic switching. The mechanical and electrical responses of the piezoelectric layer were measured under different loading combinations, to record the material state variations caused by the associated microscopic domain movements. A brief summarization of the experiments is in table 3.1.

Table 3.1: Calibration Experiments Summary

	I	II	III
Sample type	Piezoelectric plate	Beam unimorph	Beam and plate unimorph
Driving field	$\mathcal{E}_3$	σ_α	$\mathcal{E}_3$
Total fields	$\mathcal{E}_3$	σ_α	$\mathcal{E}_3$, σ_α
Switching condition	Ferroelectric	Ferroelastic	Combined

Two types of driving fields were applied to the samples: the through thickness electric field $\mathcal{E}_3$ and the in-plane stress field σ_α. Depending on the type of sample tested, the resulting total fields that acted on the piezoelectric layer could have three combinations, to cause different types and directions of domain movements in the material. Results of the measurements and discussions will be presented in section 3.5 together with model calibration algorithms. Test set-ups for each loading condition are first described in the following sections. All tests were conducted under quasi-static loading rates.

The measurements presented below were conducted on commercially available lead zirconate-titanate PZT-5A4E (Industry type 5A, Navy type II) thin plates from Piezo Systems Inc©, referred as piezoelectric plates in the remainder of the chapter. Unimorph structures were constructed from the same piezoelectric plates. Its composition belongs to a standard 'soft' type of piezoelectric material. Its solid solution is at the morphotropic phase boundary in the composition-temperature phase diagram, which exploits the transitions between tetragonal, rhombohedral, and intermediary phases to achieve large dielectric permittivity and piezoelectric coefficients [130].

3.4.1 Calibration Experiment I: Ferroelectric Switching Tests

In the first set of tests, an electric field $\mathcal{E}$ exclusively drove the domain evolution of the piezoelectric material. A strong, cyclic electric field was applied parallel to the poling direction of piezoelectric ceramics with the following form:

$$\mathcal{E}_3 = \mathcal{E}_0 \sin(\frac{2\pi t}{T}) \tag{3.40}$$

The material response in this case was estimated as:

$$
\begin{aligned}
D_3 &= \kappa_3 \mathcal{E}_3 + P_3^r \\
\varepsilon_\alpha &= d_{3\alpha} \mathcal{E}_3 + \varepsilon_\alpha^r
\end{aligned}
\tag{3.41}
$$

D_3 and ε_α were measured experimentally. Piezoelectric plates of two thicknesses (127 µm and 200 µm) were tested. The plates were pre-poled along the thickness direction, and had dimensions of 7 cm × 7 cm. The top and bottom surfaces were coated with a thin layer of nickel electrodes. A schematic of the experiment is shown in figure 3.7.

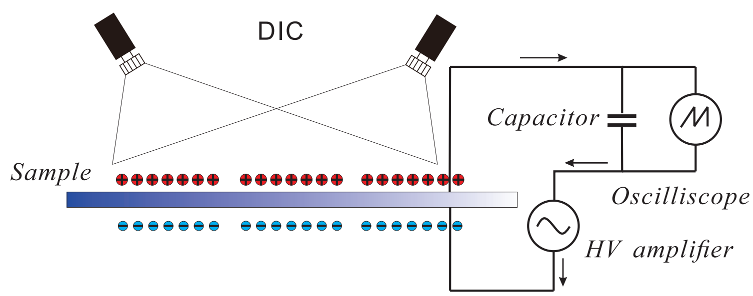

(a)

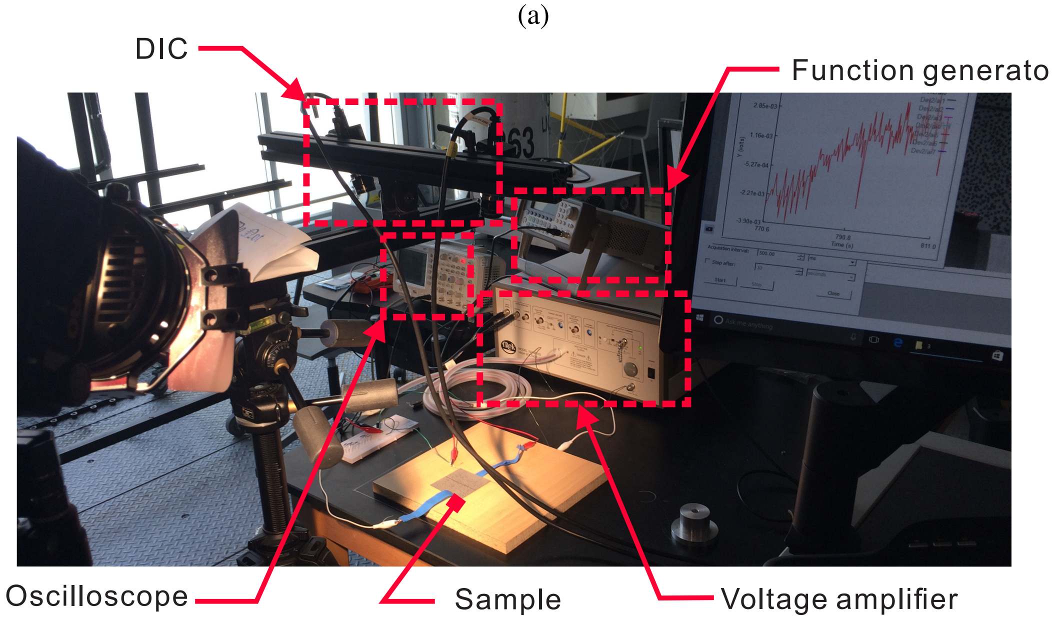

(b)

Figure 3.7: Ferroelectric switching test illustration and experiment setup. In-plane strain and dielectric response were measured concurrently.

The driving field signal was generated using an Agilent 33210A function generator and was amplified by a Trek© model 10/10B-HS high voltage amplifier. Rate dependent phenomena were beyond the scope of this chapter, so $T = 60$ s was chosen as the actuation period. E_0 was chosen as 3 MV/m, which is 1.5 times the polarization field stated in the provided material data sheet. A Sawyer-Tower-type circuit [131] was used to record the electric displacement D_3 of the actuated plates. A 10 µF sensing capacitor was used in the circuit, and its voltage was measured with an oscilloscope. The Correlated-Solution© Digital Image Correlation (DIC) system was used to record the in-plane strain ε_α during actuation.

3.4.2 Calibration Experiment II: Ferroelastic Switching Tests

In the second set of tests, mechanical stress was the driving field that induced the material nonlinearity. During the tests, thin piezo plates were loaded under in-plane tension or compression. These unique loading conditions were achieved by conducting four-point bending tests on piezoelectric unimorph samples. Piezoelectric material only covered the center portions of the samples and were subjected to pure tension or compression during the bending tests, as shown in figure 3.9a. The tests reproduced the stress field of the piezoelectric layer in an actuated unimorph, but excluded the existence of electric fields. In this case, the material responses were modeled as:

$$\begin{aligned} D_3 &= d_{3\alpha}\sigma_\alpha + P_3^r \\ \varepsilon_\alpha &= s_{ijkl}^R\sigma_\alpha + \varepsilon_\alpha^r \end{aligned} \tag{3.42}$$

D_3, ε_α, and the moment M were recorded during the experiments.

3.4.2.1 Sample Preparation

To prepare the unimorph samples, small patches of 20 mm × 15 mm ×127 µm were cut from the same type of piezoelectric plates using a Universal© laser cutter. To eliminate potential thermally-induced switching during the cutting process, finished patches were re-poled by applying a strong positive electrical loading cycle up to $2E_0$. The patches were then vacuum-bonded to ultra-thin carbon fiber plates made from North Thinply© $[0/90]_s$ laminates. This substrate material was chosen, due to its extremely low thickness, such that the residual deformation induced by remnant strain of the piezoelectric layer could be observed. Epoxy 301 from Epotek© was used for bonding between the laminate and the piezoelectric layer and samples fabricated were considered residual-stress free. The sample geometry is shown in figure 3.8.

The dimensions were as follows: $L_1 = 60$ mm, $L_2 = 20$ mm, $W_1 = 15$ mm, and $W_2 = 14.9$ mm. Finished samples had a uniform bonding layer thickness of 10 µm,

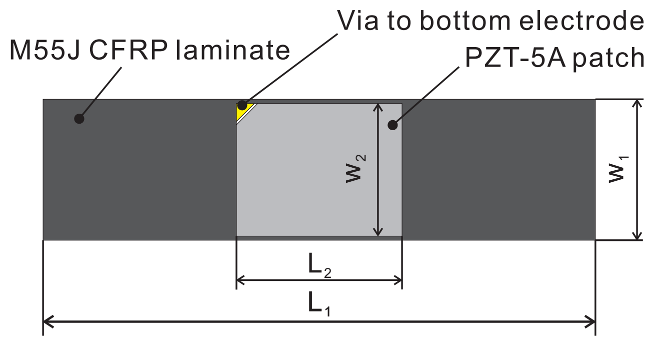

Figure 3.8: Top view of the piezoelectric unimorph sample. The piezoelectric layer is bonded to the top of the samples.

which will be considered in estimations within following sections. The mechanical properties of a single-ply M55J prepreg and the piezoelectric plates are listed in table 3.2.

Table 3.2: Mechanical Properties of Single Ply Materials for Sample Construction

	E_1 (GPa)	E_2 (GPa)	ν_{12}	G_{12} (GPa)	t (μm)	Areal density (g/m^2)
Thin ply composite	400	6.3	0.33	4.24	30	30
PZT-5A	62	62	0.31	23.66	200	1.56×10^3

In order to access the bottom electrode after bonding, an electrical 'via' was created at the tip of the piezoelectric patch. The via was introduced by dipping the patch tip into conductive silver ink, and it was then baked in an oven at 200°C for two hours to cure. The via was separated from the top electrode by sanding the top nickel layer along the hypotenuse.

3.4.2.2 Experiment Setup

Loading was applied using a displacement-controlled bending fixture on an Instron test machine, with the sample top surface facing upwards (compression) or downwards (tension). The in-plane strain field on the top surface of the piezo layer was recorded using DIC. Electric displacement was measured using the same Sawyer-Tower circuit. To prevent signal leakage, the voltage signal readout of the sensing capacitor used a Keithley© 6517B electrometer. The test and setup is shown in figure 3.9.

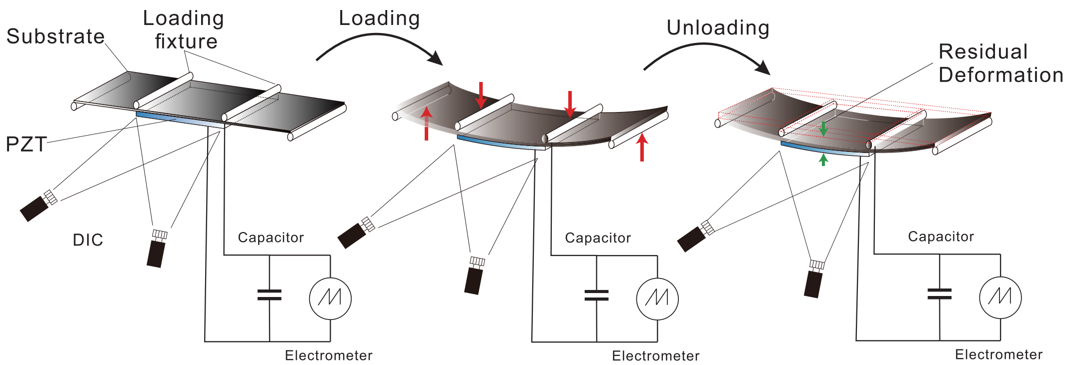

(a)

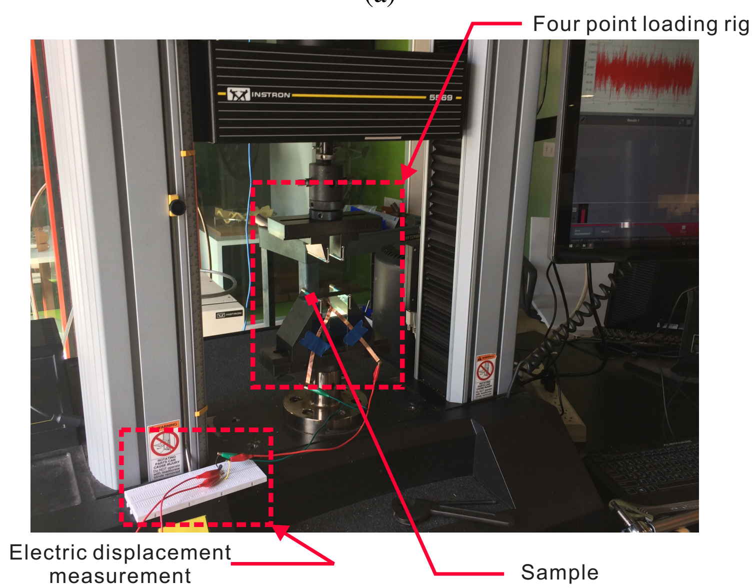

(b)

Figure 3.9: In-plane ferroelastic switching test sequence and setup with four-point bending test fixture and Instron test machine. Dieletric response was measured with a sensing capacitor and an electrometer.

3.4.2.3 Determination of Loading

The displacement limit of the loading head was determined by the strain limits of the piezoelectic layer under both tension and compression. The strain limits of the piezoelectric plates were $\varepsilon_{compression} = -1.3$ % and $\varepsilon_{tension} = 0.34$ % (obtained in section 2.9). Initial predictions of the piezoelectric layer strain were made by treating the material as purely elastic. In this case, actuation terms in the equation were neglected. Assuming the tested structure to be under pure bending, the equation can be simplified to:

$$\begin{bmatrix} \mathbf{0} \\ \boldsymbol{M} \end{bmatrix} = \begin{bmatrix} \boldsymbol{A} & \boldsymbol{B} \\ \boldsymbol{B} & \boldsymbol{D} \end{bmatrix} \begin{bmatrix} \boldsymbol{\varepsilon} \\ \boldsymbol{\kappa} \end{bmatrix} \tag{3.43}$$

The piezoelectric strain limit has the expression:

$$\varepsilon^{limit} = \varepsilon^0 + z\kappa^0$$

The corresponding moment **M** was obtained from:

$$M = F \cdot L_2 \tag{3.44}$$

Loading of the samples was displacement-controlled during experiments. The maximum displacement amplitude was determined by loading a trial sample on the test machine until the estimated force F was reached.

3.4.3 Calibration Experiment III: Beam and Plate Unimorph Actuation

The last two sets of measurements focused on the actuation response of the piezoelectric ceramic under a combined electric and stress fields. This represents the most common scenario. In these tests, piezo-bonded unimorph samples with different thickness characteristics were actuated under through-thickness electric fields. Samples under plane strain and plane stress conditions were tested. From the analysis in section 3.3, the electric field induced in-plane strain will cause in-plane stress loading, due to the clamping effect from the substrate. The interaction between the two fields through the evolution of the material's micro structure in turn affects the induced strain. The material response in this case can be estimated as:

$$\begin{aligned} D_3 &= d_{3\alpha}\sigma_\alpha + \kappa_3\mathcal{E}_3 + P_3^r \\ \varepsilon_\alpha &= s_{\alpha\beta}\sigma_\beta + d_{3\alpha}\mathcal{E}_3 + \varepsilon_\alpha \end{aligned} \tag{3.45}$$

where ε_α and curvature κ were recorded in experiments.

3.4.3.1 Sample Preparation

Piezoelectric plates were bonded to thin aluminum substrates in the form of strip and plate unimorphs, as shown in figure 3.10. Sample geometries are listed below:

- Strip unimorph: $L_1 = 70$ mm, $L_2 = 60$ mm, $W_1 = 12$ mm, $L_2 = 11.8$ mm.
- Plate unimorph: $D_1 = 71$ mm, $D_2 = 70$ mm.

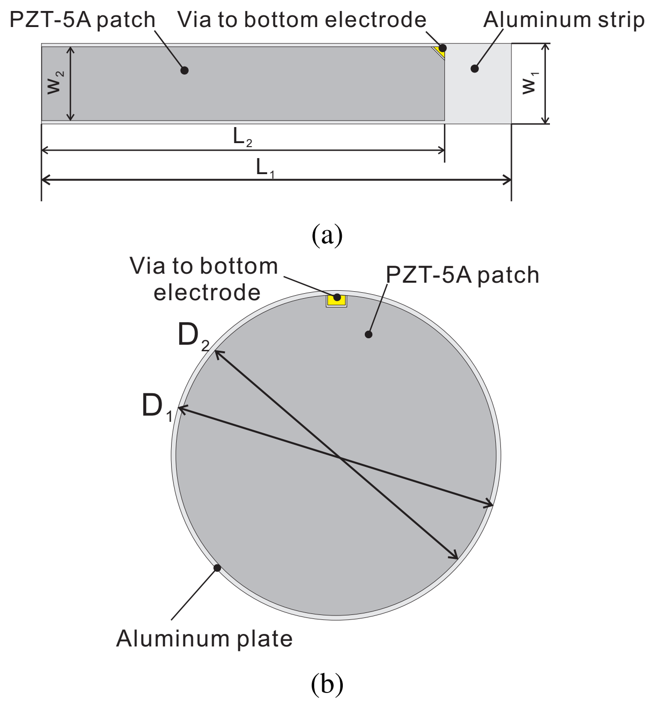

Figure 3.10: Top view of sample geometry for plane strain (strip) and plane stress (plate) unimorph samples.

The thickness ratio R was defined as:

$$R = \frac{t_a}{t_s} \tag{3.46}$$

From section 3.3.2, the electric field generated piezoelectric strain will induce mechanical stresses σ_{11} and σ_{22}, which depend on $\mathcal{E}$, R, and the sample geometry. This also determines the plane strain or stress condition. Figure 3.11 provides a demonstration of this effect based on the analysis in section 3.3. Assume $d_{31} = -120$ pC/N, the magnitudes of the induced stress in the piezoelectric layer under different electric fields correspond to different R values are shown in figure 3.11. Based on the above estimations, five different thickness ratios were chosen, illustrated as hollow squares in figure 3.11. Detailed dimensions are listed in table 3.3.

3.4.3.2 Experiment Setup

Two types of electric signals were used to actuate the piezoelectric layers of all samples:

- Incremental step-wise actuation up to 1.25 MV/m with an interval of 0.25 MV/m , shown in figure 3.12a.

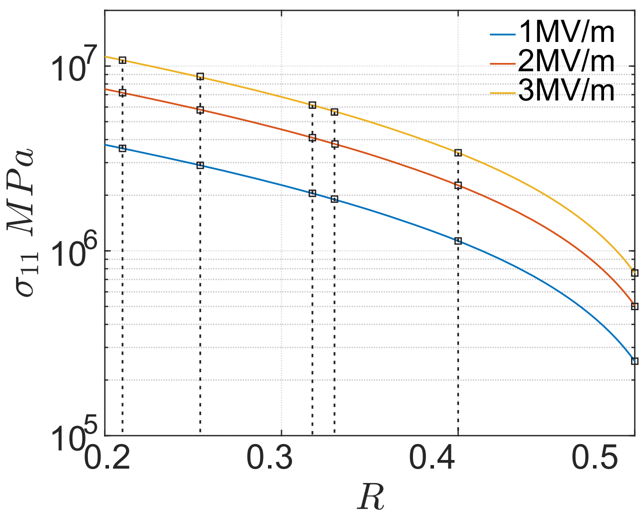

Figure 3.11: σ_{11} magnitude of piezoelectric layer in unimorph samples under peak actuation field. Hollow squares denote samples studied in this section.

Table 3.3: Sample thicknesses for actuation tests

Sample set	Piezoelectric layer (μm)	Substrate layer (μm)	R
1	127	400	0.3175
2	127	500	0.254
3	127	600	0.212
4	200	400	0.5
5	200	500	0.4
6	200	600	0.33

- Linear triangular wave with peak magnitudes of 1 MV/m , 2 MV/m or 3 MV/m , shown in figure 3.12b.

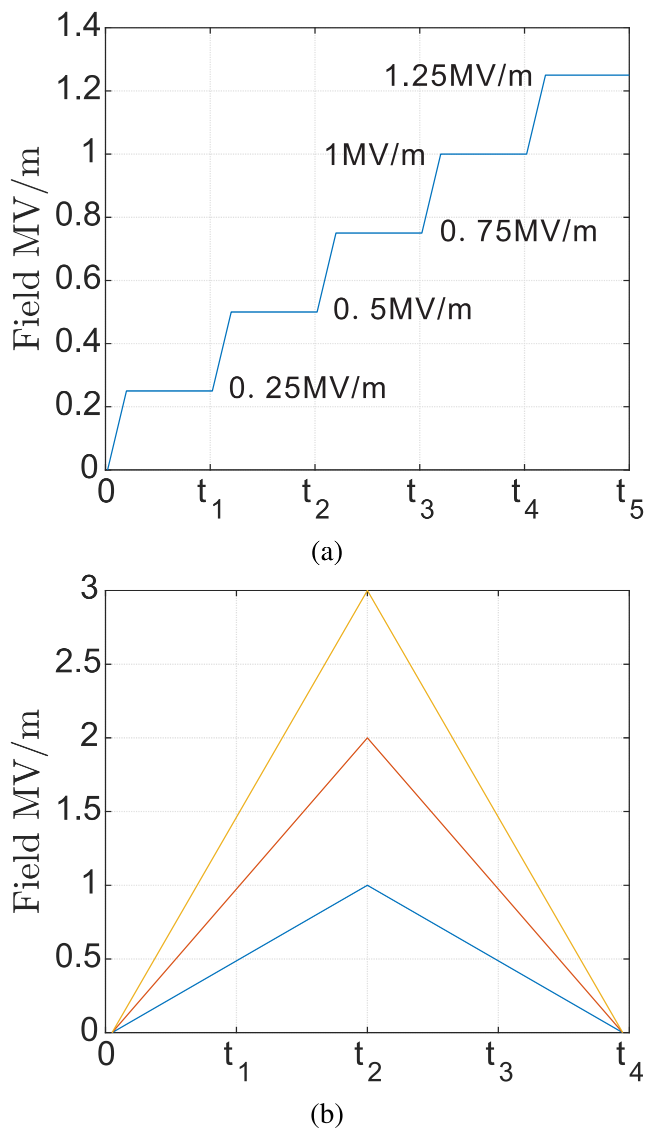

Figure 3.12: Electric field signals for unimorph actuation tests. $\Delta t = t_i - t_{i-1} = 20s$. (a) Step-wise actuation. (b) Continuous actuation.

Signals were generated using the software National Instrument SignalExpress, and amplified by a high voltage amplifier. Curvature responses of the samples were recorded using DIC. Samples were tested under different boundary conditions, as follows:

- For strip unimorphs, samples were clamped at one end for $5mm$.

- For plate unimorphs, samples were in a free standing condition.

Figure 3.13 shows the experiment setup for the plate unimorph actuation tests.

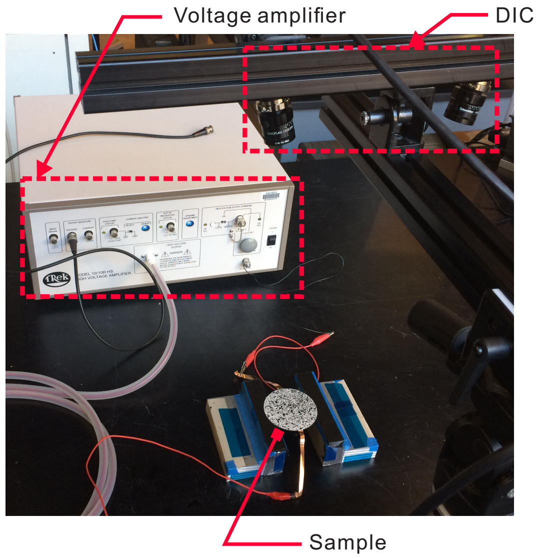

Figure 3.13: Plate unimorph actuation test setup. Samples were supported along the two sides of the bottom surface to provide a free-free boundary condition.

3.5 Model Calibration

In this section, a systematic calibration of the model parameters in the constitutive law is described, with detailed results presented. Three types of calibration tests were performed: electric field actuation on pure piezoelectric sheets, stress field loading, and plane strain and plane stress actuation on unimorph samples. The model parameters were fitted by minimizing the RMS error between measurements of material history (strain and electric displacement) and estimations. Fitting was conducted in the following order: each measurement set was fitted independently first, then the complete set was fitted. Differently fit parameters were used to cross check the RMS error under various loading conditions. An optimal parameter set was identified which yielded the minimum RMS error.

3.5.1 Calibration Scheme

The parameter fitting process was established using the following optimization problem. First, the normalized root-mean-square deviation (NRMSD) error between estimations and experimental measurements was defined:

$$\begin{aligned}\min_{\mathcal{P}} NRMSD \ &= w_{\varepsilon} \cdot \sqrt{\frac{\sum_i^{N_\varepsilon} (\varepsilon^i_{measured} - \varepsilon^i_{estimated})^2}{N_\varepsilon \varepsilon_{amp}}} \\ &+ w_e \cdot \sqrt{\frac{\sum_i^{N_D} (D^i_{measured} - D^i_{estimated})^2}{N_D D_{amp}}} \\ &+ w_K \cdot \sqrt{\frac{\sum_i^{N_K} (K^i_{measured} - K^i_{estimated})^2}{N_K K_{amp}}}\end{aligned} \tag{3.47}$$

The total error $\mathcal{E}$ was the sum of the estimation deviation of (structural) curvature response, active layer strain measurements, and electric displacement response. N_ε, N_D and N_K are the number of sample points for each measurement category. ε_{amp}, D_{amp}, and K_{amp} are the maximum absolute values of each type of measurement. w_ε , w_e and w_K are weight constants for each of the error terms. In the following sections, w_ε, w_e, and w_K are assigned to 1 exclusively in each calibration, as shown in table 3.4. The optimization problem was solved in MATLAB using the unconstrained routine `fminsearch`. The framework for the model calibration is shown in figure 3.14.

Table 3.4: Weighting Factors for Calibration

Fitting	w_ε	w_e	w_κ
Section 3.5.2	0.5	0.5	0
Section 3.5.3	0.5	0.5	0
Section 3.5.4	0	0	1
Section 3.5.5	0.33	0.33	0.33

3.5.2 Ferroelectric Calibration

Under a pure electric field, with the exception of an induced stress field, the evolution of the material state was dominated by the electric field domain movement. Correspondingly, in $\hat{E} - \hat{S}$ space, mainly the second term of the switching function

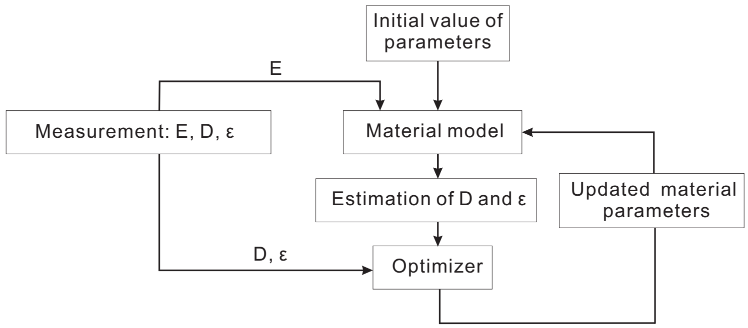

Figure 3.14: Data processing flowchart for the ferroelectric switching test.

determined the current position of the material state.

$$\frac{3\hat{S}_{ij}\hat{S}_{ij}}{2\sigma_0^2} + \underbrace{\frac{\hat{\mathcal{E}}_i\hat{\mathcal{E}}_i}{\mathcal{E}_0^2}}_{\text{Term II}} + \frac{\beta\hat{\mathcal{E}}_i P_j^r \hat{S}_{ij}}{\mathcal{E}_0 P_0 \sigma_0} - 1 = 0 \tag{3.48}$$

Parameters that possessed strong correlation with the material response during the fitting process were: H_0^E, P_{sat}, P_0, d_{31}, κ, and E_0. Among them, E_0 was determined from the butterfly curve directly, and was kept constant during parameter updates. Results of the calibration and comparison with experiment data are shown in figure 3.15.

Calibrated model achieved good agreement with both ε and D measurements. However, the tests revealed a more abrupt transition around $\mathcal{E}_0$, which was not captured by the model.

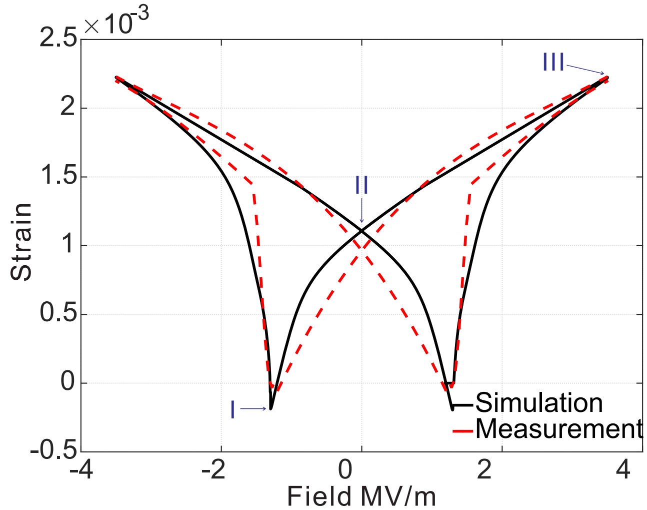

(a)

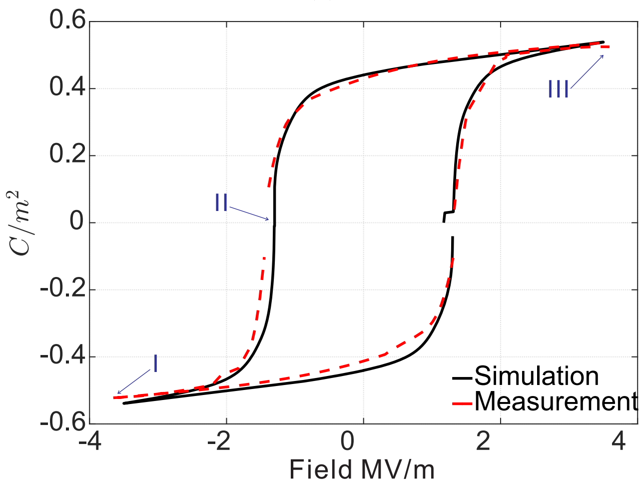

(b)

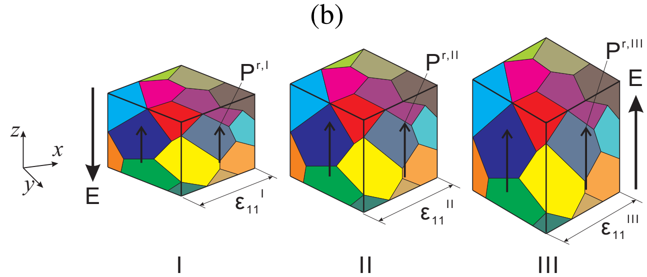

(c)

Figure 3.15: Ferroelectric experiments and fitting results: (a) Strain butterfly curve. $E_0 = 1.3MV/m$ was determined directly. (b) Dielectric hysteresis curve. (c) Microscopic illustration of electro-mechanical coupling of the peizoelectric material under an electric field. $\varepsilon_{11}^{III} > \varepsilon_{11}^{II} > \varepsilon_{11}^{I}$; $P^{r,III} > P^{r,II} > P^{r,I}$.

3.5.3 Ferroelastic Calibration

Under pure mechanical stress fields, the evolution of the material state is dominated by the stress field-induced domain movement. Correspondingly, in $\hat{E} - \hat{S}$ space, the first term of the switching function mainly determines the current position of material state.

$$\underbrace{\frac{3\hat{S}_{ij}\hat{S}_{ij}}{2\sigma_0^2}}_{\text{Term I}} + \frac{\hat{\mathcal{E}}_i\hat{\mathcal{E}}_i}{\mathcal{E}_0^2} + \frac{\beta\hat{\mathcal{E}}_i P_j^r \hat{S}_{ij}}{\mathcal{E}_0 P_0 \sigma_0} - 1 = 0 \tag{3.49}$$

Parameters that possess strong correlation with the material response in the fitting process are ε_c, ε_t, m, H_σ, and σ_0. Since it was not possible to measure the piezoelectric layer stress field σ directly, its value at each loading time step had to be estimated from the available measurements of moment M, outer surface strain ε, and sample curvature K. From equation (3.20), under pure moment loading, the actuation terms were estimated from:

$$\begin{bmatrix} F_{x\Lambda}(\varepsilon_F^r) \\ M_{x\Lambda}(\varepsilon_M^r) \end{bmatrix} = \begin{bmatrix} \boldsymbol{A} & \boldsymbol{B} \\ \boldsymbol{B} & \boldsymbol{D} \end{bmatrix} \begin{bmatrix} \varepsilon_x^0 \\ \kappa_x^0 \end{bmatrix} - \begin{bmatrix} 0 \\ M_x \end{bmatrix} \tag{3.50}$$

ε^r was taken as the mean value of ε_F^r and ε_M^r. Stress was then estimated as:

$$\sigma_{kl} = s_{ijkl}^{-1}(\varepsilon_{ij} - \varepsilon_{ij}^r) \tag{3.51}$$

A flowchart for model calibration in ferroelastic tests is shown in figure 3.16.

The calibration result and comparison with measurements are shown in figure 3.17 and 3.18 for tension tests and figure 3.20 and 3.21 for compression tests.

The main observations from the comparisons are listed below:

- For tension tests, dielectric hysteresis appeared under all stress levels, and the change in remnant polarization $\Delta P^r = P_t^r - P_0^r$ was negative. Remnant strain emerged only when loading was significantly high.

- For compression tests, dielectric hysteresis appeared under all stress levels, and the change in remnant polarization $\Delta P^r = P_t^r - P_0^r$ was negative. Remnant strain emerged at all levels of stress magnitude.

- For model calibrations, estimations for tension tests exhibited dielectric hysteresis behavior when stress reached a certain level; however, for compression tests, the calibrated model essentially behaved linearly.

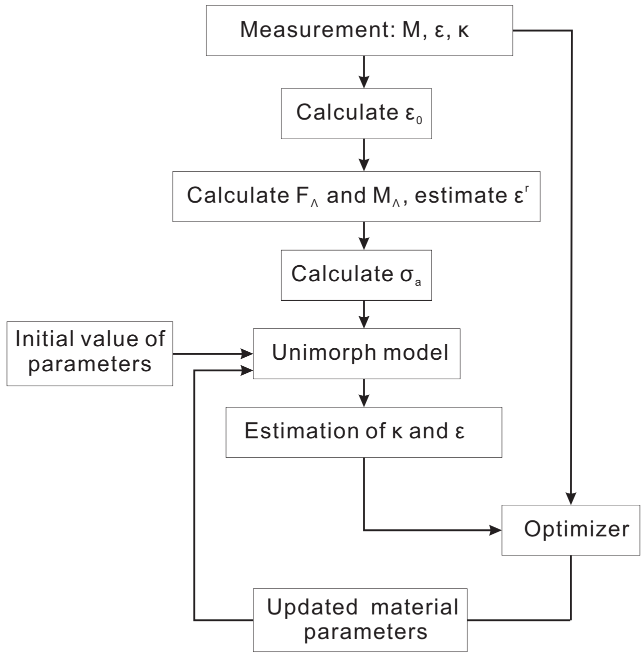

Figure 3.16: Data processing flowchart for ferroelastic calibration.

The differences between measured hysteresis and estimated linear behavior at low stress level point to the fundamental defect of kinematic hardening assumptions adopted in the model. Measurements indicated that ferroelastic switching was a gradual process; however, in the model, hardening only initiated when the material state was on the switching surface in $\hat{E} - \hat{S}$ space, and evolved quite abruptly.

The fact that ΔP^r values were negative in all sets of tests indicates that both compressive and tensile in-plane stress fields depolarized the piezoelectric layer. Moreover, under a compressive stress field, with an increase in the loading level, the dielectric displacement exhibited a 'memory' effect, evident in figure 3.21 (c) and (d). During the unloading phase, the dielectric displacement tended to lock in-phase for a short period and then later intersected with the loading curve. This may be due to the non-180°domain switching under in-plane loading, and this has not been reported in other literature to the author's best knowledge. These observations suggest that extrinsic effects dominate the piezoelectric behavior of soft polycrystalline ferroelectric materials, which cannot be captured by a linearized constitutive model.

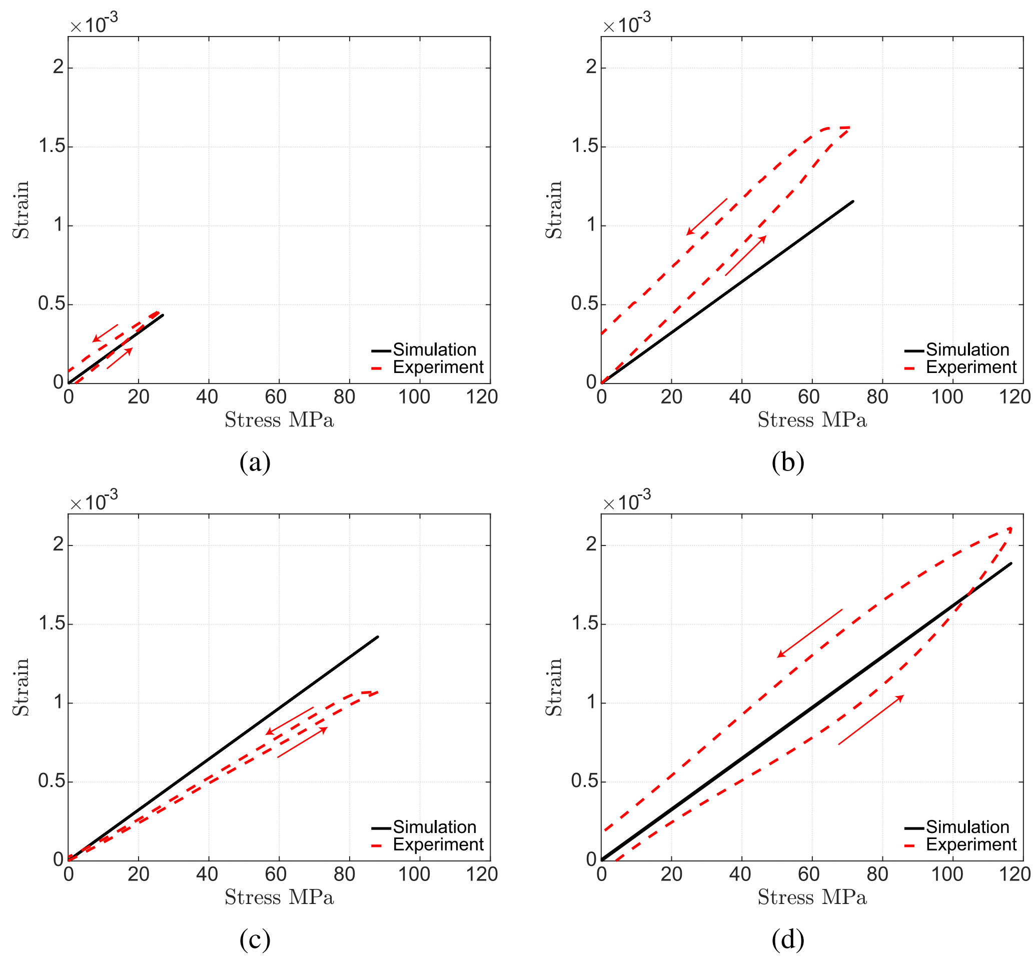

Figure 3.17: Ferroelastic switching experiments and fitting at different stress levels: PZT in tension.

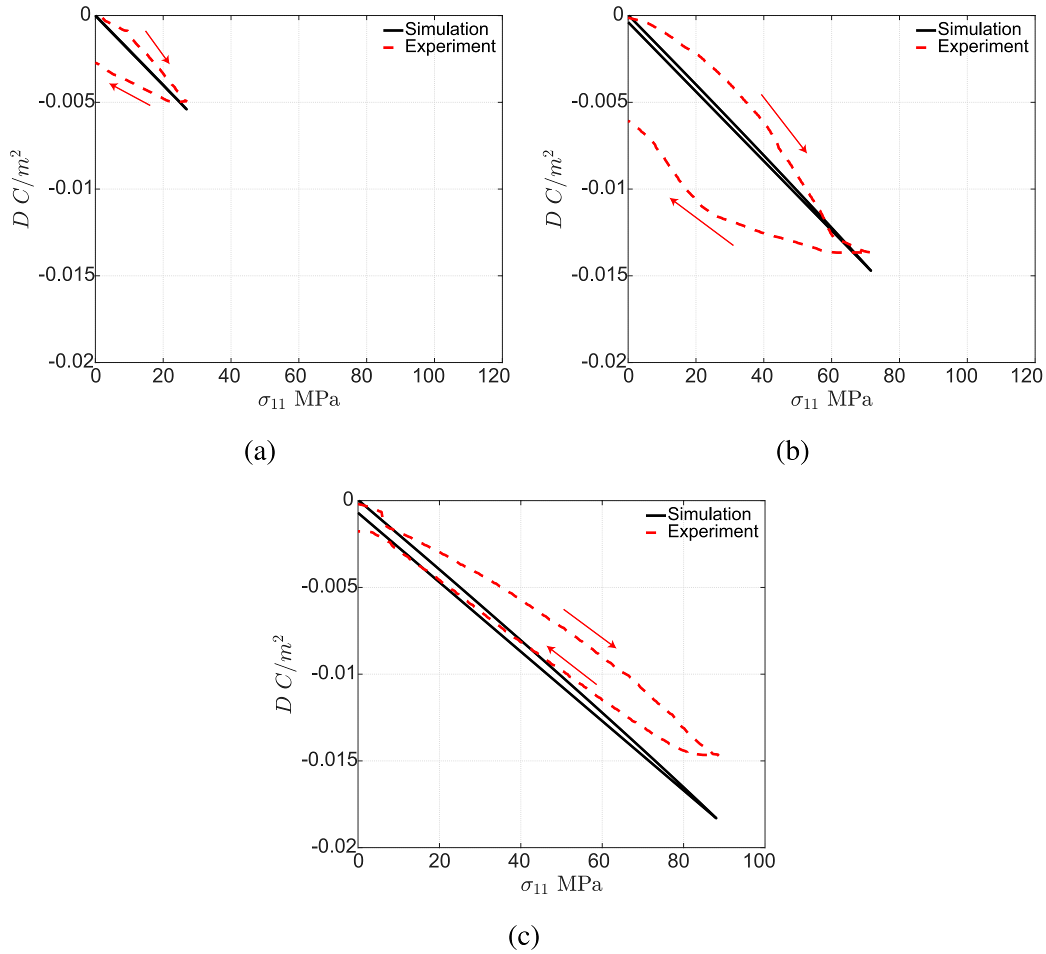

Figure 3.18: Electric displacement hysteresis in ferroelastic switching tests: piezoelectric layer under tension.

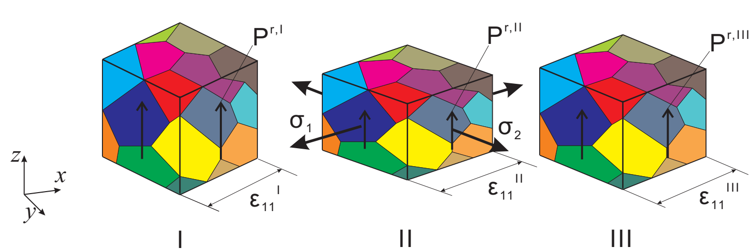

Figure 3.19: Microscopic view of the piezoelectric layer under ferroelastic switching: PZT in compression. $\varepsilon_{11}^{II} > \varepsilon_{11}^{III} > \varepsilon_{11}^{I}$, indicates post loading remnant strain. $P^{r,II} > P^{r,I} > P^{r,III}$ indicates remnant polarization decreased after loading.

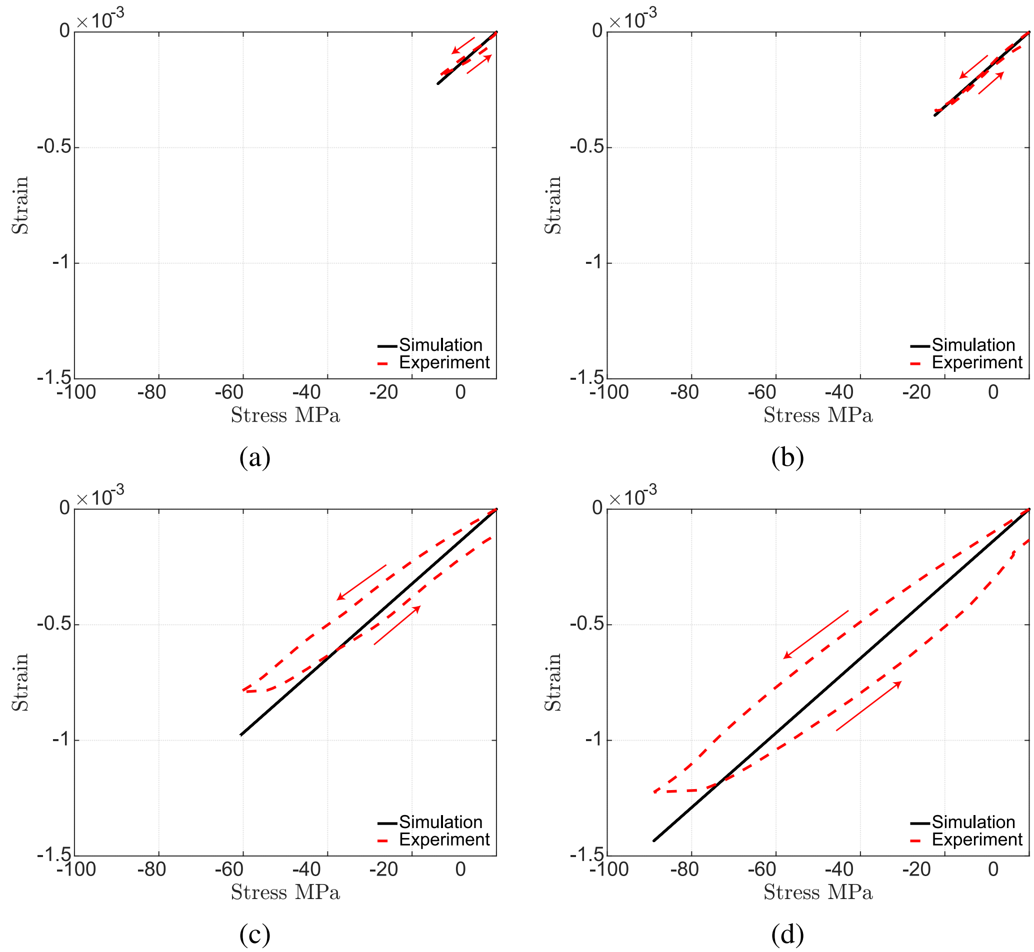

Figure 3.20: Strain hysteresis in ferroelastic switching tests and fitting: PZT layer under compression.

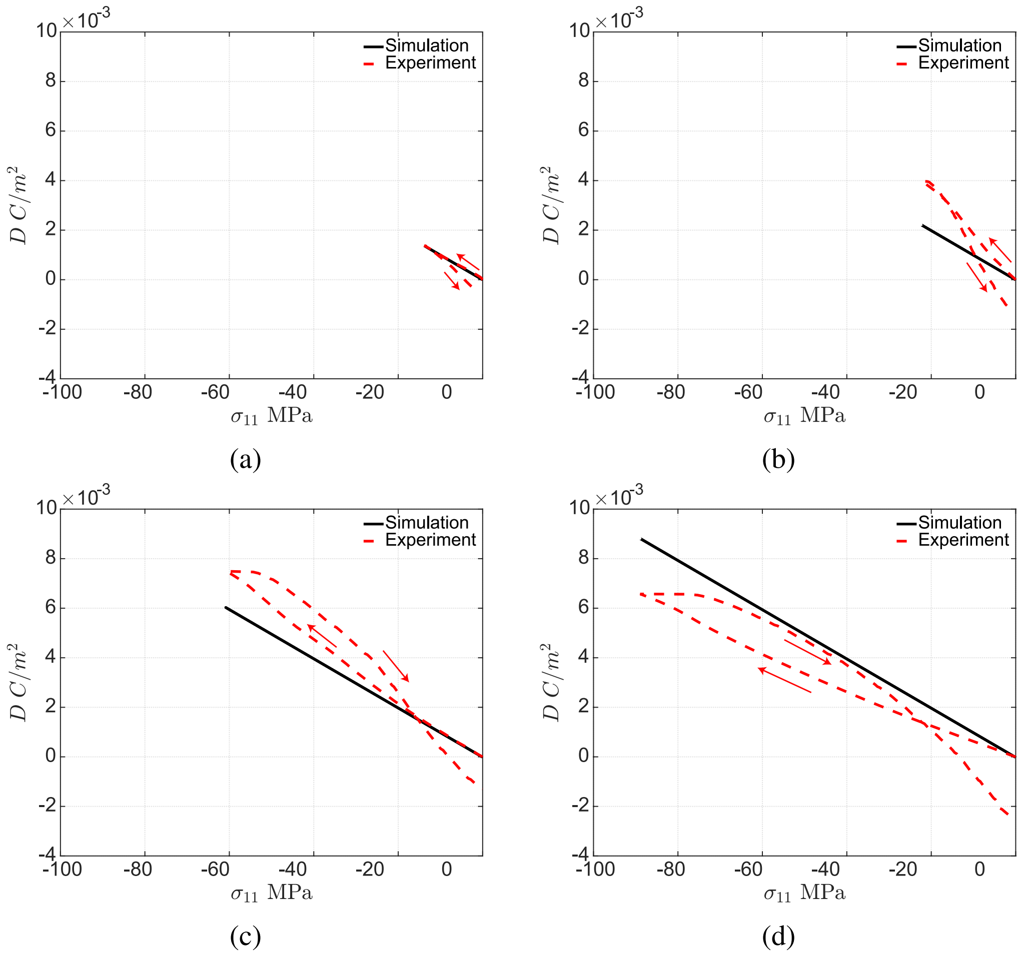

Figure 3.21: Electric displacement hysteresis in ferroelastic switching tests and fitting: piezoelectric layer under compression. End points of the curves are lower than the starting points, suggesting a decrease in remnant polarization P^r.

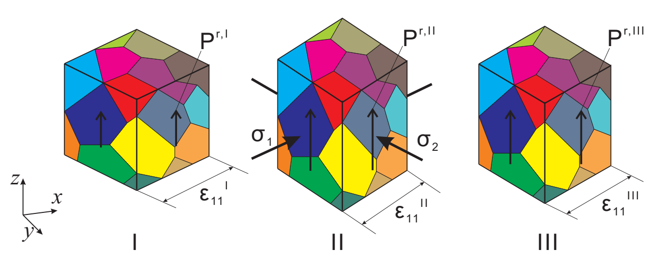

Figure 3.22: Microscopic view of piezoelectric layer under ferroelastic switching: PZT in compression. $\varepsilon_{11}^{II} > \varepsilon_{11}^{III} > \varepsilon_{11}^{I}$ indicates post-loading remnant strain. $P^{r,II} > P^{r,I} > P^{r,III}$ indicates remnant polarization decreased after loading.

3.5.4 Plane Strain and Plane Stress Actuation Calibration

In unimorph actuation tests, the electric field and the induced stress field jointly determined the current material state in $\hat{E} - \hat{S}$ space. Thus at every new loading step, all terms in the switching function contribute to the backward correction step, as follows:

$$\underbrace{\frac{3\hat{S}_{ij}\hat{S}_{ij}}{2\sigma_0^2}}_{\text{Term I}} + \underbrace{\frac{\hat{\mathcal{E}}_i\hat{\mathcal{E}}_i}{\mathcal{E}_0^2}}_{\text{Term II}} + \underbrace{\frac{\beta\hat{\mathcal{E}}_i P_j^r \hat{S}_{ij}}{\mathcal{E}_0 P_0 \sigma_0}}_{\text{Term III}} - 1 = 0 \tag{3.52}$$

Similar to section 3.5.3, the stress field had to be estimated from the measurements. Since there was no external mechanical loading, the following relation held:

$$\begin{bmatrix} \boldsymbol{\varepsilon} \\ \boldsymbol{K} \end{bmatrix} = \begin{bmatrix} \boldsymbol{F} \\ \boldsymbol{M} \end{bmatrix} \begin{bmatrix} \boldsymbol{A} & \boldsymbol{B} \\ \boldsymbol{B} & \boldsymbol{D} \end{bmatrix}^{-1} \begin{bmatrix} \boldsymbol{F}_{\Lambda} \\ \boldsymbol{M}_{\Lambda} \end{bmatrix} \tag{3.53}$$

The stress field was then estimated as

$$\sigma_{ij} = s_{ijkl}^{-1}(\varepsilon_{ij} - d_{nij}\mathcal{E}_n - \varepsilon_{ij}^r) \tag{3.54}$$

Calibrations were performed for plane strain and plane stress actuation tests separately. The experimental measurements and calibrated model estimations for plane strain and plane stress conditions are shown in figures 3.23, 3.25 and figures 3.27, 3.28.

The experimental curves in each figure represent the average of three sets of experiments. From figures 3.23 and 3.27, both the actuation condition and thickness ratio R greatly affected the electro-mechanical behavior of piezoelectric unimorph structures. For both actuation conditions, d_{31} and the nonlinearity of the curvature response were positively correlated with R. For low field actuations (less than $\mathcal{E}_0$), differences between results from both strip and plate tests were within 5%. However, at high actuation levels $\mathcal{E} > 1.3\mathcal{E}_0$, plate unimorphs showed significantly lower nonlinearity. The main reason for these phenomena is the decrease of induced in-plane stress field magnitude as the thickness of the piezoelectric layer becomes comparable with substrate layer. For a thin piezoelectric layer, the 'clamping' effect from the substrate is more obvious. This phenomenon has been widely observed in ferroelectric membranes [132].

Examining the calibrated model outputs in figure 3.23 for strip and figure 3.27 for plate unimorphs, at low actuation fields no switching effects were predicted. Thus, the model output was equivalent to a linear estimation with constant d_{31}.

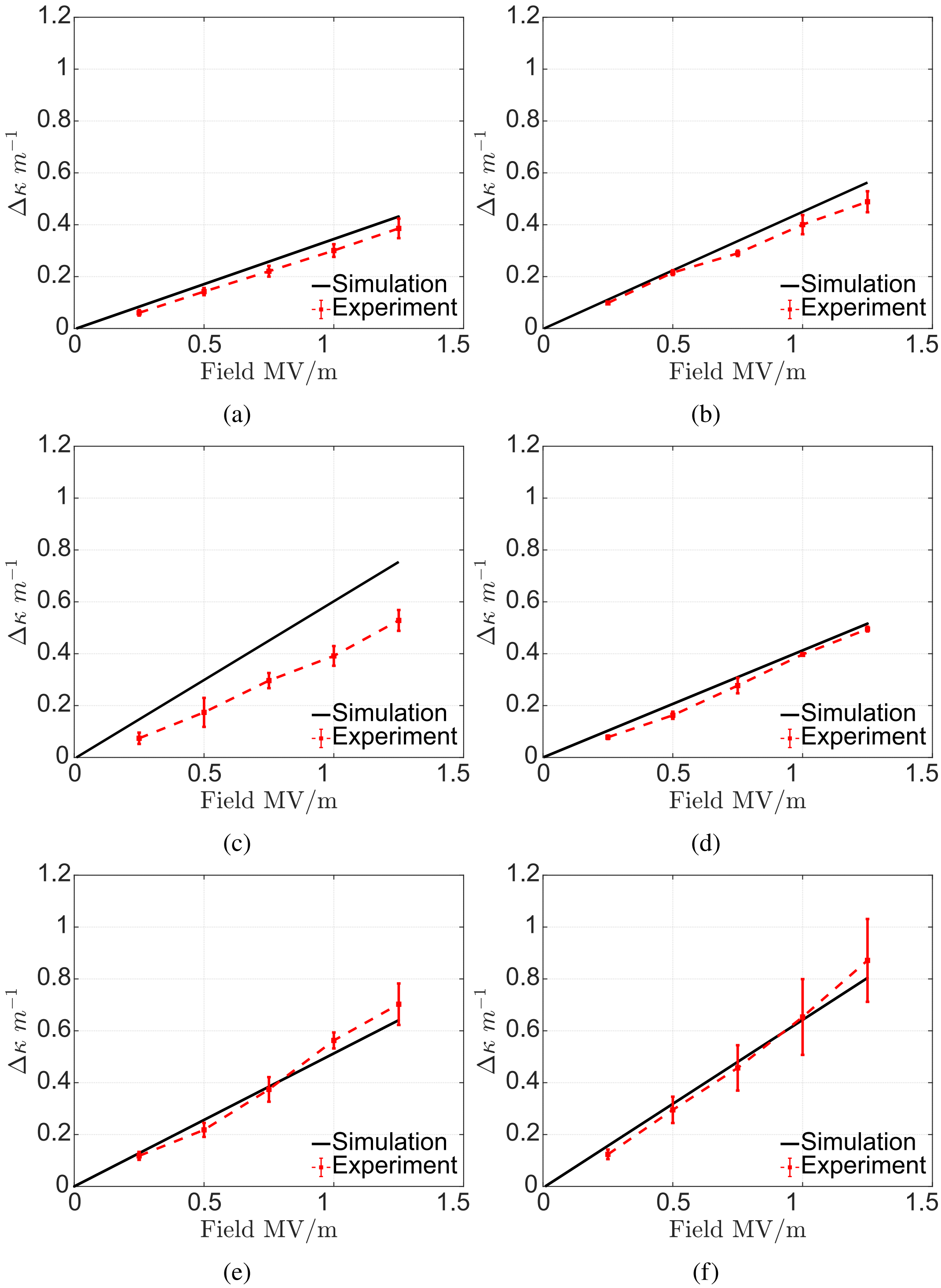

Figure 3.23: Calibration of low field unimorph actuation of different thickness ratios: plane strain condition.

However, a clear trend of increasing d_{31} was observed in the same figures based on measurements, as R increased. Thus, the heuristic potential functions adopted in

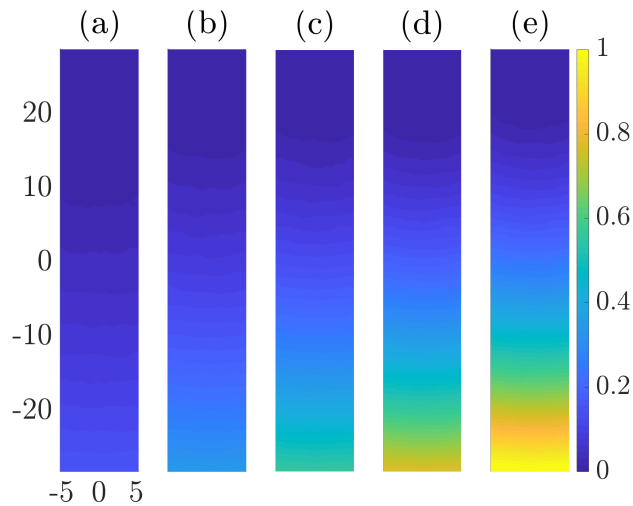

Figure 3.24: z-component of displacement for the $200/500\mu m$ unimorph strip under static actuation fields. Dimensions in mm. (a) $0V/m$. (b) $0.25MV/m$. (c) $0.5MV/m$. (d) $0.75MV/m$. (e) $1MV/m$. (f) $1.25MV/m$.

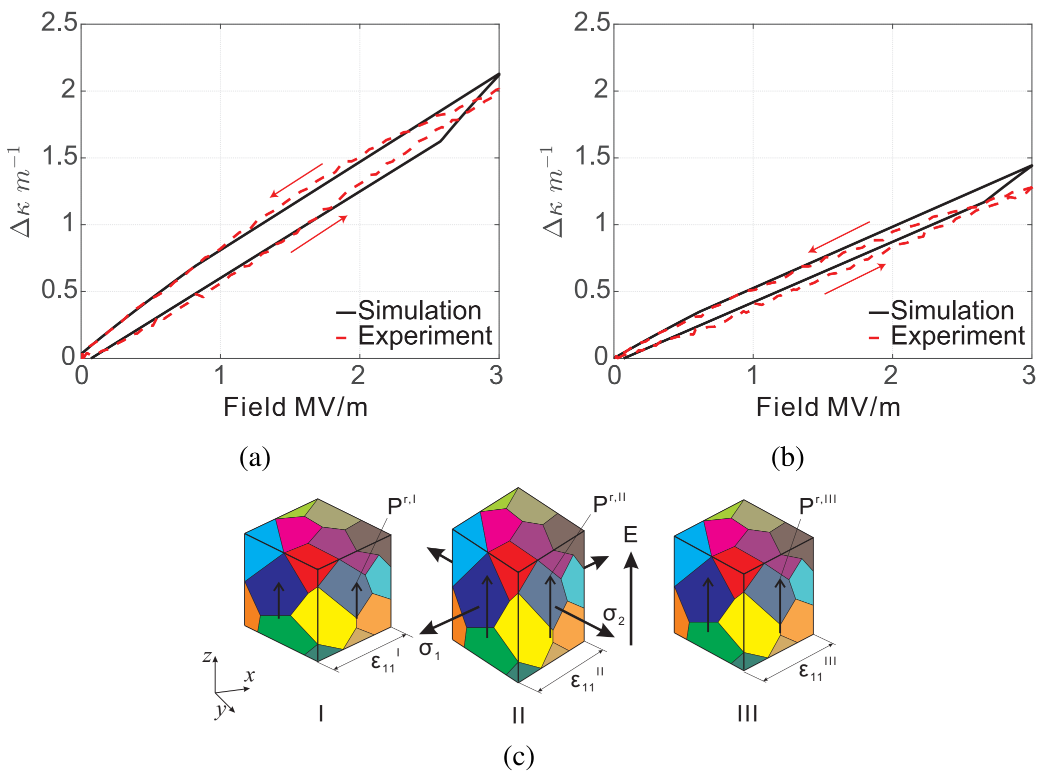

Figure 3.25: High field strip unimorph actuation experiments and fitting for: (a) Thickness ratio of 0.5. (b) thickness ratio of 0.33. (c) Schematic representation of piezoelectric layer loading history and remnant strain development. $\varepsilon_{11}^{II} > \varepsilon_{11}^{III} > \varepsilon_{11}^{I}$.

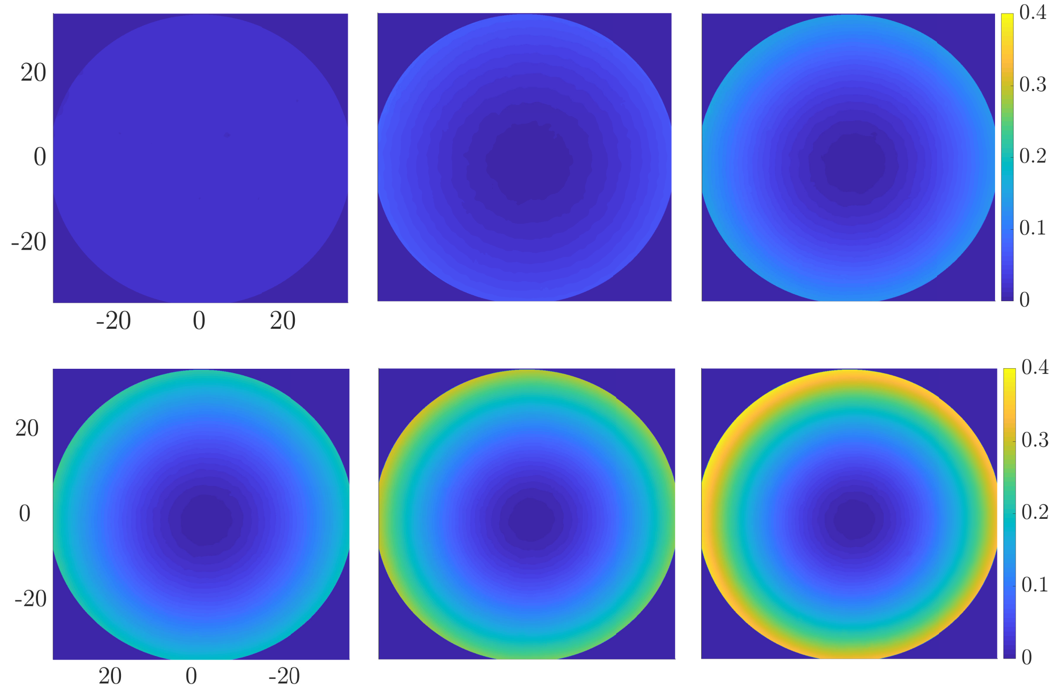

Figure 3.26: Z-component of displacement for $200/500\mu m$ unimorph plate under electric field actuation. (a) $0.25MV/m$. (b) $0.5MV/m$. (c) $0.75MV/m$. (d) $1MV/m$. (e) $1.25MV/m$.

this work did not capture the stress dependent switching when $\sigma_{ij} < \sigma_0$. In the high field tests shown in figures 3.25 and 3.28, result from calibrated model qualitatively reproduced the strain hysteresis curve. However, unlike in measurements where hysteresis smoothly emerged, switching appeared more abruptly in the estimations, as shown in figures 3.25 and 3.28. Discrepancies suggested that more realistic potential functions need to be developed.

3.5.5 Combined Calibration and Optimal Parameter Selection

Thus far, the calibrations were performed separately for independent measurements. In order to determine a set of model parameters that minimized the NRMSD for the complete measurements, all sets of data points from sections 3.5.2, 3.5.3 and 3.5.4 were fitted in single optimization process. This process is denoted as global fitting, and the results from previous sections are referred to as local fittings. Furthermore, cross validations of NRMSD were conducted on each measurement set with parameters from local fittings of different sources. The resulting values for both global and local fitting, as well as cross validations are shown in table 3.5.

In the table, diagonal entries correspond to local fittings under each parameter

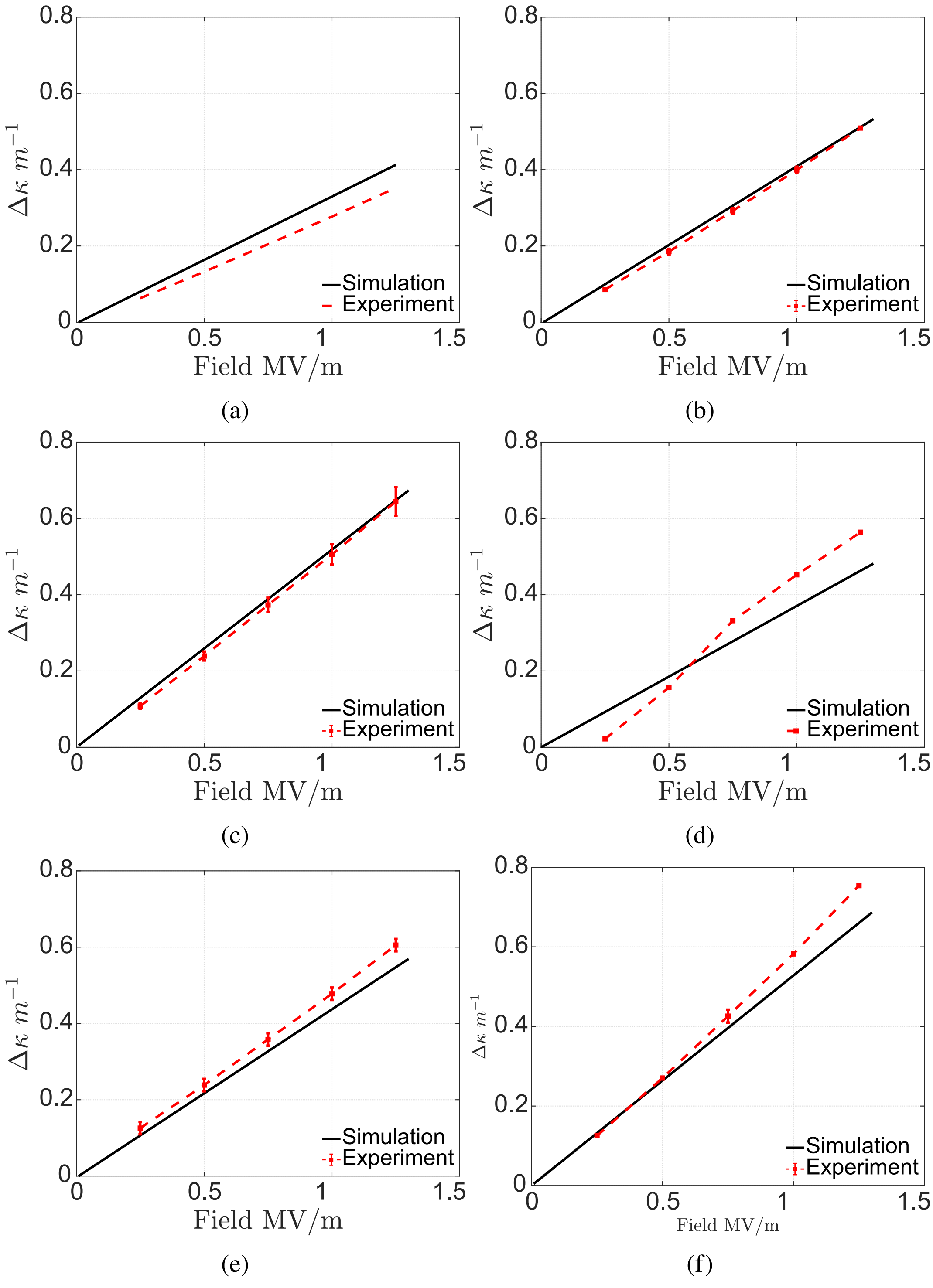

Figure 3.27: Calibration of low field unimorph actuation of different thickness ratios: plane stress condition.

set, and achieve the lowest error. Off-diagonal terms are error values from cross checking calculations. For example, the entry in row 2, column 3 is the error from the

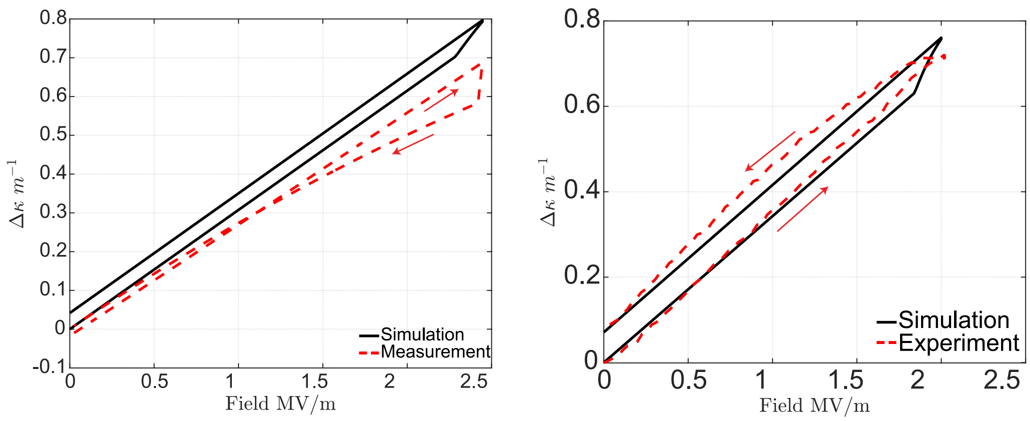

(a) (b)

Figure 3.28: High field plate unimorph actuation experiments and fitting for thickness ratios of 0.21 and 0.33.

Table 3.5: Cross Validations of RMS Error

Experiment set	Parameter set 1	Parameter set 2	Parameter set 3	Parameter set 4	Parameter set 5
1	8.5	–	–	–	38.8
2	8300	25	1100	610	38.7
3	60	37.5	7.8	24.2	18.6
4	20	46.9	16.6	8.7	13.6
Mean	2097	36.4	283.7	163.7	29

* All values in %.

estimation of ferroelastic tests based on a parameter set from plane strain calibration. To achieve a better fit with the measurements, the local approach produced lower RMS values (the diagonal terms). This result indicates that for specific loading conditions, a parameter set from local fitting will generate closer predictions. In calculations for entries $(2, 1)$, $(2, 3)$, and $(2, 4)$, integration diverged and generated a large error. Overall, parameter set 5 gave the lowest NRMSD, and was chosen as the optimal material parameters for the piezoelectric sheets studied in this research.

Table 3.6 extracts the d_{31} values fitted from four sets of measurements, and the associated loading condition for each set. Clearly, both the electric and stress fields greatly affected the effective value of d_{31} on the macroscopic level. In general, existence of an electric field along poling direction of the piezoelectric sheets enhanced the in-plane piezoelectric effect, and d_{31} depended on the magnitude of $\mathcal{E}$. Under a moderate in-plane stress field, a ferroelastically induced d_{31} value was significantly lower than that under ferroelectric actuation. When both fields are combined, the increase of in-plane stress also resulted in higher d_{31} values.

Table 3.6: Experimental Conditions and Piezoelectric Constants

	Experiment set 1	Experiment set 2	Experiment set 3	Experiment set 4
$\mathcal{E}$	√	-	√	√
σ_1	-	√	√	√
σ_2	-	-	$\sim 0.3\sigma_1$	$\sim \sigma_1$
d_{31} PC/N	−408.72	−95.08	−142.04	−183.67

3.6 Validation of Calibrated Model

In this section, the fitted constitutive law and proposed integration algorithm were validated against several application situations. Examples studied focus on PZT-5A-bonded unimorph response under strong electric and stress fields. In summary, the estimation agreed with observations qualitatively with an RMS error on the order of 15%, which justified the model calibration procedure in previous sections. Moreover, certain deficiencies of the implemented constitutive law were revealed regarding the quantitative feature of the estimation and led to further suggestions.

3.6.1 Validation of Unimorph High Field Consecutive Actuation Tests

In the first example, the remnant shape of a unimorph plate was subjected to cyclic electric field loading with varying amplitudes and directions (i.e. forward or backward with respect to the poling direction of piezoelectric sheets). In these cases, switching induced residual deformations were widely observed. The remnant curvature at the end of each loading cycle was used as a metric for the fitted model.

In this example, piezoelectric sheet-bonded aluminum unimorph samples with $R = 0.33$ and $R = 0.5$ were used in the experiments. The first set of response data was obtained by actuating the sample continuously up to 1 MV/m, 1.5 MV/m, and 2 MV/m, shown in figure 3.29. The second set of data was obtained by swapping the actuation direction between loading cycles, with the same magnitude, 1 MV/m, as shown in figure 3.30.

In both actuation cases, the sample developed remnant curvature at the end of each loading cycle with the magnitude consecutively accumulating. In the first case, no switching phenomenon was predicted for the initial two actuation cycles. At the end of the last cycle, where $\mathcal{E} \approx 2\mathcal{E}_0$, the model predicted the remnant curvature, which was quite close to the relative curvature change of the cycle. In the second case, the remnant curvature due to negative direction actuation was reproduced in the estimation precisely; however, the following positive actuation-induced remnant curvature was missed by the model. These discrepancies suggest that a constant radius switching surface assumption cannot fully capture the domain switching phenomenon at the low actuation field level. Hence the model overestimated the linear region of the material's response. In the future, a combined hardening law [133] may be introduced to further improve the phenomenological framework.

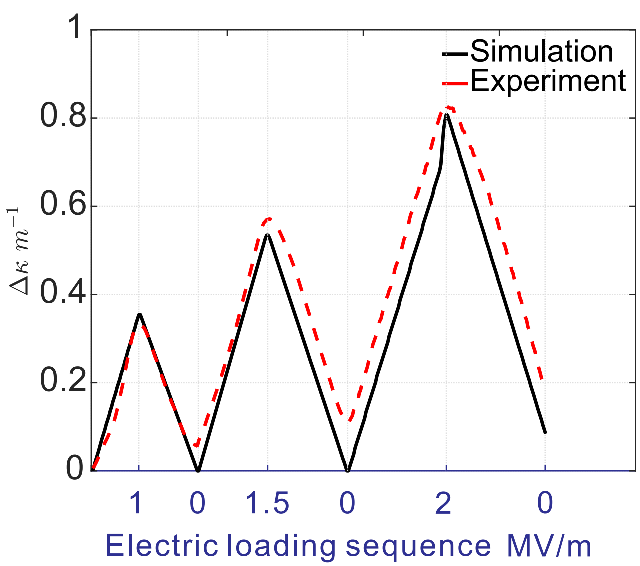

Figure 3.29: Consecutive loading of a plate unimorph with r = 0.33.

3.6.2 Ferroelastic-ferroelectric loading tests

The examples presented in this section showed the measured and estimated strain history of a thin piezoelectric plate which was subjected to ferroelectric and ferroelastic fields consecutively. The goal of this section is to show the interchangeable role of electric and stress fields in driving the domain switching of piezoelectric materials, and demonstrate the versatility of the calibrated model in predicting switching due to different sources. Similarly to section 3.5.3, piezoelectric patches were bonded to substrates with an initial poling direction through the thickness.

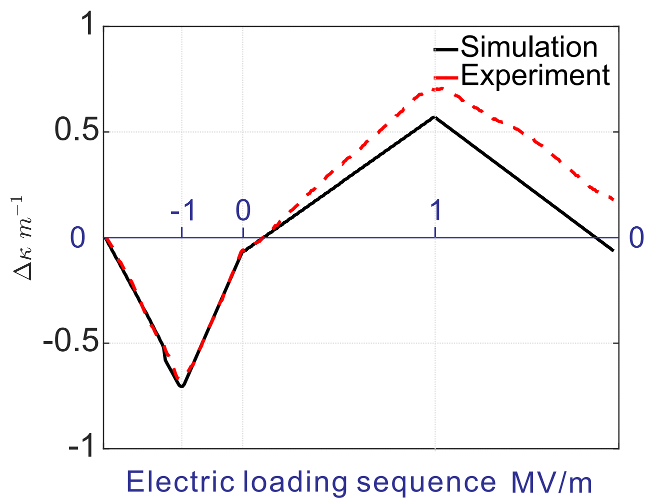

Figure 3.30: Consecutive actuation of a plate unimorph with $r = 0.5$.

As shown in figure 3.31 (a), an actuation sequence that triggered ferroelastic and ferroelectric consecutively was conducted on a unimorph sample. The sequence is further described below.

1. First, the piezoelectric layer was subjected to in-plane stretching through four-point bending. The displacement of the loading head was controlled linearly, which increased to the maximum value and then unloaded to the initial position. The evolution of the strain history on the outer surface of the piezoelectric layer was monitored through DIC.
2. At the end of the mechanical loading step, a positive, high electric field ($\sim 2\mathcal{E}_0$) was applied through the thickness direction of the piezoelectric layer.

From figure 3.31 (b), the strain hysteresis curve could be closed at the end of the complete loading cycle. As in section 3.5.3, non-180°domain switching was responsible for the in-plane remnant straining effect. The full field model successfully captured the phenomenon macroscopically.

3.7 Summary and Discussion

This chapter has presented the steps used to calibrate a multi-axial, full-field, rate independent phenomenological constitutive law for polycrystalline piezoelectric materials. An implicit, backward-Euler integration algorithm for the material model was proposed and incorporated into a simplified, homogenized model for unimorph structure actuation. Systematic experiments were conducted on pre-poled thin

PZT-5A plates and unimorph structures manufactured from the same. Material parameters incorporated in the constitutive law were fitted by minimizing the RMS error between experimental observations and corresponding estimations. A comprehensive study of the influences of different fitting sources was carried out and the resulting RMS errors were presented. The calibrated model is able to obtain less than 10 % RMS error when fitted with measurements from a single actuation/loading condition, and achieve RMS errors of around 20 % in model validations of other loading conditions.

Based on the calibrated constitutive law and the proposed estimation algorithm for unimorph structures, the curvature responses for PZT-5A-based unimorph structures under various electro-mechanical loading conditions were simulated and compared to experimental observations. Estimations reproduced the measured structural behavior with reasonable performance, especially for the remnant curvature of samples. Moreover, the constitutive law and estimation algorithm successfully captured the ferroelastically induced 90°switching and the followed ferroelectric switching phenomenon observed in the last validation experiment. Thus, the validated numerical tools can be used to track the evolution of piezoelectric material's state under complicated loading conditions. The absolute values of the observed switching-induced nonlinear deformation are small, mainly due to the thin thickness of the piezoelectric layer of the unimorph samples and the high stiffness of the substrates. Future experiments conducted at higher electric and stress fields along different angles with respect to the poling direction of the material, and on bulk piezoelectric materials would be needed to further validate the model. The model may also be used as a design tool to exploit the switching-induced deformation of piezoelectric materials in shape control applications, for example the energy-efficient actuators described in [42].

Certain deficiencies were also revealed in the comparison to experiments. First, the modeling framework was not able to predict the stress-field dependence of d_{31}, which was observed in the unimorph actuation tests. This calls for new formulations of stress potential functions in the constitutive law. Second, the homogenized unimorph actuation modeling approach oversimplified the complicated boundary conditions of piezoelectric layers in the tests conducted. The calibrated model and integration law could be incorporated into the finite element framework in the future to overcome the limitations of the homogenized model and further investigate the switching of the material in 3-dimension space.

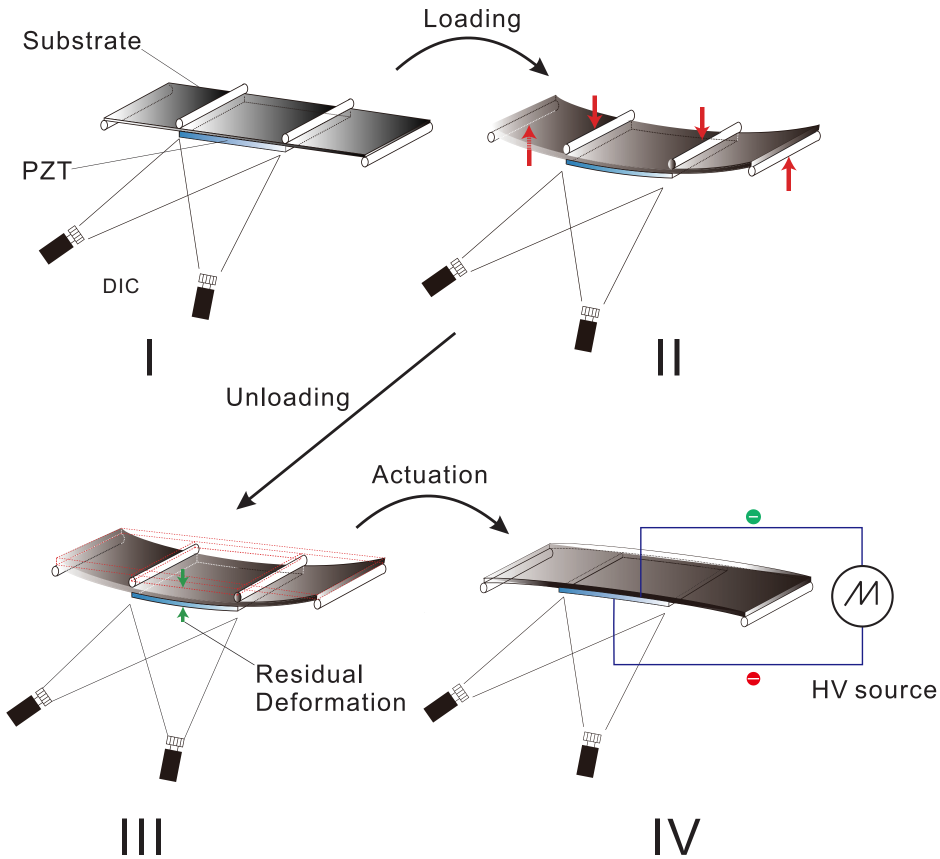

(a)

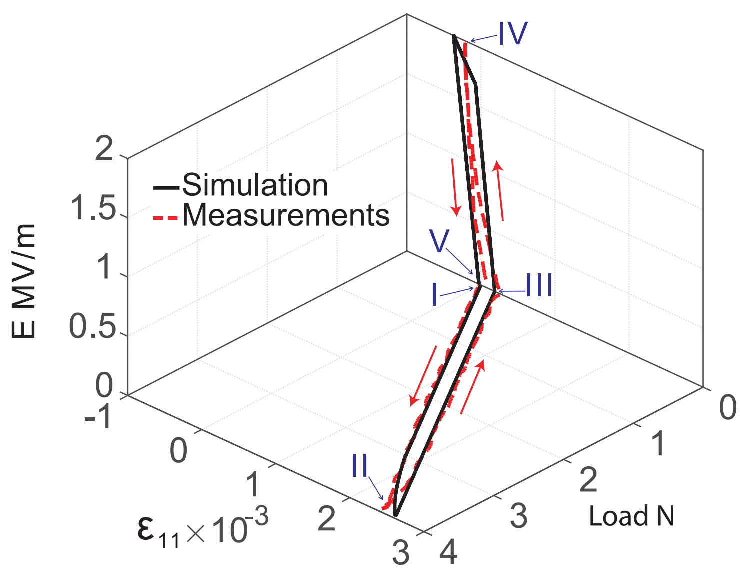

(b)

Figure 3.31: Ferroelastic-ferroelectric switching of a unimorph.The curve traced by $I \rightarrow II \rightarrow III$ represents the mechanical loading history under four-point bending. The curve traced by $III \rightarrow IV \rightarrow V$ represents the electric loading history under through-thickness electric field.

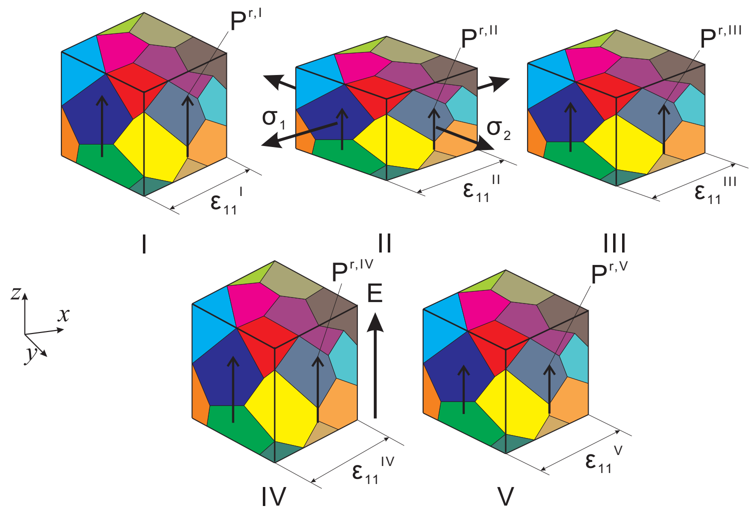

Figure 3.32: Microscopic view of ferroelastic-ferroelectric switching of the piezoelectric material studied in this section. $\varepsilon_{11}^{II} > \varepsilon_{11}^{III} > \varepsilon_{11}^{IV} > \varepsilon_{11}^{V} \approx \varepsilon_{11}^{I}$.

Chapter 4

VIBRATION CONTROL OF SELF-SENSING PIEZOELECTRIC THIN SHELL STRUCTURES

Previous chapters have analyzed and characterized the static actuation capability of piezoelectric materials in active thin shell structures. This chapter focuses on the dynamic and real-time control of piezoelectric thin shell structures for vibration mitigation.

4.1 Introduction

Piezoelectric active thin shell structures have been used in the high frequency range sensing applications due to their superior operation band width [134]. The examples that combine both sensor and actuator capability of piezoelectric thin shell structures include flutter suppression of aerospace structures [135], acoustic vibration control [136], structure health monitoring [137], and vibration jitter mitigation in optical systems [138]. Indeed, a pertinent example is the development of large segmented space telescopes proposed in the future Decadal Survey Missions such as the LUVOIR space observatories (Large Ultra Violet Optical InfraRed) [139]. These telescopes require a high stability of their line of sight to perform their scientific observations efficiently at a high level of precision. Piezoelectric active thin shell structures can have a significant impact to achieve this high stability, especially when controlled in real time and closed loop during observation. However, conventional closed-loop applications usually require separated sensor and actuator pairs, as shown in figure 4.1a. The sensor layer not only complicates the design of the active structures, it also add extra mass to the structure and may reduce the structural reliability due to the high brittleness of the piezoelectric materials.

The self-sensing architecture integrates both the sensing and actuation functions into the same piezoelectric active layer (figure 4.1b) in the structure, by making dual use of the forward and inverse piezoelectric effect at the same time [140]. By removing the extra sensor layer, it greatly reduces the structural complexity of a vibration control system. The architecture also provides true collocated control which rejects the vibration at the disturbance location and leads to better closed-loop stability [141].

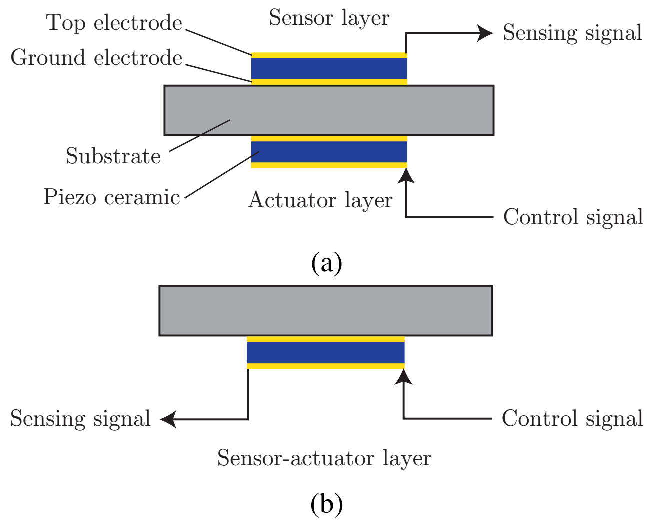

Figure 4.1: Comparison between conventional separated sensor and actuator architectures: (a) and self-sensing architecture (b) for vibration control of piezoelectric thin shell structures.

A consequence of the self-sensing architecture is that the control input voltage to the sensor-actuator layer will induce extra charge output that is mixed within the sensing signal output. One of the key challenges of implementing an effective self-sensing vibration control scheme is how to separate the control induced component from the sensing signal output to extract only the signal related to the mechanical excitation. To achieve this, analyses and implementation of an adaptive signal separation circuit and the related algorithm are the main focuses of this chapter. Another major challenge that prevents the further spread of self-sensing vibration control is the lack of efficient and accurate modeling techniques of complicated, multi-input and multi-output (MIMO) active structures. The chapter will also tackle the challenge by modeling the active structure response with thin shell elements and construct closed-loop control models based on commercial Finite Element software outputs. Both the adaptation circuit and the modeling technique will be presented and verified in experiments, with samples built from the materials characterized in previous chapters.

4.2 Background and Motivation

4.2.1 Review of Sensing Circuit Balancing Techniques

The fundamental work of self sensing was established by Dosch et al. [142]. The authors proposed two types of electrical bridge circuits, shown in figure 4.2. which are capable of measuring either strain (with capacitor bridge circuit) or the time rate of strain (with resistor bridge circuit) of the sensor-actuator layer.

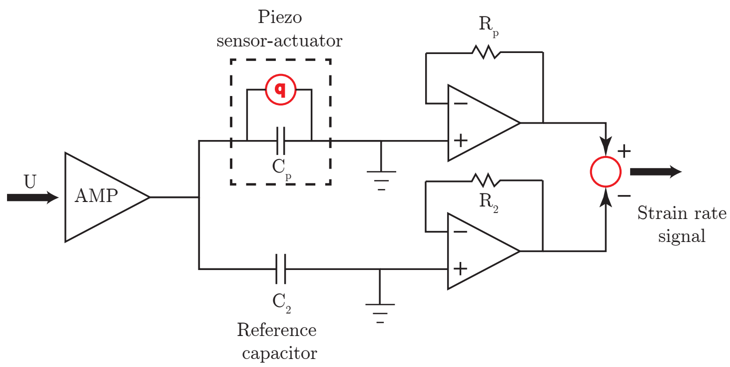

(a)

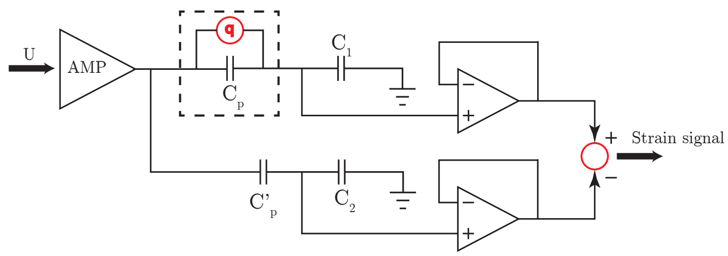

(b)

Figure 4.2: Typical bridge circuit design for signal balancing for self-sensing piezoelectric actuators. The piezoelectric layer is modeled as a charge pump connected in series with a capacitor. The sensing signal is read out through the trans-impedance amplifiers [143]

The fundamentals of a resistor bridge circuit (figure 4.2a) is based on the following considerations. Suppose the sensor-actuator layer can be modeled as a linear capacitor linked in serial with a charge source. Assume the input voltage is U and no mechanical disturbance is exciting the sensor-actuator layer, then the output signal V_{ft} from the circuit is:

$$V_{ft} = \left(R_p \cdot C_p - R_2 \cdot C_2\right) \cdot \dot{U} \tag{4.1}$$

In the following V_{ft} is referred to as the feed through signal. The circuit balance condition requires:

$$R_p \cdot C_p = R_2 \cdot C_2 \tag{4.2}$$

In this case the feedthrough signal vanishes: $V_{ft} = 0$.

For the balance of a capacitance bridge circuit (figure 4.2b), the condition is more complicated. The feedthrough signal can be expressed as:

$$V_{ft} = \left(\frac{C_p}{C_p + C_1} - \frac{C_2}{C'_p + C_2}\right) U \tag{4.3}$$

The balanced condition requires

$$\frac{C_p}{C_p + C_1} = \frac{C_2}{C_p' + C_2} \tag{4.4}$$

Starting from the two versions of the bridge circuit, different closed loop control algorithms can be developed. A systematic comparison of the two lines of development is not within the scope of this chapter. However, condition 4.2 is easier to achieve than condition 4.4 since tuning the value of resistors can be achieved conveniently in practice. For instance, R_p or R_2 can be implemented as digital or analog potentiometers. This chapter will focus on the resistor based bridge circuit hereafter.

4.2.2 Challenges and Solutions of Bridge Circuit Balancing

Achieving the circuit balance condition, described by equation 4.1 or 4.3, is challenging with piezoelectric materials due to their inherent property. As has been shown in chapter 3 and will be demonstrated experimentally later in this chapter, the dielectric properties of piezoelectric ceramic is inherently nonlinear. The electric capacitance/impedance of piezoelectric material based sensors and actuators depend on the applied electric field's frequency ω, amplitude A, the ambient temperature T, operation time t and also mechanical stress field σ:

$$C_p \sim C_p\left(\omega, A, T, t, \sigma\right) \tag{4.5}$$

Much effort has been devoted to the modification of the bridge circuit in order to estimate the piezoelectric capacitance C_p in real time [141], [144]–[146]. One major line of development is through adaptive compensation, and the concept is illustrated in figure 4.3. At the core of the adaptive compensation concept is the introduction of an extra signal U_t, denoted the training signal, and the associated adaptation algorithm. U_t is injected to the sensor-actuator layer, and is mixed together with the control signal U. The goal of the adaptation algorithm is to minimize (and ideally cancel) the feedthrough signal that originates from U and U_t in real time. It essentially corresponds to track the time-dependent and nonlinear C_p value in-situ to balance the bridge circuit. The algorithm of choice should possess fast convergence speed; at the meantime the choice of the training signal is crucial to identify the value of C_p.

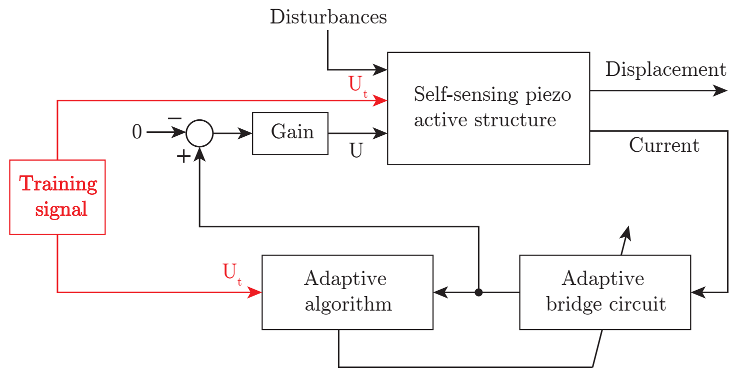

Figure 4.3: Concept of online adaptation for feedthrough signal separation for self-sensing vibration control.

4.2.3 Chapter Overview

The chapter tackles the challenge of developing self-sensing vibration control systems for piezoelectric thin shell structures both numerically and experimentally. Figure 4.4 shows an overall scheme of the numerical and experimental study presented. To demonstrate the concept feasibility and quantify the achievable damping

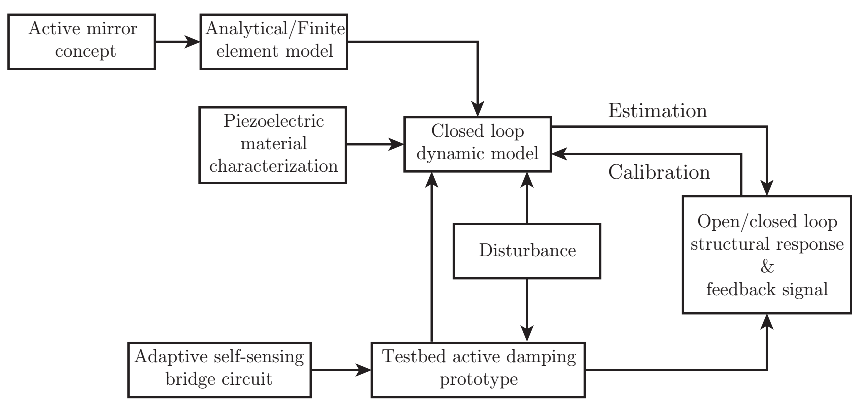

Figure 4.4: Scheme of the self-sensing active damping study presented.

performance, the chapter will:

- Develop numerical models for both open loop structural response and closed loop vibration control for self-sensing piezoelectric structures;
- Develop a test bed and perform measurements on self-sensing cantilever beam samples.

Both the modeling technique and adaptation circuit will be presented and verified by means of experiments, using test samples built from materials characterized in the previous chapter.

Section 4.3 provides an analytic model of the open-loop sensing signal of a self-sensing piezoelectric cantilever beam, in order to show the relations between signal strength, structural geometries and material properties. In order to facilitate the establishment of a closed-loop dynamics model for more general types of self-sensing piezoelectric active structures, section 4.4 develops an efficient and fast modeling technique based on thin shell elements and commercial FEM software outputs. Section 4.7 analyzes an adaptive sensing circuit based on resistor bridge, and emphasizes the importance of the choice of training signal's amplitude and frequency to correctly identify C_p. Experimental closed-loop vibration control tests are conducted based on the adaptive sensing circuit in section 4.8, and the results are compared with the closed-loop dynamics models established using the technique developed. Section 4.9 further expands the self-sensing scheme to MIMO piezoelectric shells with the validated model, and investigates the shape stability of a large, two electrode curved active shell.

4.3 Vibration Induced Sensing Signal of Piezoelectric Unimorph Structures

This section introduces the the analytical model for the simplest class of self-sensing structures, which is a cantilever beam bonded to a thin and narrow piezoelectric strip. The unimorph beam is assumed to be excited by both an input electric field and a mechanical disturbance at the base. The goal of the following analyses is to gain understanding of the electric signal feedback from the piezoelectric layer due to the excitations from both sources.

4.3.1 Governing Equations

For a fixed-end cantilever beam attached to a surface parallel length-wise piezoelectric actuator, as shown in figure 4.5, the equation of motion is [147]:

$$\frac{\partial^2 M(x,t)}{\partial x^2} + c_a \frac{\partial w_{rel}(x,t)}{\partial t} + m \frac{\partial^2 w_{rel}(x,t)}{\partial t^2} = -m \frac{\partial^2 w_b(t)}{\partial t^2} - c_a \frac{\partial w_b(t)}{\partial t} \tag{4.6}$$

$M(x,t)$ is the internal bending moment, w_{rel} is the relative deformation of the beam with respect to the fixed end, and the base displacement is w_b. The terms on the right hand side are related to the inertial loading term $w_b(t)$.

The elastic constitutive equation of the piezoelectric layer:

$$T_1^p = Y_p(S_1^p - d_{31}E_3) \tag{4.7}$$

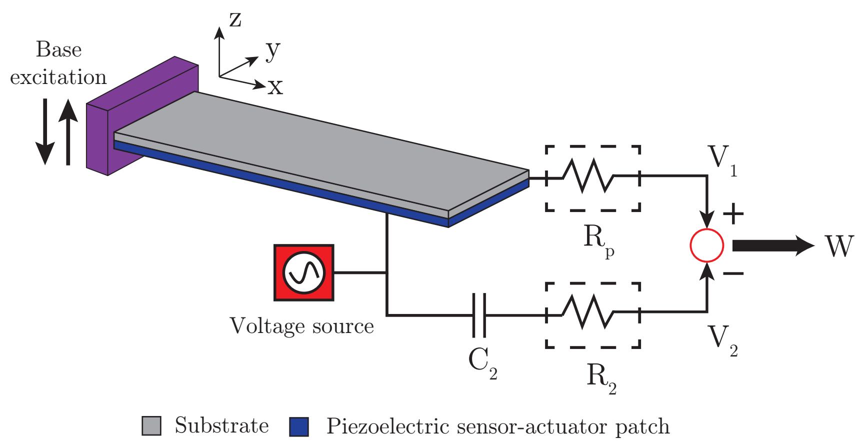

Figure 4.5: A self-sensing cantilever beam connected to a resistor bridge circuit with fixed component values. Dotted square around the resistor symbol represents the trans-impedance circuit with op-amp. W is the sensing signal.

where T_1^p is the in-plane stress of the layer. The internal bending moment $M(x,t)$ is:

$$\begin{aligned} M(x,t) = &\int_{h_a}^{h_b} Y_s b \frac{\partial^2 w_{rel}(x,t)}{\partial x^2} y^2 dy + \int_{h_b}^{h_c} Y_p b \frac{\partial^2 w_{rel}(x,t)}{\partial x^2} y^2 dy \\ &- \int_{h_b}^{h_c} U(t) Y_p b \frac{d_{31}}{h_p} y dy \end{aligned} \tag{4.8}$$

where h_p is the thickness of the piezo layer, b is the width of the beam, h_a, h_b, h_c are the positions from bottom of the substrate, bottom of the piezoelectric layer, and top of the piezoelectric layer to the neutral axis. $U(t)$ is the applied voltage over piezoelectric layer. Y_s and Y_p are the elastic modulus of the substrate and piezoelectric material. Equation 4.8 can be simplified to:

$$M(x,t) = YI \frac{\partial^2 w_{rel}(x,t)}{\partial x^2} + \vartheta U(t) \tag{4.9}$$

and $YI = b\left[\dfrac{Y_s(h_b^3 - h_a^3) + Y_p(h_c^3 - h_b^3)}{3}\right]$ is the equivalent bending inertial. The coupling term ϑ is $\vartheta = -\dfrac{Y_p d_{31} b}{2h_p}(h_c^3 - h_b^3)$. Then the governing equation can be reformulated as:

$$YI \frac{\partial^4 w_{rel}(x,t)}{\partial x^4} + c_a \frac{\partial w_{rel}(x,t)}{\partial t} + m \frac{\partial^2 w_{rel}(x,t)}{\partial t^2} + \vartheta U(t) = -m \frac{\partial^2 w_b(t)}{\partial t^2} - c_a \frac{\partial w_b(t)}{\partial t} \tag{4.10}$$

Equation 4.10 describes the relative motion of the beam with respect to the fixed end. It can be solved through a modal expansion of the beam, and time convolution integral of the forcing terms $U(t)$ and $w_b(t)$. The detailed solution steps were documented by Erturk and Inman [147].

4.3.2 Governing Equation of Sensing Voltage

The constitutive equation for the piezoelectric layer, considering the nonlinear dielectric response, is:

$$D_3 = d_{31}T_1 + \varepsilon_{33}^T E_3 + P^r \tag{4.11}$$

ε_{33}^T is the permittivity at constant stress, and P^r is the remnant polarization term defined in chapter 3. In general, P^r depends on both the frequency and the amplitude of the applied voltage:

$$P^r = P^r(v(f, V_0)) \tag{4.12}$$

where f and V_0 are the frequency and amplitude of the applied voltage. The $P_r - v(f, V_0)$ relation can be determined experimentally. Let h_{pc} be the distance between the center of the piezoelectric layer to the neutral axis, then $S_1(x,t) = -h_{pc}\dfrac{\partial^2 w_{rel}(x,t)}{\partial x^2}$, so:

$$D_3(x,t) = -d_{31}Y_p h_{pc}\frac{\partial^2 w_{rel}(x,t)}{\partial x^2} + \varepsilon_{33}^T\frac{U(t)}{h_p} + P^r \tag{4.13}$$

The total charge generated under base excitation and applied voltage is then:

$$q(t) = \int_A \mathbf{D}\cdot\mathbf{n}dA = \int_0^l \left(-d_{31}Y_p b h_{pc}\frac{\partial^2 w_{rel}(x,t)}{\partial x^2} + \varepsilon_{33}^T\frac{U(t)}{h_p} + P^r\right)dx \tag{4.14}$$

where $\mathbf{D}$ is the electric displacement vector. The total current generated is then:

$$i(t) = \frac{dq(t)}{dt} = \underbrace{-\int_0^l d_{31}Y_p b h_{pc}\frac{\partial^3 w_{rel}(x,t)}{\partial x^3}dx}_{I_1} + \underbrace{\varepsilon_{33}^T bL\frac{dU(t)}{h_p dt}}_{I_2} + \underbrace{bL\dot{P}^r}_{I_3} \tag{4.15}$$

Regarding the three terms I_1, I_2, and I_3:

- I_1 is the vibration induced sensing signal, related to the relative motion of the beam with respect to the base.
- I_2 is the linear dielectric response of the piezoelectric layer under the electric field.
- I_3 is the nonlinear dielectric response of the piezoelectric layer under the electric field.

Since the linear capacitance of the piezoelectric layer is related to the linear part of the dielectric property ε_{33}^{T}:

$$C_p^{linear} = \frac{\varepsilon_{33}^{S} bL}{h_p} \tag{4.16}$$

then the term $bL\dot{P}^r$ can be used to define the nonlinear capacitance of the piezoelectric layer:

$$C_p^{nonlinear} \cdot U(t) = bL\dot{P}^r(U(t)) \tag{4.17}$$

Here P^r not only depends on $U(t)$, but it is also history dependent as discussed in chapter 3. When the piezoelectric layer is connected to a sensing resistor R_p, the voltage signal is then expressed as;

$$V_1 = R_p(I_1 + I_2 + I_3) \tag{4.18}$$

4.3.3 The Modified Circuit Balance Condition of Resistor Bridge Circuit

Considering the nonlinear component of the dielectric response of the piezoelectric layer, the circuit balance condition represented by equation 4.1 needs to be reformulated as follows:

$$R_p \cdot (C_p^{linear} + C_p^{nonlinear}) = R_2 \cdot C_2 \tag{4.19}$$

The final voltage output of the resistor bridge circuit under the condition above is then:

$$\begin{aligned} W &= V_1 - V_2 \\ &= R_p I_1 = -R_p \int_0^l d_{31} Y_p b h_{pc} \frac{\partial^3 w_{rel}(x,t)}{\partial x^3} dx \end{aligned} \tag{4.20}$$

W is only related to the dynamic response of the beam w_{rel}. In order to satisfy condition 4.19, different strategies can be taken. This chapter chooses the strategy to adjust the value of R_2 adaptively, and the details will be given in section 4.7.

4.4 Discretized Dynamic Model from Finite Element for Self-Sensing Vibration Control

Although analytical solutions to equation 4.10 are useful to obtain fundamental understanding of the dynamics of piezoelectric structures and influence of the nonlinear dielectric response on the output sensing signal, constructing similar models for curved thin shell structures with complex piezoelectric layer topology can be a daunting task. The finite element modeling method provides a universal framework for solving electromechanically coupled systems. However, the majority of the literature employing finite element models for piezoelectric thin shell structures have developed customized FEM codes from bottom up, which usually handle simple geometries exclusively and have limited functionalities [148]. This section proposes an efficient and precise modeling technique for general piezoelectric thin shell structures based on the output of the commercial multi-field finite element software Abaqus and its inherent thin shell element library. The technique is derived based upon the linear piezoelectric constitutive relations; however, it can be further extended to incorporate the nonlinear piezoelectric material models like the one characterized in the previous chapter.

4.4.1 Constitutive Model of the Piezoelectric Materials

The following two sections present the fundamentals of the electromechanically-coupled dynamics of piezoelectric structures to facilitate the understanding of the numerical modeling techniques presented later [149]. The linear constitutive relation of the sensor and actuator operation mode of piezoelectric structures is commonly written as follows:

$$\begin{aligned} \boldsymbol{\varepsilon} &= \boldsymbol{s}^{\boldsymbol{E}}\boldsymbol{\sigma} + \boldsymbol{d}^{\boldsymbol{T}}\boldsymbol{E} \\ \boldsymbol{D} &= \boldsymbol{d}\boldsymbol{\sigma} + \boldsymbol{\epsilon}^{\boldsymbol{\sigma}}\boldsymbol{E} \end{aligned} \tag{4.21}$$

Here $\boldsymbol{s}^{\boldsymbol{E}}$ is the elastic compliance constant matrix of the material, $\boldsymbol{d}$ is the electro-mechanical coupling coefficient matrix, $\boldsymbol{E}$ is the applied electric field vector, $\boldsymbol{\varepsilon}^{\boldsymbol{\sigma}}$ is the dielectric constant matrix under constant stress, $\boldsymbol{D}$ is the electric displacement vector, and $\boldsymbol{\sigma}$ is the stress vector. An equivalent formulation essential for the derivation of finite element model is written in terms of strain and electric field:

$$\begin{aligned} \boldsymbol{\sigma} &= \boldsymbol{c}^{\boldsymbol{E}}\boldsymbol{\varepsilon} - \boldsymbol{e}\boldsymbol{E} \\ \boldsymbol{D} &= \boldsymbol{e}\boldsymbol{\varepsilon} + \boldsymbol{\epsilon}^{\boldsymbol{\varepsilon}}\boldsymbol{E} \end{aligned} \tag{4.22}$$

$\boldsymbol{c}^{\boldsymbol{E}}$ is the elastic stiffness matrix of the material. The electric field-stress coupling matrix $\boldsymbol{e}$, and the dielectric coefficient matrix are defined under the condition of constant strain, and have the following forms:

$$\begin{aligned} \boldsymbol{e} &= \boldsymbol{d}\boldsymbol{c}^{\boldsymbol{E}} \\ \boldsymbol{\epsilon}^{\boldsymbol{\varepsilon}} &= \boldsymbol{\epsilon}^{\boldsymbol{\sigma}} - \boldsymbol{d}\boldsymbol{c}^{\boldsymbol{E}}\boldsymbol{d}^{\boldsymbol{T}} \end{aligned} \tag{4.23}$$

The following derivations define the 3^{rd} direction as the thickness direction, and assume that it is the direction of spontaneous polarization of the piezoelectric material. Then the general form of material property matrix defined above have the following forms:

$$\boldsymbol{\sigma}^T = \begin{bmatrix} \sigma_1 & \sigma_2 & \sigma_3 & \sigma_4 & \sigma_5 & \sigma_6 \end{bmatrix} \tag{4.24}$$

$$\boldsymbol{D}^T = \begin{bmatrix} D_1 & D_2 & D_3 \end{bmatrix} \tag{4.25}$$

$$\boldsymbol{\varepsilon}^T = \begin{bmatrix} \varepsilon_1 & \varepsilon_2 & \varepsilon_3 & \varepsilon_4 & \varepsilon_5 & \varepsilon_6 \end{bmatrix} \tag{4.26}$$

$$\boldsymbol{c}^E = \begin{bmatrix} c_{11}^E & c_{12}^E & c_{13}^E & 0 & 0 & 0 \\ c_{21}^E & c_{22}^E & c_{23}^E & 0 & 0 & 0 \\ c_{31}^E & c_{32}^E & c_{33}^E & 0 & 0 & 0 \\ 0 & 0 & 0 & c_{44}^E & 0 & 0 \\ 0 & 0 & 0 & 0 & c_{44}^E & 0 \\ 0 & 0 & 0 & 0 & 0 & c_{66}^E \end{bmatrix} \tag{4.27}$$

$$\boldsymbol{d} = \begin{bmatrix} 0 & 0 & 0 & 0 & d_{15} & 0 \\ 0 & 0 & 0 & d_{15} & 0 & 0 \\ d_{31} & d_{31} & d_{33} & 0 & 0 & 0 \end{bmatrix} \tag{4.28}$$

$$\boldsymbol{\epsilon}^\sigma = \begin{bmatrix} \epsilon_{11}^\sigma & 0 & 0 \\ 0 & \epsilon_{22}^\sigma & 0 \\ 0 & 0 & \epsilon_{33}^\sigma \end{bmatrix} \tag{4.29}$$

4.4.2 Finite Element Discretization of the Piezoelectric Electro-mechanical System

This section formulates the governing equation for a general, active thin shell structure bonded with a piezoelectric layer, using the Rayleigh-Ritz method [140]. The generalized form of Hamilton's principle for a piezoelectric active structure system is written as:

$$\int_{t_1}^{t_2} \partial \left[K_E - U_P + W_e + W_f \right] dt = 0 \tag{4.30}$$

Here K_E and U_P are the kinetic and potential energy, W_e is the electrical energies, W_f is the work of non-conservative forces. The energies can be expressed as follows:

$$K_E = \int_{V_s} \frac{1}{2} \rho_s \dot{\boldsymbol{u}}^T \dot{\boldsymbol{u}} dV + \int_{V_p} \frac{1}{2} \rho_p \dot{\boldsymbol{u}}^T \dot{\boldsymbol{u}} dV \tag{4.31}$$

$$U_P = \int_{V_s} \frac{1}{2}\rho_s \boldsymbol{\varepsilon}^T \boldsymbol{\sigma} dV + \int_{V_p} \frac{1}{2}\rho_p \boldsymbol{\varepsilon}^T \boldsymbol{\sigma} dV \tag{4.32}$$

$$W_e = \int_{V_p} \frac{1}{2}\boldsymbol{E}^T \boldsymbol{D} dV \tag{4.33}$$

$$W_f = \int_{V_s} \boldsymbol{u}^T \boldsymbol{f} dV + \int_{V_p} \boldsymbol{u}^T \boldsymbol{f} dV - \int_{v_p} \varphi q dV \tag{4.34}$$

The subscript s denotes the substrate structure, subscript p denotes the piezoelectric sensor-actuator. ρ represents the material density, $\boldsymbol{u}$ is the mechanical displacement (translation and rotation), $\boldsymbol{f}$ is the vector of applied force, φ is the electrical potential scalar, and q is the charge applied to the piezoelectric material.

Define the rotation matrices $\boldsymbol{R}_s$ and $\boldsymbol{R}_E$ as the transformation matrices between the local and global coordinate system:

$$\begin{aligned} \boldsymbol{\varepsilon}' &= \boldsymbol{R}_s \boldsymbol{\varepsilon} \\ \boldsymbol{E}' &= \boldsymbol{R}_E \boldsymbol{E} \end{aligned} \tag{4.35}$$

Through the transformation, the constitutive equation of the piezoelectric material is:

$$\begin{bmatrix} \boldsymbol{D} \\ \boldsymbol{\sigma} \end{bmatrix} = \begin{bmatrix} \boldsymbol{R}_E^T \boldsymbol{\epsilon}^s \boldsymbol{R}_E & \boldsymbol{R}_E^T \boldsymbol{e} \boldsymbol{R}_s \\ -\boldsymbol{R}_s^T \boldsymbol{e}^T \boldsymbol{R}_E & \boldsymbol{R}_s^T \boldsymbol{c}^E \boldsymbol{R}_s \end{bmatrix} \begin{bmatrix} \boldsymbol{E} \\ \boldsymbol{\varepsilon} \end{bmatrix} \tag{4.36}$$

Constitutive equation for the structure is:

$$\boldsymbol{\sigma} = \boldsymbol{c}^s \boldsymbol{\varepsilon} \tag{4.37}$$

$\boldsymbol{c}^S$ is the elastic matrix of the substrate material. Under the assumption of small deflection, the strain-displacement relation is:

$$\boldsymbol{\varepsilon} = \boldsymbol{L}_u \boldsymbol{u} \tag{4.38}$$

L_u is the linear differential operator for the geometry under study. The electric field-potential relation is:

$$E = -\nabla\varphi \tag{4.39}$$

The electric potential φ of the piezoelectric layer can be expressed as:

$$\varphi = \Psi_u U \tag{4.40}$$

here U is the voltage applied on the electrodes of the piezoelectric layer, and Ψ_u represents the spatial distribution of the electric potential within the layer.

4.4.3 Weak form of Hamilton's Principle

By substituting the equations 4.31 to 4.39 into equation 4.30 leads to the following weak form for the electro-mechanical system [149]:

$$\int_{t_1}^{t_2}\Big[\int_{V_s}\rho_s\delta\dot{\boldsymbol{u}}^T\dot{\boldsymbol{u}}dV+\int_{V_p}\rho_p\delta\dot{\boldsymbol{u}}^T\dot{\boldsymbol{u}}dV-\int_{V_s}\delta\boldsymbol{\varepsilon}^T\boldsymbol{c}^E\boldsymbol{\varepsilon}-\int_{V_p}\delta\boldsymbol{\varepsilon}^T\boldsymbol{R}_s^T\boldsymbol{c}^E\boldsymbol{R}_s\boldsymbol{\varepsilon}dV \\ +\int_{V_p}\delta\boldsymbol{\varepsilon}^T\boldsymbol{R}_s^T\boldsymbol{e}^T\boldsymbol{R}_E\boldsymbol{E}dV+\int_{V_p}\delta\boldsymbol{E}^T\boldsymbol{R}_E^T\boldsymbol{e}\boldsymbol{R}_s\boldsymbol{\varepsilon}+\int_{V_p}\delta\boldsymbol{E}^T\boldsymbol{R}_E^T\boldsymbol{\epsilon}^{\varepsilon}\boldsymbol{R}_E\boldsymbol{E}dV \\ +\int_{V_s}\delta\boldsymbol{u}^T\boldsymbol{f}dV+\int_{V_p}\delta\boldsymbol{u}^T\boldsymbol{f}dV-\int_{v_p}\delta\varphi q dV\Big]dt=0 \tag{4.41}$$

Define the mass matrices:

$$\boldsymbol{M}_s=\int_{V_s}\boldsymbol{\Psi}^T\rho_s\boldsymbol{\Psi}dV \quad \boldsymbol{M}_p=\int_{V_p}\boldsymbol{\Psi}^T\rho_p\boldsymbol{\Psi}dV \tag{4.42}$$

and the stiffness matrices:

$$\boldsymbol{K}_s=\int_{V_s}\boldsymbol{N}_r^T\boldsymbol{c}^s\boldsymbol{N}_r dV \quad \boldsymbol{K}_p=\int_{V_p}\boldsymbol{N}_r^T\boldsymbol{R}_s^T\boldsymbol{c}^p\boldsymbol{R}_s\boldsymbol{N}_r dV \tag{4.43}$$

$\boldsymbol{\Psi}$ is the array of interpolating functions. When the modeling approach is the finite element method, i.e.:

$$\boldsymbol{u}=\boldsymbol{\Psi}_n\boldsymbol{u}^n \tag{4.44}$$

$\boldsymbol{u}^n$ is the vector of nodal degree of freedoms. When the modeling approach is modal expansion,

$$\boldsymbol{u}=\boldsymbol{\Psi}_r\boldsymbol{u}^r \tag{4.45}$$

$\boldsymbol{u}^r$ is the vector of modal coordinates. The electro-mechanical coupling matrix is defined as:

$$\boldsymbol{\Theta}=\int_{V_p}\boldsymbol{N}_r^T\boldsymbol{R}_s^T\boldsymbol{e}^T\boldsymbol{R}_E\boldsymbol{N}_u dV \tag{4.46}$$

or:

$$\boldsymbol{\Theta}=\int_{V_p}\boldsymbol{N}_n^T\boldsymbol{R}_s^T\boldsymbol{e}^T\boldsymbol{R}_E\boldsymbol{N}_u dV \tag{4.47}$$

Here $\boldsymbol{N}_r=\boldsymbol{L}_u\boldsymbol{\Psi}_r$, $\boldsymbol{N}_n=\boldsymbol{L}_u\boldsymbol{\Psi}_n$ and $\boldsymbol{N}_u=\boldsymbol{L}_\varphi\Psi_u$. $\boldsymbol{L}_u$ is the strain-displacement differential operator and $\boldsymbol{L}_\varphi$ is the field-potential differential operator. The electro-mechanical coupling matrix $\mathbf{\Theta}$ converts the voltage applied to the piezoelectric layer to the nodal displacement of the discretized structure; in reverse, the deflection of structure will induce charge feedback due to the inverse piezoelectric effect.

In sum, the dynamics model of a piezoelectric activated structure can be written in general as:

$$\begin{aligned} \boldsymbol{M}\ddot{\boldsymbol{r}} + \boldsymbol{\Delta}\dot{\boldsymbol{r}} + \boldsymbol{K}\boldsymbol{r} - \boldsymbol{\Theta}\boldsymbol{U} &= \boldsymbol{B}^f \boldsymbol{f} \\ \boldsymbol{\Theta}^T \boldsymbol{r} + \boldsymbol{C}_p \boldsymbol{U} &= \boldsymbol{B}^q \boldsymbol{q} \end{aligned} \tag{4.48}$$

where $\boldsymbol{M} = \boldsymbol{M}_s + \boldsymbol{M}_p \in \mathbb{R}^{m\times m}$, and $\boldsymbol{K} = \boldsymbol{K}_s + \boldsymbol{K}_p \in \mathbb{R}^{m\times m}$. m is the total mechanical DOF of the discretized structure. The first equation is the electromechanically coupled structural dynamics equation, and the second equation is referred to as the sensing equation. Here $\boldsymbol{r} \in \mathbb{R}^m$ represents the nodal degree of freedom of the finite element discretization, or the modal degree of freedom depending on the choice of modeling approach. Under the assumption of small displacement, $\boldsymbol{M}$ and $\boldsymbol{K}$ are not functions of $\boldsymbol{r}$. The vector $\boldsymbol{q} \in \mathbb{R}^n$ is the generalized charge vector which comes from the direct piezoelectric effect. n is the number of electrodes of the structure. $\boldsymbol{B}^f \in \mathbb{R}^{m\times l}$ is the forcing matrix and $\boldsymbol{B}^q \in \mathbb{R}^{n\times n}$ is the sensing matrix. Here l is number of external mechanical loading on the structure. Define $\boldsymbol{U} \in \mathbb{R}^n$ as the physical voltage applied to each electrode. Under this definition, $\boldsymbol{C}_p \in \mathbb{R}^n$ are the capacitances of each individual piezoelectric sensor-actuator patch, and $\boldsymbol{B}^q = \boldsymbol{I}$.

To establish $\boldsymbol{B}^f$, a quasi-static 'calibration' step is defined in the finite element simulation, in which a unit amplitude loading $\boldsymbol{f} = \boldsymbol{I}$ is applied to all the nodes in the system. $\boldsymbol{B}^f$ is then calculated from the nodal displacements and the stiffness matrix:

$$\boldsymbol{K}\boldsymbol{r}_{calibration} = \boldsymbol{B}^f \tag{4.49}$$

where $r_{calibration}$ is the nodal displacement vector under unit loading. The strategy to establish the electro-mechanical coupling matrix $\boldsymbol{\Theta} \in \mathbb{R}^{m\times n}$ for general types of linear piezoelectric sensor-actuators is the core of the proposed fast-modeling method. An efficient way to estimate $\boldsymbol{\Theta}$ that circumvents the usage of high-order piezoelectric elements provided by the commercial software is presented in the following content.

4.4.4 Thermal Expansion Analogy of the Piezoelectric Coupling Matrix

An important property of the governing equations 4.48 is the transpose relation of the electro-mechanical coupling matrix $\boldsymbol{\Theta}$. This section makes use of this feature to obtain the complete set of governing equations with a thermal expansion analogous model built in the commercial FEM software Abaqus. The method developed allows easy and quick establishment of the coupling matrix of complicated piezoelectric thin structures with general topology, and is a further extension of the method used by Laslandes, Pellegrino, Steeves, *et al.* [150] to find the influence functions of a multi-electrode active mirror.

In the unimorph operation mode, among the 5 electro-mechanical coupling coefficients in equation 4.28, only d_{31} and d_{32} are of interest, because they the sources of distributed bending moments. For thin shell structures, the normal stress component σ_{33} can also be neglected, thus the electromechanical coupling matrix $\boldsymbol{d}$ can be simplified to:

$$\boldsymbol{d} = \begin{bmatrix} 0 & 0 & 0 & 0 & 0 & 0 \\ 0 & 0 & 0 & 0 & 0 & 0 \\ d_{31} & d_{32} & 0 & 0 & 0 & 0 \end{bmatrix} \tag{4.50}$$

For a piece of piezoelectric actuator operating in transverse actuation mode with thickness t, the equivalent thermal expansion coefficient of the corresponding 'pseudo' material is:

$$T \cdot \alpha = \frac{U}{t} \cdot d_{3i} \tag{4.51}$$

here $i = 1, 2$, T is the temperature change of the 'pseudo' material defined in Abaqus, and U is the voltage applied to the piezoelectric material it represents. Thus α represents the equivalent change of in-plane strain of the 'pseudo' material in simulation, when a unit voltage is applied to the physical piezoelectric material. To obtain the coupling matrix $\boldsymbol{\Theta}$ through the thermal analogy, a quasi-static calibration step is set up in Abaqus during which a unit temperature change is applied to the simulated sensor-actuator layer. Assume the piezoelectric material is in-plane isotropic ($d_{31} = d_{32}$) and has only one conductive electrode on both sides (U is constant over the whole sensor-actuator):

$$\begin{aligned} \boldsymbol{Kr} &= \boldsymbol{\Theta U}_{unit} \\ &= \boldsymbol{\Theta T}_{unit} \cdot \frac{\alpha t}{d_{31}} \\ \Rightarrow \boldsymbol{\Theta} &= \boldsymbol{Kr} \cdot \frac{d_{31}}{\alpha t} \end{aligned} \tag{4.52}$$

For multi-electrode active structures, the derivations follow a similar path, and the calibrations need to be performed on each single piezoelectric patch which is connected through a common electrode.

The advantage of the proposed simulation technique is that the thin shell elements can be employed to construct the structural model, which is not yet compatible with the piezoelectric constitutive model in the latest version of Abaqus/Standard. In this way, the overall model order is greatly reduced compared to the alternative of modeling with high order, multi-node brick elements defined with the complete piezoelectric constitutive relations at all the elemental integration points. The technique can be easily adapted to work with other finite element software packages.

4.4.5 From Finite Element Model to System Dynamics

In order to convert the system dynamics equation 4.48 into the state space form:

$$\begin{aligned} \dot{\boldsymbol{\xi}} &= \boldsymbol{A}\boldsymbol{\xi} + \boldsymbol{B}_f \boldsymbol{f} + \boldsymbol{B}_u \boldsymbol{U} \\ \boldsymbol{\chi} &= \boldsymbol{C}\boldsymbol{\xi} + \boldsymbol{D}_f \boldsymbol{f} + \boldsymbol{D}_u \boldsymbol{U} \end{aligned} \tag{4.53}$$

the state vector $\boldsymbol{\xi}$ is defined as the nodal displacement and velocity (including both translational and rotational degree of freedom):

$$\boldsymbol{\xi} = \begin{bmatrix} \boldsymbol{r} \\ \dot{\boldsymbol{r}} \end{bmatrix} \tag{4.54}$$

The state matrix $\boldsymbol{A}$ and forcing matrix $\boldsymbol{B}$ are defined as:

$$\begin{aligned} \boldsymbol{A} &= \begin{bmatrix} 0 & \boldsymbol{I} \\ -\boldsymbol{M}^{-1}\boldsymbol{K} & -\boldsymbol{M}^{-1}\boldsymbol{\Delta} \end{bmatrix} \\ \boldsymbol{B}_f &= \begin{bmatrix} 0 \\ \boldsymbol{M}^{-1}\boldsymbol{B}^f \end{bmatrix} \\ \boldsymbol{B}_u &= \begin{bmatrix} 0 \\ \boldsymbol{M}^{-1}\boldsymbol{\Theta} \end{bmatrix} \end{aligned} \tag{4.55}$$

The observation matrices $\boldsymbol{C}$ and $\boldsymbol{D}$ for self-sensing structures depend on the choice of observed variables and the signal condition circuit, and will be defined and analyzed in section 4.7. The remaining unknown variable within the matrices 4.55 is the material damping matrix $\boldsymbol{\Delta}$. It has to be calibrated experimentally and a characterization is performed in section 4.8 on the tested samples.

A potential pitfall of the method comes from the boundary condition handling. The finite element software usually enforce the fixed boundary conditions by assigning large real numbers (typically on the order of 10^8) to the corresponding entries of the stiffness matrix $\boldsymbol{K}$. Rows and columns containing the boundary nodes need to be removed during matrix operations.

4.5 Closed-loop Active Damping Simulation of Unimorph Cantilever Beam

To demonstrate the modeling technique, the following simulations are based upon a single-electrode cantilever beam. The materials and thicknesses of the self-sensing cantilever beam's components studied in this chapter are shown in figure 4.6a. The substrate is made from 6061-aluminum, and the bonding epoxy is made of Epotek-301. The PZT-5A sensor-actuator layer covers one side of the beam. All three layers are considered in the finite element modeling. Physical samples with exactly the same geometry shown in figure 4.6a will be manufactured and tested later, and model validations will be presented in section 4.8.

4.5.1 Finite Element Model Setup

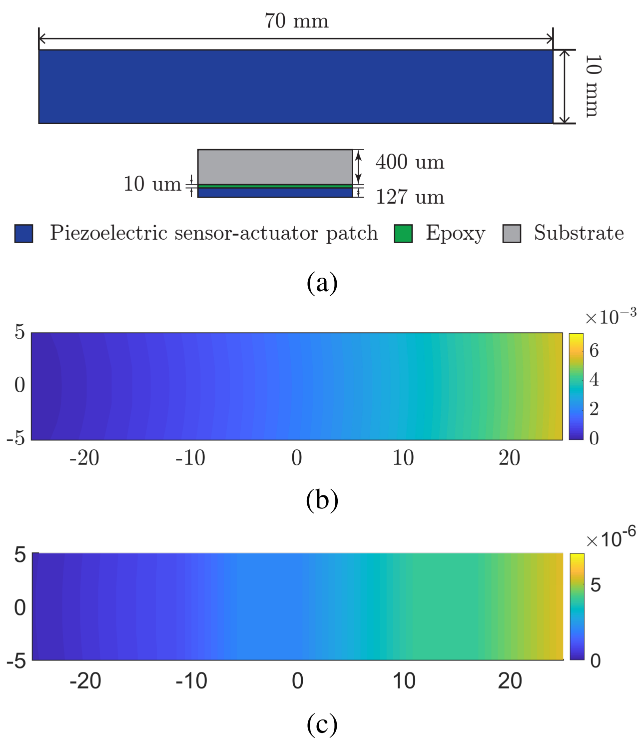

Figure 4.6: (a) Top view and cross section view of the simulated beam. The substrate and the piezoelectric layers are bonded by a thin layer of epoxy with $10\mu m$ thickness. (b) Cantilever beam out of plane response from equivalent thermal actuation simulation. (c) Simulated out of plane response under base acceleration. Units in mm.

Following the modeling procedure described in section 4.4, K and M are obtained directly from quasi-static analyses from Abaqus/Standard. $\boldsymbol{\Theta}$ and $\boldsymbol{B}_f$ are calculated indirectly by outputting the deformed shape from both the thermal actuation step and the acceleration loading step. The finite element model shown in figure 4.6b and 4.6c consists of 18 eight-node quadratic thin shell elements with reduced integration, in total 73 nodes. Each node has 3 translational and 3 rotational degrees of freedom, adding up to 438 degrees of freedom. The resulted $\boldsymbol{A}$ matrix has an order of 876.

For larger dimension models, model degree of freedom will grow exponentially and may create enormous computational burden and greatly elongates the simulation time. It is then necessary to reduce the model order while preserving the dynamics of the full model, within the range of the bandwidth of interest.

4.5.2 Order Reduction of Discretized FEM Model

The system dynamics can be truncated through Hankel singular value decomposition [151]. The algorithm generates a reduced model with bounded error:

$$\|G - G_{red}\|_{\infty} \leq 2 \sum_{n+1}^{n} \sigma_i \tag{4.56}$$

The norm depends on the 'tails' of the Hankel singular values σ_i of the system. The model reduction toolbox in MATLAB was used to reduce the model order from an initial value of 876 down to 10. Figure 4.7a and figure 4.7b below compare the bode plots of the tip node displacement excited by base acceleration and voltage input, before and after model reduction. By comparison, the reduced order model produces exactly the same frequency and phase response within the bandwidth of 50 ~ 120 Hz. It took less than 1 s CPU time to calculate the time history of the reduced dynamic model for 1 s simulation time on a laptop. An alternative technique to reducing the system order and obtaining diagonal $\boldsymbol{M}$, $\boldsymbol{K}$ and $\boldsymbol{\Delta}$ matrices is through a modal transformation which leads to a decoupled system description. Details of this technique can be found in [152] and will not be used here.

4.5.3 Closed-loop Active Damping System Dynamics

For a resistor-based sensing circuit (figure 4.8), the output signal W depends on the strain rate of the sensor-actuator patch:

$$V_1 = -R_p(C_p\dot{U} + \boldsymbol{\Theta}^T \cdot \dot{\boldsymbol{r}}) \tag{4.57}$$

Here U is the voltage applied to the actuator from the real time controller after amplification, W is the feedback voltage from the bridge circuit. The observed variable χ is defined as the chosen nodal displacements and sensing voltage output of the circuit:

$$\chi = \begin{bmatrix} \boldsymbol{r} \\ W \end{bmatrix} \tag{4.58}$$

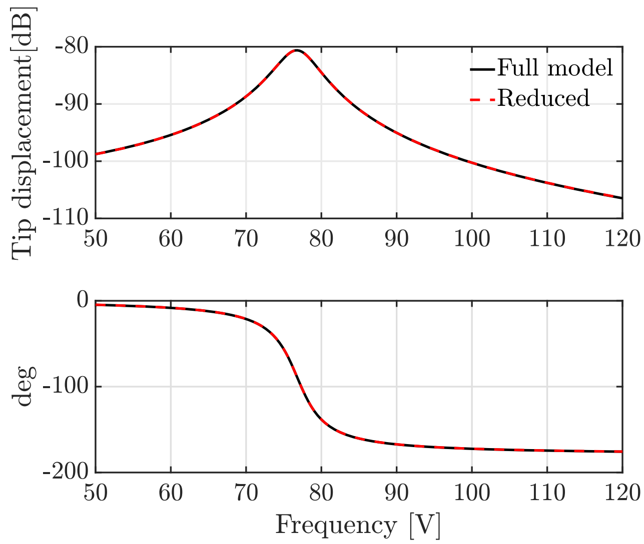

(a)

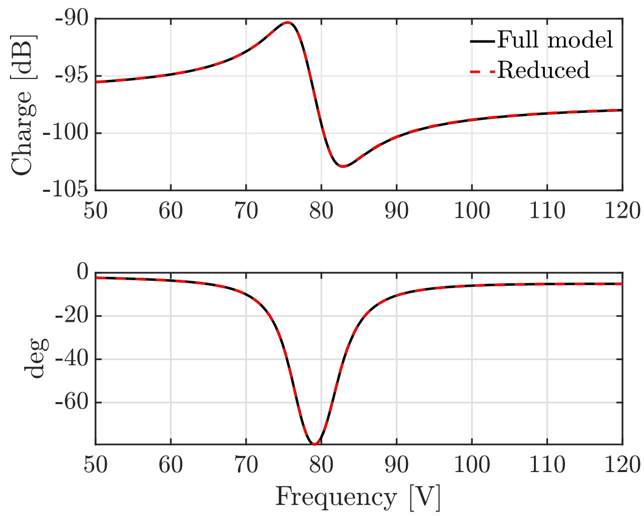

(b)

Figure 4.7: (a) Tip node displacement spectrum comparison between full (876 DOF) and truncated (10 DOF) model. (b) Charge response spectrum comparison between full and truncated model.

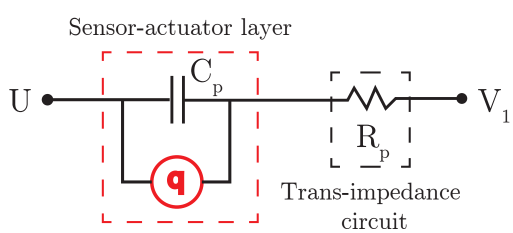

Figure 4.8: Simplified view of the sensor-actuator leg of the bridge circuit.

Under the above definition, the output and feed-forward matrices C and D are defined as follows:

$$\begin{aligned} \boldsymbol{C} &= \begin{bmatrix} C_{node} & \boldsymbol{0} \\ \boldsymbol{0} & -R_p\boldsymbol{\Theta}^T \end{bmatrix} \\ \boldsymbol{D}_f &= \begin{bmatrix} 0 \\ 0 \end{bmatrix} \\ \boldsymbol{D}_U &= \begin{bmatrix} 0 \\ C_p \end{bmatrix} \end{aligned} \tag{4.59}$$

Here an important assumption about the voltage feed-forward term is introduced: the (adaptive) bridge circuit is able to cancel the feedthrough signal $-R_pC_p\dot{U}$ completely (refer to section 4.3 for ideal balanced conditions):

$$\boldsymbol{D}_U = 0 \tag{4.60}$$

In the observation equation, the only remaining term is related to the rate of change of nodal DOF's:

$$V_1 = -R_p\boldsymbol{\Theta}^T\dot{\boldsymbol{r}} \tag{4.61}$$

The same assumption applies to all the closed-loop simulations in this chapter.

Using the proportional feedback as the closed-loop control law, assume:

$$U = GV_1 \tag{4.62}$$

G is the scalar feedback gain for the single-electrode beam considered in this section. The closed-loop dynamical equation can then be re-formulated as:

$$\begin{aligned} \dot{\boldsymbol{\xi}} &= \boldsymbol{A}\boldsymbol{\xi} + \boldsymbol{B}_f f - \boldsymbol{B}_u R_p G\boldsymbol{\Theta}^T\dot{\boldsymbol{r}} \\ \chi &= \boldsymbol{C}\boldsymbol{\xi} \end{aligned} \tag{4.63}$$

4.5.4 Discussion of Closed-loop Stability

The adopted closed-loop control scheme is an implementation of the direct velocity feedback (DVFB), in which the feedback commands based on the velocity sensor output are applied directly to the collocated actuators. Balas [153] first pointed out that the DVFB scheme is guaranteed to be stable regardless of the value of gain G. The proof is adapted for the forced vibration system studied in this section. For a system governed by equation 4.48, define the following energy function:

$$E(t) = \frac{1}{2}\left(\dot{\boldsymbol{r}}^T\boldsymbol{M}\dot{\boldsymbol{r}} + \boldsymbol{r}^T\boldsymbol{K}\boldsymbol{r}\right) \tag{4.64}$$

Time derivative of $E(t)$ is then expressed as:

$$\dot{E}(t) = \dot{\boldsymbol{r}}^T \boldsymbol{M}\ddot{\boldsymbol{r}} + \dot{\boldsymbol{r}}^T \boldsymbol{K}\boldsymbol{r} \tag{4.65}$$

By substituting the system dynamics equation 4.48 and the feedback law 4.62, $\dot{E}(t)$ is reformulated as:

$$\begin{aligned} \dot{E}(t) &= -\dot{\boldsymbol{r}}^T \boldsymbol{\Delta}\dot{\boldsymbol{r}} + \dot{\boldsymbol{r}}^T \boldsymbol{\Theta}\boldsymbol{U} + \dot{\boldsymbol{r}}^T \boldsymbol{B}^f f \\ &= -\dot{\boldsymbol{r}}^T \boldsymbol{\Delta}\dot{\boldsymbol{r}} - GR_p \dot{\boldsymbol{r}}^T \boldsymbol{\Theta}\boldsymbol{\Theta}^T \dot{\boldsymbol{r}} + \dot{\boldsymbol{r}}^T \boldsymbol{B}^f f \\ &= -\dot{\boldsymbol{r}}^T \left(\boldsymbol{\Delta} + GR_p \boldsymbol{\Theta}\boldsymbol{\Theta}^T\right) \dot{\boldsymbol{r}} + \dot{\boldsymbol{r}}^T \boldsymbol{B}^f f \end{aligned} \tag{4.66}$$

Here G and R_p are scalars, and the matrix $\boldsymbol{\Theta}\boldsymbol{\Theta}^T \in \mathbb{R}^{m\times m}$ is positive definite. Thus, when the system has no external input, $f = 0$, the time derivative of the energy of the unforced system $E_{un}(t)$ is:

$$\dot{E}_{un}(t) = -\dot{\boldsymbol{r}}^T \left(\boldsymbol{\Delta} + GR_p \boldsymbol{\Theta}\boldsymbol{\Theta}^T\right) \dot{\boldsymbol{r}} \tag{4.67}$$

Since the damping matrix $\boldsymbol{\Delta} > 0$, and $GR_p\boldsymbol{\Theta}\boldsymbol{\Theta}^T > 0$ for $R_p, G > 0$:

$$\dot{E}_{un}(t) < 0 \tag{4.68}$$

thus $E_{un}(t) \geq 0$ can be chosen as the Lyapunov function of the system. Since $\dot{E}_{un}(t) \leq 0$, the unforced system is asymptotically stable, regardless of the value of G. For the forced vibration system 4.63, the general solution of $\boldsymbol{\xi}$ is:

$$\boldsymbol{\xi}(t) = e^{\boldsymbol{A}_{cl}(t)}\boldsymbol{\xi}(0) + \int_0^t e^{\boldsymbol{A}_{cl}(t-\tau)} \boldsymbol{B}_f f(\tau) d\tau \tag{4.69}$$

here $\boldsymbol{A_{cl}} = \boldsymbol{A} - R_p G \boldsymbol{B}_u \boldsymbol{\Theta}^T$ is the system matrix of the closed-loop system, $\boldsymbol{\xi}(0)$ is the initial condition. Define λ as the minimum absolute value of all the eigenvalue of $\boldsymbol{A_{cl}}$:

$$\lambda_{max}(\boldsymbol{A}_{cl}) = -\lambda \tag{4.70}$$

then if the disturbance is bounded $\|f\| \leq f_{max}$, by the comparison lemma:

$$\lim_{t\to\infty} \|\boldsymbol{\xi}\| \leq \sup_t \frac{\|\boldsymbol{B}_f \dot{f}\|}{\lambda} = \frac{\|\boldsymbol{B}_f \dot{f}_{max}\|}{\lambda} \tag{4.71}$$

Thus $\dot{\boldsymbol{r}}$ is also bounded and the following expression holds:

$$||\dot{\boldsymbol{r}}^T \boldsymbol{B}^f f|| \leq C_1 \tag{4.72}$$

here C_1 is a finite constant.

$$\begin{aligned} \dot{E}(t) &= \dot{E}_{un}(t) + \dot{\boldsymbol{r}}^T \boldsymbol{B}^f f \\ &\leq \dot{E}_{un}(t) + C_1 \end{aligned} \tag{4.73}$$

Equation 4.73 suggests that $E(t) < C_2$, $C_2 = const$. The forced vibration system has bounded-input bounded-output stability [154] regardless of the value of G, if the disturbance is bounded.

4.5.5 Closed-Loop Simulations

The closed-loop response spectrum of the system 4.63 was calculated in MATLAB/Simulink, near the first fundamental frequency of the beam. In the following simulations, the observed node was chosen at the tip of the beam. Figure 4.9 shows the bode plots for the open- and closed-loop responses of the tip node displacement and the feedback voltage signal, under the base acceleration excitation. Responses from two different feedback gains G_1 and G_2 were plotted, and $G_2 > G_1$.

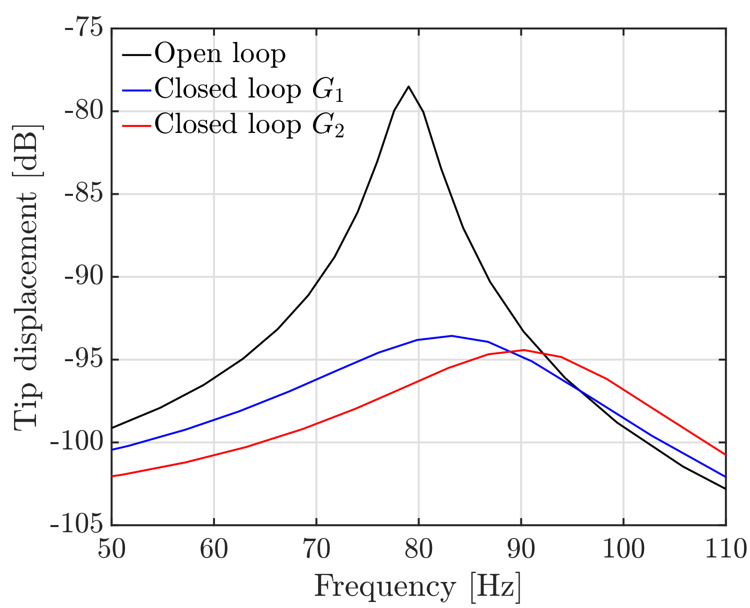

(a)

From the bode plots, the feedback voltage W decreases with the increase of closed loop gain G. However, the closed-loop tip node response r_{tip} remains at the same order of magnitude even if $G_2 \gg G_1$. This is due to the fact that the feedback sensing signal V_1 from a single-electrode piezoelectric layer does not possess observability of r_{tip}; nor does the active layer's topology possess controllability over r_{tip}. This can be illustrated more clearly by the discrepancies between the actuated shape and

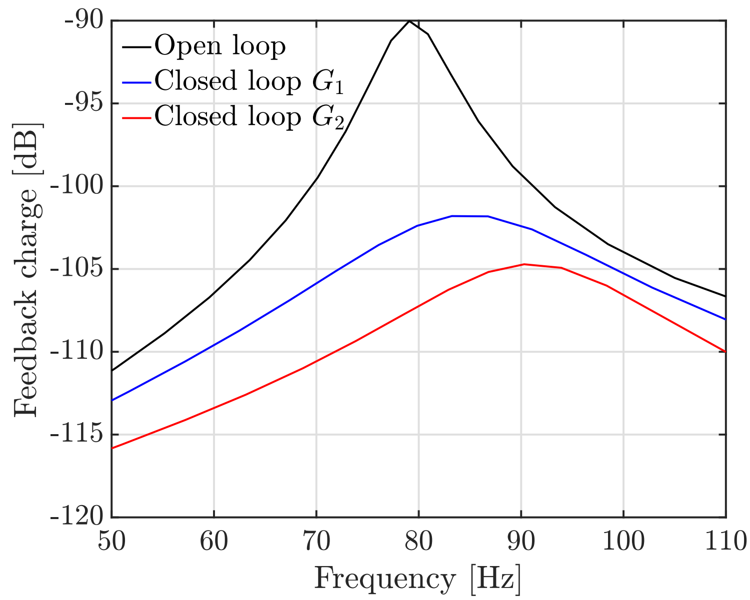

(b)

Figure 4.9: Bode plots for the open- and closed-loop self-sensing beam. Responses are based on two feedback gains $G_2 > G_1$: (a) Bode plot for the displacement of the beam's tip. (b) Bode plot for the feedback voltage.

the first vibration mode shape in figure 4.10. During the closed-loop control around the first fundamental frequency of the beam, the feedback voltage will spill over to higher order vibration modes of the beam.

4.6 Measurement of Piezoelectric Dielectric Hysteresis at High Frequency

From the analysis in section 4.2, a precise estimation of $C_p = C_p^{linear} + C_p^{nonlinear}$ is crucial for the balancing of the bridge circuit, which also justifies the assumption made in the closed-loop system modeling. In this section, the $C_p - U$ relation is measured at various frequencies f_U and amplitudes A_U, and the measurements are conducted through the Active Sawyer-Tower circuit [155] shown in figure 4.11.

Transfer function of the circuit is:

$$\frac{V_{out}}{U} = -\frac{R_M(1 + R_p C_p)}{R_p(1 + R_M C_M)} \tag{4.74}$$

Its main difference compared to a conventional version of the Sawyer-Tower circuit is the introduction of the operational amplifier (op-amp) at the output side. Due to the infinite input impedance of the op-amp, the tested piezoelectric component is linked to the virtual ground. The resulted benefits are: 1) Characterization voltage over the tested piezoelectric component is equal to the input voltage U. 2) The cutoff

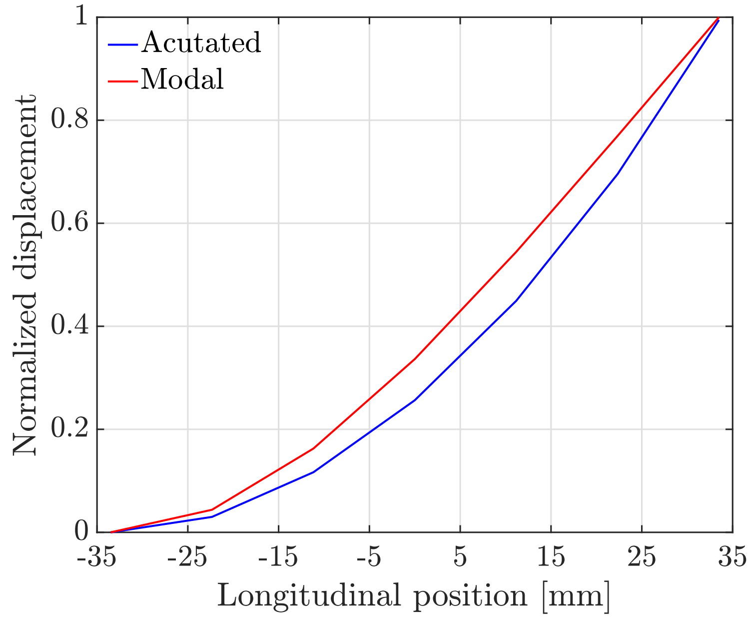

(a)

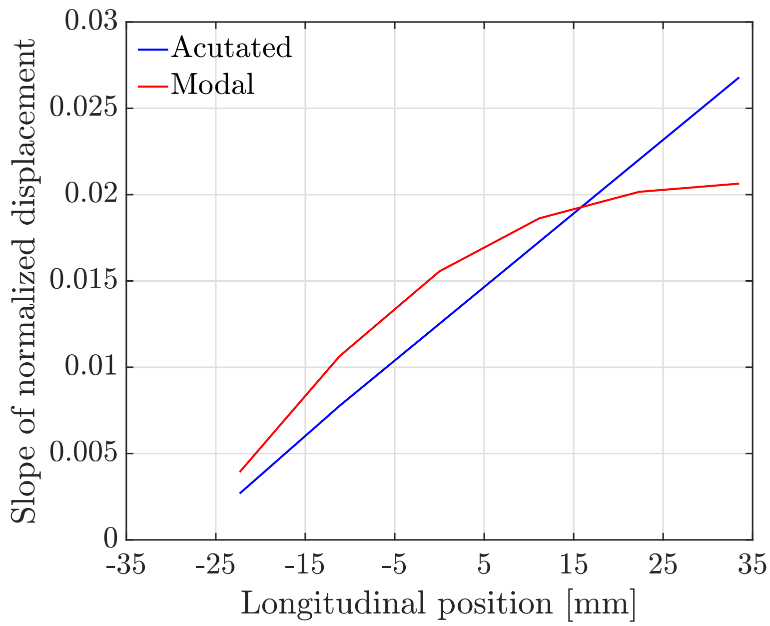

(b)

Figure 4.10: (a) Actuated shape and the first fundamental mode shape of the single-electrode self sensing beam. Amplitudes are normalized by tip displacement. (b) Slope of the normalized displacements from actuated and modal shapes.

frequency of the circuit f_p only depends on the values of the measurement resistor and capacitor R_M and C_M:

$$f_p = \frac{1}{2\pi R_M C_M} \tag{4.75}$$

Thus f_p won't be affected by the nonlinear shift of C_p at different ω_U and A_U values.

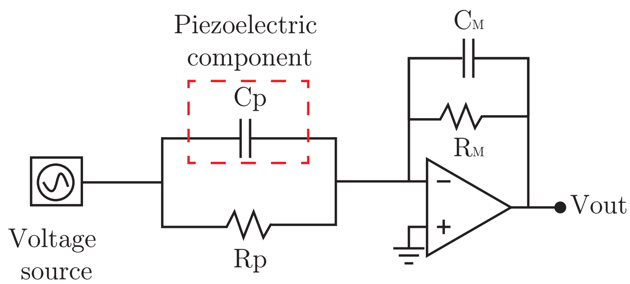

Figure 4.11: The active Sawyer-Tower circuit for high frequency characterization of piezoelectric material. The piezoelectric component is represented as a nonlinear capacitor C_P and is connected in parallel with resistor R_P.

Component values of the circuit are shown in table 4.1. V_{out} is measured through a

Table 4.1: Components for Active Sawyer-Tower Circuit

Op-Amp	R_M	C_M	R_P
LM-741J	500 $K\Omega$	10 μF	10 $M\Omega$

32-bit DAQ system running with a D/A frequency of 4 KHz. A series of sinusoidal voltage waves were used as the characterization signals U, with f_U ranging from 40 to 100 Hz and A_U = 5, 10, 20, 40 V. All measurements were carried out on free-standing 127μm thick PZT-5A plates.

4.6.1 Low Field Dielectric Response Measurement Results

The charge responses of piezoelectric plates under low field input voltage, for $A_U \leq 20$ V at $f_U = 40$ Hz, 70 Hz and 100 Hz, are shown in figure 4.12.

Based on the measurements, the hysteresis effect of C_p grows significantly as f_U increases. Only at lower amplitudes and frequencies ($A_U \leq 10$ V and $f_U \leq 40$ Hz), the responses are approximately linear. The observations correlate to the nonlinear dielectric response due to the extrinsic effect of piezoelectric materials which is characterized by $C_P^{nonlinear}$.

Comparing the overall slope of the output voltage by only examining the linear part of the curves, which corresponds to the dielectric response due to C_p^{linear}, the C_p^{linear} value is also voltage dependent. The slope of the $U - V_{out}$ changed by 30% between $A_U = 5$ V and $A_U = 40$ V even when f_U is relatively low.

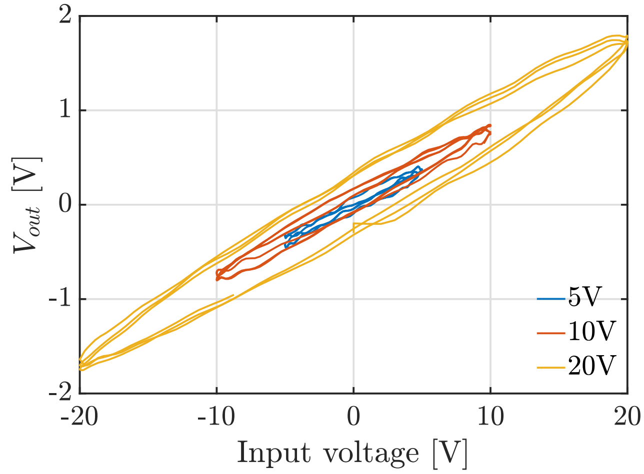

(a) 40 Hz

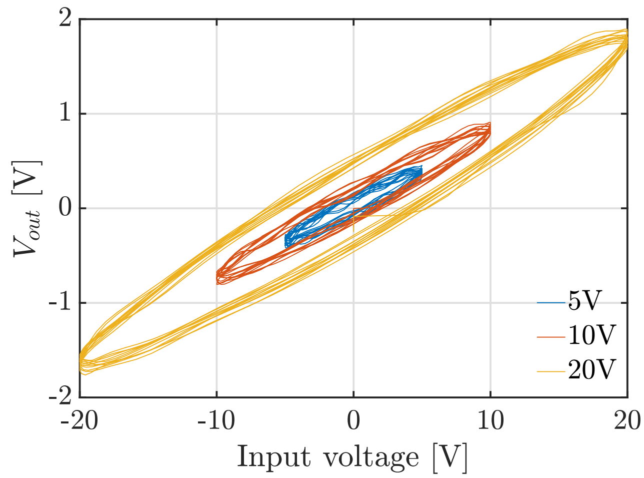

(b) 70 Hz

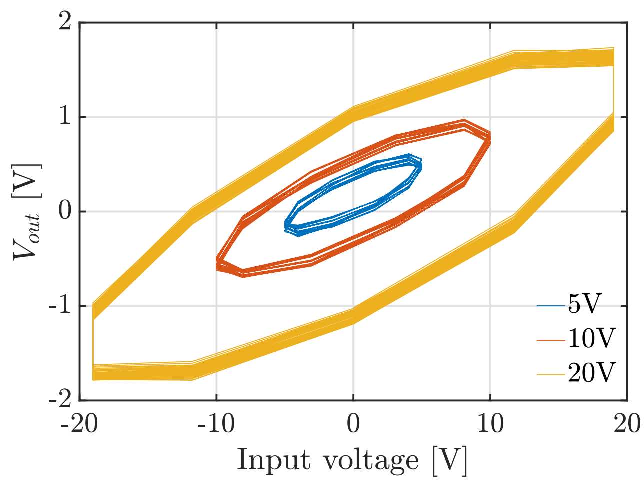

(c) 100 Hz

Figure 4.12: Low field dielectric response measurements of PZT-5A thin plates at $U \leq 20V$.

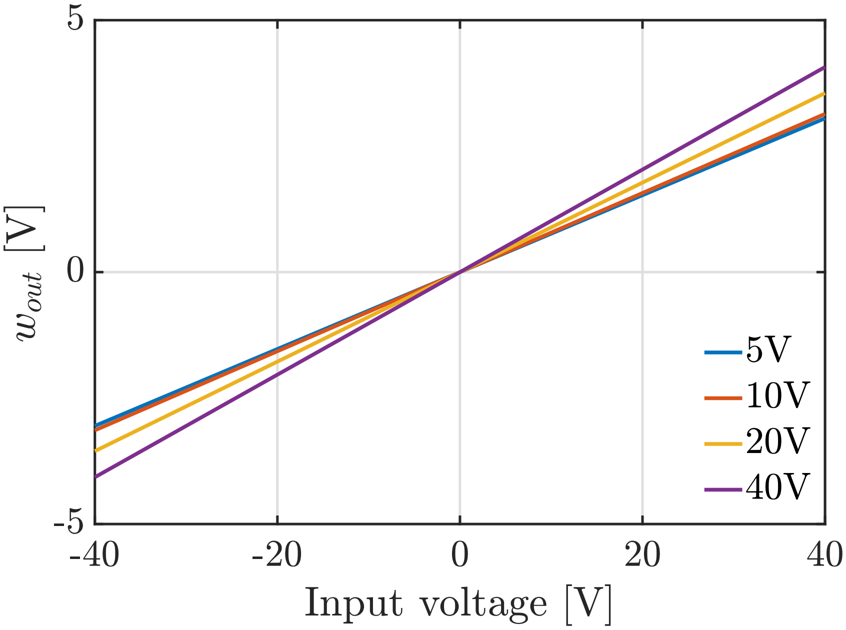

Figure 4.13: Change of peak to peak dielectric response of sensor-actuator layer at 70 Hz as a function of input voltage amplitudes. The slope changes are due to changes the values of C_p^{linear}.

4.6.2 High Field Measurement Results

Measurement results when $A_U \geq 40\ V$ are shown in figure 4.14. The hysteresis not only develops significantly, but the switching like behaviors also start to emerge as $f_U \geq 70\ Hz$, where the high peaks of V_{out} recorded are out of phase with the characterization signals U (figure 4.14b and 4.14c). Amplitudes of V_{out} were limited within 10 V due to the voltage limit of the operation amplifiers used.

The physical mechanism which causes the irregular outputs of V_{out} is still unclear. Similar measurements of bulk piezoelectric materials and films at higher frequencies can be found in [156], [157] and handbooks like [158].

4.6.3 Discussion

The above experiments demonstrate that for PZT-5A thin piezoelectric plates the capacitance C_p is highly-nonlinear, and $C_p \sim C_p(A_U, f_U)$. In practice, the results imply that tuning of the bridge circuit depends on the operation conditions of the active structures. Moreover, the manual tuning process with fixed component values for the bridge circuit is inadequate to satisfy the balance condition for a potentially broad range of input control voltages. In-situ identification and adaptive adjustment of C_p during operation are necessary.

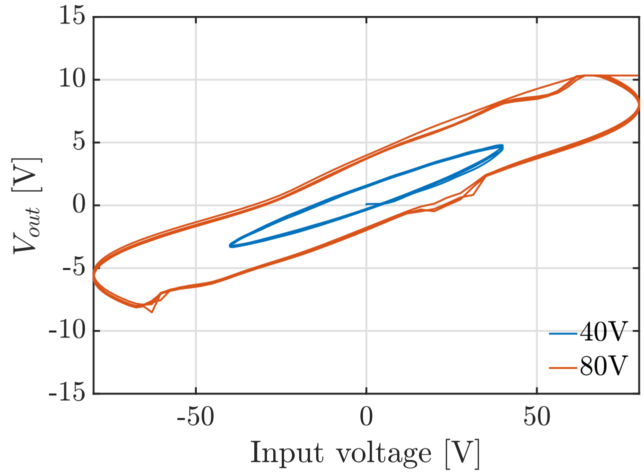

(a) 40 Hz

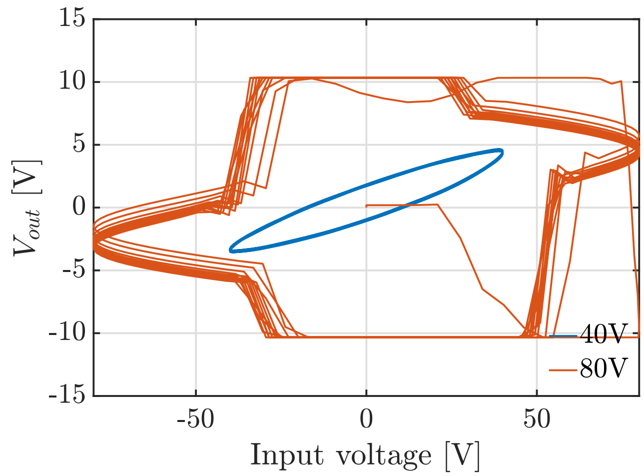

(b) 70 Hz

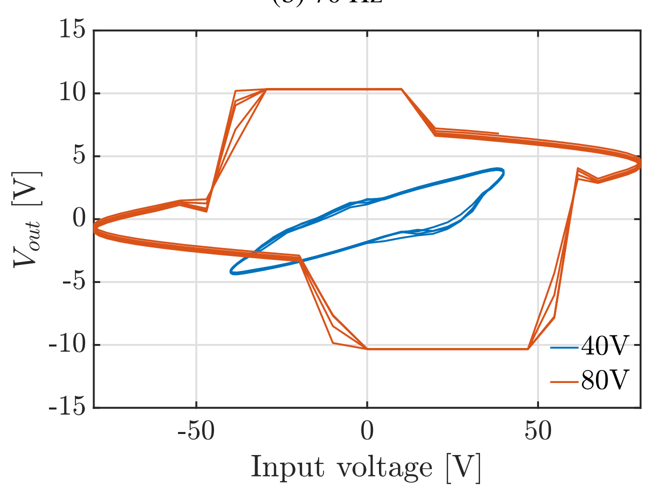

(c) 100 Hz

Figure 4.14: High field dielectric response measurements at $U \geq 40\,V$. Large peaks of dielectric responses appear with a phase shift with respect to the input voltage. Peak values are cut off for $U = 80V$ due to the voltage limit of the DAQ system.

4.7 Analysis of Adaptive Bridge Circuit

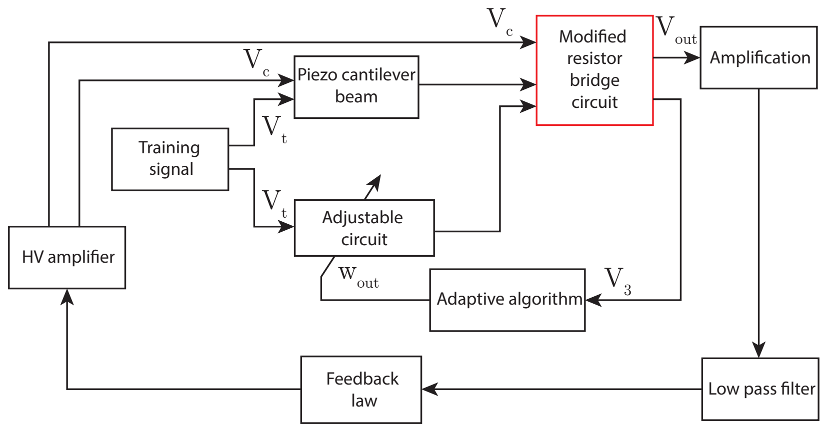

(a)

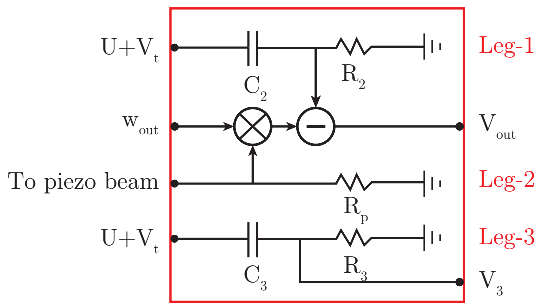

(b)

Figure 4.15: (a) Concept of adaptive self-balancing circuit with feedback control loop. (b) Detailed view of the modified resistor bridge circuit.

A detailed view of the adaptive closed-loop control system for self-sensing piezoelectric structures is shown in figure 4.15. The modified resistor bridge circuit highlighted in red (shown in detail in figure 4.15b) and the concept of piezoelectric capacitance online adaptation was first proposed by Vipperman and Clark [146]. Its function is mainly fulfilled by the adaptive algorithm running in conjunction with the injected training signal U_t. Similar to the system identification applications, the training signal should have sufficient characteristics to excite the appropriate properties of the piezoelectric capacitance C_p in order to minimize or cancel the feedthrough signal induced by certain control signal V_c. This first requires the understanding of signal compositions within the output V_{out} from the adaptive bridge circuit. The following analyses of V_{out} are derived for self-sensing structures with a single electrode piezoelectric layer. The same analyses have to be conducted on each sensor/actuator component defined by separated electrodes of multi-electrodes self-sensing active structures.

4.7.1 Analysis of V_{out} Signal Components

During the closed-loop active control, the output from leg-1 (consisting of the piezoelectric layer and R_p) V_1 which contains the self sensing piezoelectric actuator can be explicitly expressed as:

$$V_1 = R_1 C_p(\dot{V}_c + \dot{V}_t) + R_1 \dot{q}_m \tag{4.76}$$

Here V_c is the control voltage, V_w is the training signal. $q_m = \boldsymbol{\Theta r}$ is mechanically induced charge. Voltage signal from leg-2 (consisting of C_2 and R_2) is:

$$V_2 = R_2 C_2(\dot{V}_c + \dot{V}_t) \tag{4.77}$$

Leg-3 (consists of C_3 and R_3) only receives the training signal, and its function is to convert V_t to the same phase and magnitude as $R_2 C_2 \dot{V}_t$:

$$V_3 = R_3 C_3 \dot{V}_t \tag{4.78}$$

The analog signal separation circuit performs the multiplication and subtraction function to filter out the mechanical disturbance related signal $R_1 \dot{q}_m$:

$$V_{out} = V_1 - V_2 \cdot w_{out} \tag{4.79}$$

w_{out} is the weighing term output from the adaptation algorithm. This chapter considers the least mean square (LMS) algorithm which is commonly used in adaptive signal processing as the algorithm to compute the weighing term w_{out}.

4.7.2 Least Mean Square (LMS) Algorithm for Piezoelectric Bridge Circuit Balancing

In the LMS algorithm, the cost function e is defined as V_{out}, and the reference signal V_3 is the input from leg-3 . From the classical LMS algorithm, the update law for the coefficient w_{out} is:

$$\begin{aligned} w(k+1) &= w(k) - \mu \nabla E[V_{out}^2] \\ &= w(k) + 2\mu E[V_{out} \cdot \frac{V_2}{10}] \\ &= w(k) + 2\mu V_{out} \frac{V_2}{10} \\ &= w(k) + 2\mu e \frac{V_2}{10} \end{aligned} \tag{4.80}$$

here μ is the convergence parameter that controls the convergence rate of the algorithm. It is widely known that the weighing term w_{out} will converge to the optimal Wiener filter weight [159]:

$$w_{out} = w_{opt} = \boldsymbol{R}^{-1}\boldsymbol{p} \tag{4.81}$$

where:

$$\begin{aligned}\mathbf{R} &= E[x(n)x^T(n)] \\ \mathbf{p} &= E[d(n)x^T(n)]\end{aligned} \tag{4.82}$$

Operator $E[]$ calculates the expected value of the discrete signal from A/D. In the current circuit setting, $\boldsymbol{R}$ is the input correlation matrix, $\boldsymbol{p}$ is the cross correlation vector between input to the filter (i.e. the conditioned 'training signal') and the desired output signal $\mathbf{d}$. In this case, the desired signal d is V_1, input signal x is V_{03}. Thus the optimal gain w_{opt} is:

$$w_{opt} = \frac{E[V_1(n)V_3^T(n)]}{E[V_3(n)V_3^T(n)]} \tag{4.83}$$

Substitute the expressions of each components into the above equation:

$$w_{opt} = \frac{E[R_1C_pR_3C_3(\dot{V}_c(n)\dot{V}_t(n) + \dot{V}_t(n)\dot{V}_t(n)) + R_1R_3C_3\dot{q}_m(n)\dot{V}_t(n)]}{E[(R_3C_3\dot{V}_t(n))^2]} \tag{4.84}$$

4.7.3 Selection of Training Signal V_t

In the original concept proposed [146], the white noise was suggested as the training signal V_t. Since V_t is not correlated to either V_c or q_m:

$$\begin{aligned}E[\dot{V}_c(n)\dot{V}_w(n)] &= 0 \\ E[\dot{q}_m(n)\dot{V}_w(n)] &= 0 \\ E[(\dot{V}_t(n))^2] &= \sigma_w^2\delta(n) \neq 0\end{aligned} \tag{4.85}$$

then the optimal weighing term output w_{out} from the algorithm will be:

$$\begin{aligned}w_{out} = w_{opt} &= \frac{R_1C_p}{R_3C_3} \cdot \frac{\sigma_w^2}{\sigma_w^2} \\ &= \frac{R_1C_p}{R_3C_3}\end{aligned} \tag{4.86}$$

In this case the feedthrough signal is canceled completely. However, an inherent assumption of the above analysis is that the unknown property C_p is independent of the training signal V_t, which does not hold true for general piezoelectric materials as is verified in the previous section. Indeed, for the soft piezoelectric material-based samples, the injected white noises with σ_t on the same order of V_c caused the algorithm to quickly diverge in experiments. When $\sigma_t \ll V_c$, the output w_{out} was also unable to cancel the feedthrough signal completely. Instead, the harmonic signal is chosen as the training signal:

$$V_t = A_t \sin(2\pi f_t t) \tag{4.87}$$

and when the frequency of the training signal $f_t \ll f_{rl}$ or $f_t \gg f_{rh}$, where f_{rl} andf_{rh} are the lowest and highest resonant frequencies of the structure within the mechanical disturbance bandwidth, the feedthrough signal can be canceled on the tested cantilever beams. The mechanism is analyzed as follows:

- Under open-loop conditions when performing off-line identification ($V_t = 0$) of the piezoelectric capacitance, since $V_t \gg R_1\dot{q_m}$ and are not correlated at off-resonance frequency, $E[\dot{q}_m(n)\dot{V}_w(n)] \approx 0$, thus, the adaptive gain will converge to:

$$\begin{aligned} w_{out} = w_{opt} &= \frac{R_1 C_p}{R_3 C_3} \cdot \frac{E[(\dot{V}_t(n))^2]}{(\dot{V}_t(n))^2} \\ &= \frac{R_1 C_p}{R_3 C_3} \end{aligned} \tag{4.88}$$

- During closed-loop experiments when $V_c \neq 0$, when the control loop frequency f_c is significantly higher than the training signal ($f_c \gg f_t$):

$$E[\dot{V}_c(n)\dot{V}_t(n)] \sim 0 \tag{4.89}$$

Thus the result in equation 4.88 still holds. The following tests (both open- and closed-loop) have adopted harmonic signals as the training signals.

4.7.4 Implementation of Circuit Balancing with Analog-Digital Adaptive Circuit

Figure 4.16 shows the analog-digital implementation of the adaptation circuit concept shown in figure 4.15. The real time controller is a National Instrument PXIe-8840 running a real-time operating system, and the feedback law is implemented with Labview. The DC shift in the output is removed by the offset nulling component before entering the A/D hardware. An initial estimation of the C_p value is necessary to guarantee that w_{out} is within the analog output range of the real time controller. This can be achieved by adjusting the component values on the bridge circuit legs. The LMS algorithm is implemented with the feedback node in Labview, shown in figure 4.17. In experiments, the convergence parameter μ is taken as 0.02. A comprehensive discussion about the choice of the convergence parameter μ can be found in the monograph [160].

4.7.5 Open-Loop C_p Adaptation Tests

The complete adaptation system is put into test with the self-sensing beam's sensor-actuator layer under open-loop condition, when no mechanical disturbance is added

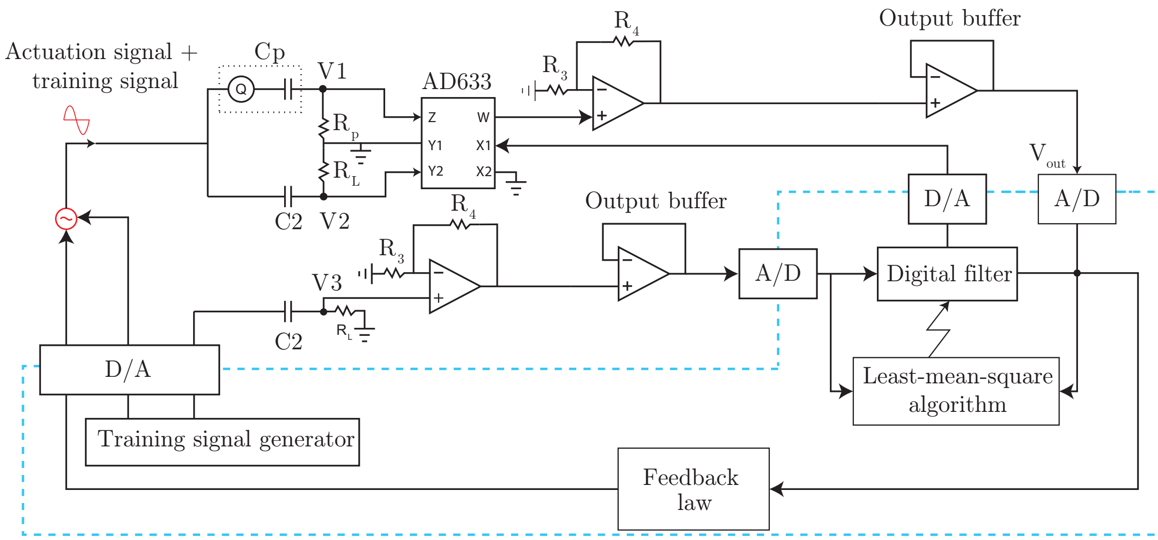

Figure 4.16: Implementation of the adaptive balancing circuit with real time controller. The multiplication chip AD633 executes the adaptation calculation 4.79 analogly. The feedback loop is activated in section 4.8.

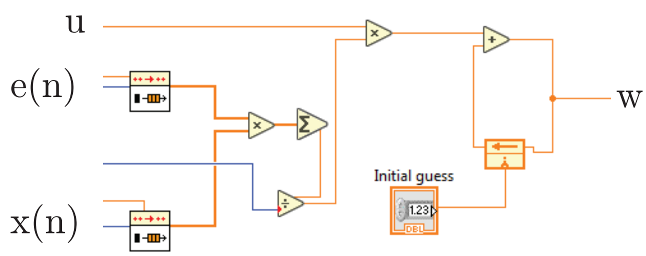

Figure 4.17: LMS algorithm implementation in Labview with feedback node and FIFO array.

and the feedback loop is inactive. Three groups of training signals are used to excite the dielectric response of the sensor-actuator layer: $f_t = 70\ Hz,\ 100\ Hz,\ 200\ Hz$ and at different amplitudes ranging from $1\ Vpp$ to $10\ Vpp$. Here V_pp represents the peak-to-peak value of the input voltage. Figure 4.18 shows the trend of converged w_{out} values from the algorithm output.

Figure 4.19 provides a snapshot of the steady state feedthrough signal before and after adaptation, at $f_t = 70\ Hz$ and $A_t = 5Vpp$. The algorithm started with an initial guess of w_{out}, and the convergence times were all under 0.1 s. The remaining noise mainly came from the cabling of the breadboard.

The results reflect the strong dependence of C_p with respect to the characteristics of the training signal. They also suggest that during closed-loop vibration damping, in order to remove the feedthrough component $R_1 C_p \dot{V}_c$ due to control input completely,

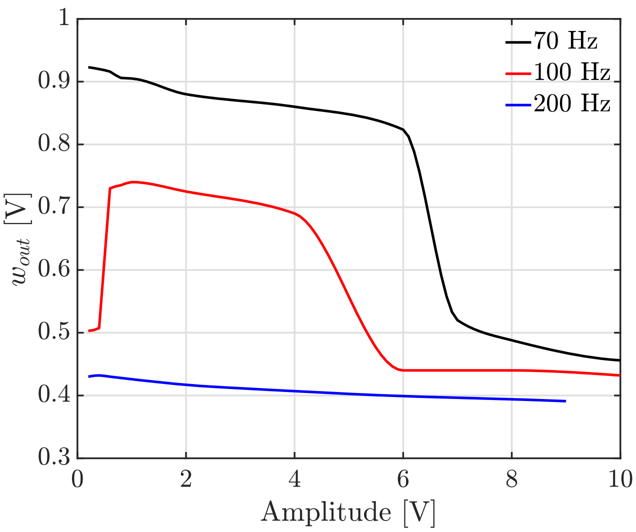

Figure 4.18: Adaptation algorithm output w_{out} for bridge circuit balancing under different training signal V_t frequency and amplitudes.

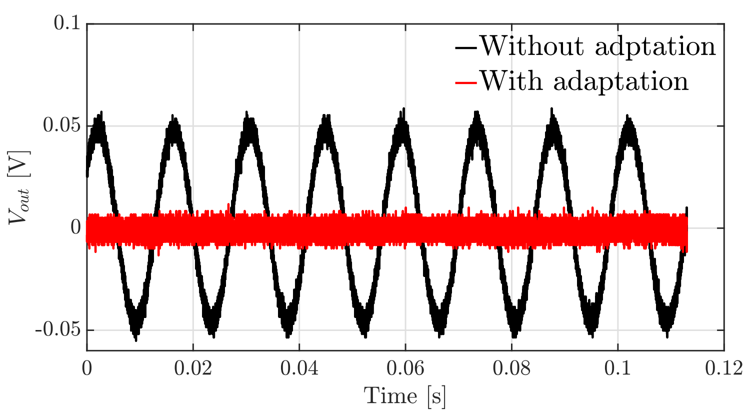

Figure 4.19: Feedthrough signal adaptive cancellation at off-resonant frequency (70 Hz).

V_t should possess similar frequency and amplitude characteristics as V_c. However from section 4.7.3, conforming to such requirements will generate a non-vanishing covariance term $E[\dot{V}_c(n)\dot{V}_t(n)] \neq 0$ and the weighing output w_{out} may not converge to the desired value $\frac{R_1C_p}{R_3C_3}$. Currently only A_t is matched with A_c. Tests with f_t close to f_c or switching to other training signal forms will be left as future work.

4.8 Closed-Loop Active Damping Experiments

A series of tests were conducted near the first resonant frequency of the cantilever beam in this section, in order to: (1) Verify the effectiveness of the self-sensing vibration control architecture. (2) Verify the performance adaptation circuit in close loop. (3) Validate the modeling technique established in previous sections. The test specimens were built following the same geometry as shown in figure 4.6a with one end of the substrate longer than the sensor-actuator layer for clamping to the shaker. The bottom electrode of the sensor-actuator layer which was glued to the substrate was introduced to the outer surface via conductive ink.

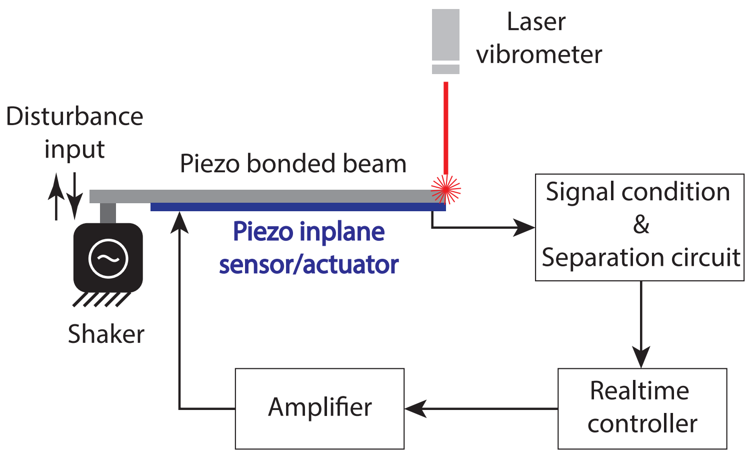

(a)

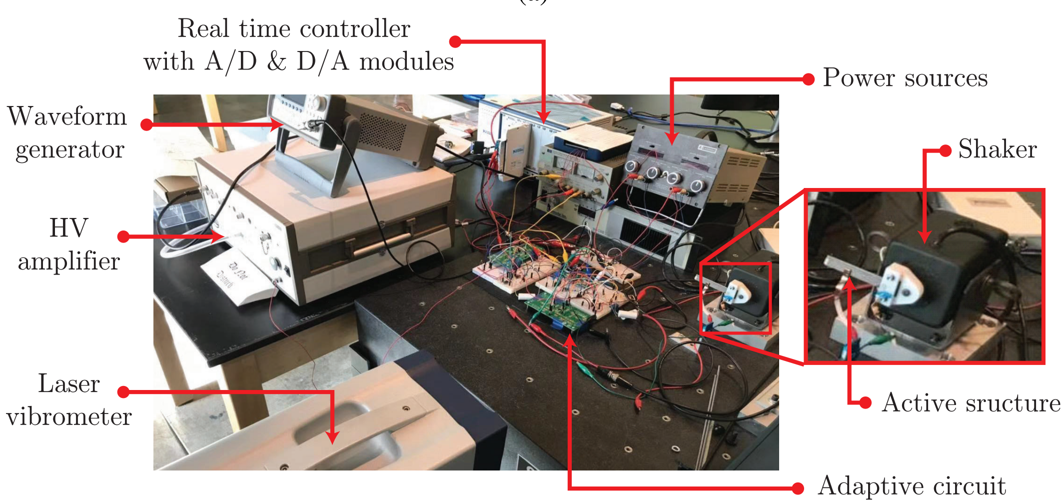

(b)

Figure 4.20: (a) Closed-loop active damping experiment overview. (b) Complete experiment setup.

In the closed-loop tests the mechanical disturbance was introduced through an electromagnetic shaker that is clamping the beam at the root. The tip displacement and velocity is measured by a Polytech^{TM} Doppler laser vibrometer, as illustrated in figure 4.20a. The complete experiment setup is shown in figure 4.20b. Open- and closed-loop dynamic models were built based on the nominal sample geometry, following the procedures described in section 4.4.

4.8.1 Open-Loop Calibration

Prior to the closed-loop damping experiments, open-loop calibrations were conducted on the beam samples which were only mechanically excited. The goal of the calibrations was to evaluate the d_{31} value and the damping ratio Δ of the tested samples. Before the mechanical excitation started, an identification step was run with a training signal of $f_t = 100\,Hz$ and $A_t = 5\,Vpp$ to balance the adaptive sensing circuit. The converged output from the adaptive gain w_{out} was then kept constant during calibration for each beam. The beam was then mechanically excited by the shaker under a series of discrete frequencies around the first fundamental mode, while keeping the shaker input power constant. The sensing signal V_{out} and tip velocity $\dot{r}_{tip}$ were recorded by the real time controller while the feedback loop was deactivated. Acceleration amplitudes of the shaker head were also recorded and used as inputs to the numerical model. Comparison of the open-loop sensing voltage with

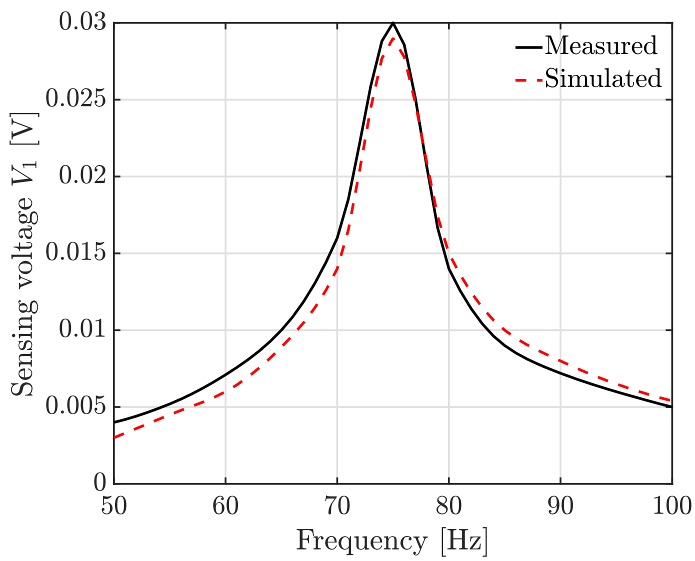

Figure 4.21: Calibration of open-loop sensing voltage under mechanical excitation.

the calibrated model output from one sample is shown in figure 4.21; comparisons of open-loop tip velocities can be found in figure 4.22 and figure 4.23. Comparing the measurement and estimations at off-resonance frequencies, it is found that both d_{31} and the damping ratio Δ of the structure is frequency dependent.

4.8.2 Closed-Loop Active Damping Experiments

The calibrated open-loop models were used for constructing the closed-loop dynamics in order to estimate the damping performances. The closed-loop experimental responses were measured at the calibrated frequencies with continuous harmonic disturbances provided by the shaker at each excitation frequency point. The steady state responses of the tip node were recorded and compared to the estimations. Two types of tests were run with the adaptive identification system and the feedback loop: offline adaption (figure 4.22) and online adaptation (figure 4.23). In the offline adaptation tests, the adaptive sensing circuit was first pre-balanced without mechanical disturbance. w_{out} was then kept constant through the closed-loop damping experiments at different mechanical excitation frequencies, without the injection of training signals. During the online adaptation tests, the adaptive balancing with training signal injection and the feedback control loop were running at the same time. The tests were conducted on two separate samples. Tip node displacements measurements from the two sets of tests conditions are shown in figure 4.22 and figure 4.23.

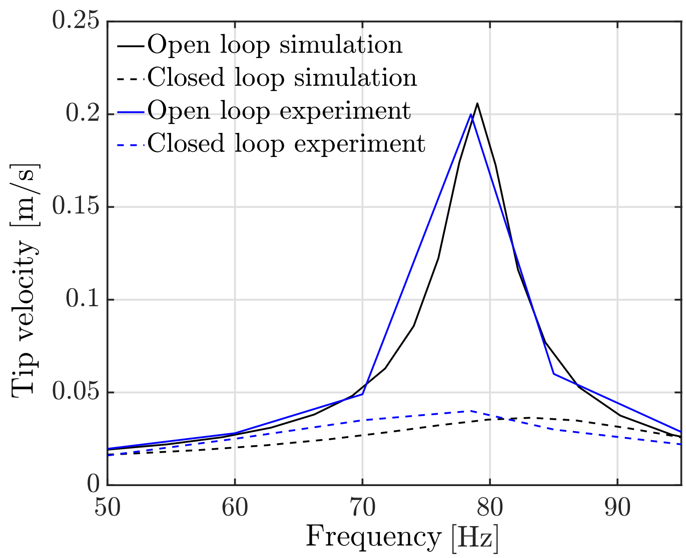

Figure 4.22: Comparisons of the tip velocities under closed-loop damping from measurements and simulations. Calibrated open-loop responses are shown in parallel. Sensing circuit was balanced with offline adaptation.

Both sets of tests validated that the single-electrode self-sensing architecture was able to decrease the resonant peak by 75% (-12 bB). The closed-loop damping performances were captured precisely by the calibrated model. No distinctive differences could be observed for the two types of tests regarding the closed-loop response. This result indicated that C_p was stable for the range of V_c output from the controller's feedback loop, which was less than 20 Vpp. The result was consistent with the low field dielectric response measurements in figure 4.12c. The quantitatively good correlations with the estimations also indicated that the feedthrough signal

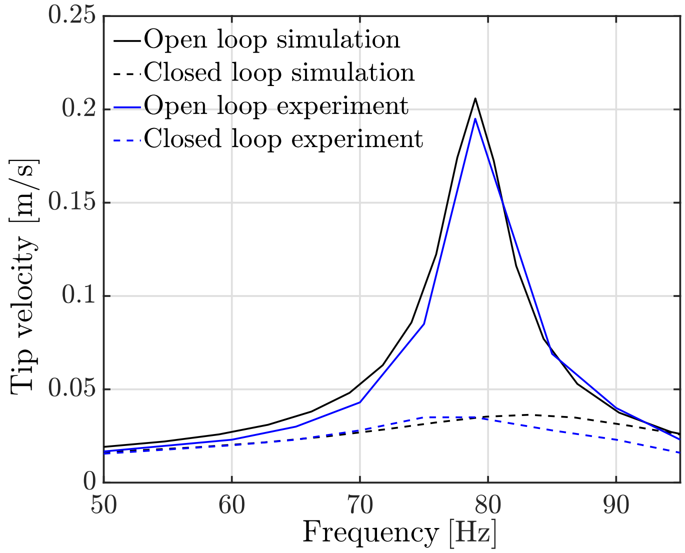

Figure 4.23: Comparisons of the tip velocities under closed-loop damping from measurements and simulations. Calibrated open-loop responses are shown in parallel. Sensing circuit was balanced with online adaptation.

was effectively canceled, which is the fundamental assumption of the closed-loop dynamic model. Moreover, the results indicated that during the online adaptation tests, the selected training signal was not interfering with the compensated feedback sensing signal q_m.

4.8.3 Measurements of Piezoelectric Capacitance Degradation

In all the tests on self-sensing beam samples, the PZT-5A based sensor-actuator layer exhibited significant decay in damping capability as the test time duration increased, with the peak damping less than 1 dB at the resonance frequency. Figure 4.24 shows drastic changes of w_{out} from the adaptive algorithm of one of the tested self-sensing beam, after 30 min at 100 Hz, 10 Vpp electric field cycling without mechanical disturbances. Compared to figure 4.18, post cycling w_{out} values had dropped by an order of magnitude at all frequencies, and the initial differences among different frequencies have disappeared. The measurements indicate significant changes of the C_p value, which leads to a vanishing feedback signal and partially explains the degradation of closed-loop damping performance. This change of the electromechanical coupling coefficient d_{31} over time requires further investigation.

4.8.4 Discussions

A new strategy for the online identification of the piezoelectric capacitance is proposed in this section, and implemented on an analog-digital adaptive circuit.

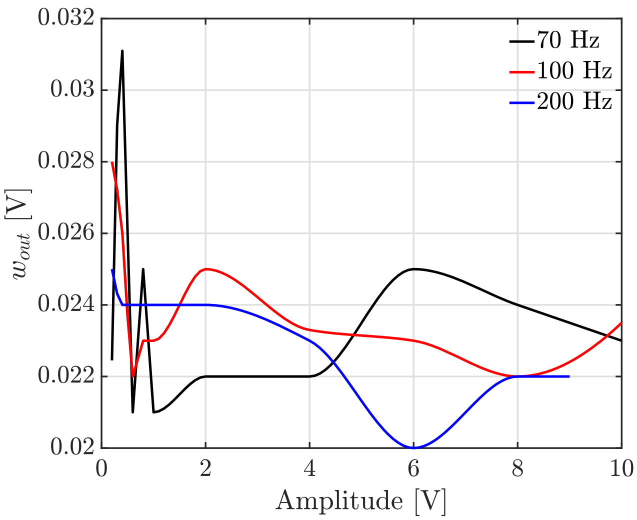

Figure 4.24: Adaptation algorithm output w_{out} for bridge circuit balancing for a tested beam after 30min of electric field cycling. Comparing to figure 4.18, w_{out} has shifted over an order of magnitude.

Closed-loop vibration damping experiments were performed on single-electrode piezoelectric self-sensing beams with the direct velocity feedback law analyzed in section 4.5. Two types of closed-loop tests regarding the usage of the adaptive circuit were conducted, which are divided by the on-line and off-line injection of the C_p identification training signals. Under the conditions of small disturbance amplitudes and low actuation fields, both tests achieved similar damping performances. The calibrated model predicted the damped tip velocities of the beams with high fidelity, and the validated modeling technique will be adopted in the following section.

4.9 Vibration Control Simulations of a Multi-Electrode Self-Sensing Piezoelectric Shell

This section further extends the techniques developed in the previous parts of this chapter, which include self-sensing architecture with piezoelectric capacitance adaptation and fast closed-loop modeling methods, to the design and active damping of curved active thin shell concepts. The test case presented was chosen for its potential applications in future large aperture segmented space telescopes as the background.

Traditionally, large dimension mirrors for ground or space based telescopes are designed with high stiffness to withstand environmental disturbances passively. Over the past two decades, active and adaptive optical systems have been successfully used to improve the image quality under atmospheric turbulences [161], [162]. These systems usually implement adaptive mirrors and wave front sensors in the optical paths. Since weight is not a major constraint for the ground based systems, most of the existing designs feature bulky actuators and complex sensing and control systems [163], [164]. One prominent benefit of the self-sensing architecture compared to classical adaptive optics approach is that the external metrology systems like wavefront sensors are precluded from the control loop, which can greatly simplify the system complexity and the band which is not limited by the optical feedback loop. Meanwhile, active thin shell designs with low areal density and integrated piezoelectric layers are able to incorporate the controllability and observability considerations of the closed-loop system during the design process, which may grant higher control authority.

4.9.1 Model Description

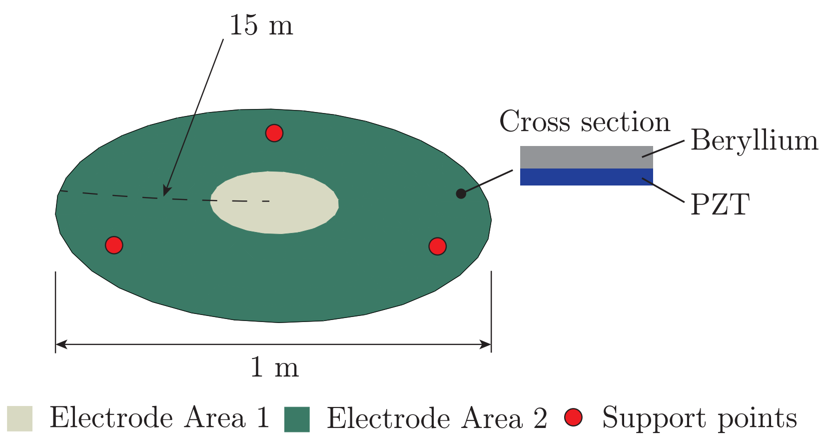

Figure 4.25: Geometry of the beryllium-piezoelectric two electrodes curved shell. The piezoelectric sensor/actuator layer is assumed to fully cover the back surface, and is divided by two separate electrodes: the center circle (electrode area 1) and the outer ring (electrode area 2).

The shape stability of a hypothetical large dimension active thin shell with self-sensing piezoelectric layer is investigated in the following. The design is illustrated in figure 4.25. The active shell design conceived is driven by the concept of low areal density and high shape adaptability. It is assumed to be constructed from the laminate of two types of isotropic materials: beryllium as the substrate and PZT-5A as the sensor-actuator. Beryllium is chosen as the substrate material for its superior stiffness to weight ratio and high strength [165]. It is also assumed that the PZT-5A sensor-actuator layer covers the whole bottom surface of the shell, and is patterned by two independent electrodes as shown in figure 4.25. Table 4.2 lists the key geometry, material parameters and model information of the hypothetical shell. The modeling framework can be easily applied to model other active thin shell structures with different electrode pattern designs and material selections, including different types of active materials.

Table 4.2: Parameters of the simulated two-electrode piezoelectric mirror

Parameter	Value
Diameter	1 m
Radius of curvature	15 m
Mass of shell	2.75 kg
Substrate layer material	Beryllium
Substrate layer thickness	500 μm
Sensor-actuator layer	PZT-5A
Sensor-actuator layer thickness	300 μm
Electrode 1 diameter	0.15 m
Number of support points	3
Radius of support points position	0.3 m
Number of elements	66
Number of nodes	211
Element type	8 nodes thin shell element (S8R)
Coupling coefficient d_{31}	-190×10^{-12} m/V

4.9.2 Closed-Loop Model

A closed-loop model is built for the structure to demonstrate the active damping system performance under dynamic disturbances. In general for a piezoelectric thin shell with n electrodes, the electrical forcing matrix $\boldsymbol{B}_u$ is defined as:

$$\boldsymbol{B}_u = \begin{bmatrix} \boldsymbol{B}_{u1} & \boldsymbol{B}_{u2} & \dots & \boldsymbol{B}_{un} \end{bmatrix} \tag{4.90}$$

and in the closed-loop dynamics equations, the feedback damping term $RK\boldsymbol{\Theta}^T$ for the SISO system is replaced with:

$$\begin{bmatrix} R_1 G_1 \boldsymbol{\Theta}_1^T \\ R_2 G_2 \boldsymbol{\Theta}_2^T \\ \dots \\ R_n G_n \boldsymbol{\Theta}_n^T \end{bmatrix} \tag{4.91}$$

R_1 and G_1 are the sensing resistor value and controller gain, respectively, for each sensor-actuator feedback channel. $\boldsymbol{B}_{ui}$ and $\boldsymbol{\Theta}_i^T$, $i = 1 \dots n$ need to be calibrated for each sensor-actuator patch.

The conceived shell has two separate self-sensing channels from two adjacent sensor-actuators. The actuation responses from two independent patches under unit voltage actuation are shown in figure 4.26 for the calibration of $\boldsymbol{B}_{u1}$ and $\boldsymbol{B}_{u2}$. The first four

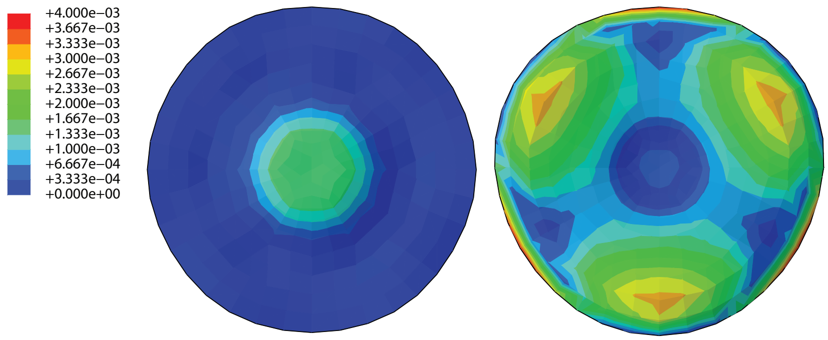

Figure 4.26: Left to right: displacement map by applying unit voltage to electrode 1 and 2. Unit: µm.

fundamental modes of the shell are shown in figure 4.27. The plots indicate the out-of-plane direction displacements.

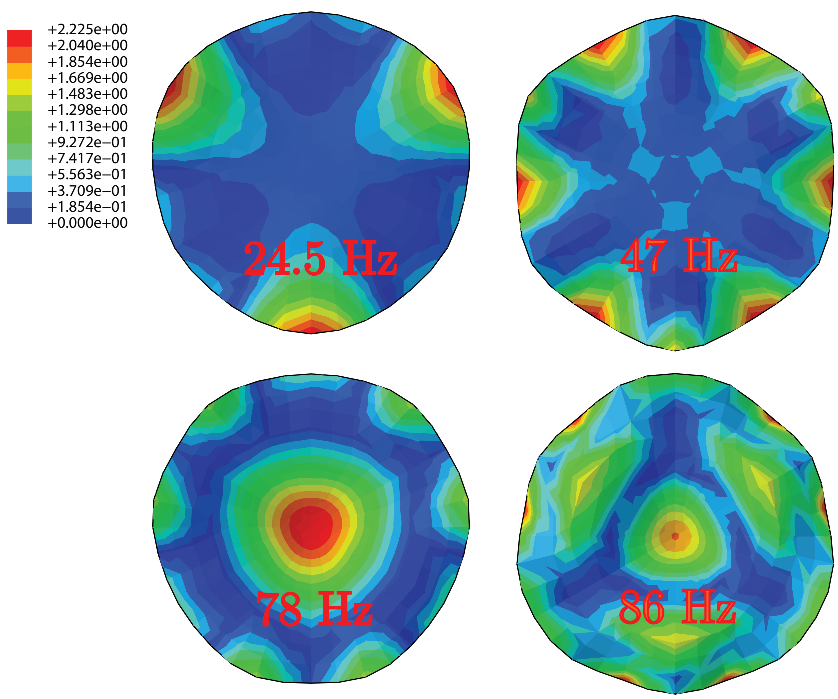

Figure 4.27: Top view of first four fundamental modes of the beryllium-piezoelectric shell. Color maps represent normalized modal displacements along the out-of-plane direction.

It is assumed that both channels are independently linked to separate adaptive bridge circuits developed in section 4.7. The assumptions considered in section 4.5 are carried over here, which assumes the complete cancellation of feedthrough signals of each channel. The feedback gain G_1 and G_2 were chosen to be the same value and tuned in MATLAB/Simulink.

4.9.3 Closed-Loop Simulation Results

4.9.3.1 Frequency Response

Figure 4.28 shows the Bode plots of the center node response to acceleration excitation along the normal direction of the shell. Overall, the closed-loop adaptive self-sensing system is effective in damping the disturbance over a broad band width. From the comparison of open and closed-loop responses under self-sensing active damping, the 1st and 2nd modes are damped by -7 and -2 dB respectively, with a slight shift of frequencies. The maximum damping appears around the 3rd and 4th

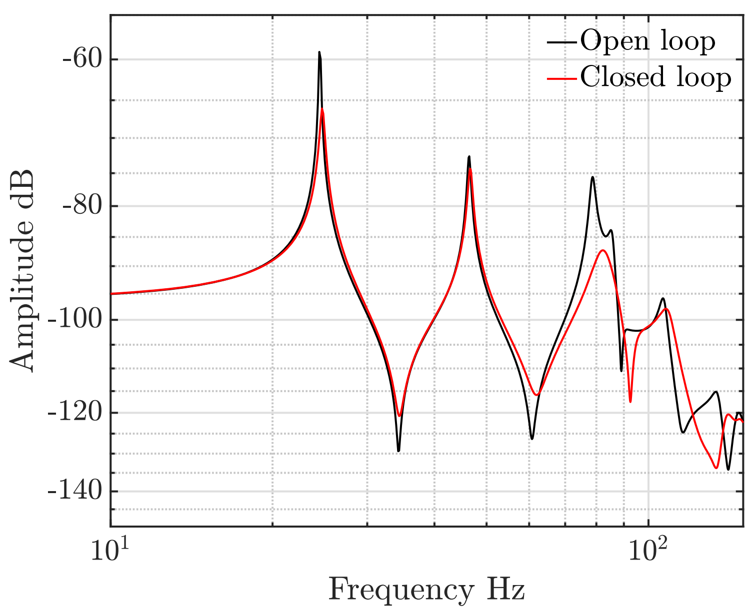

Figure 4.28: Open- and closed-loop bode plots of the center node with respect to base acceleration excitation.

modes of the shell (bottom row of figure 4.27). The spatial displacement distribution of these two modes are well correlated with the actuation responses from the two actuators, comparing the bottom row of figure 4.27 with the separated actuation responses from figure 4.26. Thus, the two modes are controllable under the chosen actuator design. Following the same arguments, the first two modes are neither observable nor controllable, which explains the relatively low closed-loop damping performance at the corresponding frequencies.

4.9.3.2 Response Time History Under Harmonic Acceleration Excitation

In this section the time history of the shell under open- and closed-loop conditions are calculated under the same base disturbance. The shell is assumed to be excited under constant harmonic base excitation at the first fundamental frequency with an amplitude of 10×10^{-3} G, G being the gravity acceleration value. The shell is initially still, and the excitation starts at time 0 s. The response of the shell over a time span of 2 s is simulated with the reduced order model. The peak to valley deformation, and the RMS error over the full surface are shown in figure 4.29. At

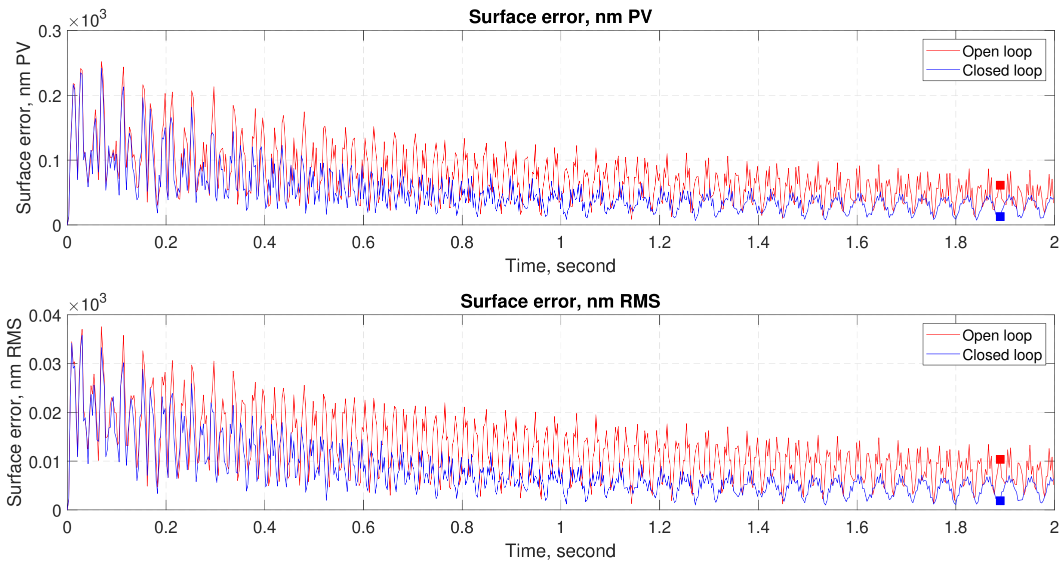

Figure 4.29: Peak to valley and RMS error of the complete surface, under constant harmonic excitation at first fundamental frequency.

the steady state, both metrics for the closed-loop system are approximately half of the values of the open-loop responses.

4.9.4 Discussion

Compared to traditional vibration damping systems for large shell structures such as tuned mass dampers and viscoelastic materials based passive damping inclusions, the system presented is superior based on the following factors:

- Light weight sensor/actuators, low overall system mass penalty
- Broad bandwidth
- True collocated control

However, the system has put higher requirements on the computation and signal processing capabilities compared to the passive approaches, and needs high voltage amplifiers with sufficient power to drive the piezoelectric sensor/actuators. Meanwhile, at a fixed frequency the feedback signal scales linearly with the excitation amplitudes. For small amplitude disturbances like the example considered in this section, low noise electronic design is required to improve the signal to noise ratio of the sensing circuit.

4.10 Summary and Discussion

This chapter has developed the vibration control techniques for piezoelectric thin shell structures with the self-sensing architecture, emphasizing the real-time adaptation of the piezoelectric sensor-actuator layer's capacitance, the numerical modeling techniques for both open- and closed-loop piezoelectric structure dynamics and the experimental validations of the proposed methodologies. After an introduction to the fundamentals of piezoelectric self-sensing, the chapter first identified the components and sources of nonlinearity of the feedback signal. A modeling framework for the general piezoelectric thin shell structures through finite element method is proposed and validated. Instead of deriving the modeling framework from bottom up, outputs from commercial software is utilized to efficiently build linear, accurate and low order dynamical model for piezoelectric thin shells with arbitrary geometries and sensor-actuator topologies. The dielectric responses of PZT thin plates were measured under electric fields of different frequencies and amplitudes. The effective piezoelectric capacitance was proved to be highly dependent on the electric excitation for the soft piezoelectric material tested. A resistor based, adaptive bridge circuit and the associated identification algorithm were then implemented for the balancing of the signal separation circuit.

The chapter then pointed out that the training signal for online identification needs to be chosen carefully in order to excite the proper characteristics of the dielectric response of piezoelectric materials. The effectiveness of the adaptive circuit and the modeling framework were verified through vibration control experiments on self-sensing cantilever beams based on single electrode PZT. Performance of the closed-loop vibration control system was validated by monitoring the forced vibration response of the beam's tip. Accurate predictions of the closed-loop damping performances of the cantilever beam can be obtained using the calibrated numerical model. The system's performances using both offline and online adaptation were compared which demonstrated that similar damping performance can be achieved under low external disturbances and at low control voltage ranges.

Through the identifications with the adaptive sensing circuit, the capacitance of the piezoelectric sensor/actuator layer was found to degrade significantly under electric cycling. The phenomenon was accompanied by the degradation of closed-loop vibration damping capability of the self-sensing beam. Further validation is needed on the change of the value of d_{31} with time and electric cycling.

The MIMO closed-loop vibration control simulations were carried out on a large curved thin shell with two independent piezoelectric sensor-actuators supported on three points, which was challenging to model analytically. The case study demonstrated that effective self-sensing vibration control of curved thin shells can be achieved when the sensor-actuator spatial distribution was able to monitor certain vibration modes. Building on the established modeling tools, sensing and control of specific vibration modes are possible through the optimization of the sensor-actuator topology.

Chapter 5

CONCLUSIONS AND FUTURE WORK

5.1 Summary and Contributions

This thesis has established a complete set of building blocks for a new class of deployable thin shell structures. The innovative new features of the foldable active thin shell structures proposed in this study include:

- Concurrent folding of thin shells with edge support spatial mechanisms
- Local folding to avoid global deformation of the shell
- Modular design which can be tessellated to form deployable surface arrays
- Surface parallel actuation scheme to change the global curvature of the shell

Due to these novel features, the proposed methodologies have opened up a wider design space of deployable structures using a combination of rigid mechanism with flexible thin shells. The methodologies enable storage and deployment of doubly curved shells in a determinant, precise fashion. The proposed concepts also attain high shape correctability and structural rigidity of the shell-mechanism assembly in the deployed states. Feasibility of the proposed concept has been validated by prototypes and are supported by the following material characterizations:

- Prototype for a foldable surface module has been manufactured. The module is composed of a flat CFRP shell co-cured with metallic glass sheets at the folding region, and 3D-printed mechanism with rolling hinges.
- A doubly curved, full CFRP shell with blended layup has been designed and manufactured. The shell has been proved to be compactly foldable, and able to achieve high surface precision.
- The flexural strain limits of ultra thin CFRP laminates and piezoceramic sheets have been measured under large bending deformations. Based on the measured failure strain, achievable folding limits of the different designs are determined.

The thesis has established electro-mechanically fully coupled, efficient estimation algorithms for piezoelectric unimorph structures. The need for such models comes from the high applied electric field required to achieve high actuation authority in active shell structures, and the complex loading conditions during the folding and deployment processes, which have not been considered in the literature. The algorithm incorporates a phenomenological model of nonlinear piezoelectricity, which is characterized experimentally with the following steps:

- A unique set of experimental methods has been developed for measurements of mechanical and electrical responses of thin piezoceramics and the unimorph structures made from them.
- Complete characterization of a phenomenological model of piezoelectricity has been achieved through a combination of ferroelectric and ferroelastic tests. Such a complete characterization has never before been achieved in literature.
- Complex loading experiments on piezoceramic unimorph samples revealed that non-180°domain switching can alter the global shape of thin unimorph structures. The phenomenon has been successfully captured by the characterized material model and estimation algorithms.

The thesis further discusses the self-sensing vibration control with multi-electrode piezoelectric unimorph thin shells. Self-sensing control architecture makes dual use of the same piece of piezoceramic component embedded in the structure as both sensor and actuator. In this work, the emphasis is put on compensating the variation of piezoelectric properties of the sensor-actuator layer of the shell:

- The time-varying and field dependent dielectric properties of soft piezoceramic have been characterized experimentally.
- An online adaptation signal conditioning circuit has been implemented together with the adaptive signal processing algorithm. Criteria for selection of identification signal for signal adaptation are proposed and analyzed.
- Measurements have been carried out to provide proof of damping functionality with single electrode cantilever beams. Online adaptation measurements with the beam samples validated the importance of choosing the appropriate identification signal according to the operation range and disturbance level.

- An efficient and accurate modeling technique has been proposed that allows for fast building of closed-loop control models for self-sensing piezoelectric thin shells with arbitrary geometries and electrode topologies. The model successfully predicted the closed-loop performance of cantilever beam samples.

- The damping performance of a large, multi-electrode self-sensing piezoelectric thin shell has been simulated with the validated closed-loop modeling technique. Simulation results revealed that the spatial distribution of the electrode significantly affects the damping capability of the self-sensing active shell structures.

5.2 Future Work

The following areas of research are proposed to expand the application range and feasibility of the concepts and techniques established in the thesis.

- First, apart from the foldable module and deployable structures synthesized in chapter 2, there potentially exist a larger family of feasible solutions that combine foldable thin shells with deployable mechanisms. It is expected that the process of converting classical origami folding patterns into edge-supported, foldable thin shell structures may be automated following the proposed guidelines, and generalized for arbitrary surface geometries.

- The reduced thickness smooth folds adopted in the current solutions may be replaced with compliant mechanisms. By making periodic cut-outs on a thick plate, the out-of-plane bending stiffness can be designed and tailored to the desired specifications, even achieving large bending deformation while keeping the local strain within the elastic range.

- In chapter 3, mismatches between the estimation and measurements from ferroelectric and ferroelastic switching tests appeared when the electric actuation or mechanical loading is of low amplitudes. It is suspected that the main source of the discrepancy comes from the assumption of constant switching surface radius. In reality, both the intrinsic and extrinsic responses of polycrystalline piezoelectric materials are continuous events; however, the phenomenological model differentiates the process into linear and nonlinear regimes. A feasible improvement may be introduced by history dependent, an-isotropic switching function.

- The online adaptation of the piezoelectric capacitance technique from chapter 4 can be extended to higher electric fields. In the closed-loop damping tests, the disturbance levels were chosen so that the responses can be corrected with a relatively low operational electric field for the piezoelectric layer. As the hysteretic dielectric response becomes more evident under higher electric excitation, a model based adaptation method (in contrast to the model-free approach presented in this thesis) may improve the identification accuracy.

- So far, the simulations and experiments were conducted only for active shells with simple sensor-actuator topologies till the end of chapter 4. Controllability and observability of a multi-electrode active shell clearly depend on the distribution of the active material and the boundary conditions. Systematic studies need to be performed in this direction and may leverage the fast modeling framework proposed in this study.

BIBLIOGRAPHY

[1] C. Sickinger, L. Herbeck, T. Strohlein, and J. Torrez-Torres, "Lightweight deployable booms: Design, manufacture, verification, and smart materials application," *55-th International Astronautical Congress*, pp. 1–11, 2004.

[2] *Brane craft wins NASA award.* Retrieved from https://aerospace.org/story/brane-craft-wins-nasa-award, Apr. 2019.

[3] J. N. Footdale, M. Peterson, and J. C. Griffee, "Flexible composite shell design for the marco deployable reflector," *AIAA Scitech 2019 Forum*, p. 0756, 2019.

[4] J. Santiago-Prowald and H. Baier, "Advances in deployable structures and surfaces for large apertures in space," *CEAS Space Journal*, vol. 5, no. 3-4, pp. 89–115, 2013.

[5] T. Vinogradova, "Northrop Grumman-Caltech Space Solar Power Initiative (SSPI) technology maturation.," Retrieved from https://www.mtu.edu/ece/department/faculty/full-time/zekavat/pdfs/ssp-2017/ng-caltechpanel-sspi-technology-maturation-approved.pdf, 2017.

[6] A. C. Henry, G. Molinari, J. R. Rivas-Padilla, and A. F. Arrieta, "Smart morphing wing: Optimization of distributed piezoelectric actuation," *AIAA Journal*, pp. 1–10, 2019.

[7] C. Dagdeviren, Y. Su, P. Joe, R. Yona, Y. Liu, Y.-S. Kim, Y. Huang, A. R. Damadoran, J. Xia, L. W. Martin, *et al.*, "Conformable amplified lead zirconate titanate sensors with enhanced piezoelectric response for cutaneous pressure monitoring," *Nature Communications*, vol. 5, p. 4496, 2014.

[8] Q. Chen, D. Natale, B. Neese, K. Ren, M. Lin, Q. Zhang, M. Pattom, K. Wang, H. Fang, and E. Im, "Piezoelectric polymers actuators for precise shape control of large scale space antennas," *Electroactive Polymer Actuators and Devices (EAPAD) 2007*, vol. 6524, 65241P, 2007.

[9] T. Meressi and B. Paden, "Buckling control of a flexible beam using piezoelectric actuators," *Journal of Guidance, Control, and Dynamics*, vol. 16, no. 5, pp. 977–980, 1993.

[10] S. R. Moheimani and A. J. Fleming, *Piezoelectric transducers for vibration control and damping*. Springer Science & Business Media, 2006.

[11] S. Faegh, N. Jalili, and S. Sridhar, "A self-sensing piezoelectric microcantilever biosensor for detection of ultrasmall adsorbed masses: Theory and experiments," *Sensors*, vol. 13, no. 5, pp. 6089–6108, 2013.

[12] P. A. Lightsey, C. B. Atkinson, M. C. Clampin, and L. D. Feinberg, "James Webb Space Telescope: Large deployable cryogenic telescope in space," *Optical Engineering*, vol. 51, no. 1, p. 011 003, 2012.

[13] T. L. Team, "LUVOIR engineering design update," Retrieved from https://asd.gsfc.nasa.gov/luvoir/events/events/meetings/2018-11-27/presentations/01_bolcar.pdf, 2018.

[14] J. M. Hedgepeth and R. K. Miller, "Structural concepts for large solar concentrators," in *Innsbruck International Astronautical Federation Congress*, 1986.

[15] S. Kendrew, P. Doel, D. Brooks, C. Dorn, C. Yates, R. M. Dwan, I. M. Richardson, and G. Evans, "Development of a carbon fiber composite active mirror: Design and testing," *Optical Engineering*, vol. 45, no. 3, p. 033 401, 2006.

[16] *NASA's TDRS-M space communications satellite begins final testing*. Retrieved from https://www.nasa.gov/feature/goddard/2017/nasa-s-tdrs-m-space-communications-satellite-begins-final-testing/, Apr. 2019.

[17] L. Datashvili, H. Baier, E. Wehrle, T. Kuhn, and J. Hoffmann, "Large shell-membrane space reflectors," *51st AIAA/ASME/ASCE/AHS/ASC Structures, Structural Dynamics, and Materials Conference*, p. 2504, 2010.

[18] R. C. Romeo, A. B. Meinel, M. P. Meinel, and P. C. Chen, "Ultralightweight and hyperthin rollable primary mirror for space telescopes," *UV, Optical, and IR Space Telescopes and Instruments*, vol. 4013, pp. 634–640, 2000.

[19] R. Taylor, D. Turse, P. Keller, and L. Adams, "Large aperture, solid surface deployable reflector," in *Earth Science Technology Forum*, 2010.

[20] P. C. Chen, R. J. Oliversen, and R. Romeo, "Fabrication and testing of ultra-lightweight gossamer-class composite mirrors," *Highly Innovative Space Telescope Concepts*, vol. 4849, pp. 339–348, 2002.

[21] J. Fernandez, J. Banik, and E. Ardelean, "Creep effects and deployment characterization of rollable composite shell reflectors," *53rd AIAA/ASME/ASCE/AHS/ASC Structures, Structural Dynamics and Materials Conference*, p. 1955, 2012.

[22] T. Keil and J. Banik, "Stowage and deployment strength of a rollable composite shell reflector," *52nd AIAA/ASME/ASCE/AHS/ASC Structures, Structural Dynamics and Materials Conference 19th AIAA/ASME/AHS Adaptive Structures Conference 13t*, p. 2103, 2011.

[23] N. Turner, B. Goodwine, and M. Sen, "A review of origami applications in mechanical engineering," *Proceedings of the Institution of Mechanical Engineers, Part C: Journal of Mechanical Engineering Science*, vol. 230, no. 14, pp. 2345–2362, 2016.

[24] T. Tachi, "Geometric considerations for the design of rigid origami structures," *Proceedings of the International Association for Shell and Spatial Structures (IASS) Symposium*, vol. 12, no. 10, pp. 458–460, 2010.

[25] K. Kyoichi, "Lessons learned from the Space Flyer Unit (SFU) mission," *Acta Astronautica*, vol. 51, no. 11, pp. 797–806, 2002.

[26] S. A. Zirbel, R. J. Lang, M. W. Thomson, D. A. Sigel, P. E. Walkemeyer, B. P. Trease, S. P. Magleby, and L. L. Howell, "Accommodating thickness in origami-based deployable arrays," *Journal of Mechanical Design*, vol. 135, no. 11, p. 111 005, 2013.

[27] R. A. Hyde, S. N. Dixit, A. H. Weisberg, and M. C. Rushford, "Eyeglass: A very large aperture diffractive space telescope," *Highly Innovative Space Telescope Concepts*, vol. 4849, pp. 28–40, 2002.

[28] K. Miura, "Triangles and quadrangles in space," in *Symposium of the International Association for Shell and Spatial Structures (50th. 2009. Valencia). Evolution and Trends in Design, Analysis and Construction of Shell and Spatial Structures: Proceedings*, Editorial Universitat Politècnica de València, 2009.

[29] A. Vergauwen, "The design and physical modelling of deployable structures based on curved-line folding," *WIT Transactions on The Built Environment*, vol. 136, pp. 145–155, 2014.

[30] J. Mitani, "A design method for 3d origami based on rotational sweep," *Computer-Aided Design and Applications*, vol. 6, no. 1, pp. 69–79, 2009.

[31] S. J. Callens and A. A. Zadpoor, "From flat sheets to curved geometries: Origami and kirigami approaches," *Materials Today*, vol. 21, no. 3, pp. 241–264, 2018.

[32] Y. Xu, *Ferroelectric materials and their applications*. Elsevier, 2013.

[33] K. Uchino, *Piezoelectric actuators and ultrasonic motors*. Springer Science & Business Media, 1996, vol. 1.

[34] T. Bifano, "Adaptive imaging: MEMS deformable mirrors," *Nature Photonics*, vol. 5, no. 1, p. 21, 2011.

[35] Y. Hishinuma and E.-H. Yang, "Piezoelectric unimorph microactuator arrays for single-crystal silicon continuous-membrane deformable mirror," *Journal of microelectromechanical systems*, vol. 15, no. 2, pp. 370–379, 2006.

[36] E.-H. Yang, Y. Hishinuma, J.-G. Cheng, S. Trolier-McKinstry, E. Bloemhof, and B. M. Levine, "Thin-film piezoelectric unimorph actuator-based deformable mirror with a transferred silicon membrane," *Journal of Microelectromechanical ystems*, vol. 15, no. 5, pp. 1214–1225, 2006.

[37] B. R. Fernández, M. A. Bouchti, and J. Kubby, "High-stroke, high-order MEMS deformable mirrors," *Journal of Micro/Nanolithography, MEMS, and MOEMS*, vol. 12, no. 3, p. 033 012, 2013.

[38] P. Rausch, S. Verpoort, and U. Wittrock, "Unimorph deformable mirror for space telescopes: Environmental testing," *Optics Express*, vol. 24, no. 2, pp. 1528–1542, 2016.

[39] S. A. Cornelissen, A. L. Hartzell, J. B. Stewart, T. G. Bifano, and P. A. Bierden, "MEMS deformable mirrors for astronomical adaptive optics," *Adaptive Optics Systems II*, vol. 7736, p. 77362D, 2010.

[40] D. C. Redding, G. Hickey, G. Agnes, P. Eisenhardt, J. Green, J. Krist, L. Peterson, K. Stapelfeldt, W. Traub, S. Unwin, *et al.*, "Active optics for a 16-meter advanced technology large aperture space telescope," *Jet Propulsion Laboratory, Caltech, CA*, 2008.

[41] J. Steeves, *Multilayer active shell mirrors*. California Institute of Technology, 2015.

[42] S. C. Bradford, D. C. Hofmann, S. N. Roberts, J. B. Steeves, C. S. Wojnar, and D. M. Kochmann, "Energy-efficient active reflectors with improved mechanical stability and improved thermal performance," *3rd AIAA Spacecraft structures conference*, p. 0702, 2016.

[43] S. M. Ammons, M. Hart, B. Coughenour, R. Romeo, R. Martin, and M. Rademacher, "Demonstration of 17 cm robust carbon fiber deformable mirror for adaptive optics," *Astronomical Adaptive Optics Systems and Applications IV*, vol. 8149, p. 81490C, 2011.

[44] L. Lan, S. Jiang, Y. Zhou, H. Fang, Z. Wu, and J. Du, "Shape control of a reflector based on generalized zernike functions," *3rd AIAA Spacecraft Structures Conference*, p. 0704, 2016.

[45] K. Bhattacharya and G. Ravichandran, "Ferroelectric perovskites for electromechanical actuation," *Acta Materialia*, vol. 51, no. 19, pp. 5941–5960, 2003.

[46] D.-J. Kim, J.-P. Maria, A. I. Kingon, and S. Streiffer, "Evaluation of intrinsic and extrinsic contributions to the piezoelectric properties of pb (zr 1- xtx) o 3 thin films as a function of composition," *Journal of Applied Physics*, vol. 93, no. 9, pp. 5568–5575, 2003.

[47] B. P. Bruno, A. R. Fahmy, M. Stürmer, U. Wallrabe, and M. C. Wapler, "Properties of piezoceramic materials in high electric field actuator applications," *Smart Materials and Structures*, vol. 28, no. 1, p. 015 029, 2018.

[48] H. H. Krueger, "Stress sensitivity of piezoelectric ceramics: Part 1. sensitivity to compressive stress parallel to the polar axis," *The Journal of the Acoustical Society of America*, vol. 42, no. 3, pp. 636–645, 1967.

[49] ——, “Stress sensitivity of piezoelectric ceramics: Part 3. sensitivity to compressive stress perpendicular to the polar axis,” *The Journal of the Acoustical Society of America*, vol. 43, no. 3, pp. 583–591, 1968.

[50] L. Yao, J. Zhang, L. Lu, and M. Lai, “Nonlinear dynamic characteristics of piezoelectric bending actuators under strong applied electric field,” *Journal of Microelectromechanical Systems*, vol. 13, no. 4, pp. 645–652, 2004.

[51] Q.-M. Wang, Q. Zhang, B. Xu, R. Liu, and L. E. Cross, “Nonlinear piezoelectric behavior of ceramic bending mode actuators under strong electric fields,” *Journal of Applied Physics*, vol. 86, no. 6, pp. 3352–3360, 1999.

[52] S. Sherrit and B. K. Mukherjee, “Characterization of piezoelectric materials for transducers,” *arXiv preprint arXiv:0711.2657*, 2007.

[53] M. Weickgenannt, O. Sawodny, S. Neuhaeuser, and W. Sobek, “Active vibration control of a double-curved shell structure using the example of stuttgart smartshell,” *ASME 2012 International Mechanical Engineering Congress and Exposition*, pp. 1297–1304, 2012.

[54] H. Allik and T. J. Hughes, “Finite element method for piezoelectric vibration,” *International Journal for Numerical methods In Engineering*, vol. 2, no. 2, pp. 151–157, 1970.

[55] A. Preumont, *Vibration Control of Active Structures: An Introduction*. Springer, 2018, vol. 246.

[56] H. H. Tzou, *Piezoelectric Shells: Sensing, Energy Harvesting, and Distributed Control, Second Edition*. Springer, 2018, vol. 247.

[57] H. Yue, Y. Lu, Z. Deng, and H. Tzou, “Experiments on vibration control of a piezoelectric laminated paraboloidal shell,” *Mechanical Systems and Signal Processing*, vol. 82, pp. 279–295, 2017.

[58] R. Boulandet, A. Pelletier, P. Micheau, and A. Berry, “Active vibration control using self-sensing actuators: An experimental comparison of piezoelectric and electromagnetic technologies,” *Proceeding of the ASME 2014 International Mechanical Engineering Congress and Exposition*, no. CONF, V013T16A023, 2014.

[59] J. S. Archer and W. B. Palmer, “Antenna technology for quasat application,” *In NASA. Langley Research Center Large Space Antenna Systems Technol., 1984 p 251-270 (SEE N85-23813 14-15)*, 1985.

[60] Dornier, “First technology study: Multisurface control mechanism for a deployable antenna.,” *Final Report. Dornier Report RP-FA-D003*, 1987.

[61] S. Guest and S. Pellegrino, “A new concept for solid surface deployable antennas,” *Acta Astronautica*, vol. 38, no. 2, pp. 103–113, 1996.

[62] M. S. Lake, J. E. Phelps, J. E. Dyer, D. A. Caudle, A. Tam, J. Escobedo-Torres, and E. P. Kasl, "Deployable primary mirror for space telescopes," *Advanced Telescope Design, Fabrication, and Control*, vol. 3785, pp. 14–26, 1999.

[63] Champagne, S. Hansen, T. Newswander, and B. Crowther, "Cubesat image resolution capabilities with deployable optics and current imaging technology," 2014.

[64] N. Schwartz, D. Pearson, S. Todd, A. Vick, D. Lunney, and D. MacLeod, "A segmented deployable primary mirror for earth observation from a cubesat platform," 2016.

[65] N. N. Lee, J. W. Burdick, P. Backes, S. Pellegrino, K. Hogstrom, C. Fuller, B. Kennedy, J. Kim, R. Mukherjee, C. Seubert, *et al.*, "Architecture for in-space robotic assembly of a modular space telescope," *Journal of Astronomical Telescopes, Instruments, and Systems*, vol. 2, no. 4, p. 041 207, 2016.

[66] J. J. Rey, A. Wirth, A. Jankevics, F. Landers, D. Rohweller, C. B. Chen, and A. Bronowicki, "A deployable, annular, 30m telescope, space-based observatory," in *Space Telescopes and Instrumentation 2014: Optical, Infrared, and Millimeter Wave*, International Society for Optics and Photonics, vol. 9143, 2014, p. 914 318.

[67] G. Durand, J. Amiaux, M. Sauvage, T. Martens, J. Austin, S. Chesne, C. Collette, J. Pareschi, Y. Penfornis, G. Valsecchi, *et al.*, "Talc a far-infrared 20m space telescope and the elicsir consortium to reach trl 3," *International Conference on Space OpticsICSO 2016*, vol. 10562, 105623R, 2017.

[68] R. C. Romeo and R. N. Martin, "Unique space telescope concepts using cfrp composite thin-shelled mirrors and structures," in *UV/Optical/IR Space Telescopes: Innovative Technologies and Concepts III*, International Society for Optics and Photonics, vol. 6687, 2007, 66870U.

[69] A. Meinel, M. Meinel, and R. Romeo, "Rollable thin shell composite-material paraboloidal mirrors," *NASA Tech Briefs*, 2003.

[70] K. Patterson, N. Yamamoto, and S. Pellegrino, "Thin deformable mirrors for a reconfigurable space aperture," in *53rd AIAA/ASME/ASCE/AHS/ASC Structures, Structural Dynamics and Materials Conference*, 2012, AIAA–2012.

[71] J. Steeves and S. Pellegrino, "Ultra-thin highly deformable composite mirrors," *54th AIAA/ASME/ASCE/AHS/ASC Structures, Structural Dynamics, and Materials Conference*, p. 1523, 2013.

[72] Y. Chen, R. Peng, and Z. You, "Origami of thick panels," *Science*, vol. 349, no. 6246, pp. 396–400, 2015.

[73] B. Audoly and Y. Pomeau, *Elasticity and geometry: from hair curls to the nonlinear response of shells*. Oxford University Press, 2010.

[74] K. Miura, “Method of packaging and deployment of large membranes in space,” *The Institute of Space and Astronautical Science Report*, vol. 618, p. 1, 1985.

[75] T. A. Evans, R. J. Lang, S. P. Magleby, and L. L. Howell, “Rigidly foldable origami gadgets and tessellations,” *Royal Society open science*, vol. 2, no. 9, p. 150 067, 2015.

[76] A. M. Watt and S. Pellegrino, “Tape-spring rolling hinges,” *Proceedings of the 36th Aerospace Mechanisms Symposium*, pp. 15–17, 2002.

[77] P. A. Halverson, “Multi-stable compliant rolling-contact elements,” 2007.

[78] H. Asada, J. J. Slotine, and J. J. Slotine, *Robot analysis and control*. John Wiley & Sons, 1986.

[79] J. J. Uicker, G. R. Pennock, J. E. Shigley, *et al.*, *Theory of machines and mechanisms*. Oxford University Press New York, NY, 2011, vol. 1.

[80] H. Mallikarachchi and S. Pellegrino, “Quasi-static folding and deployment of ultrathin composite tape-spring hinges,” *Journal of Spacecraft and Rockets*, vol. 48, no. 1, pp. 187–198, 2011.

[81] *Metglas$^{\H{o}}$, Inc.* Retrieved from http://www.metglas.com, Feb. 2019.

[82] Z. You and Y. Chen, *Motion structures: deployable structural assemblies of mechanisms*. CRC Press, 2014.

[83] *Prazisions Glas Optik Gmbh. D263 T Borosilicate Thin Glass.* Retrieved from https://www.pgo-online.com/intl/D263.html, Apr. 2019.

[84] *Beryllium O-30-L, Optical Grade.* Retrieved from http://www.matweb.com/search/datasheet.aspx?matguid=&ckck=1, Apr. 2019.

[85] K. D. Patterson, “Lightweight deformable mirrors for future space telescopes,” PhD thesis, California Institute of Technology, 2014.

[86] *Piezo Systems Inc, PZT-5A4E single sheets.* Retrieved from https://support.piezo.com/article/62-material-properties, Apr. 2019.

[87] I. M. Daniel, O. Ishai, I. M. Daniel, and I. Daniel, *Engineering mechanics of composite materials*. Oxford University Press, New York, 1994, vol. 3.

[88] *North Thin Ply Technology.* Retrieved from https://www.thinplytechnology.com/, Apr. 2019.

[89] J. M. Fernandez and T. W. Murphey, “A simple test method for large deformation bending of thin high strain composite flexures,” in *2018 AIAA Spacecraft Structures Conference*, 2018, p. 0942.

[90] D. B. Adams, L. T. Watson, O. Seresta, and Z. Gürdal, “Global/local iteration for blended composite laminate panel structure optimization subproblems,” *Mechanics of Advanced Materials and Structures*, vol. 14, no. 2, pp. 139–150, 2007.

[91] A. J. Fleming and K. K. Leang, *Design, modeling and control of nanopositioning systems*. Switzerland: Springer International Publishing, 2014.

[92] M. A. Rahman and A. A. Mamun, "Nonlinearity analysis, modeling and compensation in pzt micro actuator of dual-stage actuator system," *IEEE/ASME Transactions on mechatronics*, vol. 14, no. 1, pp. 21–31, 2009.

[93] I. L. APC, *Piezoelectric ceramics: principles and applications, 2nd ed*. APC International, 2011.

[94] M. Vijaya, *Piezoelectric materials and devices: applications in engineering and medical sciences*. CRC Press, 2016.

[95] C. M. Landis, "Non-linear constitutive modeling of ferroelectrics," *Current Opinion in Solid State & Materials Science*, vol. 8, pp. 59–69, 2004.

[96] P. R. Potnis, N. T. Tsou, and J. E. Huber, "A review of domain modelling and domain imaging techniques in ferroelectric crystals," *Materials*, vol. 4, no. 2, pp. 417–496, 2011.

[97] J. Shieh, J. E. Huber, and N. A. Fleck, "An evaluation of switching criteria for ferroelectrics under stress and electric field," *Acta Materialia*, vol. 51, no. 20, pp. 6123–6137, 2003.

[98] J. E. Huber, *Electromechanical Models of Ferroelectric Materials*. Springer, Cham, 2018.

[99] Y. Su and C. M. Landis, "Continuum thermodynamics of ferroelectric domain evolution: Theory, finite element implementation, and application to domain wall pinning," *Journal of the Mechanics and Physics of Solids*, vol. 55, no. 2, pp. 280–305, 2007.

[100] D. e. a. Schrade, "Continuum thermodynamics of ferroelectric domain evolution: Theory, finite element implementation, and application to domain wall pinning," *Computer methods in applied mechanics and engineering*, vol. 196, no. 41, pp. 4365–4374, 2007.

[101] A. Vidyasagar, W. L. Tan, and D. M. Kochmann, "Predicting the effective response of bulk polycrystalline ferroelectric ceramics via improved spectral phase field methods," *Journal of the Mechanics and Physics of Solids*, 2017.

[102] W. Zhang and K. Bhattacharya, "A computational model of ferroelectric domains. part i: Model formulation and domain switching," *Acta Materialia*, vol. 53, no. 1, pp. 185–198, 2005.

[103] ——, "A computational model of ferroelectric domains. part ii: Grain boundaries and defect pinning," *Acta Materialia*, vol. 53, no. 1, pp. 199–209, 2005.

[104] A. Kontsos and C. M. Landis, "Computational modeling of domain wall interactions with dislocations in ferroelectric crystals," *International Journal of Solids and Structures*, vol. 46, pp. 1491–1498, 2009.

[105] B. e. a. Völker, “Multiscale modeling for ferroelectric materials: A transition from the atomic level to phase-field modeling,” *Continuum Mechanics and Thermodynamics*, vol. 23, no. 5, pp. 435–451, 2011.

[106] S. C. Hwang and R. M. McMeeking, “The predictions of switching in polycrystalline ferroelectric ceramics,” *Ferroelectrics*, vol. 207, pp. 465–495, 1998.

[107] C. S. Lynch, “On the development of multiaxial phenomenological constitutive laws for ferroelectric ceramics,” *Journal of Intelligent Material System*, vol. 9, no. 7, pp. 555–563, 1998.

[108] A. C. F. Cocks and R. M. McMeeking, “A phenomenological constitutive law for the behaviour of ferroelectric ceramics,” *Ferroelectrics*, vol. 228, no. 1, pp. 219–228, 1999.

[109] M. Kamlah and C. Tsakmakis, “Phenomenological modeling of the non-linear electro-mechanical coupling in ferroelectrics,” *International Journal of Solids and Structures*, vol. 36, no. 5, pp. 669–695, 1999.

[110] ——, “A thermodynamically and microscopically motivated constitutive model for piezoceramics,” *International Journal of Solids and Structures*, vol. 28, pp. 409–418, 2003.

[111] C. M. Landis, “Fully coupled, multi-axial, symmetric constitutive laws for polycrystalline ferroelectric ceramics,” *Journal of the Mechanics and Physics of Solids*, vol. 50, no. 1, pp. 127–152, 2002.

[112] ——, “In-plane complex potentials for a special class of materials with degenerated piezoelectric properties,” *International Journal of Solids and Structures*, vol. 41, pp. 695–715, 2004.

[113] C. M. Landis, J. Wang, and J. Sheng, “Micro-electromechanical determination of the possible remnant strain and polarization states in polycrystalline ferroelectrics and the implications for phenomenologcial constitutive theories,” *Journal of intelligent material systems and structures*, vol. 15, pp. 513–525, 2004.

[114] Klinkel and S., “A thermodynamic consistent 1d model for ferroelastic and ferroelectric hysteresis effects in piezoceramics,” *Communications in Numerical Methods in Engineering*, vol. 22, no. 7, pp. 727–739, 2006.

[115] ——, “A phenomenological constitutive model for ferroelastic and ferroelectric hysteresis effects in ferroelectric ceramics,” *International Journal of Solids and Structures*, vol. 43, no. 22, pp. 7197–7222, 2006.

[116] S. Maniprakash, R. Maniprakash, A. Menzel, and A. Arockiarajan, “Experimental investigation, modeling and simulation of rate-dependent response of 1-3 ferroelectric composites,” *Mechanics of Materials*, vol. 94, pp. 91–105, 2016.

[117] S. Maniprakash, R. Maniprakash, and A. Menzel, "A multi-surface model for ferroelectric ceramics application to cyclic electric loading with changing maximum amplitude," *Philosophical Magazine*, vol. 96, no. 13, pp. 1263–1284, 2016.

[118] S. Stark, P. Neumeister, and H. Balke, "A hybrid phenomenological model for ferroelectroelastic ceramics. part ii: Morphotropic pzt ceramics," *Journal of the Mechanics and Physics of Solids*, vol. 95, pp. 805–826, 2016.

[119] W. L. Tan and D. M. Kochmann, "An effective constitutive model for polycrystalline ferroelectric ceramics: Theoretical framework and numerical examples," *Computational Materials Science*, vol. 136, pp. 223–237, 2017.

[120] D. K. Dusthakar, M. Andreas, and B. Svendsen, "Laminate-based modelling of single and polycrystalline ferroelectric materialsapplication to tetragonal barium titanate," *Mechanics of Materials*, vol. 117, pp. 234–254, 2018.

[121] S. Stark, P. Neumeister, and H. Balke, "A hybrid phenomenological model for ferroelectroelastic ceramics. part i: Single phased materials," *Journal of the Mechanics and Physics of Solids*, vol. 95, pp. 774–804, 2016.

[122] C. S. Lynch, "The effect of uniaxial stress on the electro-mechanical response of 8/65/35 plzt," *Acta Materialia*, vol. 44, no. 10, pp. 4137–4148, 1996.

[123] E. F. Crawley and K. B. Lazarus, "Induced strain actuation of isotropic and anisotropic plates," *AIAA Journal*, vol. 29, no. 6, pp. 944–951, 1991.

[124] D. L. DeVoe and A. P. Pisano, "Modeling and optimal design of piezoelectric cantilever microactuators," *Journal of Microelectromechanical systems*, vol. 6, no. 3, pp. 266–270, 1997.

[125] S. Prasanna and S. M. Spearing, "Materials selection and design of microelectrothermal bimaterial actuators," *Journal of Microelectromechanical Systems*, vol. 16, no. 2, pp. 248–259, 2007.

[126] K. J. Yoon, K. H. Park, S. K. Lee, N. S. Goo, and H. C. Park, "Analytical design model for a piezo-composite unimorph actuator and its verification using lightweight piezo-composite curved actuators," *Smart Materials and Structures*, vol. 13, no. 3, p. 459, 2004.

[127] E. F. Crawley and K. B. Lazarus, "Use of piezoelectric actuators as elements of intelligent structures," *AIAA Journal*, vol. 25, no. 10, pp. 1373–1385, 1987.

[128] S. Stark, P. Neumeister, and H. Balke, "Some aspects of macroscopic phenomenological material models for ferroelectroelastic ceramics," *International Journal of Solids and Structures*, vol. 80, pp. 359–367, 2016.

[129] T. Belytschko, W. K. Liu, B. Moran, and K. Elkhodary, *Nonlinear finite elements for continua and structures*. John wiley & sons, 2013.

[130] D. Damjanovic, "A morphotropic phase boundary system based on polarization rotation and polarization extension," *Applied Physics Letters*, vol. 97, no. 6, p. 062 906, 2010.

[131] J. Sinha, "Modified Sawyer and Tower circuit for the investigation of ferroelectric samples," *Journal of Scientific Instruments*, vol. 42, no. 9, p. 696, 1965.

[132] M. Wallace, R. L. Johnson-Wilke, and et al, "In situ measurement of increased ferroelectric/ferroelastic domain wall motion in declamped tetragonal lead zirconate titanate thin films," *Journal of Applied Physics*, vol. 117, no. 5, p. 054 103, 2015.

[133] A. Haug, V. Knoblauch, and R. M. McMeeking, "Combined isotropic and kinematic hardening in phenomenological switching models for ferroelectric ceramics," *International Journal of Engineering Science*, vol. 1, pp. 887–901, 2003.

[134] S. S. Aphale, S. Devasia, and S. R. Moheimani, "High-bandwidth control of a piezoelectric nanopositioning stage in the presence of plant uncertainties," *Nanotechnology*, vol. 19, no. 12, p. 125 503, 2008.

[135] J.-H. Han, J. Tani, and J. Qiu, "Active flutter suppression of a lifting surface using piezoelectric actuation and modern control theory," *Journal of Sound and Vibration*, vol. 291, no. 3-5, pp. 706–722, 2006.

[136] K. C. Sahu, J. Tuhkuri, and J. Reddy, "Active structural acoustic control of a softcore sandwich panel using multiple piezoelectric actuators and reddy's higher order theory," *Journal of Low Frequency Noise, vibration and Active Control*, vol. 34, no. 4, pp. 385–411, 2015.

[137] S. Bhalla and C. K. Soh, "Structural health monitoring by piezo–impedance transducers. ii: Applications," *Journal of Aerospace Engineering*, vol. 17, no. 4, pp. 166–175, 2004.

[138] L. Liu, M. A. Vorontsov, E. Polnau, T. Weyrauch, and L. A. Beresnev, "Adaptive phase-locked fiber array with wavefront phase tip-tilt compensation using piezoelectric fiber positioners," *Atmospheric Optics: Models, Measurements, and Target-in-the-Loop Propagation*, vol. 6708, 67080K, 2007.

[139] M. R. Bolcar, L. Feinberg, K. France, B. J. Rauscher, D. Redding, and D. Schiminovich, "Initial technology assessment for the large-aperture uv-optical-infrared (luvoir) mission concept study," *Space Telescopes and Instrumentation 2016: Optical, Infrared, and Millimeter Wave*, vol. 9904, 99040J, 2016.

[140] E. Anderson, N. Hagood, and J. Goodlife, "Self-sensing piezoelectric actuation-analysis and application to controlled structures," *33rd Structures, Structural Dynamics and Materials Conference*, p. 2465, 1992.

[141] G. E. Simmers Jr, J. R. Hodgkins, D. D. Mascarenas, G. Park, and H. Sohn, "Improved piezoelectric self-sensing actuation," *Journal of Intelligent Material Systems and Structures*, vol. 15, no. 12, pp. 941–953, 2004.

[142] J. J. Dosch, D. J. Inman, and E. Garcia, "A self-sensing piezoelectric actuator for collocated control," *Journal of Intelligent material systems and Structures*, vol. 3, no. 1, pp. 166–185, 1992.

[143] R. L. Clark, W. R. Saunders, G. P. Gibbs, *et al.*, "Adaptive structures: Dynamics and control," 1998.

[144] S. Kuiper and G. Schitter, "Active damping of a piezoelectric tube scanner using self-sensing piezo actuation," *Mechatronics*, vol. 20, no. 6, pp. 656–665, 2010.

[145] W. W. Law, W. Liao, and J. Huang, "Vibration control of structures with self-sensing piezoelectric actuators incorporating adaptive mechanisms," *Smart Materials and Structures*, vol. 12, no. 5, p. 720, 2003.

[146] J. S. Vipperman and R. L. Clark, "Implementation of an adaptive piezoelectric sensoriactuator," *AIAA Journal*, vol. 34, no. 10, pp. 2102–2109, 1996.

[147] A. Erturk and D. J. Inman, "A distributed parameter electromechanical model for cantilevered piezoelectric energy harvesters," *Journal of Vibration and Acoustics*, vol. 130, no. 4, p. 041 002, 2008.

[148] S. Raja, P. Sinha, G. Prathap, and D. Dwarakanathan, "Thermally induced vibration control of composite plates and shells with piezoelectric active damping," *Smart Materials and structures*, vol. 13, no. 4, p. 939, 2004.

[149] E. Grasso, *Self sensing techniques for piezoelectric vibration applications*. Logos Verlag Berlin GmbH, 2014.

[150] M. Laslandes, S. Pellegrino, J. Steeves, and K. Patterson, "Optimization of electrode configuration in surface-parallel actuated deformable mirrors," *Adaptive Optics Systems IV*, vol. 9148, p. 914 843, 2014.

[151] K. Zhou, J. C. Doyle, K. Glover, *et al.*, *Robust and optimal control*. Prentice Hall, New Jersey, 1996, vol. 40.

[152] M. Weickgenannt, S. Neuhaeuser, B. Henke, W. Sobek, and O. Sawodny, "Optimal sensor placement for state estimation of a thin double-curved shell structure," *Mechatronics*, vol. 23, no. 3, pp. 346–354, 2013.

[153] M. J. Balas, "Direct velocity feedback control of large space structures," *Journal of Guidance, Control, and Dynamics*, vol. 2, no. 3, pp. 252–253, 1979.

[154] H. K. Khalil and J. W. Grizzle, *Nonlinear systems*. Prentice Hall, New Jersey, 2002, vol. 3.

[155] E. Grasso, N. Totaro, H. Janocha, and D. Naso, "Piezoelectric self sensing actuators for high voltage excitation," *Smart Materials and Structures*, vol. 22, no. 6, p. 065 018, 2013.

[156] L. Jin, "Broadband dielectric response in hard and soft pzt," EPFL, Tech. Rep., 2011.

[157] Q. Zhou, S. Lau, D. Wu, and K. K. Shung, "Piezoelectric films for high frequency ultrasonic transducers in biomedical applications," *Progress in Materials Science*, vol. 56, no. 2, pp. 139–174, 2011.

[158] Z.-G. Ye, *Handbook of advanced dielectric, piezoelectric and ferroelectric materials: Synthesis, properties and applications*. Elsevier, 2008.

[159] L. Lindbom, M. Sternad, and A. Ahlén, "Tracking of time-varying mobile radio channels. 1. the wiener lms algorithm," *IEEE Transactions on Communications*, vol. 49, no. 12, pp. 2207–2217, 2001.

[160] S. M. Kuo and D. Morgan, *Active noise control systems: algorithms and DSP implementations*. John Wiley & Sons, Inc., 1995.

[161] J. P. How, E. H. Anderson, D. W. Miller, and S. R. Hall, "High-bandwidth control for low-area-density deformable mirrors," *Structures Sensing and Control*, vol. 1489, pp. 148–163, 1991.

[162] D. Alaluf, R. Bastaits, K. Wang, M. Horodinca, G. Martic, B. Mokrani, and A. Preumont, "Unimorph mirror for adaptive optics in space telescopes," *Applied Optics*, vol. 57, no. 14, pp. 3629–3638, 2018.

[163] A. Riccardi, G. Brusa, P. Salinari, D. Gallieni, R. Biasi, M. Andrighettoni, and H. M. Martin, "Adaptive secondary mirrors for the large binocular telescope," *Adaptive Optical System Technologies II*, vol. 4839, pp. 721–733, 2003.

[164] *Giant Magellan Telescope Science and technology.* Retrieved from `https://www.gmto.org/resources/`, Apr. 2019.

[165] H. P. Stahl, L. D. Feinberg, and S. C. Texter, "JWST primary mirror material selection," *Optical, Infrared, and Millimeter Space Telescopes*, vol. 5487, pp. 818–825, 2004.